



SAPIENZA
UNIVERSITÀ DI ROMA

Doctor of Philosophy in Biophysics - XXIX Cycle

**A novel mechanism of contrast in MRI:
pseudo super-diffusion of water molecules unveils
microstructural details in biological tissues.**

Alessandra Caporale

PhD Coordinator:

prof. Alfredo Colosimo

Thesis Advisor:

dott.ssa Silvia Capuani

Declaration

“I hereby declare that this submission is my own work and that, to the best of my knowledge and belief, it contains no material which to a substantial extent has been accepted for the award of any other degree or diploma of the university or other institute of higher learning, except where due acknowledgment has been made in the text.”

*To my Brother,
to my Mum, and Dad.*

'[...] L'essentiel est invisible pour les yeux.'
(Antoine de Saint-Exupery, *The Petit Prince*)

'Well this is true for humans, but not for a water molecule...'
(Alessandra Caporale, *My PhD revelation*)

Abstract

The goal of this work is to investigate the properties of the contrast provided by Anomalous Diffusion (AD) γ -imaging technique and to test its potential in detecting tissue microstructure. The collateral purpose is to implement this technique by optimizing data acquisition and data processing, with the long term perspective of adoption in massive *in vitro*, *in vivo* and clinical studies.

The AD γ -imaging technique is a particular kind of Diffusion Weighted-Magnetic Resonance Imaging (DW-MRI). It represents a refinement of conventionally used DW-MRI methods, sharing with them the advantage of being non invasive, since it uses water as an endogenous contrast agent. Besides, it is more suitable to the study of complex tissues, because it is based on a theoretical model that overcomes the simplistic Gaussian assumption. While the Gaussian assumption predicates the linearity between the average molecular displacement of water and the diffusing time, as in case of diffusion in isotropic, homogeneous and infinite environments, a number of experiments performed *in vitro* and *in vivo* on both animals and humans showed an anomalous behavior of water molecules, with a non linear relation between the distance travelled and the elapsed time.

In particular, the γ -parameter quantifies water *pseudo* super-diffusion, a peculiarity due to the fact that water diffusion occurs in multi-compartments and it is probed by means of MRI. In fact, a restricted diffusion is rather predicted for water diffusing in biological tissues.

Recently, the trick that allows to make the traditional DW-MRI acquisition sequence suitable for *pseudo* super-diffusion quantification has been unveiled, and in short it consists in performing DW experiments varying the diffusion gradient strengths, at a constant diffusive time. The γ -parameter is extracted by

fitting DW-data to a stretched-exponential function. Finally, probing water diffusion in different directions allows to reconstruct a γ -tensor, with scalar invariants that quantify the entity of AD and its anisotropy in a given volume element.

In vitro results on inert materials revealed that γ correlates with internal gradients arising from magnetic susceptibility differences ($\Delta\chi$) between neighboring compartments, and that it reflects the multi-compartmentalization of the space explored by diffusing molecules. Furthermore, values of γ compatible with a description of super-diffusive motion were found. This anomaly can be explained considering that the presence of $\Delta\chi$ induce an additional attenuation to the signal, simulating a *pseudo* super-diffusion. Finally, *In vivo* results on human brain showed that γ is more effective in discriminating among different brain regions compared to conventional DW-MRI parameters.

These studies suggest that the contrast provided by AD γ -imaging is influenced by an interplay of two factors, $\Delta\chi$ -effects on one hand, multi-compartmentalization on the other hand, through which γ could reflect tissue microstructure.

With the aim to shed some light on this issue I performed AD γ -imaging in excised mouse spinal cord (MSC) at 9.4 T and healthy human brain at 3.0 T. The adoption of MSC was motivated by its current use in studies of demyelination due to an induced pathology that mimics Multiple Sclerosis alterations, and by its simplified geometry. I acquired DW-data with parameters optimized for the particular system chosen: the MSC was scanned along 3 orthogonal directions, thus an apparent γ was derived; for the *in vivo* studies I used more directions and I extracted a γ -tensor.

I found that γ and its anisotropy reflected the microstructure of spinal cord tracts (such as the axon diameters and the axonal density). I investigated both

in MSC and human brain the relation between γ and the rate of relaxation ($R2^*$), a parameter well-known to reflect $\Delta\chi$, and found significant linear correlations. Because of this γ was able to differentiate white matter regions on the basis of their spatial orientation, and gray matter regions on the basis of their intrinsic iron content in human brain imaged at 3.0 T.

These results suggest that AD γ -imaging could be an alternative or complementary technique to DW-MRI in the field of neuroscience. Indeed it could be useful for the assessment of the bulk susceptibility inhomogeneity, which reflects iron deposition, the hallmark of several neurodegenerative diseases.

The part of this thesis work concerning the *in vivo* experiment in human brain gave rise to a paper published on NeuroImage, a relevant scientific journal in the field of MRI applied to brain investigation.

Acknowledgments

The word 'thank you' is a sort of prayer. Whenever we say it, we give the thanked person and ourselves a sense of relief. Someone could think there might be little place for emotionality in a scientific thesis, but I believe the Acknowledgments session is a big place, though.

Usually what comes after is a sort of list with the names of the people we would like to thank, and here I must follow the rule.

Thank you Dr. Silvia Capuani, the One who bet on me and struggled to make me understand my value. You have been there, ready to answer to my questions, as well as ready to question me about the correctness of my answers. I cannot say I have understood everything, but I am pretty sure this three years-PhD has changed (in better) the microstructure of my brain. Thank you for having showed me your proficiency, and how an NMR spectrometer works, and how it does not.

Thank you to Prof. Felix Wehrli and to your scientific team, for providing the most beautiful fixed mouse spinal cord I have ever seen.

Thank you to Dr. Marco Bozzali, for offering me your knowledge on neuroanatomy and allowing me to acquire in vivo data at the Santa Lucia Foundation.

Thank you Dr. Marco Palombo, for having shared with me some really useful MATLAB code, that was the early basis of the data processing of this work, and thank you for your patience and delightful explanations on demand.

Thank you Dr. Giulia Di Pietro, for having shared with me doubts, certainties, joy and pain. Thank you for showing me your discipline, your organization, and your pragmatism, and how to get the best from Microsoft Office.

Thank you Dr. Daniele Mascali, for your colorful smile, your availability and kindness, for having shared with me some explorations of ERICE's ruins, and having supported me with your timeless positivity.

Thank you Dr. Michele Guerreri, for your precious support in making some useful \$-code, for your sharpness and positivity in the critical moments; thank you Dr. Maria Giovanna Di Trani, for your happiness and your patience in drawing masks on DW-images; thank you Guglielmo Genovese, simply for being there.

Since during these years the work place has become for me a kind of second house, these people have become a kind of second family.

Finally, thank you Prof. Alfredo Colosimo for your priceless commitment in organizing seminars, stimulating discussions and a healthy climate of competitiveness.

Table of contents

Table of contents	13
List of Figures and Tables	18
List of abbreviations	21
Introduction	23
Outline of the thesis.....	25
Chapter 1 Magnetic Resonance Imaging: imaging matter exploiting nuclear magnetism	27
1.1 Where does the signal come from?	27
1.1.1 The spin	28
1.1.2 The magnetism.....	30
1.1.3 The nuclear magnetism and Larmor precession.....	31
1.1.4 The macroscopic magnetization.....	33
1.2 How to reveal the signal?	35
1.2.1 The transverse magnetization and the Free Induction Decay	36
1.2.2 The semi-classical description.....	37
1.2.3 The Bloch equation and relaxation phenomena.....	40
1.2.4 Signal detection and spin manipulation.....	42
1.2.4.1 The Spin Echo sequence	44
1.2.4.2 The Stimulated Echo sequence	45
.....	49
1.3 How to perform 3D imaging?.....	50
1.3.1 Magnetic field gradients and k-space.....	51
1.3.2 Selective excitation	53

1.3.3	Image reconstruction	54
1.3.3.1	An example of k-space sampling: Echo Planar Imaging	55
1.3.4	Image parameters	56
1.3.4.1	The sampling rate	56
1.3.4.2	The Field of View	57
1.3.4.3	The spatial resolution.....	57
1.3.4.4	The Signal to Noise Ratio and the Contrast to Noise Ratio.....	58
1.3.4.5	Spatial coordinates and imaging planes.....	59
 Chapter 2 Diffusion Weighted Imaging: imaging matter exploiting molecular diffusion		63
2.1	Molecular diffusion examined at a macroscopic scale: classic description	64
2.1.1	The first Fick's law	64
2.1.2	The second Fick's law	65
2.1.3	Anisotropic diffusion and the diffusion tensor.....	67
2.2	Molecular diffusion examined at a microscopic scale: probabilistic description	71
2.2.1	Self-diffusion and self-correlation function.....	72
2.3	How to exploit molecular diffusion in MRI?	75
2.3.1	Spin labeling with the use of diffusion gradients	76
2.3.2	Pulsed Gradient Spin Echo and Stimulated Echo sequences.....	79
2.3.3	Diffusion Weighting Imaging and Diffusion Tensor Imaging	81
2.4	DWI based on the Gaussian assumption: state of the art	87
2.4.1	Clinical applications of Gaussian-DWI and DTI.....	88
 Chapter 3 Anomalous diffusion: when water diffuses in complex media		91
3.1	When the Gaussian assumption is not enough.....	91
3.2	From random walk to Continuous Time Random Walk	92

3.2.1	Brownian diffusion and the random walk	93
3.2.2	Anomalous diffusion and the Continuous Time Random Walk ...	94
3.3	CTRW: particular cases	96
3.3.1	The super-diffusion or Lévy walks	97
3.3.2	The sub-diffusion	98
3.3.3	Anomalous diffusion phase diagram.....	99
3.4	Relationship between the NMR signal and the motion propagator ..	102
3.5	Pseudo super-diffusion of water: state of the art.....	104

Chapter 4 Pseudo super-diffusion of water in mouse spinal cord: in vitro study.109

4.1	Rationale.....	109
4.1.1	Anatomy of the spinal cord	109
4.1.1.1	Gross anatomy of mouse spinal cord	110
4.1.1.2	Motivations of the chosen sample for the in vitro investigation 111	
4.1.2	Multiple water pools.....	112
4.1.3	Rate of relaxation and magnetic field inhomogeneity	112
4.2	Materials and Methods	113
4.2.1	Data acquisition	113
4.2.2	Data analysis	114
4.2.2.1	Selection of Regions of Interest (ROIs)	116
4.3	Results	119
4.4	Discussion.....	127
4.5	Conclusions	130

Chapter 5 Pseudo super-diffusion of water in healthy human brain: in vivo study.....133

5.1	Rationale.....	133
-----	----------------	-----

5.1.1	Anatomy of the human brain	133
5.1.1.1	White Matter (WM) fibers.....	135
5.1.1.2	Subcortical Gray Matter (GM).....	135
5.1.2	Magnetic susceptibility differences in the brain and their evaluation.....	136
5.2	Materials and Methods	138
5.2.1	Data acquisition	138
5.2.2	Data analysis	139
5.2.2.1	Correction of eddy current induced distortions.....	140
5.2.2.2	Extraction of parametric maps	141
5.2.2.3	Signal to Noise Ratio and its effect on AD- γ estimation.....	142
5.2.2.4	Automated selection of WM and GM regions and fibers orientation estimation.....	144
5.2.2.5	Iron content and magnetic susceptibility of selected ROIs	146
5.3	Statistical analysis.....	146
5.4	Results	149
5.4.1	Signal to Noise Ratio and its effect on AD γ estimation	149
5.4.2	Anomalous diffusion in WM vs free diffusion in CSF	154
5.4.3	R2* reflects magnetic inhomogeneity in WM and GM ROIs	155
5.4.4	AD-metrics provide a peculiar contrast compared to DTI-metrics 158	
5.4.5	AD-metrics correlates with R2* in WM and GM ROIs.....	160
5.4.6	Relation between AD-metrics and magnetic susceptibility	161
5.5	Discussion.....	164
5.5.1	Overview of experimental methods and reliability of DWIs	164
5.5.2	R2* reflects magnetic susceptibility inhomogeneity in WM and GM ROIs	165
5.5.3	AD-metrics relation with χ and R2*	166
5.5.4	Magnetic susceptibility inhomogeneity in WM	167

5.5.5	Discrimination of WM and GM ROIs.....	168
5.5.6	Is AD-imaging appealing in the field of neurology?	169
5.5.7	Critical points, limitations and improvements	171
5.6	Conclusions	175
Conclusions.....		177
References		181
Appendix A – Basics and collateral knowledge		191
A1.	The Polarization of Electromagnetic Waves	191
Appendix B – Scientific dissemination.....		193
B1 -	The γ -parameter of Anomalous Diffusion quantified in human brain by MRI depends on local magnetic susceptibility differences	193

List of Figures and Tables

FIGURE 1.1 - THE SPLITTING OF ENERGY LEVELS DUE TO ZEEMAN EFFECT AND LARMOR PRECESSION.	35
FIGURE 1.2 - SKETCH OF NMR SIGNAL DETECTED FROM A LONGITUDINAL AND A TRANSVERSAL COIL..	47
FIGURE 1.3 - THE EMERGING OF TRANSVERSAL MAGNETIZATION.....	47
FIGURE 1.4 - MACROSCOPIC MAGNETIZATION IN DIFFERENT REFERENCE FRAMES.....	48
FIGURE 1.5 - AXIAL HUMAN BRAIN MAPS OF T1 AND T2 RELAXATION TIME.. ..	48
FIGURE 1.6 - FREE INDUCTION DECAY (FID) AND THE ABSORPTION SPECTRUM.. ..	49
FIGURE 1.7 - SKETCH OF A SPIN ECHO SEQUENCE.....	49
FIGURE 1.8 - SKETCH OF A STIMULATED ECHO SEQUENCE.....	50
FIGURE 1.9 - SAMPLING OF K-SPACE OR RECIPROCAL-SPACE.	61
FIGURE 1.10 - SPIN ECHO-ECHO PLANAR IMAGING SEQUENCE AND EPI SAMPLING OF K-SPACE.....	61
FIGURE 1.11 - IMAGING PLANES COMMONLY USED IN MRI.	62
FIGURE 2.1 - SKETCH REPRESENTING A PARALLELEPIPED WHERE MOLECULES OF SOLUTE ARE DIFFUSING INSIDE A SOLVENT, WHEN THERE IS A CONCENTRATION GRADIENT BETWEEN TWO COMPARTMENTS.....	70
FIGURE 2.2 - DIFFUSION ELLISSOIDS.....	71
FIGURE 2.3 - GAUSSIAN DISTRIBUTION OF DISPLACEMENTS AND A RANDOM WALK TRAJECTORY.....	75
FIGURE 2.4 - CUMULATIVE PHASE DIAGRAM RELATIVE TO THE FORMATION OF A SPIN ECHO IN THE PRESENCE OF A STEADY MAGNETIC FIELD GRADIENT.....	84
FIGURE 2.5 - PULSED GRADIENT SPIN ECHO (PGSE) SEQUENCE AND THE STIMULATED ECHO VERSION.	85
FIGURE 2.6 - CUMULATIVE PHASE DIAGRAM FOR SPIN ECHO FORMATION IN THE PGSE EXPERIMENT.	86
FIGURE 2.7 - DTI PARAMETRIC MAPS OF HEALTHY HUMAN BRAIN.....	87
FIGURE 2.8 - DWI AND DTI APPLICATIONS. A) ADC PARAMETRIC MAP SHOWING A LEFT HEMISPHERE ISCHEMIA.....	89
FIGURE 3.1 - SKETCH REPRESENTING RANDOM MOTION AND ITS GENERALIZATIONS.	96
FIGURE 3.2 - PROPAGATOR PROBABILITY DENSITY FUNCTIONS.	101
FIGURE 3.3 - ANOMALOUS DIFFUSION PHASE DIAGRAM AND THE MSD.....	101
FIGURE 3.4 - DEVIATIONS FROM MONO-EXPONENTIAL SIGNAL DECAY.	106
FIGURE 3.5 - MEAN Γ VALUES ($M\Gamma$), MEASURED USING PGSTE (BLACK DATA POINTS) AND BIPOLAR GRADIENT PGSTE (GRAY DATA POINTS).....	106
FIGURE 3.6 - DISCRIMINATION AMONG DIFFERENT BRAIN REGIONS: $M\Gamma$ AND MD	107

FIGURE 4.1 – IN VITRO STUDY OF MOUSE SPINAL CORD.	117
FIGURE 4.2 – DIRECTIONS AND PLANES OF ACQUISITION.	118
FIGURE 4.3 – OPTICAL MICROSCOPY OF VARIOUS WHITE MATTER SPINAL CORD TRACT FROM THE C6/C7 SECTION.	118
FIGURE 4.4 – TABLE OF CHARACTERISTICS OF THE CONSIDERED SPINAL CORD TRACTS.	119
FIGURE 4.5 – DIFFUSION WEIGHTED IMAGES OF AN AXIAL SLICE.	121
FIGURE 4.6 – PLOT OF THE NORMALIZED DW-SIGNAL VS Q-VALUE FOR A SELECTED VOXEL.	121
FIGURE 4.7 – PARAMETRIC MAPS OF AD Γ EXPONENT.	122
FIGURE 4.8 – MEAN- Γ ($M\Gamma$) PARAMETRIC MAPS OF AXIAL, CORONAL AND SAGITTAL SLICES.	122
FIGURE 4.9 – Γ -ANISOTROPY ($A\Gamma$) PARAMETRIC MAPS OF AXIAL, CORONAL AND SAGITTAL SLICES.	123
FIGURE 4.10 – PARAMETRIC MAPS OF 3 SUCCESSIVE AXIAL SLICES.	124
FIGURE 4.11 – PLOTS OF AD-METRICS AS A FUNCTION OF R_2^*	125
FIGURE 4.12 – Γ -ANISOTROPY ($A\Gamma$) VS HISTOLOGICAL CHARACTERISTICS OF SPINAL CORD TRACTS.	126
FIGURE 4.13 RADIAL- Γ (Γ_{\perp}) VS HISTOLOGICAL CHARACTERISTICS OF SPINAL CORD TRACTS.	127
FIGURE 4.14 – MYELIN IN THE CENTRAL NERVOUS SYSTEM.	130
FIGURE 5.1 – GRADIENT VECTORS SCHEME.	147
FIGURE 5.2 - FLOW-CHART ILLUSTRATING THE METHODS.	79
FIGURE 5.3 - GRAY MATTER (GM) AND WHITE MATTER (WM) SELECTED ROIS.	149
FIGURE 5.4 - SIGNAL TO NOISE RATIO (SNR) OF DWIS AS A FUNCTION OF B-VALUE AND DIFFUSION GRADIENT DIRECTION.	85
FIGURE 5.5 - MEAN VALUES OF γ PLOTTED AGAINST THE SNR OF B_0 IMAGE, FOR A ROI PLACED IN THE SPLENIUM AND IN THE THALAMUS.	151
FIGURE 5.6 – EFFECT OF Rician NOISE OVER DWIS APPEARANCE.	152
FIGURE 5.7 – EFFECT OF Rician NOISE OVER SIGNAL, CONTRAST AND $M\Gamma$ ESTIMATION.	153
FIGURE 5.8 - ESTIMATED $M\Gamma$ VALUES AS A FUNCTION OF THE B-VALUES RANGE.	154
FIGURE 5.9 – ANISOTROPIC BEHAVIOR OF THE DW SIGNAL VS B-VALUE.	155
FIGURE 5.10 – R_2^* DEPENDENCE ON MAGNETIC INHOMOGENEITY IN WM AND GM.	157
FIGURE 5.11 – AD-METRICS, DTI-METRICS AND R_2^* PARAMETRIC MAPS IN THE SUBJECT’S NATIVE SPACE, FOR THE SAME AXIAL SLICE (OBTAINED FROM A SINGLE SUBJECT).	159
FIGURE 5.12 - MEAN- Γ ($M\Gamma$) AND MEAN DIFFUSIVITY (MD) PARAMETRIC MAPS FOR A RANDOMLY CHOSEN SUBJECT IN THE COHORT, AND MAGNIFICATION OF THE AREA CONTAINING THE THALAMUS, THE SPLENIUM OF CORPUS CALLOSUM, AND THE VENTRICLES.	160
FIGURE 5.13 - AD-METRICS PLOTTED VS R_2^*	93
FIGURE 5.14 - R_2^* AND AD-DERIVED PARAMETERS PLOTTED AGAINST χ IN WM AND GM ROIS.	163
FIGURE 5.15 - SUSCEPTIBILITY ANISOTROPY IN WM WITH RESPECT TO THE STATIC MAGNETIC FIELD.	173
FIGURE 5.16 – PICTORIAL VIEW OF THE OXIDATIVE STRESS HYPOTHESIS PROPOSED BY ZECCA ET AL.	174

FIGURE 5.17 – ANALYSIS OF THE EFFECT OF FA AND V1-THRESHOLDS ON THE SIGNIFICANCE OF
CORRELATIONS BETWEEN AD-METRICS AND R^2 *..... 174

List of abbreviations

Abbreviation	Explanation
AD	Anomalous Diffusion
ADC	Apparent Diffusion Coefficient
CNR	Contrast to Noise Ratio
CSF	Cerebro-Spinal Fluid
CTRW	Continuous Time Random Walk
DW	Diffusion Weighted
EPI	Echo Planar Imaging
FA	Fractional Anisotropy
FID	Free-Induction Decay
FOV	Field Of View
FSL	FMRIB Software Library
GM	Gray Matter
MD	Mean Diffusivity
MP	Motion Propagator
MRI	Magnetic Resonance Imaging
MSC	Mouse Spinal Cord
NMR	Nuclear Magnetic Resonance
PDE	Partial Differential Equation
PDF	Probability Density Function
PGSE	Pulsed Gradient Spin Echo
PGSTE	Pulsed Gradient Stimulated Echo
RF	Radio Frequency
ROI	Region Of Interest
SEM	Standard Error of the Mean
SD	Standard Deviation
SI	International System of units
SNR	Signal to Noise Ratio
TE	Echo Time
TR	Repetition Time
WM	White Matter
ROI abbreviation	Explanation
acr	anterior corona radiata
bcc	body of corpus callosum
caud	caudate nucleus
cp	cerebral peduncle
dCST	dorsal Cortico-Spinal Tract
fg	funiculus gracilis
gcc	genu of corpus callosum

hipp	hippocampus
pall	pallidum
plic	posterior limbs of internal capsule
ptr	posterior thalamic radiations
put	putamen
ReST	Reticulo-Spinal Tract
rRST	right Rubro-Spinal Tract
scc	splenium of corpus callosum
ss	sagittal stratum
STT	Spino-Thalamic Tract
thal	thalamus
VST	Vestibulo-Spinal Tract

Introduction

In this work I present my research activity of the last three years. I was concerned with the investigation of a novel contrast mechanism in Magnetic Resonance Imaging (MRI) based on the *pseudo* super-diffusion of water molecules in biological tissues. The *pseudo* super-diffusion is a form of anomalous diffusion, in the specific case treated here a self-diffusion of water molecules in wet samples with statistical properties not fully described by the conventional theory.

In the last 20 years Diffusion Weighted-MRI (DW-MRI) led to a stunning and rapid development in diagnostic, in particular in the field of neuroimaging [1-4]. DW-MRI is based on the endogenous contrast provided by water molecules travelling in tissue micro-environments, driven by thermal random motion. Because of this, this imaging modality does not require the use of potentially harmful exogenous contrast agents to enhance image contrast. This technique, indeed, allowed to achieve spatial resolutions beyond the conventional MRI, reaching the micrometric length scale travelled by diffusing molecules [5]. Therefore, DW-MRI introduced an exquisite way to probe tissue microstructure *in vivo* and non-invasively [4, 6-12]. This technique carried unexpected improvement in the diagnosis of stroke [13] and in the follow-up of several neurodegenerative diseases, such as Multiple Sclerosis [4, 9, 14], Alzheimer's disease, and other demyelinating pathologies [2-4], as well as in brain cancer evaluation [4, 15]. The first and most famous application in diagnostics was the early diagnosis of brain ischemia [3, 13], that paved the way for the introduction of DW-MRI as a routinary acquisition protocol.

Regarding brain microstructure alterations connected to the onset of pathologies, experimental evidences showed the relevance of a timely pharmacological treatment in decelerating the development of several neurodegenerative diseases [16, 17]. Here, however, the conventional DW-MRI fails, revealing a poor sensitivity and a scarce specificity relatively to the premature assessment of tissue alterations, especially in brain [18, 19].

Recently, novel methods exploiting the properties of diffusion but with a different theoretical approach, proved to be more sensitive and specific in detecting structural changes compared to the conventional DW-MRI [20-24]. These innovative techniques are based on non-Gaussian diffusion models.

Without going into technicalities at this point of the dissertation, it is sufficient to mention that these models overcome the Gaussian approximation of water diffusion in biological tissues, that generalizes the random motion of water molecules to free-diffusion, which does not reflect the effective behavior of water tissues. In fact, a conspicuous amount of both *in vitro* [20, 25, 26] and *in vivo* studies [19, 21-24, 27-29] showed that the presence of barriers, cellular organelles, tortuous or fractal geometries, and multi-scale complexity typical of the living matter causes the emergence of anomalous statistical properties of the diffusing water protons (nuclear spins, in MRI jargon). Whenever the conditions of the Gaussian diffusion do not hold anymore, the process is named 'anomalous diffusion' (AD)[30], and the related techniques quantifying the anomalous behavior are named AD-imaging techniques. The theory underneath the AD was condensed in the so called Continuous Time Random Walk (CTRW) model, a mathematical description of anomalous transport [31, 32], contemplating superdiffusion and subdiffusion processes. In particular, superdiffusion is quantified by the parameter γ .

AD γ -imaging technique has already been applied in systems of polystyrene micro-beads [25], excised human tissue [20], rat brain [24] and human brain [22, 27] and despite of the variety of complex tissues investigated, it showed that the γ -exponent was mainly influenced by two factors: the presence of multiple micro-compartments and the presence of magnetic inhomogeneity at the interfaces between them. In fact, γ exhibited significant inverse linear correlation with the internal gradients (G_{int}) arising from magnetic susceptibility inhomogeneity [26]. Furthermore, these two factors could explain the peculiarity of the contrast provided by AD- γ parametric maps in excised brain tissues, in *in vivo* imaging of human prostate [33] and *in vivo* imaging of human brains [20, 22]. The interplay between multi-compartmentalization and magnetic susceptibility differences determining water *pseudo* superdiffusion (the term 'pseudo' refers here to the artificial additional attenuation provoked by the effect of the second factor) bestows a certain diagnostic potential to the imaging of AD- γ parameter regarding normal and tissue pathological alterations [34]. Indeed the assessment of magnetic susceptibility inhomogeneity in the human brain is of paramount importance in the field of MRI diagnostics, because the link between an abnormal iron deposition in brain gray matter and the onset and development of several neurodegenerative diseases is a matter of fact at the state of the art [17, 35-37]. Furthermore, the density and the orientations of myelinated fibers is another

well-known source of magnetic susceptibility inhomogeneity in human brain [38-40].

This thesis work is focused on the evaluation of γ stretched exponent, the investigation of the contrast provided, and the implementation of the technique that allows to reconstruct 3D parametric maps of γ and related scalar invariants. Moreover, the potential of AD- γ imaging in detecting the microstructure of biological tissues was here investigated.

Towards my goal I performed *in vitro* and *in vivo* experiments and examined the relation between the measured γ and microstructural features of the system imaged. I started with a simple cylindrical geometry in the case of mouse spinal cord imaged at high field (9.4 T) in order to better enhance the effect of internal gradients, then I moved a step further by computing a γ tensor in the case of a more complex geometry to map healthy human brain at clinical magnetic field (3.0 T), starting from the effective approach of De Santis et al., developed in the laboratory where I conducted my research activity, and implementing it. The results shown here suggest a potential impact of AD- γ imaging in the field of neuroimaging aimed at monitoring both microstructural changes and alterations due to iron accumulation in the brain [41-43].

Outline of the thesis

The thesis is basically structured in two sections, a theoretical and an experimental one. The theory at the basis of MRI, conventional DW-MRI and Anomalous Diffusion is provided in the first three chapters, in order to facilitate the comprehension of the experimental part, that presents the *in vitro* and *in vivo* results of the application of AD- γ imaging.

The theory of MRI is reported in Chapter 1, where the principles of signal generation and detection, and the technique that allows for the formation of a 3D image of the investigated sample are described.

The theory of diffusion and DW-MRI is presented in Chapter 2, where all the theoretical concepts useful to the comprehension of the key chapters of this thesis are collected.

Chapter 3 deals with the description of Anomalous Diffusion processes, from the rigorous mathematical framework of CTRW to the introduction of a motion propagator, which allows to link the theory to the experimentally measured signal from diffusing spins in DW-MRI.

In Chapter 4 I present the results obtained by performing AD γ -imaging on fixed mouse spinal cord *in vitro*. Here I introduce the experimental derivation of the γ exponent for a simple geometry, and I discuss the outcomes regarding the correlation of γ with magnetic susceptibility inhomogeneity and microstructural features of spinal cord tracts.

In Chapter 5, the very main body of the thesis, I show how to perform AD γ -imaging in *in vivo* experiments on human brain, characterized by a complex geometry. Here I explain the need of a more sophisticated data-processing, accounting for diffusion-related image artifacts. Then I extract a γ -tensor, derive its scalar invariants, and investigate the relation between *pseudo* super-diffusion of water and magnetic susceptibility differences between regions with myelinated axons variously oriented in space, and between regions with distinct iron contents. Finally I illustrate the implications of these results in the field of MRI-diagnostics.

The path connecting the initial goal and the outcomes of my research work is resumed in the Conclusion section, where the use of AD γ -imaging technique and the contrast provided by *pseudo* super-diffusion are discussed in a critical way, contemplating limitations and anticipating future concrete perspectives.

Finally, in the Appendix section the reader will find the manuscript concerning the *in vivo* results, published on NeuroImage [41].

A collateral study concerning the diagnostic potential of DW-MRI in the diagnosis of prostate adenocarcinoma was submitted to MRI journal [44]. This study was not included in the thesis work because it was a bit out of the main topic, nevertheless it corroborated the idea of pushing further the sensitivity of DW-MRI investigations by using an increasing gradient strengths DW protocol.

Chapter 1 Magnetic Resonance Imaging: imaging matter exploiting nuclear magnetism

The phenomenon of magnetic resonance is such a complex and intriguing physical trick to analyze both hard and soft matter, that is arduous to summarize it in a synthetic and exhaustive description. This introductory chapter provides an overview of the fundamental theoretic concepts behind magnetic resonance imaging in liquid systems, explaining the principles of signal generation and detection, and the technique that allows for the formation of a tri-dimensional image of the investigated sample, without claiming to be comprehensive. Nevertheless, this brief outline will facilitate the full comprehension of the subsequent chapters.

1.1 Where does the signal come from?

The technique of Magnetic Resonance Imaging (MRI) involves the acquisition of Nuclear Magnetic Resonance (NMR) signal in the presence of a magnetic field gradient. The signal in NMR comes from *nuclei* provided with a *magnetic moment* (or a spin moment), which interact with local or external magnetic fields and are put on *resonance* in a specific way. MRI thus exploits two fundamental properties of atoms: the magnetism and the spin. These properties seem in fact less tangible compared to others, such as the mass and the electric charge, which produce a direct effect on the chemical and physical properties of substances. Let us depict them so that they become more concrete.

1.1.1 The spin

The spin is an intrinsic property of any elementary¹ and subatomic particle. It is a form of rotational angular momentum, being associated to the rotation of a particle around some axis, but it differs from the orbital angular momentum (usually indicated by l) because it is neither due to an orbital revolution nor acquired by energetic collisions, and for this reason it exists even at absolute zero ($T = 0$ K). The spin is defined by a magnitude and a direction, which sometimes is named *polarization axis*. The spin moment of any physical system is quantized, and it may assume one of the following allowed values:

$$S = \hbar\sqrt{s(s+1)} \quad (1.1)$$

The spin magnitude is usually expressed in units of reduced Planck constant \hbar (where $\hbar \cong 1.054 \cdot 10^{-34}$ J · s), so that a spin is denoted by its *spin* quantum number s , a dimensionless quantity which is a non-negative half-integer for the fermions ($s = 1/2, 3/2, 5/2\dots$) and a non-negative integer for the bosons ($s = 0, 1, 2\dots$). Particles with spin s have $2s + 1$ energetic sublevels (corresponding to an azimuthal quantum number $m_s = -s, -s + 1, \dots, s$, which denotes the component of the spin moment measured along a z axis), that are degenerate in the absence of external fields, but which may have different energy if a magnetic or electric field is applied [45].

The fermions follow the Pauli principle, which states that two fermions cannot have identical quantum states. This implicates that a pair of electrons belonging to the same energy level in an atom will have opposite (anti-parallel) spins. For the same reason, a proton and a neutron which are made up of 3 quarks, will have $s = 1/2$, because the anti-parallel spin configuration for two of them gives rise to a net $s = 1/2$.

The total spin of a system consisting of two sources of spin is provided by a combination rule which applies also for angular momenta: the total spin moment of the system of two spins, s_1 and s_2 , is given by $S = \hbar\sqrt{s_3(s_3 + 1)}$, where s_3 may vary within:

¹ The *elementary particles* are fundamental particles which either constitute matter or carry forces. The quarks and leptons (including electrons and neutrinos) make up what we classically call matter, they are named fermions, and they have spin quantum number $s = 1/2$. The photon, carrying the electromagnetic force, the gluon carrying the strong nuclear force, and the W and Z bosons carrying the weak nuclear force are all named bosons and have spin quantum number $s = 1$.

$$|s_2 - s_1|, |s_2 - s_1| + 1, \dots, |s_2 + s_1| \quad (1.2)$$

Matter is composed of molecules, which are basically electron clouds containing more than one nucleus (consisting of protons and neutrons, also called nucleons). A molecule is interested by many different motions, for example the motion of electrons around the nuclei, the motion of the nuclear framework around the center of mass of the molecule, the spinning of electrons and the spinning of nucleons. Therefore, the total angular momentum (usually indicated by \mathbf{J}^2) is given by the sum of the total orbital momentum (\mathbf{L}) and the total spin momentum (\mathbf{S}), calculated for nucleons and electrons. At the 'ground state', that is the lowest energy state of a chemically stable molecule, the electron orbital angular momenta and the electron spins cancel out, and the only sources of angular momentum come from the molecular rotation and the nuclear spins.

When dealing with atomic nuclei, the nuclear spin moment is given by $I_{tot} = \hbar\sqrt{I(I+1)}$, the spin quantum number is conventionally denoted as I , and its azimuthal quantum number as $m_I = -I, -I+1, \dots, I$. In a sense, atomic nuclei are characterized by states which are quantum mechanical in their behavior, meaning that their properties belong to a discrete set of possibilities. In NMR however, we get a signal from a number of Avogadro ($N_A \cong 6.022 \cdot 10^{23}$) of nuclei. At the microscopic level these nuclei exhibit 'discrete' behaviors, whereas at the macroscopic level the behavior is 'continuous', namely an *ensemble*³ behavior, in the reasonable hypothesis of spins acting independently of each other. Similarly, the spins behavior can be described either by means of a quantum description, or by means of a semi-classical one. For a brief and clear description of elementary quantum mechanics and nuclear magnetization I suggest the reader to refer to the monograph by P.T. Callaghan [46], while the semi-classical description is presented in short in the following paragraphs.

² From now on I will adopt the following notation: the vectors will be conventionally marked in bold, both in the text and in the formulas, while their modulus will be written with normal formatting.

³ The term *ensemble* in statistical mechanics indicates a group of microscopic states with their probability to occur in a system. The *canonical* ensemble is associated to a closed system, thus it is able to perform energetic exchanges with the heat bath, but the number of particles N is kept constant (differently from the case of *grand canonical* ensemble, which exchanges both energy and matter with the bath). Spins in NMR may be represented by a canonical ensemble.

1.1.2 The magnetism

The magnetism is a fundamental property of each substance, that gives it the capability to interact with magnetic fields. The entity of such interaction depends on the magnitude of the magnetic field, and less trivially, on the magnetic dipole moment $\boldsymbol{\mu}$ of the substance. Basically a magnetic dipole moment inserted in a magnetic field ‘feels’ a torque.

A magnetic field is a vector field, specified at any given point by a direction and a magnitude (or strength). The same term is used to indicate two distinct vector fields, \mathbf{B} and \mathbf{H} . The \mathbf{B} -field (also named the magnetic flux density) is defined by the force it produces on a magnetic dipole, and it is measured in Tesla (T) or in $N/(m \cdot A)$ in the International System of Units (SI). The \mathbf{H} -field (or the magnetic field strength) classically denotes the magnetic field itself, and it is measured in Oersted (Oe) or A/m in SI. Finally, the magnetization produced in a material because of the presence of H-field is represented by \mathbf{M} , defined as the net magnetic dipole moment per unit volume of a region of material, measured in A/m in SI.

The relation between these 3 vectors is: $\mathbf{H} = \frac{\mathbf{B}}{\mu_0} - \mathbf{M}$, with $\mu_0 = 4\pi \cdot 10^{-7} H/m$ the magnetic permeability of vacuum. The magnetic dipole moment, or simply the magnetic moment, $\boldsymbol{\mu}$, is given by the product between \mathbf{M} and the volume V , and measured in $A \cdot m^2$. In technical MRI language, and hereafter, we refer to the magnetic flux density B by naming it ‘static magnetic field’, or simply ‘magnetic field’.

In some substances the magnetic moment is permanent, thus it persists even in the absence of any magnetic field. Most of substances, instead, exhibit an induced magnetism, and their dipole moment is proportional to the magnetic field B_0 , to their volume V and to the magnetic susceptibility χ_m :

$$\mu_{ind} = \frac{V\chi_m B_0}{\mu_0} \quad (1.3)$$

The diamagnetic materials which have $\chi_m < 0$ (such as the water molecule, with $\chi_{H_2O} \cong -9.05 \text{ ppm}$) will be repelled by the magnetic field, whereas the paramagnetic materials with $\chi_m > 0$ will be attracted.

Among the sources of magnetism in a molecule there are the circulating charges, the electron spins, and the nuclear spins, the last of which is the

weakest component. In paramagnetic substances the electric magnetism dominates, because of the presence of unpaired electrons. In diamagnetic substances, which present paired electrons, the electron spins cancel out, in favour of the other two sources. If we consider the magnetic susceptibility of hydrogen nucleus ^1H in H_2O , for example, deriving it from [45]:

$$\chi_m = \frac{\mu_0 \hbar^2 \gamma^2 c}{4k_B T} \quad (1.4)$$

with k_B the Boltzmann constant $k_B \cong 1.38 \cdot 10^{-23} \text{J/K}$, γ the gyromagnetic ratio, equal to 42.58 MHz/T, and c the concentration of protons per unit volume, at room temperature ($T_{room} \sim 297\text{K}$) it is in the order of 10^{-9} , whereas $\chi_{e-} \sim 10\text{ppm}$, that is 4 orders of magnitude greater. Here we are concerned with NMR experiments performed on diamagnetic samples, with molecules at the 'ground state', therefore we will focus on nuclear magnetism. Since the strong electronic diamagnetism shows no time dependence, it can be accounted for by means of a corrective term [45]. On the other hand, the signal coming from the nuclei will be electronically amplified in order to be registered.

1.1.3 The nuclear magnetism and Larmor precession

The magnetic dipole moment $\boldsymbol{\mu}$ is proportional to the total angular momentum \mathbf{J} through a constant of proportionality called the gyromagnetic ratio γ , specific for each substance.

For atomic nuclei \mathbf{J} coincides with the spin total moment \mathbf{I}_{tot} , and the gyromagnetic ratio γ is positive for almost every nucleus (except for ^{15}N , ^{29}Si), thus:

$$\boldsymbol{\mu} = \gamma \mathbf{I}_{tot} = \gamma \hbar \sqrt{I(I+1)} \quad (1.5)$$

The magnetic energy associated to the interaction between $\boldsymbol{\mu}$ and the magnetic field is described both classically and quantum-mechanically by the Zeeman Hamiltonian (or energy) operator, which in a first approximation is the product between the magnetic field and the magnetic moment:

$$H = -\boldsymbol{\mu} \cdot \mathbf{B} = -\gamma \mathbf{I}_{tot} \cdot \mathbf{B} = -\gamma \hbar \sqrt{I(I+1)} B_0 \cos\theta \quad (1.6)$$

considering a magnetic field oriented along the z-axis $\mathbf{B} = (0, 0, B_0)$, with θ the angle between $\boldsymbol{\mu}$ and \mathbf{B} . Because of the allowable discrete values of the azimuthal quantum number m_l a splitting of the nuclear energy levels into $2I + 1$ sub-levels occurs (known as the *Zeeman effect*), with the energy of each level being:

$$E_{m_l} = -\gamma \hbar B_0 m_l \quad (1.7)$$

The energy gap between two successive sub-levels is thus $\Delta E = \gamma \hbar B_0$, and it is independent of the spin of the particle. The nucleus of the main isotope⁴ of hydrogen ^1H , consisting of a proton, has spin $I = 1/2$, thus the energy is splitted into two sub-levels with $m_l = \pm 1/2$, as shown in **Figure 1.1a**. The two sub-levels host spins respectively oriented parallel to \mathbf{B} (for $m_l = 1/2$), with a lower energy (namely the ground state), and spins oriented anti-parallel to \mathbf{B} (for $m_l = -1/2$), with a higher energy (namely the excited state).

An object with a permanent $\boldsymbol{\mu}$ which is free to move (like a compass needle), tends to align along the external magnetic field so as to minimize its magnetic energy. In the case of nuclear spins which possess an angular momentum as well as an induced $\boldsymbol{\mu}$, the actual response of the spin polarization axis will be the so called *Larmor precession*, moving on a cone around the B_0 direction, at a constant angle θ (**Figure 1.1b**) and with a specific Larmor (angular) frequency, given by:

$$\omega_0 = -\gamma B_0 \quad (1.8)$$

with the minus sign indicating a clockwise precession (except in case of ^{15}N , ^{29}Si), and measured in rad/s. The respective frequency is obtained dividing ω_0 by a factor of 2π . For the ^1H inserted in a $B_0=9.4$ T with a gyromagnetic ratio of $\gamma \cong 42.58 \text{ MHz/T}$, the Larmor frequency is $f \cong 400 \text{ MHz}$, meaning that it completes 400 million of cycles of precession every second. Comparing (1.5)

⁴ The *isotope* of an element is an atom which shares the same atomic number Z , or number of protons of that element, but has a different number N of neutrons (thus a different mass number, given by the sum of protons and neutrons). The isotopes of an element are stable if N approximately equals Z . Hydrogen (^1H) and deuterium (^2H) are stable isotopes, where ^1H contains a single proton and ^2H contains a proton and a neutron.

and (1.6) one retrieves the precession angle between $\boldsymbol{\mu}$ and \mathbf{B} , which for ^1H is $\theta = \pm 54.74^\circ$.

The relation in (1.7) may be derived considering the energy carried by an electromagnetic wave with a specific polarization⁵, so that it equals the energy gap between two adjacent sub-levels: $\hbar\omega_0 = \Delta E = \gamma\hbar B_0$. When the spins of the sample are excited by such a wave they are able to ‘jump’ at the higher energy level, thus inverting their own orientation with respect to \mathbf{B} .

1.1.4 The macroscopic magnetization

Let us consider ^1H in a sample of water. In the absence of an external magnetic field, the spin polarization axes are uniformly distributed, and the total magnetic moment of the sample is close to zero. If a B_0 is turned on, the spins begin performing Larmor precession around the field direction moving at ω_0 . Now because of the heterogeneity of molecular surrounding, the net magnetic field ‘seen’ by each spin will be the sum of the static external field, and small fluctuating fields, causing tiny fluctuations in the polarization axes in the order of 10^{-4} degrees [45]. The small fluctuating fields from the thermal environment cause a gradual breakdown of the constant-angle cone precession, and over a timescale of seconds the orientation of $\boldsymbol{\mu}$ wanders around. The wandering is driven by energetic convenience, so that $\boldsymbol{\mu}$ is turned towards an orientation with lower magnetic energy, leading to a stable anisotropic distribution of nuclear spin polarizations, called *thermal equilibrium*. At the thermal equilibrium the net distribution of spin orientations parallel to B_0 is slightly more probable than that one of anti-parallel spins, as shown in **Figure 1.1a**. In case of ^1H the energy gap between the sub-levels of energy described by (1.6) is of about $\Delta E = \gamma\hbar B_0 \cong 2.6 \cdot 10^{-25}\text{J}$. This energy is about 4 orders of magnitude lower than the available thermal energy at a room temperature of 297 K: $\Delta E(T_{room}) = k_B T \cong 4.1 \cdot 10^{-21}\text{J}$. It means that the jump between the lower and the higher energy sub-levels is quite probable, and that the distribution of the ground state is only slightly larger than the excited one. Ideally the magnetic moments associated to the spins are equally distributed over two cones of angles $\theta = \pm 54.74^\circ$ for ^1H . There is no net magnetization perpendicular to the

⁵ For more information on the polarization of electromagnetic waves, please refer to the Appendix A.

field, because the distribution of μ at thermal equilibrium is on the ensemble average, cylindrically symmetrical around the z-axis.

A macroscopic longitudinal magnetization may still emerge providing that a difference between the two populations of spins occupying the ground state, and the excited state, exists. According to the fundamental Boltzmann law of statistical mechanics, the population of each level is proportional to $P_{m_l} \propto e^{-\frac{E_{m_l}}{k_B T}}$, and for a sample with a total number of spins N the net macroscopic magnetization is given by:

$$M = N\gamma\hbar \frac{\sum_{m_l=-l}^l m_l e^{-\frac{\gamma\hbar B_0 m_l}{k_B T}}}{\sum_{m_l=-l}^l e^{-\frac{\gamma\hbar B_0 m_l}{k_B T}}} \quad (1.9)$$

At $T_{\text{room}} \Delta E_{m_l} \ll k_B T$, hence it is possible to use the power series expansion for $t = \frac{\gamma\hbar B_0}{k_B T}$, and one obtains:

$$M \sim N\gamma\hbar \frac{\sum_{m_l=-l}^l (m_l + m_l^2 t)}{\sum_{m_l=-l}^l (1 + m_l t)} = 2N\gamma\hbar t \frac{\sum_{m_l=1}^l m_l^2}{(2l+1)} = \frac{2N\gamma\hbar t l(l+1)(2l+1)}{6(2l+1)} \quad (1.10)$$

Where, expliciting t again, one finds the Curie law for the macroscopic magnetization:

$$\mathbf{M} = \frac{N\gamma^2 \hbar^2 l(l+1) \mathbf{B}_0}{3k_B T} = \chi \mathbf{B}_0. \quad (1.11)$$

\mathbf{M} is a longitudinal magnetization (M_z) in the hypothesis of a B-field oriented along the z-axis, as in (1.5).

The macroscopic magnetization of an ensemble of nuclear spins gives rise to the signal in NMR. From (1.10) we notice that NMR signal is proportional to the abundance of the nucleus, to its gyromagnetic ratio, and to the B-field. In biological tissues ^1H represents the nucleus with the highest abundance and the highest γ , and the latest trend in the field of *in vivo* MRI is the development of more performing spectrometers with high B_0 strength, in the respect of the patients and animal safety, because it clearly translates into a signal amplification.

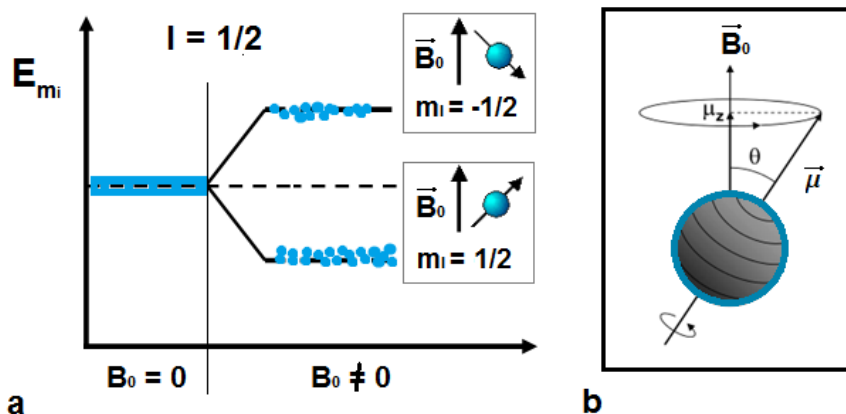


Figure 1.1 - The splitting of energy levels due to Zeeman effect and Larmor precession. a) Sketch showing two degenerate energy levels of nuclear spins in the absence of static magnetic field, and two sublevels corresponding to the azimuthal quantum number $m_i = \pm 1/2$ in the presence of B_0 . The low energy level is slightly more populated than the other one, so that spins parallel to B_0 are more than those oriented antiparallel to B_0 . b) A nucleus with an induced magnetic moment μ performs a Larmor precession around the direction of the magnetic field. The projection of the magnetic moment along this direction is indicated by μ_z .

1.2 How to reveal the signal?

The longitudinal magnetization described above is unfortunately undetectable, and it is impractical to measure [45]. The approach adopted by NMR is to measure the transversal magnetization instead, by rotating \mathbf{M}_z into the xy-plane. This is achieved using a radiofrequency (RF)-pulse, that is an oscillating magnetic field of appropriate frequency and duration. The transversal magnetization \mathbf{M}_{xy} keeps on precessing around the B-field direction, and its oscillating magnetic flux induces an electromagnetic force (e.m.f.), thus a detectable electric signal, in a transversal coil, usually the same used to generate the RF-pulse (this is visually explained in **Figure 1.2**). The NMR spectrometer is basically a device capable of magnetizing the nuclear spins, rotating their polarization through the use of an RF-pulse, and detecting the small oscillating electric currents. For more details about NMR device see

Levitt's book [45]; in the next sections the formation and evolution of M_{xy} are described.

1.2.1 The transverse magnetization and the Free Induction Decay

With the term *RF-pulse* we indicate an oscillating magnetic field (usually denoted with the symbol B_1 , to discriminate it from the static magnetic field B_0) with a fixed duration Δt and frequency ω . In the jargon of NMR the term *RF-excitation* is often used, indicating that the provided pulse, when polarized in the xy-plane and $\omega \approx \omega_0$, excites the spins, puts them *on resonance*, and allows them to jump the energy gap between sub-levels, with the result of more spins in the anti-parallel configuration compared to B_0 . This eventually has the effect of cancelling the disproportion between the spins populations of the two sub-levels, neutralizing thus M_z .

Another approach is to consider that the RF-pulse B_1 rotates spins polarization by $\pi/2$ about the x- (or y-) axis, thus the net spin polarization along the z-axis is transferred into a net spin polarization along the y- (or x-) axis (see **Figure 1.3**). The macroscopic magnetization emerging from the ensemble of spins when they reach the thermal equilibrium in a B-field (namely M_0), initially oriented along z-axis, is then rotated into the xy-plane, and hence called transverse magnetization, \mathbf{M}_{xy} . After Δt , when the RF-pulse is turned off, the spins will resume their precessional motion, causing the bulk magnetic moment, and thus M_{xy} , to precess around the z-axis in the xy-plane, with a precession frequency that equals the nuclear Larmor frequency ω_0 . The evolution of the two components of \mathbf{M}_{xy} may be described by:

$$M_x(t) = M_0 \sin \omega_0 t \cdot e^{-\frac{t}{T_2}}$$

$$M_y(t) = -M_0 \cos \omega_0 t \cdot e^{-\frac{t}{T_2}} \quad (1.12)$$

with M_0 the magnetization at the thermal equilibrium, and T_2 the transverse relaxation time⁶, or coherence decay time, or spin-spin relaxation time. M_{xy} amplitude decays as in a damped oscillator (see **Figure 1.2b**), because the nuclear magnets start precessing at the same time, but then they lose

⁶ More precisely, the transverse magnetization decays more rapidly, with the time constant $T_2^* < T_2$, that will be described in the next paragraphs. Usually some textbooks refer to this decay considering solids or macromolecules with a slow dynamics, for which the two time constants are almost the same, and thus interchangeable.

synchrony, or in other words, they lose phase coherence. This decay, or *relaxation* process is irreversible, and it is called spin-spin relaxation because it does not involve energy exchanges with the thermal bath. It is rather due to the fact that spins experience slightly different magnetic fields, thus they precess at slightly different frequencies (even not considering the mutual interactions of spins). Actually the scenario is more complex, because there are effective interactions (such as the dipolar interaction and the chemical shift), which contribute to further dephasing of spins. Since these interactions present energy several orders of magnitude ($1/10^4$) lower than that provided by the linear Hamiltonian of (1.5), we will neglect them.

A magnetic field which varies during time is associated to an oscillating electric current through Maxwell's equation:

$$\nabla \times \mathbf{E} = -\frac{\partial \mathbf{B}}{\partial t} \quad (1.13)$$

The small induced electric current circulates into the windings of the RF-coil which is perpendicular to the B_0 direction. The whole process is called *free-induction decay* (FID), as it describes the decay of M_{xy} and thus of the induced electric current, and it is the very heart of the NMR signal.

1.2.2 The semi-classical description

In the case of independent spin nuclei the motion of the ensemble of spins may always be described in terms of the precession of the magnetization vector \mathbf{M} . In such a model the macroscopic angular momentum vector is $\mathbf{J} = \mathbf{M}/\gamma$, with γ the nuclear gyromagnetic ratio [46]. Classically, the torque of a body along the axis of rotation determines the rate of change of its angular momentum:

$$\boldsymbol{\tau} = \frac{d\mathbf{J}}{dt} \quad (1.14)$$

and in the case of a magnetic moment inserted in a B-field, the torque is given by:

$$\boldsymbol{\tau} = \boldsymbol{\mu} \times \mathbf{B} \approx \mathbf{M} \times \mathbf{B} \quad (1.15)$$

where the symbol \approx here denotes the passage to the macroscopic average on the ensemble of spins. Combining (1.13) and (1.14), one obtains:

$$\frac{d\mathbf{M}}{dt} = \gamma \mathbf{M} \times \mathbf{B} \quad (1.16)$$

which describes the evolution of the magnetization vector. The rate of change of \mathbf{M} is orthogonal to both \mathbf{M} and \mathbf{B} , thus the equation describes a precession of \mathbf{M} around \mathbf{B} . Considering the Poisson relation for a vector \mathbf{u} between a fixed reference frame (f) and a rotating one (r):

$$\left(\frac{d\mathbf{u}}{dt}\right)_f = \boldsymbol{\omega} \times \mathbf{u} + \left(\frac{d\mathbf{u}}{dt}\right)_r \quad (1.17)$$

neglecting the second term, and comparing with (1.15), one finds again the expression of ω_0 Larmor angular frequency reported in (1.7).

The *resonance* phenomenon results by the application of a transverse magnetic field B_1 oscillating at $\omega_{RF} \approx \omega_0$:

$$\mathbf{B}_1(t) = \hat{i}2B_1 \cos \omega_{RF}t \quad (1.18)$$

where \hat{i} indicates the x-direction. A linearly polarized wave may be always decomposed into two counter-rotating circularly polarized⁷ components: we retain only the relevant one, that is the left-component rotating clockwise, thus in the same sense as the spin precession [46]:

$$\mathbf{B}_{1L}(t) = \hat{i}B_1 \cos \omega_0t - \hat{j}B_1 \sin \omega_0t \quad (1.19)$$

Thus, considering also the static magnetic field oriented along z-axis, the total B-field may be expressed as:

$$\mathbf{B} = \hat{i}B_1 \cos \omega_0t - \hat{j}B_1 \sin \omega_0t + \hat{k}B_0 \quad (1.20)$$

⁷ For more information on the polarization of electromagnetic waves, please refer to the Appendix A.

Substituting (1.19) into (1.15), and solving, one gets, for the on resonance condition ($\omega_{RF} \approx \omega_0$), the following evolution equations:

$$\begin{aligned}\frac{dM_x}{dt} &= \gamma(M_y B_0 + M_z B_1 \sin \omega_0 t) \\ \frac{dM_y}{dt} &= \gamma(-M_x B_0 + M_z B_1 \cos \omega_0 t) \\ \frac{dM_z}{dt} &= \gamma(-M_x B_1 \sin \omega_0 t + M_y B_1 \cos \omega_0 t)\end{aligned}\quad (1.21)$$

Which, under the initial condition $M_z(t = 0) = M_0$, provide as solutions:

$$\begin{aligned}M_x &= M_0 \sin \omega_1 t \sin \omega_0 t \\ M_y &= M_0 \sin \omega_1 t \cos \omega_0 t \\ M_z &= M_0 \cos \omega_1 t\end{aligned}\quad (1.22)$$

with $\omega_1 = \gamma B_1$. These equations imply that on application of a rotating RF-field \mathbf{B}_1 of frequency ω_0 , \mathbf{M} performs two simultaneous precessions, one about the longitudinal field at ω_0 , the other about the RF-field at ω_1 , as showed in **Figure 1.4a**, and represents the motion seen from an observer in the laboratory (or fixed) reference frame. Suppose instead that the observer is rotating together with \mathbf{B}_1 : in that case it would see only the precession of \mathbf{M} about \mathbf{B}_1 (see **Figure 1.4b**). B_1 values are typically a few 10^{-4} T, so that the precession about the RF-field, using the ^1H example again, is typically at a cyclic frequency of 10 kHz.

The behavior described above regards the on resonance case. When $\omega_{RF} \neq \omega_0$ (the so called ‘off-resonance’ case) in the rotating frame in addition to \mathbf{B}_1 there is a residual longitudinal component $\mathbf{B}'_0 = B_0 - \omega_{RF}/\gamma$, thus \mathbf{M} precesses about an effective magnetic field, \mathbf{B}_{eff} , which is the vector sum of the transversal and longitudinal contributes, as illustrated in **Figure 1.4c**. The off-resonant behavior is important in NMR because it is exploited for selective excitation of spins in the sample.

Considering the rotating frame, it is clear that the use of a resonant RF-field B_1 (or RF-pulse) allows to rotate \mathbf{M} by the desired angle, which depends on the intensity and duration of the pulse:

$$\theta = \omega_1 \Delta t = \gamma B_1 \Delta t \quad (1.23)$$

In most imaging experiments the parameters are chosen in order to get multiples of 90° . The two most used excitation RF-pulses derived their names from the desired angles, which respectively are $\theta = 90^\circ$ for $\text{RF}_{\pi/2}$, and $\theta = 180^\circ$ for RF_π .

1.2.3 The Bloch equation and relaxation phenomena

The Bloch equation is a milestone in the semi-classical description of NMR signal. This phenomenological equation describes the evolution of the magnetization components, taking into account the *relaxation* phenomena. After the RF-pulse excitation the spins populations gradually drift towards their thermal equilibrium values, losing coherences, and the thermal equilibrium state is gradually re-established, over a sufficiently long time. Macroscopically this turns into the restoration of the longitudinal component and the complete decay of the transversal ones.

Shall we consider an $\text{RF}_{\pi/2}$ -pulse. After its action the magnetization has been transferred into the xy-plane, where it precesses at ω_0 . We may use a complex vector to describe this motion:

$$\mathbf{M}_{xy} = M_x + iM_y \quad (1.24)$$

which will evolve following an exponential decay:

$$M_{xy}(t) = M_0 e^{-i\omega_0 t} = M_0 \cos \omega_0 t - iM_0 \sin \omega_0 t \quad (1.25)$$

Notice that it is a compact form of the magnetization components reported in (1.11) and presented in Par. 1.2.1, except for the multiplicative attenuation factor $e^{-\frac{t}{T_2}}$. This factor cannot be neglected since we deal with a real system of spins, and we cannot avoid spins interactions and the effect of the thermal bath they exchange energy with.

The Bloch equation treats separately the evolution of longitudinal and transversal \mathbf{M} components, influenced respectively by the *spin-lattice* relaxation, due to the energy exchanges with the thermal bath, and by the *spin-spin* relaxation (see Par. 1.2.1), that is an adiabatic process, associating their relative longitudinal (T_1) and transversal (T_2) time constants:

$$\frac{d\mathbf{M}}{dt} = \mathbf{M} \times \gamma \mathbf{B}_0 - \frac{iM_x + jM_y}{T_2} - \frac{\hat{\mathbf{k}}(M_z - M_0)}{T_1} \quad (1.26)$$

Considering the contribute of relaxation processes the evolution of transverse magnetization corrects as follows:

$$M_{xy}(t) = M_0 e^{-i\omega_0 t} e^{-\frac{t}{T_2}} \quad (1.27)$$

that is nothing but (1.11). T_2 represents the time during which the transversal magnetization reduces to about 37% of the initial value. The interactions between adjacent spins provoke fluctuations of the Larmor frequency, that turn into the loss of phase coherence among spins, which does not involve any energy exchange with the surroundings, but increases the entropy of the system in a non-reversible way.

The spin-lattice relaxation (or T_1 -relaxation) instead has an effect on the longitudinal component of \mathbf{M} , restoring it to the initial equilibrium value of M_0 :

$$M_z(t) = M_0 \left(1 - e^{-\frac{t}{T_1}}\right) \quad (1.28)$$

with T_1 representing the time necessary for the restoration of about 63% of the equilibrium value. The term 'lattice' was inherited from the first NMR studies on solids with a crystalline structure, and represents the ensemble of other nuclei in the sample interacting with the spins of interest. The technique that measures T_1 and T_2 relaxation time constant is known in the field of MRI as T_1/T_2 -relaxometry. An example of the derived parametric maps is reported in **Figure 1.5** for an axial slice of human brain. The intensity of the pixels is proportional to the constant, so that these maps are also named T_1/T_2 -weighted.

In order to restore M_z is necessary to elicit the return of spins at the ground state, a process known as *stimulated* emission⁸. In fact the RF-pulse excitation cause them to jump at the excited state, but the inverse process needs some energy release because at the RF regime the spontaneous emission is not likely. This energy is exchanged with the thermal bath, which employs the gained energy to jump at the excited state (a transition that is very frequent for the thermal bath).

Either the relaxation processes here described are strictly influenced by the molecular dynamics, and reflects the chemical structure of the molecules. The molecular dynamics causes the emergence of a spectrum of radiofrequencies, rather than a single Larmor frequency. An opportune choice of the experimental parameters in the NMR experiment allows to highlight some particular characteristics of the ensemble of spins.

1.2.4 Signal detection and spin manipulation

In the previous paragraph the spin were presented as capable of both receiving and emitting and RF signal at the same time. The NMR device is equipped with an RF-emitter and an RF-receiver, which works by mixing the weak electromagnetic force (e.m.f.), in the order of μV , with the output from a reference RF oscillator [46]. This process is known as *heterodyning*. It consists in mixing the e.m.f. with two heterodyne references signals with a phase shift of 90° , in order to obtain separate in-phase and quadrature phase output signals which are proportional to the magnetization in x- and y-planes and thus able to detect M_x and M_y . NMR experiments can also be performed using a single phase of detection, but the use of dual phase detection presents numerous advantages, and actually this method is very commonly employed. For reference mixing frequencies ω_{ref} different from the Larmor frequency the signal oscillates at the offset frequency $\Omega_0 = \omega_0 - \omega_{ref}$. The heterodyne signal is proportional

⁸ The *stimulated emission* is the process by which an incoming photon of a specific frequency can interact with an excited atomic electron (or other excited molecular state), causing it to drop to a lower energy level. The liberated energy transfers to the electromagnetic field, creating a new photon with a phase, frequency, polarization, and direction identical to the photons of the incident wave. This is in contrast to *spontaneous emission*, which occurs at random intervals without regard to the ambient electromagnetic field.

through S_0 to the magnetization at the thermal equilibrium M_0 , and has a total phase that is the sum of 3 contributions: the absolute receiver phase Φ , the oscillating pulse at the offset frequency Ω , and the factor which accounts for the decay of coherences which scales as the inverse of T_2 :

$$S(t) = S_0 e^{i\Phi} e^{i\Omega_0 t - \frac{t}{T_2}} \quad (1.29)$$

This signal is commonly addressed as the Free Induction Decay (FID, see Par. 1.2.1), and it is clearly acquired in the time domain. By means of the Fourier Transform the FID is converted into the frequency domain to get absorption and dispersion spectra, which have the form of Lorentzian curves⁹.

Let us consider for the sake of simplicity, $\Phi = 0$, and use the rate of relaxation $R_2 = 1/T_2$. The Fourier Transform (indicated with the symbol \mathfrak{F}) of the signal in (1.29) has thus the form:

$$\mathfrak{F}[S(t)] = S(\Omega) = \int_0^\infty S(t) e^{-i\Omega t} dt \quad (1.30)$$

The result in the real part of the domain is a Lorentzian lineshape centered in Ω_0 and with a Full Width at Half Maximum (FWHM) equal to R_2/π :

$$S(\Omega) = \frac{1}{R_2 + i(\Omega - \Omega_0)} \quad (1.31)$$

which has Real and Imaginary parts respectively equal to:

$$\begin{aligned} Re[S(\Omega)] &= \frac{R_2}{R_2^2 + (\Omega - \Omega_0)^2} \\ Im[S(\Omega)] &= -\frac{\Omega - \Omega_0}{R_2^2 + (\Omega - \Omega_0)^2} \end{aligned} \quad (1.32)$$

representing an absorption curve (see **Figure 1.6b**) and a dispersion curve. The imaginary dispersion spectrum exists because the signal is acquired for

⁹ This is a simplification of the actual processing of signal acquired in the time domain, since the NMR spectrometer employs the Fast Fourier Transform instead, with the requirement of a number of discrete time points that is a power of 2 (generally $2^{10} = 1024$, $2^{11} = 2048$, $2^{12} = 4096$).

positive time only [46]. The width of the absorption curve depends on the rate of relaxation, meaning that for substances where spins quickly lose phase coherence there will be a broad peak in the absorption spectrum, whereas a slower decay will result in a narrow peak.

In order to gain information about the structure of the investigated sample it is necessary to project ad hoc pulse sequences in order to manipulate the spin system under the influence of the Zeeman Hamiltonian and the T_1 and T_2 relaxation processes. Among the sequences first introduced (and still most used in practice) there are the Spin Echo (or Hahn echo), and the Stimulated Echo sequence, which are described in the next sections and represent the basis to build acquisition sequences for the imaging of ^1H in diffusing water molecules.

1.2.4.1 The Spin Echo sequence

The Spin Echo (SE, or Hahn echo) is one of the most widely diffused sequences and it represents the starting point for obtaining diffusion-weighted images (DWIs), i.e. images which take into account the diffusive motion of spins. The inhomogeneity of the external static magnetic field, B_0 , and of local internal gradients (due to χ_m inhomogeneity) will result in a field spread across the sample.

This loss of coherence is more rapid than the spin-spin relaxation, and it occurs in a time $T_2' < T_2$, where T_2 represents the spin-spin relaxation time constant. The time constant associated to the decay of the transversal component (or the dephasing of spins) that takes into account the two effects is T_2^* , and its inverse scales as:

$$\frac{1}{T_2^*} = \frac{1}{T_2'} + \frac{1}{T_2} \quad (1.33)$$

The loss of coherence due to magnetic field inhomogeneity is a reversible process. Following a 90_x RF-pulse, i.e. a magnetic field pulse in which the parameters had been set to rotate the magnetization of 90° around the x-axis, the transverse magnetization M_{xy} will be progressively dephased by such a spread. The application of a second 180_y RF-pulse after a time delay $TE/2$ will cause refocusing at $t = TE$, reversing the phase of the spins and generating an

'echo' of the signal as showed in **Figure 1.7**. The intensity of the echo relative to the initial signal is given by:

$$M_y(TE) = M_0 e^{-\frac{TE}{T_2}} \quad (1.34)$$

The formation of the echo is predicated on the assumption that nuclei experience the same local Larmor frequency during the successive dephasing and rephasing parts of the cycle. In **Figure 1.7** we can notice that the echo has a lower intensity compared to the initial signal: this is due to the irreversible and unavoidable loss of phase coherence among spins, owing to the spin-spin interactions. By acquiring several FIDs (varying the TE) it is possible to fit the signal decay to derive T_2 .

Since there is a correspondence between the nuclear position and the local magnetic field (which will be clarified later in the manuscript, see Par. 1.3.1), this assumption is equivalent to requiring that the nuclei do not move in translation along the gradient direction. But since the molecular diffusion cannot be removed, it is possible to take advantage of this phenomenon to quantify the molecular displacement spectrum, as it will be shown in Par. 2.3.2.

1.2.4.2 The Stimulated Echo sequence

In many materials the transverse relaxation time T_2 is considerably shorter than the longitudinal relaxation time T_1 . Ideally, if we change the polarization of the magnetization vector from the xy-plane to the longitudinal direction, we would be able to preserve it from the attenuation due to the transversal dephasing. It would be useful to employ this magnetization at a later time, for example to analyze the motion of molecules containing NMR nuclei. The stimulated echo sequence is designed to satisfy this request (see **Figure 1.8**). The first 90_x pulse rotates the magnetization into the y-axis. The second 90_x pulse, applied after an interval time of τ , has the effect of rotating the y-component of magnetization into longitudinal polarization along the z-axis, where only T_1 relaxation will occur. Obviously the x-component of the magnetization will be unaffected, so that only half the transverse magnetization can be stored in this way. Applying a third 90_x pulse, after an interval time of T

from the second one, leads to the formation of an echo (that has been stimulated) at time τ after the last RF-pulse [46].

This sequence generates two additional spin echoes apart from the stimulated echo, originated respectively by the second 90_x -pulse (echo of the initial FID), and by the third 90_x -pulse (echo of the intermediate FID). These additional echoes may interfere with the stimulated echo, and in order to minimize their effect a homogeneity-spoiling magnetic field gradient pulse is usually placed in between the second and the third 90_x -pulses. This spoiling gradient destroys the unwanted transverse magnetization, without affecting the magnetization stored along the z-axis.

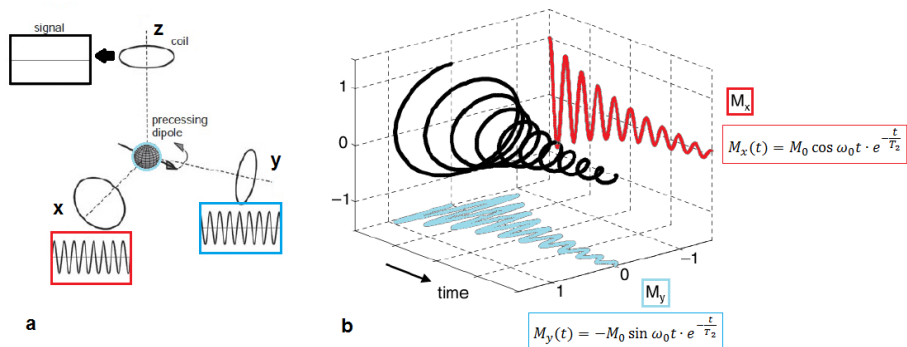


Figure 1.2 - Sketch of NMR signal detected from a longitudinal and a transversal coil. a) Three different coils and the respective recorded signal from the precession of a magnetic dipole, occurring in the xy-plane: the coil centered in the z-axis measures a constant magnetic flux, hence no induced current is registered; the coils centered in the x-axis and y-axis measure an oscillating magnetic flux, thus two signals with a phase shift of 90° are registered. b) M_x and M_y components of transversal magnetization follow an exponential decay, occurring on timescale in the order of μs for solids to s for liquids. Their intensity follows the behavior of amplitude in a damped oscillator.

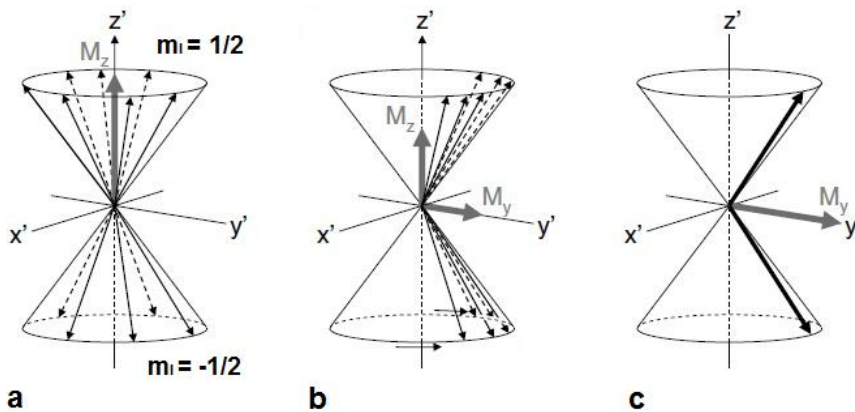


Figure 1.3 - The emerging of transversal magnetization. a) The bulk magnetic moment is longitudinal, and given by the residual magnetization of spins distributed parallel ($m_l=1/2$) and anti-parallel ($m_l=-1/2$) to the B_0 -field. b) When the field B_1 in the x' -direction is turned on, the spin transition from the ground state to the excited state occurs, and the magnetization is transferred into the transverse plane. c) After the action of RF-pulse the magnetization has only a transversal component (along the y' -axis).

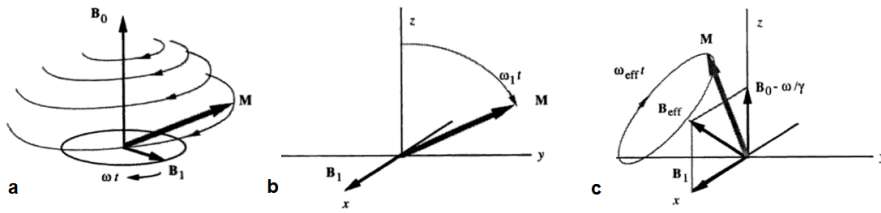


Figure 1.4 – Macroscopic magnetization in different reference frames. a) The magnetization view in the laboratory (fixed) reference frame, is precessing simultaneously about B_0 at ω_0 and about B_1 at ω_1 , at the on resonance condition. b) The same situation described in (a) is depicted here in a rotating reference frame where B_1 is stationary. The effective longitudinal field is zero on resonance, and only the precession about B_1 is apparent. c) The same situation described in (b), but when the RF field is off-resonant. In this case the magnetization precesses about an effective B-field (B_{eff}), determined by the RF-field and the offset frequency. (Images adapted from Callaghan's book, [46]).

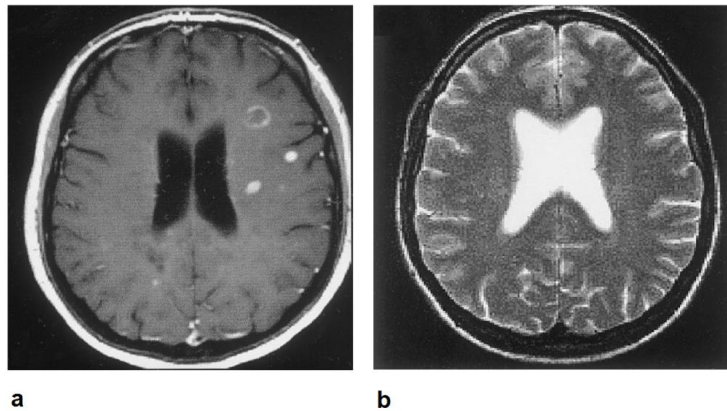


Figure 1.5 – Axial human brain maps of T_1 and T_2 relaxation time. a) Axial T_1 -weighted image from a multiple sclerosis (MS) patient (an MS lesion is recognizable in the enhanced ring on the left hemisphere). The brighter the pixels, the higher the T_1 constant, meaning that the spins interact more with the lattice: for this reason the myelinated axons which compose the white matter appear lighter, while the ventricles containing cerebro-spinal fluid appear darker. b) Axial T_2 -weighted image from a healthy control. The brighter the pixels, the higher the T_2 constant. The image contrast is inverted compared to (a): here the white matter appears darker than the other two tissues. The gray matter, comprising the body of neurons, has an intermediate tone, while the ventricles are hyperintense.

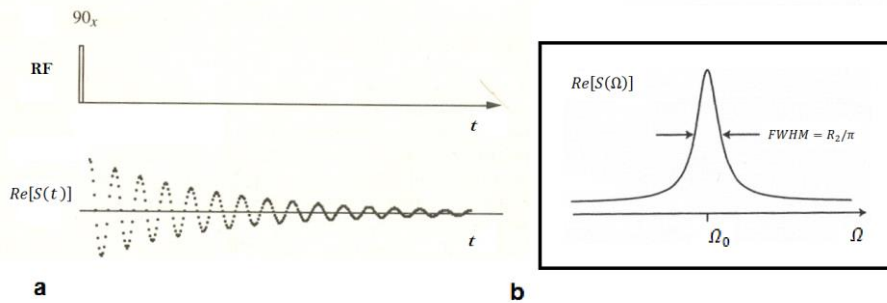


Figure 1.6 – Free Induction Decay (FID) and the absorption spectrum. a) FID following a single RF 90° pulse. Only the real part of the signal, corresponding to the in-phase receiver output, is shown. The receiver phase is set to 0. b) Real part of the spectrum obtained by Fourier Transforming the FID in (a). The FWHM and the center of the absorption spectrum are indicated. (Images adapted from Callaghan's book, [46]).

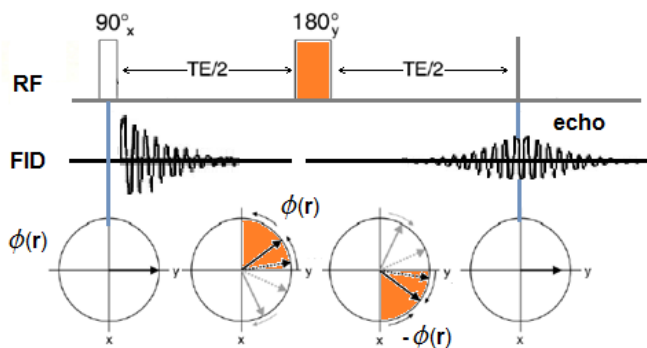


Figure 1.7 – Sketch of a Spin echo sequence. Following the RF 90° -pulse the magnetization is transferred into the y-axis. During the first interval time $TE/2$ the spins lose phase coherence because of the inhomogeneity of the magnetic field. The RF 180° -pulse inverts the M_y component, so that the spins experience a rephasing. When $t = TE$ the complete refocusing of the spin phases generates a signal echo. A certain irreversible phase loss occurs during TE , which results in a lower signal intensity of the echo compared to the initial signal.

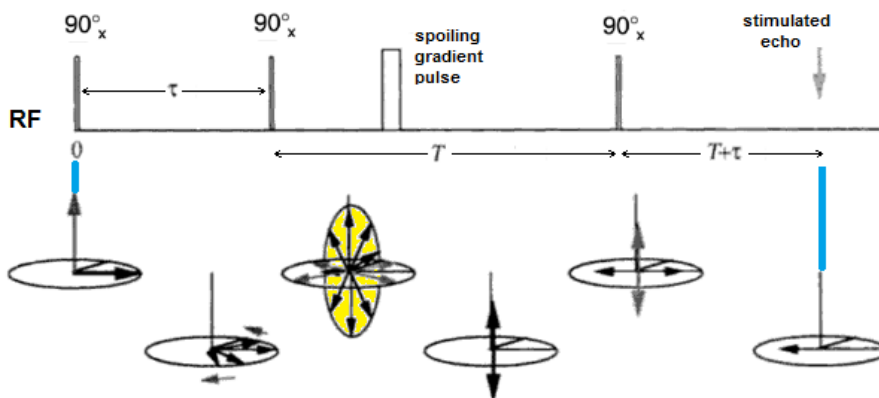


Figure 1.8 – Sketch of a stimulated echo sequence. Following the RF 90° -pulse the magnetization is transferred into the y -axis. During the first interval time τ the spins lose phase coherence because of the inhomogeneity of the magnetic field. The second RF 90° rotates these components into longitudinal polarization along the z -axis, storing in this way the transversal magnetization. A spoiling gradient is applied during this storage period to destroy the unwanted transverse magnetization. The final RF 90° , applied after T , refocuses all the spins causing the formation of an echo at $T + \tau$. (Images adapted from Callaghan's book, [46]).

1.3 How to perform 3D imaging?

MRI, or NMR microscopy, differs from NMR spectroscopy because it provides images of the investigated samples, where the intensity of each volumetric element, or voxel, is proportional to a determined NMR parameter, rather than measuring an average value over the entire volume of the sample. Since the first introduction of gradients by Paul Lauterbur in 1973 [47], and the contemporary introduction of the reciprocal space vector and approach by Peter Mansfield [48] this powerful resource made NMR so popular, because it was shown how to encode the spatial information using a signal sampled over time, with the possibility of highlighting different characteristics depending on the chosen contrast. Furthermore, a dynamic analogue of NMR microscopy was developed, to perform imaging in samples characterized by moving molecules, for example molecules interested by diffusion processes. In MRI the NMR signal is acquired in the presence of a magnetic field linear gradient, i.e. a magnetic

field changing linearly with the position across the sample, introducing a spatial dependence in the Larmor frequency of spins. In the following, the basic principles of the imaging technique will be reviewed.

1.3.1 Magnetic field gradients and k-space

Magnetic field gradients are magnetic fields which vary with the position. In MRI we make use of linear gradients, which cause the static field B_0 to increase linearly with the position on a selected direction:

$$\mathbf{G} = (G_x, G_y, G_z) = \left(\frac{dB}{dx}, \frac{dB}{dy}, \frac{dB}{dz} \right) \quad (1.35)$$

Since the gradient causes additional fields much smaller than the polarizing field magnitude, B_0 , the Larmor frequency is affected only by any components parallel to $\mathbf{B} = (0, 0, B_0)$, while orthogonal components only have the effect of slightly tilting the net field direction [46].

When a magnetic field gradient parallel to B_0 is applied, a i.e. $dB/dz \neq 0$, the local Larmor frequency becomes:

$$\omega(\mathbf{r}) = \gamma B_0 + \gamma \mathbf{G} \cdot \mathbf{r} \quad (1.36)$$

where \mathbf{G} is defined as the gradient of the field component parallel to \mathbf{B} . Consider now the nuclear spins at position \mathbf{r} in the sample, occupying an element of volume dV . Assuming that T_2 relaxation is much slower than the transversal dephasing due to the spread in frequencies, then the signal arising from a volume element is:

$$dS(\mathbf{r}, \mathbf{G}, t) = \rho(\mathbf{r}) dV e^{i\omega(\mathbf{r})t} = \rho(\mathbf{r}) dV e^{i(\gamma B_0 + \gamma \mathbf{G} \cdot \mathbf{r})t} \quad (1.37)$$

If we choose the reference frequency to be γB_0 (the *on-resonance* condition), the signal obtained oscillates at $\gamma \mathbf{G} \cdot \mathbf{r}$, and so the integral becomes:

$$S(\mathbf{G}, t) = \int_V \rho(\mathbf{r}) e^{i(\gamma \mathbf{G} \cdot \mathbf{r})t} d\mathbf{r} \quad (1.38)$$

where $d\mathbf{r}$ represents integration over the volume element. Now we use the reciprocal space vector \mathbf{k} introduced by P. Mansfield in 1973 [48]:

$$\mathbf{k} = \frac{\gamma \mathbf{G} t}{2\pi} \quad (1.39)$$

The reciprocal \mathbf{k} -space may be traversed by moving either in time or in gradient magnitude, that means in fact moving either using a gradient in x- or y-direction (see Par. 1.3.3). In practice, the sampling of \mathbf{k} -space takes place as we sample the FID at successive time intervals in the presence of a gradient. This technique of acquisition, where the \mathbf{k} -space is associated to a Cartesian raster, is known as *two-dimensional Fourier Imaging*¹⁰. The signal $S(\mathbf{k})$ is measured in the time domain, while the spin density $\rho(\mathbf{r})$ expressed in the formalism of \mathbf{k} -space is measured in the frequency domain. In fact the signal and the spin density in \mathbf{k} -space formalism are linked by a couple of mutually conjugate Fourier Transforms:

$$\begin{aligned} S(\mathbf{k}) &= \int_V \rho(\mathbf{r}) e^{i2\pi \mathbf{k} \cdot \mathbf{r}} d\mathbf{r} \\ \rho(\mathbf{r}) &= \mathfrak{F}[S(\mathbf{k})] = \int_V S(\mathbf{k}) e^{-i2\pi \mathbf{k} \cdot \mathbf{r}} d\mathbf{k} \end{aligned} \quad (1.40)$$

This is the fundamental relationship of MRI. To derive such equation, we assumed that the signal was simply proportional to the spin density (as shown in (1.37)). Nevertheless, as seen previously, there are many physical parameters which can affect the NMR signal, so that what is actually imaged is a contrasted spin density, rather than the simple spin density. This issue can be easily addressed introducing a contrast factor $C(\mathbf{r})$ in (1.37), which means that what is imaged will be the term $C(\mathbf{r})\rho(\mathbf{r})$ rather than $\rho(\mathbf{r})$. Clearly, by normalizing images obtained with and without the contrast effect, a map of $C(\mathbf{r})$ can be obtained. This normalization is applied in Diffusion Weighted Imaging (DWI), where the images acquired with a diffusion weight are divided by the intensity of the image acquired with no diffusion weight (see Par. 2.3.3).

¹⁰ Another approach consists in the so called *two-dimensional projection reconstruction*. In this case the imaging gradient G is applied in some arbitrary direction, and a series of signal points are obtained along a radial line in \mathbf{k} -space, which is sampled in a polar raster. The main advantage of this technique towards the two-dimensional Fourier Imaging is a slightly higher signal-to-noise ratio; the main drawback is that the distortions due to magnetic susceptibility inhomogeneity are more widespread.

1.3.2 Selective excitation

MRI in a sample is practically performed by spatially *selecting* a voxel of that sample, which is achieved by using a selective excitation. This type of excitation involves applying an RF-pulse which affects only a specific region of the NMR frequency spectrum. In the presence of a magnetic field gradient, the selective RF-pulse may be used to excite only those spins within some specified layers of the sample. This phenomenon is based on the principle that the frequency bandwidth of an RF-pulse is inversely proportional to the pulse duration T , given that the turn angle is determined by the product $\gamma B_1 T$ (as was shown in (1.23)). To understand what happens to the magnetization, we write the Bloch equations for a field gradient applied along z (neglecting the relaxation):

$$\begin{aligned}\frac{dM_x}{dt} &= \gamma M_y G_z z \\ \frac{dM_y}{dt} &= \gamma(-M_x G_z z + M_z B_1(t)) \\ \frac{dM_z}{dt} &= -\gamma M_y B_1(t)\end{aligned}\tag{1.41}$$

Now let us consider the situation from the frame of reference that rotates about the z -axis at an angular frequency of $\gamma G_z z$, $x'y'z'$. Under the linearity assumption, i.e. z -component of magnetization changing only slightly so that $dM_{z'}/dt = 0$ and $M_{z'} = M_0$:

$$\begin{aligned}\frac{dM_{x'}}{dt} &= -\gamma M_0 B_1(t) \sin[\gamma G_z z(t + T)] \\ \frac{dM_{y'}}{dt} &= \gamma M_0 B_1(t) \cos[\gamma G_z z(t + T)] \\ \frac{dM_{z'}}{dt} &= 0\end{aligned}\tag{1.42}$$

If we treat $M_{x'}$ and $M_{y'}$ as real and imaginary part of a complex number, M_{+} , (1.42) becomes:

$$\frac{dM_{+}}{dt} = i\gamma M_0 B_1(t) e^{i\gamma G_z z(t+T)}\tag{1.43}$$

Integrating and returning to the laboratory frame $M_{+}(T) = M_{+}(T) e^{-i\gamma G_z z 2T}$ gives:

$$M_+ = i\gamma M_0 e^{-i\gamma G_z z T} \int_{-T}^T B_1(t) e^{i\gamma G_z z t} dt \quad (1.44)$$

Thus, the equation states that the FID signal is proportional to the amplitude of the RF spectrum at z . If we want to excite a rectangular slice, then we will need a rectangular spectrum. Besides, (1.44) contains a net phase shift, $\gamma G_z z T$, which is a nuisance in a plane normal to z and which will be removed by applying an opposite sign z -gradient of magnitude $-G_z$ for a time T . Since the Fourier Transform of a rectangular function is a *sinc* function, where $\text{sinc}(x) = \frac{\sin(x)}{x}$, the RF-pulse will have the form of:

$$\mathbf{B}_1(t) = B_1(t)(\hat{i} \cos \omega_0 t - \hat{j} \sin \omega_0 t) \quad (1.45)$$

that is the same expression as (1.19) with a variable amplitude over time.

1.3.3 Image reconstruction

To perform the in-plane reconstruction, we need to sample the signal in presence of a gradient, obtaining points along a single line in \mathbf{k} -space. With the use of a G_x -gradient, or *read gradient* (G_r), we move in the read direction, and we sample a line in the \mathbf{k} -space. The intercept of this line along the orthogonal axis can be changed by imposing a G_y -gradient, or phase gradient (G_ϕ) for a fixed period before the sampling begins. This term phase gradient is due to the fact that it imparts a phase modulation to the signal, dependent on the position of the volume elements along the y -axis. With the use of a phase gradient we can sample a column in the \mathbf{k} -space, as shown in **Figure 1.9**.

Let us imagine that we have chosen an axial slice (i.e. a slice cut orthogonally to the polarizing field). This slice has thickness = a , and we want to obtain the spin density distribution across that slice. In order to 'choose' the slice we adopt a G_z -gradient, or *slice gradient* (G_s), and integrating the signal over a we are able to derive an expression depending on the other two components of \mathbf{k} -vector (k_x and k_y).

The signal will be then:

$$S(k_x, k_y) = \int_{-a/2}^{a/2} \left(\int_{-\infty}^{\infty} \int_{-\infty}^{\infty} \rho(x, y, z) e^{i2\pi(k_x x + k_y y)} dx dy \right) dz \quad (1.46)$$

To obtain the density $\rho(x, y, z)$ or, more interestingly, the contrast factor defined in Par. 1.3.1, one needs to calculate the inverse Fourier transform of (1.46):

$$\rho(x, y) = \int_{-\infty}^{\infty} \int_{-\infty}^{\infty} S(k_x, k_y) e^{-i2\pi(k_x x + k_y y)} dk_x dk_y \quad (1.47)$$

where the outer integral, which simply represents the process of averaging across the slice, was neglected. Since the density is a real quantity, the signal is subject to *hermitian* symmetry¹¹ $S(-k_x, -k_y) = S^*(k_x, k_y)$, with * indicating the complex conjugate, so in principle, only two out of four quadrants of the $k_x k_y$ -plane must be sampled.

1.3.3.1 An example of k-space sampling: Echo Planar Imaging

Echo Planar Imaging (EPI) is an example of fast imaging sequences that are fundamental for MRI experiments, because it allows to sample the entire \mathbf{k} -space with just one initial RF-pulse. While the duration of a sequence illustrated in **Figure 1.9a** is $N \times TR$ (with TR the repetition time, that is the interval time between two successive repetition of the main RF90°-pulse, and N the lines in \mathbf{k} -space) because each \mathbf{k} -space row is filled after a selective pulse, the total duration of an EPI acquisition is about a TR. The **Figure 1.10b** shows a typical sampling of \mathbf{k} -space with an EPI sequence. The \mathbf{k} -space sampling starts in the point indicated by 1, and when G_r is turned on, the first gradient-echo is acquired along the first \mathbf{k} -space line. A so called *blip* phase encoding gradient changes the position in \mathbf{k} -space till the point indicated by 2. After another refocusing ($-G_r$) the second acquisition starts. Iterating this process the \mathbf{k} -space is completely sampled. Maximum echo formation is achieved in \mathbf{k} -space origin

¹¹ In mathematical analysis, a *Hermitian symmetry* is the characteristic property of a Hermitian function, that consists in the fact that the complex conjugate is equal to the original function with the variable changed in sign. Generally speaking, f is a Hermitian function if and only if the real part of f is an even function, and the imaginary part of f is an odd function.

where the initial negative phase encoding gradient is completely refocused by the sum of all blip gradient.

While the most important EPI advance is the shortness of the acquisition time, it suffers for a main drawback. The fact that the magnetic field inhomogeneities are not refocused because of the absence of a RF180°-pulse (as in the Spin Echo sequence, see Par. 1.2.4.1). For this reason the images are distorted and, since T_2^* is smaller, the signal intensity is lower because it decays faster. The use of a Spin-Echo (SE) EPI sequence permits to overcome this inconvenience (see **Figure 1.10a**).

1.3.4 Image parameters

As we have seen in the previous sections, the images are formed by means of the Fourier transform. In this section the most important image parameters, such as the Nyquist rate, the field of view, the spatial resolution, and the signal and contrast to noise ratio are briefly presented. Finally, a synthetic description of the anatomical planes considered in animal and human imaging will be provided.

1.3.4.1 The sampling rate

In MRI we are concerned primarily with the sampling in the frequency domain. We define the sampling period Δk_x , as the interval between two successive acquisitions along the x-direction of \mathbf{k} -space, and the rate of sampling as its inverse: Δk_x^{-1} . Defining with $F(k_x)$ the sampled version of a function $f(x)$, we may represent it by a string of delta functions of amplitude given by the sampled values, equally spaced of Δk_x . Fourier transforming $F(k_x)$ we obtain replicated versions of $f(x)$, separated by the rate of sampling Δk_x^{-1} . If $f(x)$ has a finite extent, and the rate of sampling is too low, the replications of $f(x)$ may overlap, resulting in a condition known as *aliasing* [49]. The minimum sampling rate that avoids aliasing is called the **Nyquist rate**, and it is equal to the total extent of $f(x)$ sampled in k -space, which can be expressed as a function of the

sampling period and the maximum frequency acquired, or as a function of the number of acquired points, N:

$$W_{k_x} = 2 \left(k_{x_{max}} + \frac{\Delta k_x}{2} \right) = \Delta k_x \cdot N_x \quad (1.48)$$

1.3.4.2 The Field of View

Considering now the formation of a 2D image: we have that during the **k**-space sampling the magnetization is acquired with sampling rate of Δk_x^{-1} along x-axis and of Δk_y^{-1} along y-axis. The imaging periods are proportional, respectively, to the intensity of the read-gradient and the acquisition time of the analog-to-digital converter, in case of Δk_x , and to the intensity of the phase-gradient and its duration in case of Δk_y . We define the effective **Field Of View (FOV)** in one spatial direction as the length corresponding to the relative sampling rate, which has dimensions of the inverse of a spatial frequency:

$$\begin{aligned} FOV_x &= \Delta k_x^{-1} \\ FOV_y &= \Delta k_y^{-1} \end{aligned} \quad (1.49)$$

1.3.4.3 The spatial resolution

We use the FOV to define another important characteristic of images, which determines how 'sharp' the images look like, that is the (in-plane) **spatial resolution**. This feature represents the capability of distinguishing two close objects, and in MRI it depends on the FOV and the number of pixels in which we divide the image. Indicating with N the number of pixels (or sampled points) in each direction, we define the spatial resolution as:

$$\delta_x = \frac{FOV_x}{N_x} = \frac{1}{\Delta k_x N_x} = \frac{1}{W_{k_x}}$$

$$\delta_y = \frac{FOV_y}{N_y} = \frac{1}{\Delta k_y N_y} = \frac{1}{W_{k_y}} \quad (1.50)$$

Given the in-plane resolution and the slice thickness, the dimension of a volumetric element of the sample, namely the voxel, can be retrieved. Given a slice thickness of Δz , the voxel volume will be:

$$V_{voxel} = \delta_x \cdot \delta_y \cdot \Delta z \quad (1.51)$$

A typical voxel volume in MRI is comprised between a minimum value of order 10^{-3} mm^3 (considering an in-plane resolution of $30 \text{ }\mu\text{m} \times 30 \text{ }\mu\text{m}$ and a slice thickness of $500 \text{ }\mu\text{m}$) in spectrometers for small samples, to a maximum value of order 10 mm^3 (considering an in-plane resolution of $1.8 \text{ mm} \times 1.8 \text{ mm}$ and a slice thickness of 3 mm) in spectrometers for in vivo human imaging.

1.3.4.4 The Signal to Noise Ratio and the Contrast to Noise Ratio

The parameter which quantifies image quality is the **signal-to-noise ratio (SNR)**, which roughly represents the ratio between the signal acquired in a particular region of interest (ROI), divided by the standard deviation of the background intensity:

$$SNR = \frac{\mu_S}{\sigma_N} \quad (1.52)$$

SNR is influenced by the particular MRI sequence, beyond the instrumental characteristics of the NMR spectrometer. In particular, NMR signal is affected by thermal noise, an electronic noise generated by the thermal agitation of the charge carriers (mainly electrons) both in the sample and in the receiver coil. The signal and the noise are distinguished by their statistical properties: the signal attenuation increases with time, and it presents reproducibility; the noise is independent of time, and it is not reproducible, but random. Thanks to these distinct properties it is possible to increase SNR by performing signal

averaging. Repeating the same sequence N times, the SNR will be improved as $SNR \sim \sqrt{N}$, with the only drawback of increasing the total acquisition time (that is roughly $\Delta t_{acq} \sim TR \cdot N$). In fact, if we consider a simple case with 2 averages, considering that the product between two random noise mediates to zero:

$$SNR' = \frac{\mu_{S_{tot}}}{\sigma_{N_{tot}}} = \frac{\mu_{S_1} + \mu_{S_2}}{\langle (\sigma_{N_1} + \sigma_{N_2})^2 \rangle^{1/2}} \sim \frac{2\mu_S}{\langle \sigma_{N_1}^2 + \sigma_{N_2}^2 + 2\sigma_{N_1}\sigma_{N_2} \rangle^{1/2}} \sim \frac{2\mu_S}{\sqrt{2}\sigma_N} \sim \sqrt{2}SNR$$

And this can be generalized to N averages.

Finally, using the formula of SNR we may define the contrast-to-noise ratio (CNR), which is the relationship of signal intensity differences between two regions, scaled to image noise. Improving CNR increases perception of the distinct differences between two areas of interest, and in fact this is a relevant parameter to establish the quality of clinical images. In short, a CNR is a summary of SNR and contrast, and may be derived by the difference in SNR between two relevant ROIs:

$$CNR = SNR_1 - SNR_2 \sim \frac{\mu_{S_1} - \mu_{S_2}}{\sigma_N} \quad (1.53)$$

1.3.4.5 Spatial coordinates and imaging planes

The NMR spectrometers make use of a reference frame which is distinct from that one of the laboratory, which can be associated to the Cartesian axes XYZ. These peculiar coordinates are important to consider when we are dealing with clinical MRI, because they represent a universally known codex in this field. The spatial coordinates used instead of XYZ are defined with regard to the human (or animal) body:

- the X axis is replaced by the left-right (L/R) direction, going from the left to the right side of the body;
- the Y axis is replaced by the anterior-posterior (A/P) direction, going from the frontal part of the body to the back;

- the Z axis is replaced by the superior-inferior (S/I) direction, going from the top of the body to the bottom.

The verse of these three orthogonal axes (L/R vs R/L, A/P vs P/A, S/I vs I/S) depends on the convention used. For example, in the radiologic convention¹² (RAS, R/L, A/P, S/I), the axis corresponding to the X-direction is oriented from right to left, and this results in an inversion of the right and left part of the image with respect to the real anatomy, as if we were looking at the imaging plane from the point of view of the patient's feet. This convention is adopted by some software for the pre-processing and analysis of DWIs, such as FMRIB Software Library (FSL, see Materials and Methods of Chapter 5 for further details).

The new spatial axes define the imaging planes, shown in **Figure 1.11**:

- the *axial* plane, generated by R/L and P/A axes, is orthogonal to an ideal vertical axis crossing the body;
- the *coronal* plane, generated by R/L and S/I axes divides the body into anterior and posterior part;
- the *sagittal* (sometimes named 'trasversal') plane, generated by P/A and S/I axes divides the body into left and right side.

¹² Conversely, the *neurologic convention* (LAS, L/R, A/P, S/I) does not invert the right and left side of the body, thus the lateralization of the image corresponds to the real anatomy of the subject.

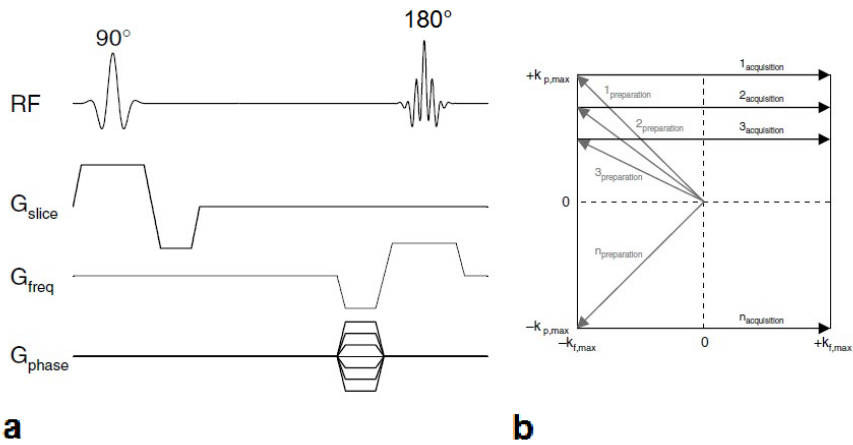


Figure 1.9 – Sampling of k -space or reciprocal-space. a) An imaging sequence is shown, with the use of slice, frequency (read) and phase encoding gradients, from top to bottom. b) The k -space sampling is achieved by moving along the y -direction through the use of phase gradient, and by sampling along a horizontal line through the use of the frequency gradient, which corresponds to acquiring a FID.

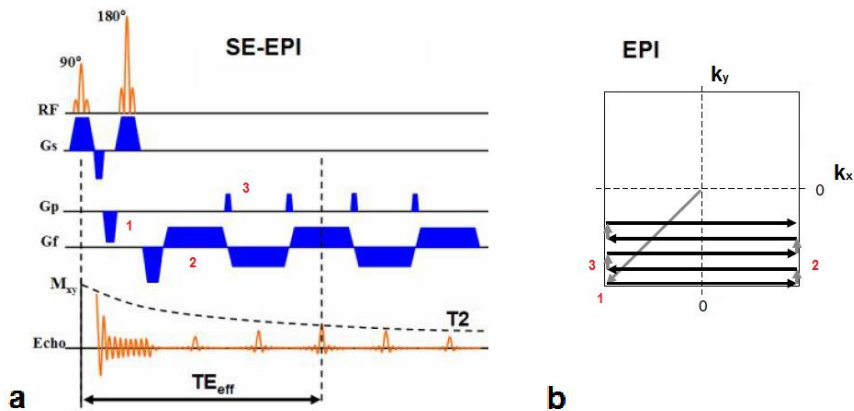


Figure 1.10 – Spin Echo-Echo Planar Imaging sequence and EPI sampling of k -space. a) A Spin Echo-EPI sequence is shown, with the use of slice, phase, and frequency (read) encoding gradients, from top to bottom. The amplitude of the FID and its echoes decreases over time and scales as e^{-t/T_2} . Blip phase gradients allow to move along the y -direction of k -space. b) EPI sampling of k -space. The first movement (1) is provided by the first phase gradient; then the acquisition proceeds along the x -direction, corresponding to the read gradient (2); the blip phase gradient makes the sampling jump a step further along the y -direction of k -space (3).

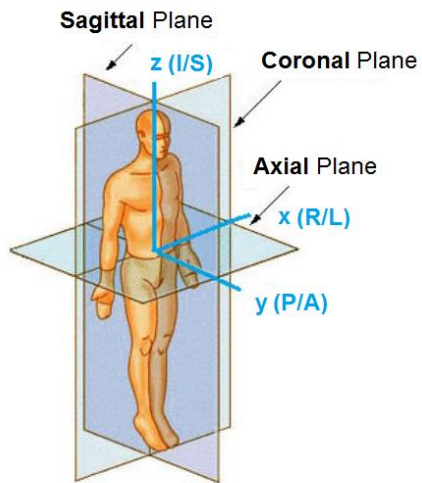


Figure 1.11 – Imaging planes commonly used in MRI. These planes are generated by the set of three orthogonal axes, indicated in the figure (R/L = right/left; P/A = posterior/anterior; I/S = inferior/superior), which are referred to an ideal origin placed in the center of gravity of the human (or animal) body.

Chapter 2 Diffusion Weighted Imaging: imaging matter exploiting molecular diffusion

NMR is one of the most powerful tools to investigate diffusion non-invasively. With the term *diffusion* we refer to a spontaneous random phenomenon occurring in any fluid where molecules possess a thermal or kinetic energy, being at temperature greater than zero Kelvin degrees. Classically, the process of diffusion is often connected to the flattening of concentration gradients, but the principle is equally applicable to the movement of molecules within a fluid composed of a single type of molecule: in this case we name the process *self-diffusion*. The Scottish botanist R. Brown was the first documented observer of diffusion, which is also known as *Brownian motion* for this reason. In 1827 he observed under microscope the random movement of pollen particles suspended in water. A formal, classical theory of diffusion was introduced by A. Fick in 1855, but it was only in 1905 that a microscopic description of molecular diffusion was provided by A. Einstein. He demonstrated that, provided that the number of particles is large enough, there is a particular linear relation between the mean squared displacement of molecules from the starting point and the observation time during which the diffusion takes place. This chapter deals with the basic principles of diffusion process, and describes the techniques that allow to analyze diffusion by means of MRI, the so-called Diffusion-Weighted Imaging (DWI) and Diffusion Tensor Imaging (DTI). According to these techniques, diffusion is modeled as an ideal process happening in a homogeneous environment.

2.1 Molecular diffusion examined at a macroscopic scale: classic description

The molecules constituting the fluid at $T > 0$ K possess kinetic energy and are therefore constantly moving: the greater the energy, the faster the movement. Their motion can be considered *random* due to the fact that their trajectories are continuously deviated by collisions with other solvent particles. Diffusion plays a role in the chemical reactions, because reactions need the collisions between reagents to take place. Generally we may consider the diffusion of solute particles in a solvent, but the focus of this thesis work is the water *self-diffusion*, by which we indicate the motion of solvent particles in the solvent itself.

At a macroscopic level molecular diffusion manifests itself as a net flux of molecules under the concentration gradient, that is from a more concentrated compartment to a less concentrated one. It is indeed a spontaneous process, involving the solute particles which drift from higher to lower concentrations so as to equalize the concentration gradients, and sometimes this process is known as *mutual diffusion*, referring to the two phases of solute and solvent.

A. Fick introduced two phenomenological laws describing the flux of molecules across a permeable membrane with a not null concentration gradient. For the sake of simplicity, let us consider an isotropic fluid, and begin to treat the mono-dimensional case.

2.1.1 The first Fick's law

The first Fick's law states that the flux density of molecules, J across a surface, i.e. the number of diffusing particles per unitary time and surface, is proportional to the concentration gradient C of the diffusing species:

$$J(x, t) = -D \frac{\partial c(x, t)}{\partial x} \quad (2.1)$$

which extends to the 3D case:

$$J(\mathbf{r}, t) = -D\nabla c(\mathbf{r}, t) \quad (2.2)$$

The sign of the equation ensures that the particles move from a higher concentrated region to a lower concentrated one. In homogeneous environments, the factor of proportionality, D , is the diffusion coefficient and depends on the characteristics of the diffusing particle and on those of the solvent. It is described by the Sutherland-Einstein equation¹³ [5]):

$$D = \frac{k_B T}{6\pi\eta r} \quad (2.3)$$

with η the fluid viscosity, and r the size (radius) of the solute particle, or the solvent particle in case of self-diffusion.

2.1.2 The second Fick's law

The second Fick's law predicts the behavior of concentration over time, linking it to the local variation of the diffusion flux. Considering the mono-dimensional case, this means:

$$\frac{\partial c(x,t)}{\partial t} = -\frac{\partial J(x,t)}{\partial x} \quad (2.4)$$

which is a form of continuity equation, or total mass conservation law inside a liquid, obtained by considering the flux variation in a parallelepiped of volume $V = S \cdot \Delta x$ across the surface S , between two positions at a distance Δx (see **Figure 2.1**):

¹³ The Sutherland-Einstein equation is derived combining the Stokes-law, which describes the viscous friction F_a of a particle of radius r moving at a speed v in a medium with viscosity η , ($F_a = -6\pi\eta r v$) and the Einstein-Smoluchowski relation, which predicts the diffusivity D of particles with mobility v/F_a at a temperature T ($D = \left| \frac{v}{F_a} \right| k_B T$).

$$\Delta J(x, t) = J(x, t) - J(x + \Delta x, t) \quad (2.5)$$

The flux is the number of diffusing particles per unitary time and surface, and expressing the number of particles as a function of concentration we have:

$$\Delta J(x, t) = \frac{\partial N}{s \partial t} = \frac{V \cdot \partial c(x, t)}{s \partial t} = \frac{S \cdot \Delta x \cdot \partial c(x, t)}{s \partial t} = \frac{\Delta x \partial c(x, t)}{\partial t} \quad (2.6)$$

By combining (2.5) and (2.6), and substituting the first Fick's law into (2.4) we get the diffusion equation for concentration $c(x, t)$:

$$\frac{\partial c(x, t)}{\partial t} = D \frac{\partial^2 c(x, t)}{\partial x^2} \quad (2.7)$$

which, in the 3D-case, becomes:

$$\frac{\partial c(\mathbf{r}, t)}{\partial t} = D \nabla^2 c(\mathbf{r}, t) \quad (2.8)$$

This is a partial differential equation (PDE). It is possible to show [50] that the solution is given by a Gaussian function centered in $\mu = 0$ and with variance $\sigma^2 = 2Dt$:

$$c(t) = \frac{A}{\sqrt{4\pi Dt}} e^{-\frac{x^2}{4Dt}} \quad (2.9)$$

It is important to underline the hypotheses of homogeneity and isotropy of the fluid, which lead to the Fick's laws. If the former (homogeneous fluid) is violated, i.e. we are dealing with heterogeneous environments, then the diffusion coefficient will vary as a function of position, thus $D = D(\mathbf{r})$. If instead the latter hypothesis (isotropic fluid) is violated, then the behavior will be direction-dependent and a single diffusion coefficient will not be able to characterize the diffusion, thus a tensor $D = \vec{D}$ will be more appropriate. The attention of the NMR community in the last 20 years has been focused on the latter violation, since anisotropy proved to be a powerful contrast tool to discriminate between different tissues.

2.1.3 Anisotropic diffusion and the diffusion tensor

The random motion of molecules in a homogeneous and isotropic medium, in the hypothesis of an unlimited space (or a space which extends more widely than the distance covered by molecules during a given time period), is called ‘free diffusion’. In biological tissues the diffusion of water molecules is rather hindered by cellular membranes, macromolecules, organelles, and other structural elements, and in such cases the term ‘restricted diffusion’ is more appropriate. Another hypothesis that does not hold in biological tissues is the isotropy of the space explored by water molecules. At a microscopic level in fact, the spatial organization of certain structures such as fibers, barriers, cells, makes the space ‘anisotropic’, that means varying depending on the direction of observation. In this case we name the diffusion ‘anisotropic diffusion’, and the use of a tensor describing the diffusive motion in each direction is more correct. An example is provided by the so called white matter (WM), which in MRI jargon is the part of brain parenchyma comprising axonal fibers covered with myelin. Both the axonal membrane and the myelin¹⁴ sheath [8] provide a barrier to water diffusion in the radial direction, and at the same time trace a guideline for the diffusion in the longitudinal direction, that will be facilitated. The diffusion tensor \vec{D} describes the mobility of particles along each direction, and the eventual correlations between couples of directions, and it is a second rank symmetric tensor:

$$\vec{D} = \begin{pmatrix} D_{xx} & D_{xy} & D_{xz} \\ D_{yx} & D_{yy} & D_{yz} \\ D_{zx} & D_{zy} & D_{zz} \end{pmatrix} \quad (2.10)$$

where each element is defined positive for the physical meaning of diffusivity, $D_{ij} > 0 \forall i, j$, and the symmetry is guaranteed by the Onsager’s reversibility principle and supported by the reasonable hypothesis that the diffusion occurring in direction $i \rightarrow j$ is the same as the one in the opposite direction $j \rightarrow$

¹⁴ The *myelin sheath* is a multilayered membrane deriving from the Schwann cells in the peripheral nervous system, and from the oligodendrocytes in the central nervous system (composed of brain and spinal cord). This membrane enrolls the axons and acts as an insulating membrane, ensuring the passage of electric currents and speeding the transmission of nervous spikes. The myelin sheath shows a periodic structure, with an alternation of phospholipid bilayers and cytoplasmic rings, enriched with membrane proteins.

i , so that $D_{ij} = D_{ji} \forall i, j$. The diagonal elements D_{ij} t.c. $i = j$ describe the diffusion along 3 orthogonal directions; the off-diagonal elements describe the correlations between them.

Considering the first Fick's law, the new formulation in case of a diffusion tensor \vec{D} is:

$$\begin{cases} -J_x = D_{xx} \frac{\partial c}{\partial x} + D_{xy} \frac{\partial c}{\partial y} + D_{xz} \frac{\partial c}{\partial z} \\ -J_y = D_{yx} \frac{\partial c}{\partial x} + D_{yy} \frac{\partial c}{\partial y} + D_{yz} \frac{\partial c}{\partial z} \\ -J_z = D_{zx} \frac{\partial c}{\partial x} + D_{zy} \frac{\partial c}{\partial y} + D_{zz} \frac{\partial c}{\partial z} \end{cases} \quad (2.11)$$

where the coefficients D_{ij} indicate the contribution of the concentration gradient along j -direction to the diffusion in the i -direction. The second Fick's law will assume the form:

$$\begin{aligned} \frac{\partial c(\mathbf{r}, t)}{\partial t} &= \vec{D} \left(\frac{\partial^2 c}{\partial x^2} + \frac{\partial^2 c}{\partial y^2} + \frac{\partial^2 c}{\partial z^2} \right) = \\ &= D_{xx} \frac{\partial^2 c}{\partial x^2} + D_{yy} \frac{\partial^2 c}{\partial y^2} + D_{zz} \frac{\partial^2 c}{\partial z^2} + 2D_{xy} \frac{\partial^2 c}{\partial x \partial y} + 2D_{yz} \frac{\partial^2 c}{\partial y \partial z} + 2D_{zx} \frac{\partial^2 c}{\partial z \partial x} \end{aligned} \quad (2.12)$$

Now the tensor is defined in the laboratory reference frame, associated to the set of axes XYZ. We can apply a coordinate transform, so that the equation (2.12) takes the form:

$$\frac{\partial c}{\partial t} = \lambda_1 \frac{\partial^2 c}{\partial u^2} + \lambda_2 \frac{\partial^2 c}{\partial v^2} + \lambda_3 \frac{\partial^2 c}{\partial w^2} \quad (2.13)$$

that is the same transform by which one derives from the equation:

$$D_{xx}x^2 + D_{yy}y^2 + D_{zz}z^2 + 2D_{xy}xy + 2D_{yz}yz + 2D_{zx}zx = cost \quad (2.14)$$

the canonic ellipsoid equation [51]:

$$\frac{1}{2\lambda_1 t} u^2 + \frac{1}{2\lambda_2 t} v^2 + \frac{1}{2\lambda_3 t} w^2 = 1 \quad (2.15)$$

The transform that links the laboratory reference frame individuated by XYZ to the diffusion reference frame individuated by UVW is equivalent to the rotation matrix which diagonalizes $\vec{\mathbf{D}}$, providing the diffusion tensor eigenvalues and eigenvectors, by solving [52]:

$$(\vec{\mathbf{D}} - \lambda_i \vec{\mathbf{I}}) \varepsilon_i = 0 \quad (2.16)$$

where $\vec{\mathbf{I}}$ is the identity matrix, thus:

$$\begin{pmatrix} D_{xx} - \lambda_i & D_{xy} & D_{xz} \\ D_{yx} & D_{yy} - \lambda_i & D_{yz} \\ D_{zx} & D_{zy} & D_{zz} - \lambda_i \end{pmatrix} \begin{pmatrix} \varepsilon_{ix} \\ \varepsilon_{iy} \\ \varepsilon_{iz} \end{pmatrix} = \begin{pmatrix} 0 \\ 0 \\ 0 \end{pmatrix} \quad (2.17)$$

where ε_i (or $\mathbf{V}_i = V_i \hat{\varepsilon}_i$) represent the *eigenvectors*, and λ_i represent the *eigenvalues* (with $i = 1,2,3$). The matricial relation (2.17) is equivalent to the homogeneous linear equation system:

$$\begin{cases} (D_{xx} - \lambda_i) \varepsilon_{ix} + D_{xy} \varepsilon_{iy} + D_{xz} \varepsilon_{iz} = 0 \\ D_{yx} \varepsilon_{ix} + (D_{yy} - \lambda_i) \varepsilon_{iy} + D_{yz} \varepsilon_{iz} = 0 \\ D_{xz} \varepsilon_{ix} + D_{zy} \varepsilon_{iy} + (D_{zz} - \lambda_i) \varepsilon_{iz} = 0 \end{cases} \quad (2.18)$$

which has a non trivial solution if $\det(\vec{\mathbf{D}} - \lambda_i \vec{\mathbf{I}}) \varepsilon_i = 0$ [52]. $\vec{\mathbf{D}}$ in its diagonal form has the eigenvalues on its diagonal:

$$\vec{\mathbf{D}}_{diag} = \begin{pmatrix} \lambda_1 & & \\ & \lambda_2 & \\ & & \lambda_3 \end{pmatrix} \quad (2.19)$$

This diagonal matrix represents $\vec{\mathbf{D}}$ estimated in the diffusion reference frame. The ellipsoid representation shown in **Figure 2.2a** is useful to attribute a physical meaning to the tensor eigenvalues and eigenvectors:

- the ellipsoid semiaxes lay on UVW, the three orthogonal axes individuated by the versors $(\hat{\varepsilon}_1, \hat{\varepsilon}_2, \hat{\varepsilon}_3)$, and known as the *main diffusion axes*;

- the spatial orientation of these semiaxes is encoded in the three diffusion *eigenvectors*, $(\mathbf{V}_1, \mathbf{V}_2, \mathbf{V}_3) = (V_1\hat{\varepsilon}_1, V_2\hat{\varepsilon}_2, V_3\hat{\varepsilon}_3)$, which are parallel respectively to UVW;
- the eigenvectors are biunivocally linked with the three *eigenvalues* $\lambda_1, \lambda_2, \lambda_3$, or eigen-diffusivities, and the semiaxes of the ellipsoid scale as the square roots of the eigen-diffusivities.

The diffusion ellipsoid is thus a 3D representation of the diffusion distance (or the square root of MSD) covered by the molecules in a given diffusion time, t . The ellipsoid shape can be either *prolate*, showing the existence of one prevalent diffusion direction (see **Figure 2.2b**), *oblate*, suggesting instead the presence of different enhanced diffusivities which lie in a plane, or *isotropic*, indicating the lack of a specific privileged path for water diffusion.

By performing DWI it is possible to associate a diffusion ellipsoid to each voxel, which describes the water diffusive motion occurring in that volume element. From an experimental point of view \vec{D} is estimated by collecting a number of samples of the DW signal, along the direction in which a particular diffusion sensitization gradient is applied (see Par. 2.3.3), using multivariate regression methods.

The concept that in anisotropic environments the diffusive dynamics may be expressed by a tensor is at the basis of the development of Diffusion Tensor Imaging (DTI). DTI is based on the evaluation of scalar invariants of the diffusion tensor, which are tissue-specific and can furnish important pieces of information about the local microstructure (see Par. 2.4).

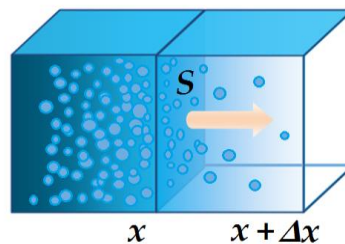


Figure 2.1 – Sketch representing a parallelepiped where molecules of solute are diffusing inside a solvent, when there is a concentration gradient between two compartments. The interface between the compartments has surface S , and represents a surface at constant concentration. The arrow indicates the density flux J , which is calculated between two positions separated by the length Δx . Molecules spontaneously move from the more concentrated compartment to the less concentrated one.

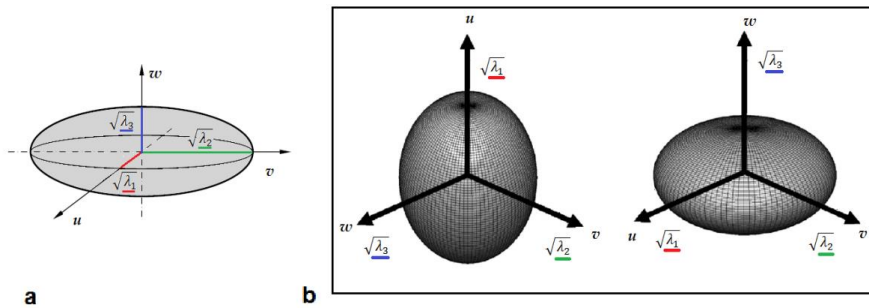


Figure 2.2 – Diffusion ellipsoids. a) The diffusion ellipsoid has semiaxes laying on the main diffusivity axes u, v, w , which define the internal diffusivity reference frame. The semiaxes are proportional to the diffusion tensor eigenvalues. b) A representation of an oblate diffusion ellipsoid (left), where the diffusion is facilitated along the vertical direction, and of a prolate diffusion ellipsoid (right), where the diffusion is enhanced in a plane. (Image adapted from Jones's paper [2]).

2.2 Molecular diffusion examined at a microscopic scale: probabilistic description

The Fick's laws describe the diffusion of solute particles dispersed in a solvent, i.e. we are dealing with a biphasic system, where at least two different species must be present. Nevertheless, also the particles inside a mono-phasic solution are interested by a translational motion, due to their kinetic energy. This phenomenon is commonly known as *self-diffusion*, and it is the physical basis of any technique of Diffusion Weighted-MRI (DW-MRI), the focus of which is the movement of water molecules in water solutions. In DW-MRI the detected signal is a coherent superimposition of signals from a very large number of spins (an *ensemble* of spins, see Par. 1.1.1), thus we need a description that deals with single molecules but is able to depict the overall behavior. It is hardly feasible to predict the pathway that any one of these molecules will take, and we cannot for sure determine any single molecule's position at a given time. In a milestone paper published in 1905 [53], Einstein derived the diffusion equation for self-diffusion using Fick's law, and he showed that, provided the number of particles is sufficiently large, at least one aspect of the behavior could be characterized, the so called *mean squared displacement*

(MSD), that is the squared displacement of molecules from their starting point over a time, t , averaged over all the molecules in the sample.

2.2.1 Self-diffusion and self-correlation function

Self-diffusion takes place without any net concentration gradient, nonetheless it can be described by the Fick's law, replacing the concentration $c(\mathbf{r}, t)$ with the probability $\Psi(\mathbf{r}, t)$ of finding a particle in a certain place, at a given time, as showed by Einstein [53]. We introduce the *self-correlation function* $P_s(\mathbf{r}_0|\mathbf{r}, t)$, a conditional probability which gives the likelihood that a molecule initially at position \mathbf{r}_0 will have moved to \mathbf{r} after a time t .

The initial condition for which the molecule occupied the position \mathbf{r}_0 at $t = 0$ is represented by a *Dirac delta function* of the position \mathbf{r} :

$$P_s(\mathbf{r}_0|\mathbf{r}, 0) = \delta(\mathbf{r} - \mathbf{r}_0) \quad (2.20)$$

For $P_s(\mathbf{r}_0|\mathbf{r}, t)$ the normalization relation holds:

$$\int P_s(\mathbf{r}_0|\mathbf{r}, t) d\mathbf{r} = 1 \quad (2.21)$$

Then the total probability of finding a particle at position \mathbf{r} at time t is given by:

$$\Psi(\mathbf{r}, t) = \int \Psi(\mathbf{r}_0, 0) P_s(\mathbf{r}_0|\mathbf{r}, t) d\mathbf{r}_0 \quad (2.22)$$

where $\Psi(\mathbf{r}_0, 0)$ is just the particle density, $\Psi(\mathbf{r}_0, 0) = \rho(\mathbf{r}_0)$, since $\Psi(\mathbf{r}, t)$ is a probability describing an ensemble behavior. Thus, the first Fick's law represented by (2.2) may be expressed as:

$$\mathbf{J}(\mathbf{r}, t) = -D\nabla P_s(\mathbf{r}_0|\mathbf{r}, t) \quad (2.23)$$

with \mathbf{J} the conditional probability flux. Since the total conditional probability is conserved, the continuity theorem applies, and:

$$\nabla \cdot \mathbf{J} = -\frac{\partial P_s(\mathbf{r}_0|\mathbf{r},t)}{\partial t} \quad (2.24)$$

Finally, combining the last two equations, we obtain the diffusion equation for $P_s(\mathbf{r}_0|\mathbf{r}, t)$:

$$\frac{\partial P_s(\mathbf{r}_0|\mathbf{r},t)}{\partial t} = D\nabla^2 P_s(\mathbf{r}_0|\mathbf{r}, t) \quad (2.25)$$

with D the molecular self-diffusion coefficient, or diffusivity. It is possible to show that if the self-diffusion holds in a homogeneous, isotropic and infinite medium, the solution of (2.25) is a normalized Gaussian function:

$$P_s(\mathbf{r}_0|\mathbf{r}, t) = \frac{1}{(4\pi Dt)^{-3/2}} e^{-\frac{(\mathbf{r}-\mathbf{r}_0)^2}{4Dt}} \quad (2.26)$$

as in case of the concentration of solute in the diffusion equation (see (2.7) and (2.9)). This is true if the special boundary condition which applies for unrestricted diffusion holds, i.e. $\lim_{r \rightarrow \infty} P_s(\mathbf{r}_0|\mathbf{r}, t) = 0$. Furthermore, we notice that the self-correlation function depends only on the net displacement $\mathbf{R} = \mathbf{r} - \mathbf{r}_0$, and not on the initial position, \mathbf{r}_0 . This characteristic reflects the Markov nature¹⁵ of Brownian motion statistics. Using the net displacement we define a function, known as the average *motion propagator* (MP), that gives the average probability for any particle to perform a dynamic displacement \mathbf{R} over a time t , and it is proportional to the particle density:

$$\bar{P}_s(\mathbf{R}, t) = \int \rho(\mathbf{r}_0) \cdot P_s(\mathbf{r}_0|\mathbf{r}_0 + \mathbf{R}, t) d\mathbf{r} \quad (2.27)$$

The average MP is in common with all the particles in the ensemble, thus we may drop the bar. The solution of the PDE in 3D is simply a Gaussian distribution centered in 0 (see **Figure 2.3**):

¹⁵ A motion may be considered a stochastic process, and we can say that it shows a *Markov nature* when the Markov property holds. This property lends its name from the Russian mathematician Andrey Markov. A stochastic process has the Markov property if the conditional probability distribution of future states of the process (conditional on both past and present states) depends only upon the present state, not on the sequence of events that preceded it.

$$P_s(\mathbf{R}, t) = \frac{1}{(4\pi Dt)^{-3/2}} e^{-\frac{\mathbf{R}^2}{4Dt}} \quad (2.28)$$

The second moment of the Gaussian probability density function (PDF), that is the variance of the distribution, is given by the integral:

$$\langle (\mathbf{r} - \mathbf{r}_0)^2 \rangle = \int_{-\infty}^{\infty} (\mathbf{r} - \mathbf{r}_0)^2 \rho(\mathbf{r}_0) P_s(\mathbf{r}_0 | \mathbf{r}, t) d\mathbf{r} \quad (2.29)$$

In the hypothesis of *unrestricted, free* self-diffusion in a homogeneous, isotropic and infinite medium the variance of the PDF grows linearly with the time t during which diffusion occurs, and it gives a measure of the **mean squared displacement** (MSD) performed on average by each water molecule, given a particular diffusivity, D :

$$MSD = \langle (\mathbf{r}(t) - \mathbf{r}_0)^2 \rangle = \langle (\mathbf{R}(t))^2 \rangle = 6Dt \quad (2.30)$$

which in one dimension becomes:

$$MSD = \langle (x(t) - x_0)^2 \rangle = 2Dt \quad (2.31)$$

and, generalizing to N dimension:

$$MSD = \langle (r(t) - r_0)^2 \rangle = 2NDt \quad (2.32)$$

In order to make the concept of MSD more concrete, let us consider a cube of water at body temperature ($T_{body} = 37^\circ C$). If we observe water molecules, after 30 ms they will have displaced, on average, $\sqrt{MSD} \sim 23 \mu m$, considering that the water diffusion coefficient at that temperature is $D = 3 \cdot 10^{-3} mm^2/s$ [2].

When the linearity relation (2.32) holds, the self-diffusion process (which henceforth will be named diffusion for the sake of simplicity), is defined as *Gaussian*.

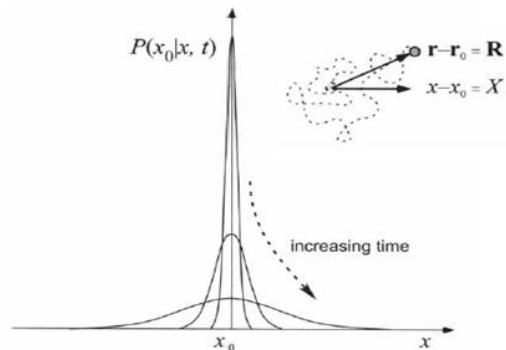


Figure 2.3 – Gaussian distribution of displacements and a random walk trajectory. a) Behavior of the conditional probability for an ensemble of particles undergoing Brownian motion in one-dimension. The width of the Gaussian distribution grows linearly with the diffusion time t . A trajectory of a diffusive particle, with the displacement along the x -direction and the displacement vector, \mathbf{R} , in 3D, is depicted in the top right (Image adapted from Callaghan's book [5]).

2.3 How to exploit molecular diffusion in MRI?

NMR is the most versatile non-invasive technique to investigate diffusion dynamics, providing information about a wide range of specimens going from liquid solutions to biological material. The idea that lies at the basis of the DW-MRI is the possibility to impress a molecular label via the characteristic Larmor frequencies of the nuclei. This label is the phase of the transverse magnetization: if a spatial label is given to nuclei at one instant of time, the motion can be in principle deduced by checking this label at a later time. Moreover, by choosing a specific time spacing, faster or lower dynamics contribution can be in turn exalted or depressed.

In Pars. 1.2.4.1 and 1.2.4.2 the Spin-Echo (SE) sequence and the Stimulated Echo sequence (STE) were introduced as methods to measure phase differences.

By adding a couple of magnetic field gradients to the basic acquisition sequence, a spatial label can be impressed to the spins, leading respectively to the Pulse-Gradient Spin-Echo (PGSE) and to the Pulsed-Gradient Stimulated Echo (PGSTE) sequences, which are widely used to measure diffusion.

The following explanation is borrowed from Callaghan's book, the milestone book regarding DW-MRI [46]

2.3.1 Spin labeling with the use of diffusion gradients

The most convenient way to depict molecular self-diffusion is to model it as a succession of discrete hops with motion resolved in one dimension, i.e. the direction of the field gradient. Let the main time between steps be τ_s and the root mean square displacement (RMSD) in one dimension (along the z-direction) be ξ . The distance travelled by the molecule after n jumps at time $t = n\tau_s$ is given by:

$$Z(t) = Z(n\tau_s) = \sum_{i=1}^n \xi m_i \quad (2.33)$$

where m_i is a random sign to $m_i \pm 1$, corresponding to the equal probability of going back and forth. The MSD can be retrieved from:

$$\overline{Z^2(t)} = \sum_{i=1}^n \sum_{j=1}^n \xi^2 \overline{m_i m_j} \quad (2.34)$$

with $m_{ij} = 0$ except for $i = j$, so all the cross-terms cancel out. The diffusion coefficient may be defined as:

$$D = \frac{\xi^2}{2\tau_s} \quad (2.35)$$

we obtain again the expression:

$$\overline{Z^2(t)} = 2Dt \quad (2.36)$$

that is the same as (2.32) in one dimension.

Now let us consider the influence of diffusion along z-direction on the transverse magnetization of spins originating at $z = 0$. The local Larmor frequency is:

$$\omega(t) = \gamma B = \gamma g \cdot Z(t) = \gamma g \cdot Z(n\tau_s) = \gamma g \sum_{i=1}^n \xi m_i \quad (2.37)$$

so that the cumulative phase angle after time $t = n\tau_s$ is:

$$\Phi(t) = \omega(t)t = \gamma g \sum_{i=1}^n \xi m_i \cdot t = \sum_{k=1}^n \gamma g \tau_s \sum_{i=1}^k \xi m_i \quad (2.38)$$

The first term is just the Larmor precession, while the second one is more interesting since it contains the phase deviation, and varies randomly across the ensemble causing the dephasing. As explained graphically in **Figure 2.4** it is possible to write the total dephasing as:

$$\Delta\Phi(t) = \gamma g \tau_s \xi \sum_{i=1}^n (n+1-i) m_i \quad (2.39)$$

What one needs to calculate is the term $\overline{e^{i\Delta\Phi}}$, the coefficient by which the ensemble-averaged transverse magnetization will be phase modulated as a result of the diffusional motion in the presence of a gradient:

$$\overline{e^{i\Delta\Phi}} = \int_{-\infty}^{\infty} P(\Delta\Phi) e^{i\Delta\Phi} d(\Delta\Phi) \quad (2.40)$$

where $P(\Delta\Phi)$ is given by the normalized Gaussian function with mean value 0 and variance $\overline{\Delta\Phi^2}$:

$$P(\Delta\Phi) = \frac{1}{\sqrt{2\pi\overline{\Delta\Phi^2}}} e^{-\frac{\Delta\Phi^2}{2\overline{\Delta\Phi^2}}} \quad (2.41)$$

so that: $\overline{e^{i\Delta\Phi}} \sim e^{-\frac{\overline{\Delta\Phi^2}}{2}}$.

The term $\overline{\Delta\Phi^2}$ is obtained by squaring equation (2.39) and taking the ensemble average:

$$\overline{\Delta\Phi^2} = \gamma^2 g^2 \tau_s^2 \xi^2 \sum_{i=1}^n (n+1-i)^2 = \gamma^2 g^2 \tau_s^2 \xi^2 \sum_{j=1}^n j^2 = \frac{1}{3} \gamma^2 g^2 \tau_s^2 \xi^2 n^3 \quad (2.42)$$

assuming that n is large. This expression represents also the mean-squared phase shift for a triangular section of cumulative phase diagram for spin echo (SE) formation. In a SE sequence the net phase shift is the sum of the phase shift

occurring before and after the RF180° pulse, and corresponds to the enclosed region in **Figure 2.4**. By substituting in (2.42) the expression of D found in (2.35) one obtains another expression for $\overline{\Delta\Phi^2}$:

$$\overline{\Delta\Phi^2} = \frac{2}{3}\gamma^2 g^2 D t^3 \quad (2.43)$$

and, finally:

$$e^{i\Delta\Phi} = e^{-\frac{1}{3}\gamma^2 g^2 D t^3} \quad (2.44)$$

The dependence of the averaged signal attenuation on the cube of diffusion time is a characteristic of self-diffusion in the presence of a steady gradient¹⁶. In the presence of *internal gradients*, i.e. local perturbations of the magnetic field due mostly to differences in magnetic susceptibility at the interface between different regions within the sample, spin relaxation is influenced and the local Larmor frequency is altered by a factor:

$$\Delta\omega_0 \sim \gamma\Delta\chi B_0 \quad (2.45)$$

In presence of internal gradients, due to their dephasing effects the signal (proportional to the magnetization) at $t = TE$ is different from the SE signal predicted by (1.34), thus: $S(TE) = S_0 e^{-\frac{TE}{T_{2eff}} - \frac{1}{12}\gamma^2 g^2 D TE^3}$ where T_{2eff} is the effective spin-spin relaxation time, due only to spins interactions because the effects of diffusion and field inhomogeneities are averaged out. It is possible to obtain T_{2eff} by employing a specific sequence called Carr-Purcell-Meiboom-Gill, which is able to average out the effects of diffusion by means of an echo train, repeating the application of RF180° pulse several times.

¹⁶ A gradient is defined *steady* when its magnitude does not change over a fixed interval of time, thus it has a constant value.

2.3.2 Pulsed Gradient Spin Echo and Stimulated Echo sequences

The dephasing of the transversal magnetization in presence of magnetic field gradients is used to measure diffusion by inserting on purpose a couple of rectangular gradients in the dephasing and rephasing part of the echo sequence. The obtained scheme is called Pulse Gradient Spin Echo (PGSE) sequence (see **Figure 2.5a**), also known as Stejskal and Tanner's sequence, introduced by them in 1965 [54]. Each gradient is characterized by an amplitude, g , and a duration, δ . The two gradients are applied before and after the RF180° pulse, and are separated by a time interval of Δ . Let us be τ the time elapsing between the RF90° and the RF180°, and 2τ the time elapsing between the RF90° and the formation of a SE, as shown in **Figure 2.5a**. The attenuation of the SE in the presence of a steady diffusion gradient g will be given by:

$$\ln\left(\frac{M(g)}{M_0}\right) = -\frac{2\tau}{T_2} - \frac{2}{3}\gamma^2 g^2 \tau^3 D \quad (2.46)$$

where the first term pertains to the attenuation due to T2-relaxation, while the second one pertains to the attenuation due to diffusion.

Following the previous arguments, from **Figure 2.6** it is apparent that the phase shifts associated with the gray areas cancel and the net phase shift is obtained by summing two uncorrelated triangular regions, each with mean square phase shift $\overline{\Delta\Phi^2} = \frac{1}{3}\gamma^2 g^2 \tau_s^2 \xi^2 n^3$, along with one uncorrelated rectangular region with $\overline{\Delta\Phi^2} = \frac{1}{3}\gamma^2 g^2 \tau_s^2 \xi^2 n^2(p - n)$. The net mean square shift is therefore:

$$\overline{\Delta\Phi^2} = \gamma^2 g^2 \tau_s^2 \xi^2 n^2 \left(p - n + \frac{2}{3}n\right) = \gamma^2 g^2 \delta^2 \left(\Delta - \frac{\delta}{3}\right) D \quad (2.47)$$

Where the product of factors other than D is known as the b-factor or b-value, a characteristic parameter of the diffusion sequence, measured in s/mm^2 :

$$b = \gamma^2 g^2 \delta^2 \left(\Delta - \frac{\delta}{3}\right) \quad (2.48)$$

In absence of diffusion gradient $b = 0$.

The attenuation of the signal in the presence of a couple of magnetic field gradients is then described by the well known Stejskal-Tanner equation [54]:

$$S(b) = S(0)e^{-bD} \quad (2.49)$$

Where S stands for the signal provided by the magnetization M in a given volume element. This equation provides a precise description of the influence of self-diffusion in the PGSE experiment and is the basis of a considerable literature pertaining to this technique.

In DW experiments the usefulness of adopting stimulated echo instead of simple spin echoes has been shown since 1970. In fact, as stated in Tanner's paper [55] the use of a three-RF-pulse sequence may extend the range of measurement of diffusion coefficients to more viscous substances or the measurement of barrier separations to wider spacings, with the only condition that the diffusing substance has $T_1 > T_2$ (which is the case of water in self-diffusion). In this case the use of the Pulsed Gradient Stimulated Echo Sequence shown in **Figure 2.5b,c** confers an advantage allowing the storage of magnetization owing to T1-relaxation (see Par. 1.2.3), and thus increasing the signal with respect to a simple PGSE sequence. Let us be τ_1 the time elapsing between the first RF90° and the second RF90°, and τ_2 the time elapsing between the second RF90° and the third RF90°. The sequence allows the formation of a Stimulated Echo (STE) at $t = \tau_1 + \tau_2$, as shown in **Figure 2.5b**. The attenuation of the STE in the presence of a steady diffusion gradient g will be given by:

$$\ln \left(\frac{M(g)}{M_0} \right) = - \frac{(\tau_2 - \tau_1)}{T_1} - \frac{2\tau_1}{T_2} - \ln 2 - \gamma^2 g^2 \tau_1^2 \left(\tau_2 - \frac{1}{3} \tau_1 \right) D \quad (2.50)$$

where the first term pertains to the T1-relaxation, the second term pertains to the T2-relaxation, and the last term pertains to the attenuation due to diffusion. It is possible to optimize the sequence in such a way to obtain the minimum non-diffusional attenuation at some fixed diffusional attenuation, selecting τ_1 and τ_2 so that $\frac{\tau_2}{\tau_1} = \frac{T_1}{T_2}$, as shown in Tanner's paper [55].

2.3.3 Diffusion Weighting Imaging and Diffusion Tensor Imaging

When dealing with homogeneous and isotropic media, the diffusive motion can be described by a single scalar value D and the PGSE sequence allow for its evaluation by means of Stejskal and Tanner's equation (2.49). When the media exhibit organizational anisotropy, the measurements with gradients applied along different directions can give very different results. In such cases, as seen in Par. 2.1.3, the diffusive motion should be described by the diffusion tensor \vec{D} . Diagonal and off-diagonal elements of \vec{D} can be related to the measured echo intensity in a PGSE experiment [56]. In fact, eq. (2.49) can be generalized for the diffusion tensor \vec{D} in the following way:

$$S(b) = S(0)e^{-\sum_{i=1}^3 \sum_{j=1}^3 b_{ij} D_{ij}} \quad (2.51)$$

where the b -matrix substitutes the scalar b -factor defined in Par.2.3. Since \vec{D} is symmetric (see in Par. 2.1.3), it has only 6 independent elements, then at least 6 different measurements are necessary to reconstruct it. This means that at least 6 PGSE experiment have to be realized with a set of 6 non-collinear gradient directions. Generally, the magnitude of the diffusion weighting which is impressed along the different gradient directions is the same for each direction and is optimized to match with the expected diffusivity value, as previously demonstrated [57]. Moreover, a b_0 image, i.e. an image with no diffusion weighting, is also acquired for normalization.

By normalizing the DW-signal with respect to the SE signal (i.e. the signal acquired with $b = 0$ s/mm²) and taking the natural logarithm on both sides of (2.49) for each sampled i -direction, there will be as many linear equations as the i -diffusion gradient directions:

$$\ln\left(\frac{S(b)}{S(0)}\right) = -bD_i \quad (2.52)$$

By extracting D_i , or apparent diffusion coefficient (ADC), one has a partial view of water self-diffusion: this is the basis of the so called Diffusion Weighting Imaging (DWI). The ADC is named 'apparent' because the value of diffusivity depends on the experimental set-up, in particular it varies depending on the chosen gradient directions and Δ [3].

However, once collected the apparent diffusivities, it is possible to diagonalize \vec{D} to derive its eigenvalues and eigenvectors. These parameters are used to derive three important quantitative meta-parameters [3], which provide features of the environment where water molecules diffuse:

- the **mean diffusivity** (MD), defined using the trace of \vec{D} , that characterizes the overall MSD of molecules, representing the average diffusion ellipsoid size (see Par. 2.1.3), and the overall presence of obstacles to diffusion. It is defined by:

$$MD = \frac{Tr\vec{D}}{3} = \frac{\sum_{i=1}^3 \lambda_i}{3} \quad (2.53)$$

The experimental values for self-diffusion coefficients of pure water have been measured to be between $(2.26 \div 2.29) \cdot 10^{-9} m^2/s$ or $(2.26 \div 2.29) \cdot 10^{-3} mm^2/s$ at $T_{room} = 298.15 K$ [58]. At a fixed temperature, the lower the MD value, the higher the barriers which are encountered during the diffusive motion.

- the **fractional anisotropy** (FA), a sort of standard deviation of MD, that quantifies the degree of anisotropy, and it is related to the presence of oriented structures. It is defined by:

$$FA = \sqrt{\frac{3 \sum_{i=1}^3 (\lambda_i - MD)^2}{2 \sum_{i=1}^3 \lambda_i^2}} \quad (2.54)$$

FA is a dimensionless parameter that ranges from 0, which means isotropic diffusion, to 1, which means complete anisotropy.

- the main direction of diffusivities provided by the 3 eigenvectors ($\mathbf{V}_1, \mathbf{V}_2, \mathbf{V}_3$), that are linked to the orientation in space of the structures.

Furthermore, considering the first eigenvalue, which is the highest in modulus, we derive a quantity named **axial-diffusivity** $D_{//} = \lambda_1$, that represents the diffusivity in the direction along which the diffusion is the most facilitated, while considering the other two eigenvalues we derive the **radial-diffusivity** $D_{\perp} = (\lambda_2 + \lambda_3)/2$, that is the diffusivity in the orthogonal plane. Both $D_{//}$ and D_{\perp} are measured in m^2/s or mm^2/s . Henceforth, the set of MD, FA, $D_{//}$ and D_{\perp} will be referred to as the *DTI-metrics*. **Figure 2.7a** shows the maps of DTI-metrics for a slice of a representative healthy human brain, while in **Figure 2.7b** a map of the first eigenvector is reported in RGB-colored encoding (see

Jones and References within [2]). The preferential direction of WM fibers in a given voxel is given by \mathbf{V}_1 . The RGB-encoding system associates a red color to the WM fibers oriented in L/R direction, a green color to the ones oriented in A/P direction, and a blue color to the ones oriented in S/I direction (for more information on the spatial coordinate system used in MRI jump back to section 1.3.4.5).

The importance of the first two parameters is that they are scalar invariant, thus they are independent from the orientation of the laboratory reference frame, allowing the extrapolation of structural features of the analyzed sample. Furthermore, it is worth to stress that, even though the image resolution depends on the reconstruction procedure, i.e. the k-space imaging, and its lower bound is about 1 mm so far, in each voxel the DTI parameters are usually selected to focus on molecular displacements, which are of the order of few μm in liquid systems. Experimental parameters can be tuned through the choice of the diffusion time Δ and the gradient strength g , which determine the b-value as shown in the previous section. It is useful to anticipate here that by changing those parameters, different dynamics can indeed be highlighted, leading to different characterizations of the same system and thus to a deeper understanding of its dynamical properties.

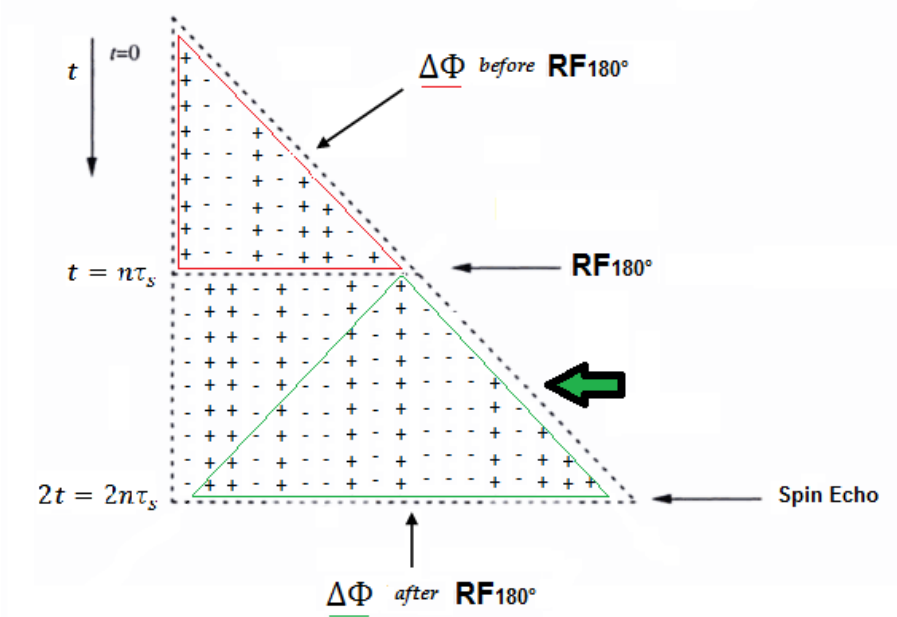


Figure 2.4 – Cumulative phase diagram relative to the formation of a spin echo in the presence of a steady magnetic field gradient. The net phase shift is the sum of two components: the phase shift accumulated before the RF180°-pulse, and the phase shift accumulated after the RF-pulse. The net phase shift is indicated by the thick arrow. (Image edited from Callaghan’s book [46]).

Diffusion Weighted Imaging: imaging matter exploiting molecular diffusion

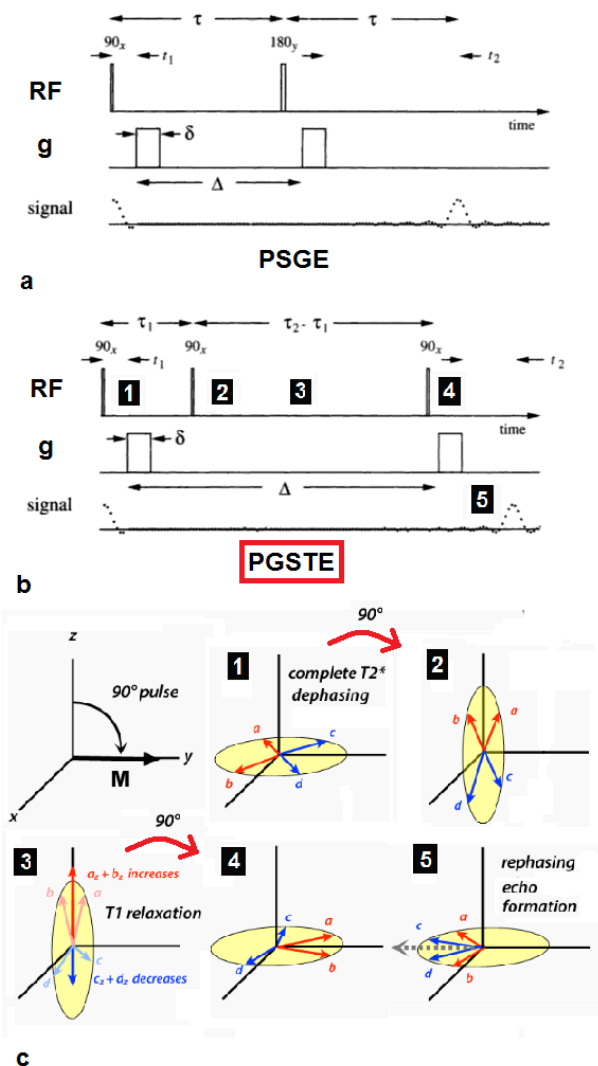


Figure 2.5 – Pulsed Gradient Spin Echo (PGSE) sequence and the Stimulated Echo version. a) The sequence employs a couple of diffusion gradients of amplitude g and duration δ , separated by a time interval of Δ , with $\Delta > \delta$. The spin echo forms at $t = 2\tau = TE$. b) Stimulated Echo (STE) version of PGSE sequence, where the single RF180° is substituted by a couple of RF90°. The numbers indicate the different phases of the RF-pulse cycle, corresponding to the magnetization vectors depicted in (c) (Images adapted from Callaghan’s book [46]). c) Formation of a stimulated echo vector by three 90°-pulses. After the second pulse we consider the z-components of the spins that do not precess but grow in the +z-direction by T1 relaxation. These stored longitudinal components are flipped back into the transverse plane by the 3rd RF-pulse, then rephase and form an STE.

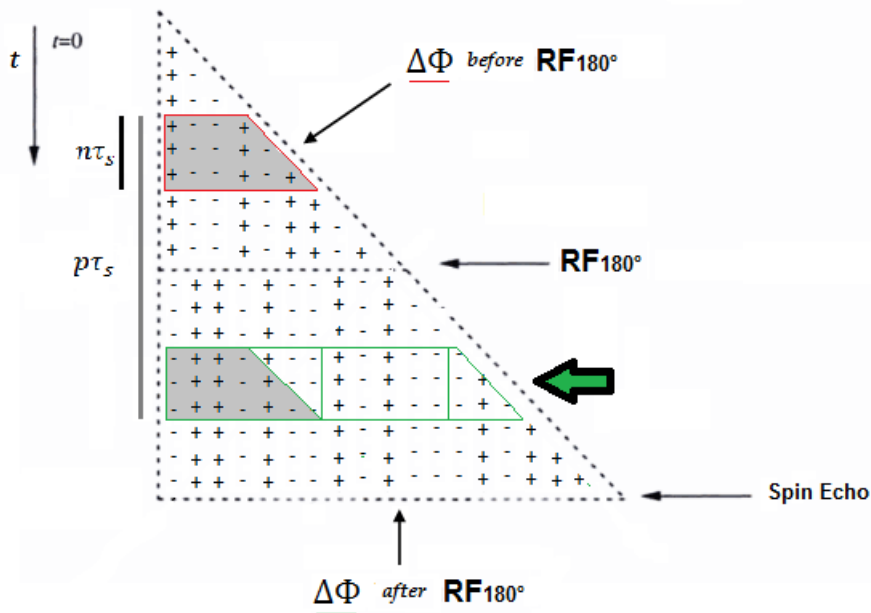


Figure 2.6 - Cumulative phase diagram for spin echo formation in the PGSE experiment. The net phase shift is the sum of two components: the phase shift accumulated before the RF180°-pulse, and the phase shift accumulated after the RF-pulse. The net phase shift is indicated by the thick arrow: the phase shifts of the gray areas cancel out. The time interval $n\tau_s = \delta$, the duration of the diffusion gradient, while $p\tau_s = \Delta$, the separation between the couple of diffusion gradients (Image edited from Callaghan's book [46]).

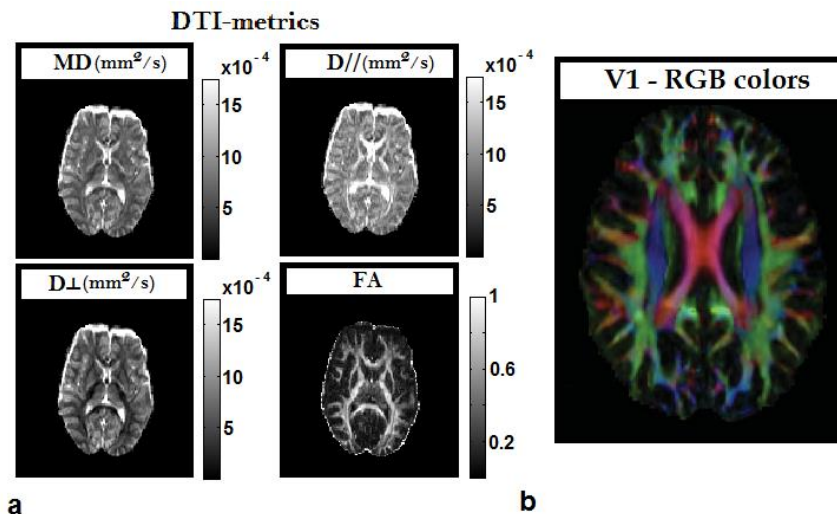


Figure 2.7 – DTI parametric maps of healthy human brain. a) Axial parametric maps of MD, $D_{//}$, D_{\perp} , FA extracted from the diffusion tensor in a slice of human brain of a representative young male subject (age 25 years). Notice the different contrast provided by each parameter. In particular, in FA map the WM fibers are enhanced with respect to the rest of the brain parenchyma (original images, see Chapter 5). b) Axial parametric map of the first eigenvector colored according to the RGB encoding. Notice the red fibers representing the corpus callosum, a WM structures that connects the two hemispheres; the green fibers are oriented in the anterior/posterior direction; the blue fibers are oriented in the superior/inferior direction, i.e. they are orthogonal to the page plane. (Image adapted from Jones's paper [2]).

2.4 DWI based on the Gaussian assumption: state of the art

In the hypothesis of unrestricted, free self-diffusion of water in a homogeneous, isotropic (and infinite) media the average MP of the ensemble of diffusing spins is represented by a Gaussian distribution, with a variance representing the MSD of particles and growing linearly with the diffusive time. When this linearity relation holds, the diffusion process is defined *Gaussian*. Considering this assumption, as seen in Par. 2.3.3, the signal decays as a mono-exponential function of the b-value, and it is well modeled by the Stejskal-Tanner equation. The introduction of the PGSE, or Stejskal-Tanner sequence, provided a strategy to turn the drawback of reduced spatial resolution in MRI due to the Brownian motion of protons into a benefit. In particular, with the development of DWI

and DTI it was possible to reveal the microstructure of tissues *in vivo* and without the use of exogenous contrast agents, in a totally non invasive way.

2.4.1 Clinical applications of Gaussian-DWI and DTI

DWI is nowadays a well-established method implemented as part of a routine protocol. The most successful application of DWI since the early 1990s has been brain ischemia (**Figure 2.8a**), following the discovery in cat brain by Moseley et al., that water diffusion drops at a very early stage of the ischemic event [13]. In the last 10 years the investigation of ADC was used as a tool for discriminating cancerous tissue from healthy tissue in different organs such as the brain (**Figure 2.8c**), the breast, the prostate, the liver, the lymph nodes (see Padhani et al. and references within [15]). Malignant tumor in fact present lower ADC values compared to the healthy tissue, and this was explained considering an increase of cellularity, tissue disorganization, and extracellular space tortuosity in the cancerous lesion (see **Figure 2.8d**).

Improvements in the imaging of water diffusion have been made by the development of the more complex DTI, which allows a direct examination, *in vivo*, of some aspects of normal and pathological tissue microstructure (**Figure 2.8b-d**). DTI, as shown in Par. 2.3.3, yields quantitative measures reflecting the integrity of white-matter fiber tracts, by taking advantage of the intrinsic directionality of water diffusion in human brain [8]. For this reason DTI became a suitable tool for the follow-up of brain maturation [10] and the assessment of pathological neurodegeneration [7, 9] and physiological alterations due to aging [4, 6]. For example, higher ADC and lower FA have been found in neonates compared to adults. The main changes in ADC occur within the first 6 months of life, and are connected to the formation of myelinated structures, whereas a decrease in FA has been shown to occur after 20 years of age, and significant age-related declines in median FA have been demonstrated in densely packed white matter fiber areas, especially the genu of the corpus callosum [6, 52].

The combination of DWI and DTI gives the chance to assess the severity of stroke at its early stages and characterizes the ischemic process better than T2-relaxometry, because of peculiar changes of ADC and DTI-metrics (**Figure 2.8a**). In fact, in the acute phase, ADC are initially reduced by 30-50% within the first hour of the onset of focal ischemia, more markedly in white matter (WM)

compared to gray matter (GM). This reduction in the ADC is due to the influx of water into cells from the extracellular compartment, producing a cytotoxic edema. After a transition period, during which ADC values are comparable to the healthy tissue, there is an increase in the ADC, within 10 days from the onset of the ischemia, and finally a stabilization of ADC at higher values in the chronic phase of injury. On the other hand, FA is interested by an acute elevation in ischemic WM, followed by a marked reduction, compared to the healthy tissue, during the chronic phase, which last months after the stroke, and it is compatible with the loss of organization and cytoarchitecture disruption [3, 4, 13].

Recently, with the aim of gaining for more specific information about tissue structure, the use of high b-values has spread. At high b-values, thus strong diffusion gradients, the slow dynamics of water molecules is highlighted, and more detailed information is gained. The *in vivo* evaluation of diffusion with the use of strong diffusion gradients, for example, allowed a more specific assessment of cancer aggressiveness in human prostate [11, 12].

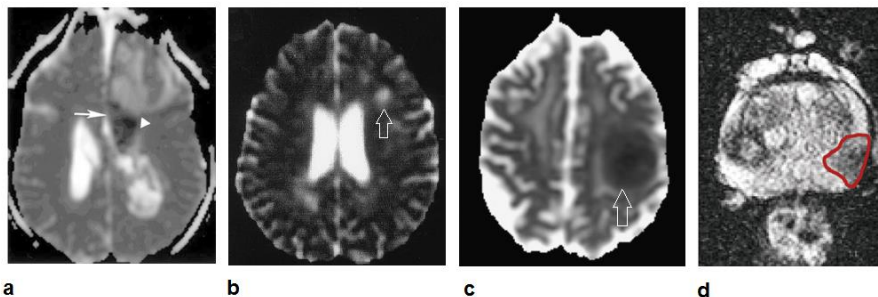


Figure 2.8 – DWI and DTI applications. a) ADC parametric map showing a left hemisphere ischemia. ADC values are decreased in the area indicated by the arrow, and increased in the area of chronic ischemia, indicated by the arrowhead (image extracted from Sundgren et al. [4]). b) MD map showing a multiple sclerosis lesion in the left hemisphere, which appears hyperintense compared with the surrounding tissue, due to the loss of structural barriers to water motion (image extracted from Filippi et al.[9]). c) ADC map of human brain with a lymphoma, indicated by the white arrow. The diffusion in the tumour is restricted due to the increased cellularity (image extracted from Padhani et al. [15]). d) MD map of a human prostate, with the contours of the peripheral cancerous lesion highlighted (image extracted from Reischauer et al. [59]).

Chapter 3 Anomalous diffusion: when water diffuses in complex media

This Chapter deals with the description of Anomalous Diffusion processes, from the rigorous mathematical framework of Continuous Time Random Walk (CTRW) to the introduction of a motion propagator, which allows to link the theory to the experimentally measured signal from diffusing spins in DW-MRI. The concept of Anomalous Diffusion will be introduced, as well as its implications in the properties of water dynamics, the mathematical theory underneath it, and its applications in DWI.

3.1 When the Gaussian assumption is not enough

The term ‘anomalous’ denotes the fact that the random motion of water molecules in certain conditions does not lead to the statistical conclusion of a Gaussian PDF of distances travelled. Imaging techniques that allow for the quantification of diffusive properties in tissues, such as DWI and DTI, have been based for ages on the Gaussian assumption, and in fact they are commonly addressed to as ‘Gaussian’ techniques. The Gaussian assumption is related to the occurrence of Brownian motion in a homogeneous, isotropic and infinite environment, so that the squared displacements of water molecules distribute on a Gaussian curve, and a peculiar linear relation between of their MSD (or the PDF variance) and the diffusive time holds. The particular way in which the DWI acquisition sequence (that makes MRI sensitive to this diffusive motion) is built offers the possibility to tune its sensitivity to faster dynamics, characterized by a high value of D , and slower dynamics, where the diffusivity

is lower. In order to move from one regime to the other it is sufficient to opportunely set the b-value, a parameter depending on the strength of the diffusion sensitizing gradient, and on the time interval between two successive diffusion gradients at inverted polarity. The experimental attenuation of the NMR signal due to diffusion in these Gaussian techniques is modeled with a mono-exponential decay as a function of b-value.

However, experimental evidences in inert samples, scaffolds, animal tissues, human tissues, and *in vivo* animal and human DW-data showed that when the water molecules diffuse in highly heterogeneous or anisotropic *milieux*, or when they move in tortuous, fractal and complex geometries, the attenuation of the signal due to their dephasing is not fully described by a mono-exponential decay. In this scenario, which is more realistic if we bear in mind the complexity of the living matter, staying anchored to the Gaussian assumption is misleading, *a fortiori* considering that the MSD effectively grows as a power of time. The unsuitability of the Gaussian assumption stimulated the need to find new mathematical treatments, and to develop novel techniques, aimed at describing the so called 'Anomalous Diffusion'.

3.2 From random walk to Continuous Time Random Walk

Anomalous dynamics is known to characterize a variety of fields, from the transport of charges in amorphous semiconductors, to the foraging of albatrosses and marine predators, quantum optics, and diffusometry of particles in complex, porous systems and systems near the percolation threshold. In particular, water molecules diffusing¹⁷ in biological tissues exhibit a bulk behavior that is not fully explicable by Brownian motion. In the following the random walk model and its generalization to anomalous dynamics through the Continuous Time Random Walk (CTRW) model are presented. The theoretical framework of CTRW is well established and has been corroborated by huge amounts of Monte Carlo simulations together with several experimental studies, mainly obtained by using fluorescent spectroscopy (see [25] and references within).

¹⁷ Specifically, here we refer to the self-diffusion of water molecules, where the solute and solvent particles belong to the same species, and no net concentration gradient is needed.

3.2.1 Brownian diffusion and the random walk

Solute particles in suspension are interested by Brownian motion, that is unavoidable at temperature higher than absolute zero. Because of this, particles change their position over time, travelling roughly homogeneous steps along the directions determined randomly by the collisions. In the hypothesis of undistinguishable particles and negligible reciprocal interactions, this phenomenon can be modeled as a random walk (see **Figure 3.1a**), where the walker jumps at each time step towards a neighbor site. The following master equation describes the probability for the walker to get to position k after Δt in case of mono-dimensional motion, starting from either $k-1$ or $k+1$ site:

$$P_k(t + \Delta t) = \frac{1}{2}P_{k-1}(t) + \frac{1}{2}P_{k+1}(t) \quad (3.1)$$

Indicating the distance travelled with Δx , in the continuous limit and considering Taylor expansions in x and t we have:

$$\begin{aligned} \lim_{\Delta t \rightarrow 0} P_k(x, t + \Delta t) &= P_k(x, t) + \Delta t \frac{\partial P_k(x, t)}{\partial t} + o(\Delta t^2) \\ \lim_{\Delta x \rightarrow 0} P_k(x + \Delta x, t) &= P_k(x, t) \pm \Delta x \frac{\partial P_k}{\partial x} + \frac{\Delta x^2}{2} \frac{\partial^2 P_k(x, t)}{\partial x^2} + o(\Delta x^2) \end{aligned} \quad (3.2)$$

which, considering the lowest orders in Δx and Δt (and dropping the subscript k), lead to the differential diffusion equation:

$$\frac{\partial P(x, t)}{\partial t} = D \cdot \frac{\partial^2 P(x, t)}{\partial x^2} \quad (3.3)$$

where $D = \frac{(\Delta x)^2}{2\Delta t}$ is the diffusion constant, with physical dimensions $[D] = mm^2/s$. The diffusion equation (3.3) is a direct consequence of the central limit theorem. For a large number of steps, or a long diffusing time, the probability density function (PDF) of being at a given site x and time t has a Gaussian shape:

$$P(x, t) = \frac{1}{\sqrt{2\pi \cdot 2Dt}} e^{-\frac{x^2}{4Dt}} \quad (3.4)$$

that is a normal distribution, given the initial condition $\lim_{t \rightarrow 0} P(x, t) = \delta(x)$, and with a variance (representing the mean squared displacement) $\sigma^2 = MSD = 2Dt$. This Gaussian PDF that solves the diffusion equation (3.3) is called the motion propagator (MP). Notice that the independence of the MP on the initial position reveals the markovian nature¹⁸ of Brownian motion.

3.2.2 Anomalous diffusion and the Continuous Time Random Walk

Let us modify the random walk model to make it more realistic, preserving the 2D-lattice sketch. Now the walker may spend a certain waiting time on a given site, or in addition it may perform longer or shorter jumps (see **Figure 3.1b,c**). Let $\Psi(x, t)$ be the PDF to perform a jump, and $\lambda(x) = \int_0^\infty \Psi(x, t) dt$ and $w(t) = \int_{-\infty}^\infty \Psi(x, t) dx$ respectively, the jump length and the waiting time PDFs, so that $\lambda(x) dx$ produces the probability of having a jump in $(x, x+dx)$, and $w(t) dt$ produces the probability of having a waiting time in $(t, t+dt)$. In the CTRW model proposed by Metzler and Klafter [31, 32] $\lambda(x)$ and $w(t)$ are supposed to be independent random variables, so that the PDF of a jump is given by their product. Under these conditions the CTRW processes can be categorized by the finiteness of these two quantities, the jump lengths variance, Σ^2 :

$$\Sigma^2 = \int_{-\infty}^{\infty} x^2 \cdot \lambda(x) dx \quad (3.5)$$

and the characteristic waiting time, T :

$$T = \int_0^\infty t \cdot w(t) dt \quad (3.6)$$

A CTRW process is described by the generalized diffusion equation:

¹⁸ A stochastic process is considered *markovian* if the conditional probability distribution of future states of the process (conditional on both past and present states) depends only upon the present state, not on the sequence of events that preceded it.

$$\eta(x, t) = \int_{-\infty}^{\infty} \int_0^{\infty} \eta(x', t') \Psi(x - x', t - t') dt' dx' + \delta(x) \delta(t) \quad (3.7)$$

which relates the PDF of having arrived at position x , at time t ($\eta(x, t)$) to the previous event of having arrived at position x' , at time t' . The second summand in (3.7) denotes the initial condition of the random walk. The PDF for a particle of getting at position x at time t is finally given by:

$$P(x, t) = \int_0^t \eta(x, t') \left[1 - \int_0^{t'} w(t'') dt'' \right] dt' \quad (3.8)$$

i.e. of arrival on that site x at time t' , not having moved since. Note that here the PDF describing the motion depends on the previous history, suggesting the non-markovian nature of anomalous diffusion. By using Fourier Transform in space ($x \rightarrow k$) and Laplace transform in time ($t \rightarrow u$), we obtain the following expression for the MP:

$$P'(k, u) = \frac{1-w(u)}{u} \cdot \frac{P'_0(k)}{1-\Psi(k, u)} \quad (3.9)$$

where $P'_0(k)$ corresponds to the Fourier Transform of the initial condition.

which, back-transformed to the (x, t) coordinates provides the Gaussian MP previously described. This approach allows to describe also super-diffusion and sub-diffusion processes.

3.3.1 The super-diffusion or Lévy walks

The super-diffusion is characterized by a diverging Σ^2 and a finite T . Due to the finiteness of T super-diffusion is a markovian process. It is possible to model the process with a Poissonian $w(t)$ and a jump length PDF that behaves as a Lévy distribution: $\lambda(x) \sim A_\mu \frac{1}{\sigma^\mu |x|^{1+\mu}}$ in the hypothesis of $|x| \gg \sigma$ and with $0 < \mu < 2$. By considering Laplace and Fourier transforms we obtain the Fourier-Laplace transform of the MP in case of super-diffusion:

$$P'(k, u) = \frac{1}{u + K^\mu |k|^\mu} \quad (3.11)$$

for which, upon Fourier-Transform inversion, the following fractional differential equation (FDE) is inferred:

$$\frac{\partial P(x, t)}{\partial t} = K^\mu {}_{-\infty}D_x^\mu P(x, t) \quad (3.12)$$

where, analogously to (3.3), $K^\mu = \frac{\sigma^\mu}{\tau}$ is the generalized diffusion constant, with physical dimensions $[K^\mu] = mm^\mu/s$, and the μ -parameter represents the order of fractional derivative in space [28]. Notice that here ${}_{-\infty}D_x^\mu$ denotes the Riesz/Weyl fractional operator¹⁹, which applied to any function $f(x)$ has the property:

$$\mathfrak{F} [{}_{-\infty}D_x^\mu f(x)] \equiv -|k|^\mu \mathfrak{F} [f(x)] = -|k|^\mu f(k) \quad (3.13)$$

¹⁹ Following the treatment reported in Metzler and Klafter's review, and according to the contemporary convention, we dropped the imaginary unit in the expression $\mathfrak{F} [{}_{-\infty}D_x^\mu f(x)] \equiv -|ik|^\mu \mathfrak{F} [f(x)]$.

where \mathfrak{F} indicates the Fourier Transform. Thus, by Fourier-transforming the whole FDE associated to super-diffusion and considering the inverse Laplace transform, we get the following expression for the super-diffusive MP:

$$P'(k, t) \sim e^{-K^\mu |k|^\mu t} \quad (3.14)$$

which is the characteristic function of a symmetric Lévy distribution. The conceptual difficulty of a diverging Σ^2 , leading consequently to a diverging MSD, may be overcome considering that the walker moves at finite speed [31].

3.3.2 The sub-diffusion

The sub-diffusion is characterized by a finite Σ^2 and a diverging T . Due to the limitlessness of T sub-diffusion is a non-markovian process. Again it is possible to model the motion with a long tailed waiting time PDF that has an asymptotic behavior $w(t) \sim A_\alpha \left(\frac{t}{\tau}\right)^{1+\alpha}$, with $0 < \alpha < 1$, and a Gaussian jump length PDF. The Laplace space asymptotic of $w(t)$ is $w(u) \sim 1 - (u\tau)^\alpha$. As usual, we obtain the Fourier-Laplace transform of the MP in case of sub-diffusion:

$$P'(k, u) = \frac{P'_0(k)/u}{1 + K_\alpha u^{-\alpha} k^2} \quad (3.15)$$

for which, upon Fourier-Transform inversion, and following the rules for the fractional integrals, the following FDE is inferred:

$$\frac{\partial P(x, t)}{\partial t} = K_\alpha {}_0D_t^{1-\alpha} \frac{\partial^2 P(x, t)}{\partial x^2} \quad (3.16)$$

where, analogously to (3.3), $K_\alpha = \frac{\sigma^2}{\tau^\alpha}$ is the generalized diffusion constant, with physical dimensions $[K_\alpha] = mm^2/s^\alpha$, and the α -parameter represents the order of fractional derivative in time [28]. Notice that here ${}_0D_t^{1-\alpha}$ denotes the Riemann/Liouville operator, which applied to any function $f(t)$ has the property:

$$\mathcal{L}[_0D_t^{-\alpha}f(t)] \equiv u^{-\alpha}\mathcal{L}[f(t)] = u^{-\alpha}f(u) \quad (3.17)$$

where \mathcal{L} indicates the Laplace Transform. Because of the presence of fractional powers of u in the MP in (3.15), the Laplace inversion is not immediate. In this case it is useful to identify the MP with its correspondent Fox function, exploiting the rules for the inversion of Fourier and Laplace transform of Fox functions, as clearly illustrated in [31]. However, for our treatment it is sufficient to know that the single modes of the FDE describing sub-diffusion present a well-known Mittag-Leffler decay in the asymptotic limit, i.e.:

$$P'(k, t) \sim E_{\alpha}[-K_{\alpha}k^2t] \quad (3.18)$$

or, more precisely:

$$P'(k, t) \sim \begin{cases} e^{-K_{\alpha}k^2t^{\alpha}} & \text{if } k^2 \ll \frac{1}{K_{\alpha}t^{\alpha}} \\ \frac{1}{K_{\alpha}k^2t^{\alpha}} & \text{if } k^2 \gg \frac{1}{K_{\alpha}t^{\alpha}} \end{cases} \quad (3.19)$$

with $0 < \alpha < 1$. The sub-diffusive MP as a function of position is shown in **Figure 3.2** and compared with the Gaussian MP.

3.3.3 Anomalous diffusion phase diagram

In the CTRW framework it is possible to define FDE describing the evolution of PDF in super-diffusive and sub-diffusive processes. These are represented respectively by equations (3.12) and (3.16). In this way the diffusion equation with integer order space and time derivatives for Brownian motion is generalized through the use of fractional order space and time derivatives. The situation could be composed in the following FDE:

$$\frac{\partial P(x,t)}{\partial t} = {}_{-\infty}D_x^\mu {}_0D_t^{1-\alpha} K_\alpha^\mu \frac{\partial^2 P(x,t)}{\partial x^2} \quad (3.20)$$

or, as some authors suggested [24, 28], using the Caputo fractional derivative in time with $0 < \alpha \leq 1$ and the Riesz fractional derivative in space with $1 < \beta \leq 2$:

$$\frac{\partial^\alpha P(x,t)}{\partial t^\alpha} = K_{\alpha,\beta} \frac{\partial^\beta P(x,t)}{\partial |x|^\beta} \quad (3.21)$$

Here the parameter β is the same as μ , indicating the fractional order in space. By considering the interplay between the two fractional orders a phase diagram of AD may be drawn. The Brownian diffusion holds for $\alpha = 1, \beta = 2$, as well as for $\alpha = \beta/2$ (see **Figure 3.3a**); when $0 < \alpha < 1$ we are in the sub-diffusion regime, for every value of $\alpha < \beta/2$; when $0 < \beta < 2$ we are in the super-diffusion regime, for every value of $\alpha > \beta/2$.

The generalization of MSD in one dimension for normal and anomalous dynamic is represented by the power law $\langle x^2(t) \rangle \sim t^{\frac{2\alpha}{\beta}}$, which for $\alpha = 1, \beta = 2$ retrieves the linear relation that holds for Brownian motion. In sub-diffusion $\frac{2\alpha}{\beta} < 1$ and in fact the MSD increases more slowly with time, the opposite situation of super-diffusion, for which $\frac{2\alpha}{\beta} > 1$. The different behaviors of MSD vs diffusion time are shown in **Figure 3.3b**.

Anomalous diffusion: when water diffuses in complex media

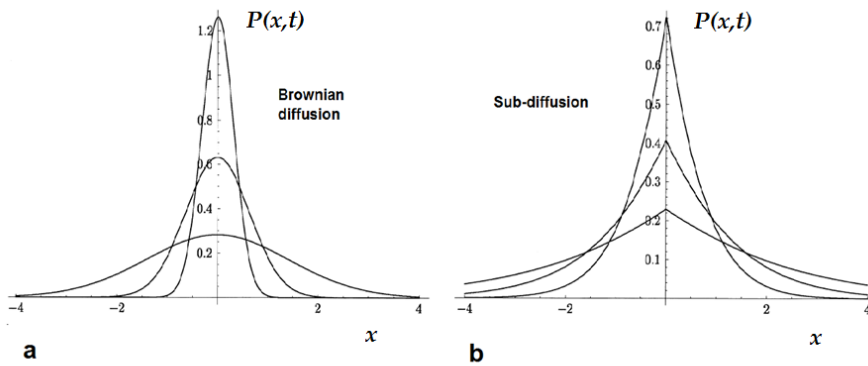


Figure 3.2 – Propagator probability density functions. a) Propagator $P(x, t)$ for Brownian diffusion ($\alpha = 1$) for the times $t = 0.05, 0.2$ and 1 with an increasing width. The curve shape is smooth. b) Propagator $P(x, t)$ for sub-diffusion with anomalous diffusion exponent $\alpha = 1/2$, drawn for the consecutive times $t = 0.1, 1, 10$. The cusp shape of the PDF is distinct.

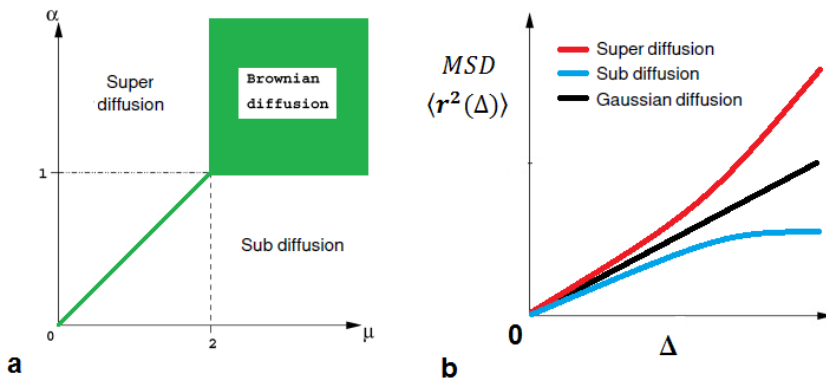


Figure 3.3 – Anomalous Diffusion phase diagram and the MSD. a) Phase diagram of the FDE depending on the two fractional order exponents, α and μ (also known as β). The Brownian diffusion holds in the green region. b) Behavior of the mean squared displacement (MSD) of water molecules as a function of the diffusing time (or observation time). The sub-diffusion is characterized by an MSD that grows slower than the Gaussian case; the super-diffusion presents an MSD that grows faster than the Gaussian one.

3.4 Relationship between the NMR signal and the motion propagator

In Chapter 2 it has been shown how to impose a label on the phase of the transverse magnetization, codifying thus the spin position. The Stejskal-Tanner equation was derived modelling the spin trajectories as a succession of discrete hops resolved in one dimension. Here, we derive the signal attenuation adopting a more analytical approach, showing how the PGSE method can be used to give information about the self-correlation function $P_s(\mathbf{r}_0|\mathbf{r}, t)$ defined in section 2.2. In the so called *narrow-pulse approximation*, i.e. $\delta \ll \Delta$, the effect of the gradient pulse is to impart a phase shift $\Delta\Phi_1 = \gamma\delta\mathbf{g} \cdot \mathbf{r}_1$ to a spin located in a position \mathbf{r}_1 at the instant of the pulse. In the PGSE sequence, this phase shift is subsequently inverted by the RF180° pulse. If the spin has moved to \mathbf{r}_2 at the time of the second pulse $t = \Delta$, the net phase shift will be $\Delta\Phi_2 = \gamma\delta\mathbf{g} \cdot (\mathbf{r}_2 - \mathbf{r}_1)$.

The total signal is given by the superimposition of transverse magnetizations, an ensemble average in which each phase term $e^{i\Delta\Phi_2}$ is weighted by the probability for a spin to begin at \mathbf{r}_1 and to move to \mathbf{r}_2 , i.e. $\rho(\mathbf{r}_1)P_s(\mathbf{r}_1|\mathbf{r}_2, \Delta)$:

$$S_\Delta(\mathbf{g}) = \int \rho(\mathbf{r}_1) \int P_s(\mathbf{r}_1|\mathbf{r}_2, \Delta) e^{i\gamma\delta\mathbf{g} \cdot (\mathbf{r}_2 - \mathbf{r}_1)} d\mathbf{r}_1 d\mathbf{r}_2 \quad (3.22)$$

We define a reciprocal vector \mathbf{q} , where:

$$\mathbf{q} = \frac{\gamma\delta\mathbf{g}}{2\pi} \quad (3.23)$$

that is another form of the \mathbf{k} -vector defined in Par. 1.3.1 ($\mathbf{k} = \frac{\gamma\mathbf{G}t}{2\pi}$ where \mathbf{G} represents the imaging gradient) and consider the relative displacement $\mathbf{R} = \mathbf{r}_2 - \mathbf{r}_1$, thus we rewrite equation (3.22) as:

$$S_\Delta(\mathbf{q}) = \int P_s(\mathbf{R}, \Delta) e^{i2\pi\mathbf{q} \cdot \mathbf{R}} d\mathbf{R} \quad (3.24)$$

Equation (3.24) states that $S_{\Delta}(\mathbf{q})$ and $P_s(\mathbf{R}, \Delta)$ are linked by a simple Fourier relationship, that in the mono-dimensional case, dropping the un-necessary subscripts, will be:

$$S(q) = \int P(x, \Delta) e^{i2\pi q \cdot x} dx \quad (3.25)$$

This means that, through the use of NMR, one can measure the signal obtained after a diffusion sensitized sequence (PGSE or PGSTE, or some other variants) and get information about the characteristics of the diffusive regime.

In the previous paragraphs, by considering the Fourier Transform of the generalized diffusion equation we obtained the expressions for the MP in case of normal diffusion, super-diffusion, and sub-diffusion at the asymptotic limit:

$$\begin{aligned} \text{normal diffusion: } P'(k, t) &\sim e^{-Dk^2 t} \\ \text{superdiffusion: } P'(k, t) &\sim e^{-K^{\mu} |k|^{\mu} t} \\ \text{subdiffusion: } P'(k, t) &\sim e^{-K_{\alpha} k^2 t^{\alpha}} \end{aligned} \quad (3.26)$$

If we substitute the vectors $k \rightarrow q$ and the diffusive time $t \rightarrow \Delta$, we obtain an expression where the connection between the MP and the DW-signal is more evident:

$$\begin{aligned} \text{normal diffusion: } P'(q, \Delta) &\sim e^{-Dq^2 \Delta} \sim e^{-Db} \\ \text{superdiffusion: } P'(q, \Delta) &\sim e^{-D_{gen} |q|^{\mu} \Delta} \\ \text{subdiffusion: } P'(q, \Delta) &\sim e^{-D_{gen} q^2 \Delta^{\alpha}} \end{aligned} \quad (3.27)$$

where D_{gen} stands for a generalized version of the diffusion constant. The relations shown in (3.27) allow us to project a PGSE or PGSTE sequence ad hoc for the desired regime. In fact, in order to extract the μ parameter quantifying super-diffusion we will simply perform multiple measurements varying q , hence the diffusion gradient strengths g , and keeping the mixing time Δ constant; instead, for extracting the α parameter quantifying sub-diffusion we will simply repeat the sequence varying Δ , at fixed diffusion gradient strength.

3.5 *Pseudo* super-diffusion of water: state of the art

Following this simple rule, Palombo et al. measured for the first time the time and space fractional derivatives or exponents α and μ simultaneously by PGSE, in samples of micro-beads dispersed in aqueous solutions [25]. Palombo and co-workers showed that μ was strictly related to another parameter, the stretched exponent γ . The stretched-exponent had been introduced previously through heuristic methods in *in vivo* animal experiments [60], as a method to quantify the deviation from the mono-exponential signal decay exhibited by NMR signal due to diffusion in complex systems (see **Figure 3.4**) for b-values higher than $b = 2000 \text{ s/mm}^2$. This evidence has been reported in a number of brain studies, both in animal model and in humans [61, 62]. However, neither the mathematical origin nor the biophysical nature of the stretched exponent had been clarified.

Conversely Palombo et al. [25] established a connection between the stretched exponent γ and the CTRW derived parameter μ ($\mu = 2\gamma$). γ is obtained by using DW data acquired as a function of b-values and collected by changing diffusion gradient (\mathbf{g}_{diff}) strength at a constant value of Δ , and quantifies, just as μ , the intravoxel diffusion heterogeneity in space. Some authors indicated this peculiar mechanism as ‘water jumping’ [24, 28]. Indeed, the γ parameter reflecting the multi-compartmentalization, showed significant correlations with the size of diffusive compartments in mono and poly-dispersed solutions [25]. An alternative analytical derivation for the stretched exponential model, using fractional order space derivatives, has been recently proposed by Magin et al. [28]. These authors emphasized that the potential utility of fractional order β parameter (which is, in practice, equal to γ parameter) to characterize the environment for molecular diffusion (as a complement to ADC) might lead to a new way to investigate tissue structural features. However, the biophysical basis of the β parameter remained elusive.

Palombo and co-workers [26] revealed a significant correlation between γ and the internal gradients G_{int} arising from magnetic susceptibility differences $\Delta\chi_m$ at the interface between neighboring compartments, and suggested that this effect could be attenuated or eliminated by the use of bipolar gradients in the DW acquisition sequence, spoiling out the local magnetic field inhomogeneity (see **Figure 3.5**). This strong correlation can be explained considering the coupling between diffusion gradients (\mathbf{g}_{diff}) and \mathbf{G}_{int} which causes an irreversible DW signal loss. Specifically, local gradients induce a phase shift to

the spins within a space region strictly close to the interfaces, which adds up to the phase shift given by the \mathbf{g}_{diff} pulse, namely originating an effective gradient $\mathbf{G}_{\text{eff}} = \mathbf{G}_{\text{int}} + \mathbf{g}_{\text{diff}}$. When \mathbf{G}_{int} and \mathbf{g}_{diff} are comparable, some spins contribute to increase the DW signal attenuation; other spins (that can be located far from the first ones) acquire a phase that will help to increase the signal. Due to indistinguishable spins associated with water molecules, this scenario mimics a super-diffusion regime. The water signal disappears in one spot and appears in another one, thus simulating long jumps of water molecules. Thus some authors referred to this mechanism with the expression '*pseudo* super-diffusion' [20, 25, 26] due to both water multi-compartmentalization and $\Delta\chi$ at the interface between different compartments.

The use of γ provides an interesting and novel source of contrast in MRI, and was soon tested in more complex systems, such as the human brain. By using a tensor representation of AD, scalar invariant indices such as the mean γ ($M\gamma$) and the γ anisotropy ($A\gamma$) were quantified by De Santis et al. [22, 23]. In De Santis' work, the method used accounts for the dependence of the stretching exponent γ from the spatial direction. The approach here is similar to that for deriving the anisotropic diffusion from tensor calculation: the stretched exponential model is assumed to be valid along three principal directions (i.e., the main axes of diffusivity) only, rather than along n arbitrary directions. Indeed, in the three-dimensional space, the motion can always be expressed by a combination of three components, which depends on the local geometry. If the measurement is performed along one of these main directions, the decay can be expressed as a simple stretched exponential. Then the signal acquired along a generic direction may be modeled as the superimposition of the decays along each of the main directions, thus involving all the three main exponents. An AD-metrics was introduced, comparable with DTI-metrics, and comprising the mean-value of the stretched exponent, $M\gamma$, and its anisotropy, $A\gamma$, and it was shown to be more effective than DTI in the discrimination among brain regions (see **Figure 3.6**).

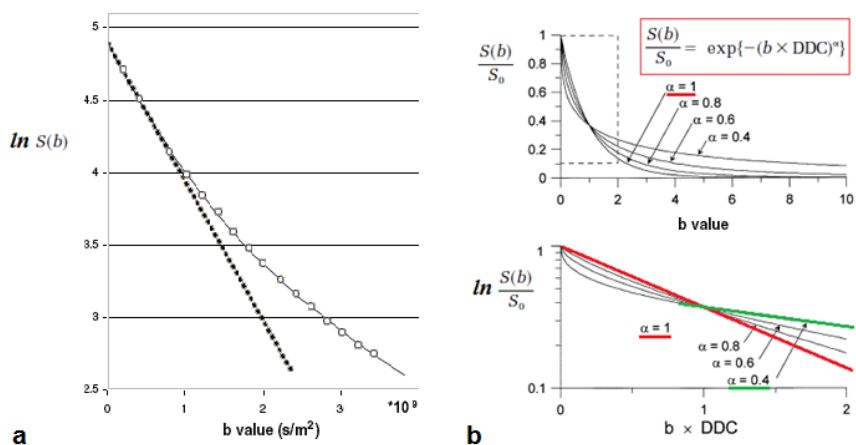


Figure 3.4 – a) Deviations from mono-exponential signal decay. Log of the acquired NMR signal (a.u.) versus the diffusion weighting or b -value, expressed in s/m^2 . The experimental points are plotted as empty circles, while the mono-exponential decay predicted by regular diffusion is shown in black (Image reproduced from De Santis work [23]). b) Normalized NMR signal with respect to the image without diffusion weight ($b=0$) plotted as a function of b -value, and its log plotted as a function of the exponential argument $b \cdot \text{DDC}$, with DDC defined as the distributed diffusion coefficient (image edited from Bennett's paper [60]).

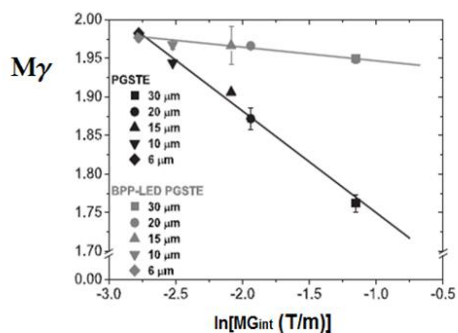


Figure 3.5 - Mean γ values (My), measured using PGSTE (black data points) and bipolar gradient PGSTE (gray data points), as a function of the internal magnetic field gradient strength (G_{int}) for samples of different suspensions of mono-dispersed beads, characterized by the sizes displayed in the left side insert. Black and gray solid line are the regression line. The linear correlations coefficient is higher than 0.9 in both cases, with the level of significance $P < 0.0001$ for single gradient PGSTE. Reproduced from [26].

Anomalous diffusion: when water diffuses in complex media

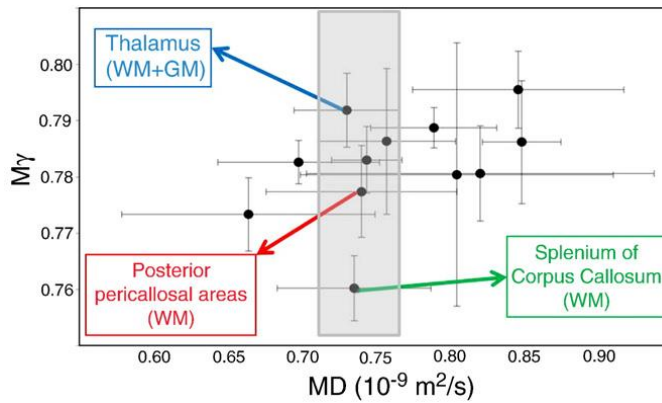


Figure 3.6 - Discrimination among different brain regions: My and MD . Correlation plot between MD and the mean value of γ (My) in which each point represents the mean value extracted from 10 healthy subjects and calculated for 12 WM and GM ROIs. Three different anatomical brain regions, which are not distinguishable on MD basis, turned out to be discriminated by their corresponding My value (image source: De Santis et al. paper [22]).

Chapter 4 *Pseudo* super-diffusion of water in mouse spinal cord: *in vitro* study

This Chapter describes the results obtained by performing AD γ -imaging on fixed mouse spinal cord *in vitro*. The experimental derivation of the γ exponent for a simple geometry is introduced, the outcomes regarding the correlation of γ with magnetic susceptibility inhomogeneity and microstructural features of spinal cord tracts are discussed [42], and inserted in a manuscript in preparation, at the state of the art [43].

The choice of this particular sample studied at high field (9.4 T) was motivated by three main reasons: the simple geometry of the spinal cord, with its cylindrical symmetry and a preferential longitudinal orientation of myelinated axons allowed to quantifying γ exponent related to *pseudo*-superdiffusion along 3 orthogonal directions; the use of high field was convenient for the enhancement of local internal gradients driven by magnetic susceptibility differences which are known to affect the γ -contrast; the mouse spinal cord is currently employed in studies of demyelination due to induced pathology that mimics Multiple Sclerosis alterations [63].

4.1 Rationale

4.1.1 Anatomy of the spinal cord

The spinal cord is the part of the central nervous system (CNS) that conducts sensory information from the peripheral nervous system to the brain, and motor information from the brain to muscular or glandular tissue.

It is thus the connection center for the reflexes as well as the afferent (sensory) and efferent (motor) pathways for most of the body below the head and neck. The spinal cord is protected by the vertebrae and the meninges, that are continuous with those of the brain. It is essentially a tubular bundle of nervous tissue that collects neurons and their axons departing from the medulla, passing through the brainstem, and reaching the second lumbar vertebra. The area within the vertebral column beyond the end of the spinal cord is called the *cauda equina*. Going from the head to the cauda equina the spinal cord is ideally divided in 5 areas: the cervical, thoracic lumbar, sacral and coccygeal segments, from which the spinal nerves depart.

The ventral side of the cord is the one oriented towards the internal organs, and presents mainly motor neurons and motor fibers; the dorsal side of the cord presents mainly sensory fibers; the central part presents interneurons connecting distal parts within the same segment. Furthermore, it is bilaterally symmetrical, incompletely divided into right and left halves by a ventral median fissure and a dorsal median septum.

The spinal cord comprises 3 types of tissues, which occupy a specific position in the cross-section:

- the innermost tissue, that is the central canal, is filled with **cerebro-spinal fluid, CSF**, and communicates with the IV cerebral ventricle;
- around it there is a butterfly-shaped **gray matter, GM**, characterized by a high density of neuron cell bodies and gliocytes, and a high capillary density;
- the outermost tissue is called **white matter, WM**, which comprises concentrated myelinated fibers, gliocytes, sensory and motor tracts, and presents a low capillary density and a variegated axonal density.

4.1.1.1 Gross anatomy of mouse spinal cord

The mouse spinal cord is made up of 34 segments: 8 cervical (C1 to C8), 13 thoracic (T1 to T13), 6 lumbar (L1 to L6), 4 sacral (S1 to S4), and 3 coccygeal (Co1 to Co3). There are two enlargements, the cervical and lumbar (lumbosacral) enlargements, which involve the segments that the nerves of the limbs are connected with. The cervical enlargement (*intumescentia cervicalis*) extends from C5 to T1, and the lumbosacral enlargement (*intumescentia lumbalis*) extends from L2 to L6. The lumbosacral enlargement is a little

narrower than the cervical enlargement, and its dorso-ventral diameter is also slightly smaller [64].

Among the differences between the anatomy of human and mouse spinal cord (MSC) let us stress two major differences concerning the WM tracts, since they are the object of investigation of this analysis:

- the corticospinal tract (CST), a descending tract, that is located in the lateral column in primates, in rodents and mice is placed in the dorsal column instead [64];
- in mice the organization of the vestibulo-spinal tract (VST), another descending pathway, is more similar to the cat's one than to the human's one [64].

4.1.1.2 Motivations of the sample choice for the *in vitro* investigation

The application of DW-MRI to the study of spinal cord (SC) has increased in the last ten years, however the literature regarding *in vivo* study is scarce compared to the one regarding brain investigation, despite the higher diffusional anisotropy exhibited in the system [65]. The *in vivo* investigation presents indeed some difficulties, mainly due to the fact that the bony structures that surround the SC contribute to significant susceptibility artifacts, and respiratory motion, cardiac pulsation, and other physiological and physical motions cause artifacts that are significantly more pronounced in the SC than in the brain [65].

Here the study was conducted *in vitro* on a fixed mouse SC, thus in absence of motion-related artifacts. The decrease of signal due to fixation [66], which is known to cause significant decreases in the longitudinal diffusivity (leaving the relative anisotropy and radial diffusivity scarcely affected) was counterbalanced by the use of high magnetic field.

SC from rodents, in particular from mice are currently employed in studies of demyelination [63, 65-67]. For example the Experimental Allergic Encephalomyelitis (EAE) may be induced in mice (generally the commonly used species is the C57 BL/6), allowing subsequent studies about the evolution of degeneration, particularly evident in the SC [63]. In fact myelin in the SC of EAE-affected mice is severely affected by the disease, and it is employed as a model of Multiple Sclerosis.

4.1.2 Multiple water pools

With the expression *multiple water pools* we refer to the presence of a multiplicity of compartments available for water diffusion.

Evidence for the presence of two or three distinct water compartments was provided by multi-exponential T_2 measurements in brain, spinal cord and nerves [8, 68-70]: a fast-relaxing component was attributed to non-exchanging water closely associated with proteins and phospholipids, that is water within myelin, and a slow-relaxing component was attributed to water from both the extra- and intra-axonal spaces, with the longest T_2 associated to the intra-cellular space, presenting a higher concentration of macromolecules.

These distinct water pools were found to exhibit distinct diffusivities as well, with a higher diffusivity assigned to the extra-cellular water, and a lower diffusivity assigned to the intra-cellular water, as shown by Chin et al. in the ex vivo study of rat SC at 9.4 T [67]. Thus it has been considered that the extracellular compartment corresponded to a *fast* diffusing pool, as water would be expected to diffuse more rapidly there than in the intracellular, more viscous compartment, or the *slow* diffusing pool. However, a mismatch between the expected volume fractions and fitted results from the DWI data [8, 71] together with diffusive studies showing multi-compartments in the intra-cellular component alone [71], made this correspondence unfeasible.

Finally, concerning multi-compartmentalization in WM tracts, a more restricted diffusion was revealed for the tracts characterized by higher axonal density [67].

4.1.3 Rate of relaxation and magnetic field inhomogeneity

The rate of relaxation is the inverse of the relaxation time constant. As illustrated in Chavhan et al. [72], transverse relaxation in specific sequences called Gradient Echo (GRE) sequences is a combination of intrinsic T_2 relaxation, and relaxation caused by magnetic field inhomogeneity. With the use of GRE sequences it is possible to collect phase and magnitude images. From the magnitude the rate of relaxation R_2^* may be extracted. This parameter is the sum of two terms:

$$R_2^* = \frac{1}{T_2^*} = \frac{1}{T_2} + \gamma B_0 \Delta\chi \quad (4.1)$$

where γ is the gyromagnetic ratio, that turns into $R_2^* = R_2 + R_2'$. The first term takes into account the spin-spin interactions, while the second term is sensitive to the field inhomogeneity due either to intrinsic defects in the magnet or to susceptibility-induced field distortions, produced by the tissue or other materials with magnetic susceptibility differences ($\Delta\chi$).

4.2 Materials and Methods

4.2.1 Data acquisition

The mouse spinal cord (MSC) was extracted after apposite treatment aimed at optimizing fixation, fully described in Ong et al. [73]. A C57 BL6 mouse, (8-9 months, 25-30 mg, Charles River, Wilmington, MA) was anesthetized with an intraperitoneal injection of 10 mg ketamine/1 mg acepromazine per ml, and perfused through the heart with 20 ml of phosphate buffer solution, and 20 ml of fixing solution with 4% glutaraldehyde and 2% paraformaldehyde in 10 mM PBS. The combination of glutaraldehyde and paraformaldehyde should ensure a better fixation of intra-axonal cytoskeletal proteins, as reported in Schwartz et al. [74] and thus a longer preservation of axonal ultra-structure. After fixation, the entire spinal cord was post-fixed with a different fixing solution for at least two weeks, and finally stored in PBS.

The capillary containing the fixed spinal cord and the PBS (see **Figure 4.1**) was then inserted in the 10 mm-internal diameter bore of a Bruker Avance-400 high resolution spectrometer operating at a magnetic field strength of 9.4 T, and equipped with a gradient unit characterized by a maximum gradient strength of 1.2 T/m and a rise time of 100 μ s. ParaVision 3.0 software was employed for data acquisition. The slice package was placed in the cervical section (**Figure 4.2a**), with slice thickness of 0.75 mm, FOV = 4.5 x 4.5 mm², matrix size 128 x 128, in-plane resolution 0.035 x 0.035 mm². The extraction of the gamma-exponent requires a set of increasing gradient strengths, which provide increasing diffusion weights, with a fixed observation time Δ : we chose different

values of gradient intensities, resulting in 10 b-values in the range (100, 4000) s/mm², plus the b₀. The DWIs were acquired by means of a PGSTE sequence along 3 orthogonal directions, one of which was parallel to the capillary walls, or to the main orientation of axons, with the following parameters: TR/TE = 4000ms/12ms, $\Delta/\delta = 40\text{ms}/2\text{ms}$.

The same acquisition parameters were used for the conventional DTI, performed along 6 directions, with b = 1500 s/mm², to increase the accuracy on the diffusion coefficient estimate [3]. T₂* relaxometry was performed by means of GRE with 13 values of TE varying in the interval (2, 40) ms. The acquisition time required for the anomalous-diffusion weighted experiment along 3 directions was 38 hours per direction, due to the high number of sample averages (NSA=16). The same number of averages was used for the conventional DTI and T₂* relaxometry. Axial, coronal and sagittal slices (**Figure 4.2b**) were acquired with the same modality, and an in-plane resolution of 0.047 x 0.047 mm² for the latter two. The temperature of the specimen was monitored and kept constant at T = 20 °C, with oscillations of +/- 0.5 °C.

4.2.2 Data analysis

The NMR signal intensity of the investigated sample is stored in particular outputs called DICOM (Digital Image and COmmunication in Medicine). The DICOM contains two distinct files: the header (.hdr) file collects numeric information such as the matrix size of image, the resolution, the spatial coordinates, some acquisition parameters (for example echo time, repetition time), and the used b-values and gradient directions; the intensity of each voxel is stored instead inside the NIFTI (.nii) file. The conversion DICOM to NIFTI is achieved through the use of a dedicated software (dcm2nii). The extracted .nii file is a 4D-matrix: the first three dimensions are the spatial coordinates, while the fourth one represents a temporal dimension, hence in this case they will represent the DWIs at different gradient directions and b-values.

The signal to noise ratio (SNR) was computed for DWIs by dividing the average intensity of a region placed in the WM to the background noise.

Data were spatially smoothed by means of a Gaussian filter with full-width-half-maximum (FWHM) of 0.06 mm. Conventional DTI analysis was performed by means of FSL 5.0 DTIFIT routine (FMRIB Software Library v5.0, FMRIB, Oxford, UK [75]), which returns the maps of MD, FA, and the 3 eigenvalues ($\lambda_1, \lambda_2, \lambda_3$)

and eigenvectors (V_1, V_2, V_3) of the diffusion tensor. The PGSTE data were fit to the theoretical model using a home-made MATLAB script (MATLAB R2012b), which employs a non-linear least square estimation procedure using trust-region reflective algorithm for minimization, and exploits the advantage of parallel computing. The theoretical model used to quantify AD- γ exploits the relation between the Fourier transform of the MP of super-diffusion and the DW signal explained in section 3.4, using the b-value instead of q , without loss in generalization (since $b \sim \Delta \cdot q^2$). Since the particular device used provides the effective b-value, which due to the use of imaging gradients is different than 0 in the image without diffusion weight, the fitting expression used is the following:

$$\frac{S(b)}{S(b_0)} = \frac{S(b_0) \cdot \exp(-D_{gen} b^\gamma)}{S(0) \cdot \exp(-D_0 b_0)} = \frac{S(b_0)}{S(0)} \cdot \exp\left(- (D_{gen} b^\gamma - D_0 b_0)\right) \quad (4.2)$$

and returns the generalized diffusion constant (D_{gen}) and the value of the γ -exponent for each of the three orthogonal directions on a voxel by voxel basis, taking about 15 minutes for the whole slice package (5 slices) on a 2.66GHz 4-cores machine with 16GB RAM. Once derived, the 3 values of the anomalous exponent were used to compute the mean- γ and its anisotropy:

$$M_\gamma = \sum_{i=1}^3 \gamma_i / 3 \quad (4.3)$$

$$A_\gamma = \sqrt{\frac{3[(\gamma_1 - M_\gamma)^2 + (\gamma_2 - M_\gamma)^2 + (\gamma_3 - M_\gamma)^2]}{2(\gamma_1^2 + \gamma_2^2 + \gamma_3^2)}} \quad (4.4)$$

and the axial- γ , $\gamma_{//} = \gamma_1$ and radial- γ ($\gamma_{\perp} = \frac{\gamma_2 + \gamma_3}{2}$), coming from the average of the 2 orthogonal directions cutting the main axonal fibers orientation, which coincides with the B-field direction. T_2^* was derived using MATLAB by a mono-exponential fit, considering the TE-weighted images. R_2^* was derived thereafter by considering the reciprocal of T_2^* .

4.2.2.1 Selection of Regions of Interest (ROIs)

Mean values together with the intra-voxel standard deviation (SD) were obtained for each parameter of the DTI-metrics, AD-metrics and R_2^* in specific spinal cord Regions Of Interest (ROIs, see **Figure 4.3**) identified in three cervical slices by using histological reference images [73, 76]. The ROIs, manually drawn by three different operators and subsequently intersected, were chosen in distinct spinal cord tracts, with peculiar axonal size, axonal size distribution, axon density and myelin fraction, extracted from histological data by Ong et al. [73], and reported in **Figure 4.4**. The axon density was derived by dividing the axon counts to the cross-section of the optical image, and expressed in number of axons over mm^2 . Among the selected ROIs, only one included ascending-sensory fibers (funiculus gracilis, *fg*), while the others were placed in descending-motor tracts: dorsal Cortico-Spinal Tract, Rubro-Spinal Tract, Reticulo-Spinal Tract, medial Vestibulo-Spinal Tract, Spino-Thalamic Tract (respectively, *dCST*, *RST*, *ReST*, *VST*, *STT*). Other ROIs including the GM, the interface between the WM and GM, and the surrounding medium (fluid), were automatically selected through ad-hoc filters made on the basis of the MD-maps.

Homogeneity of variances was tested by using Levene's test. Pairwise comparisons were made using a Welch ANOVA. Games-Howell corrections were performed to correct for multiple testing. Relationship between pairs of parameters were assessed with linear correlation analysis (Pearson's r coefficient). P-values < 0.05 were considered statistically significant.

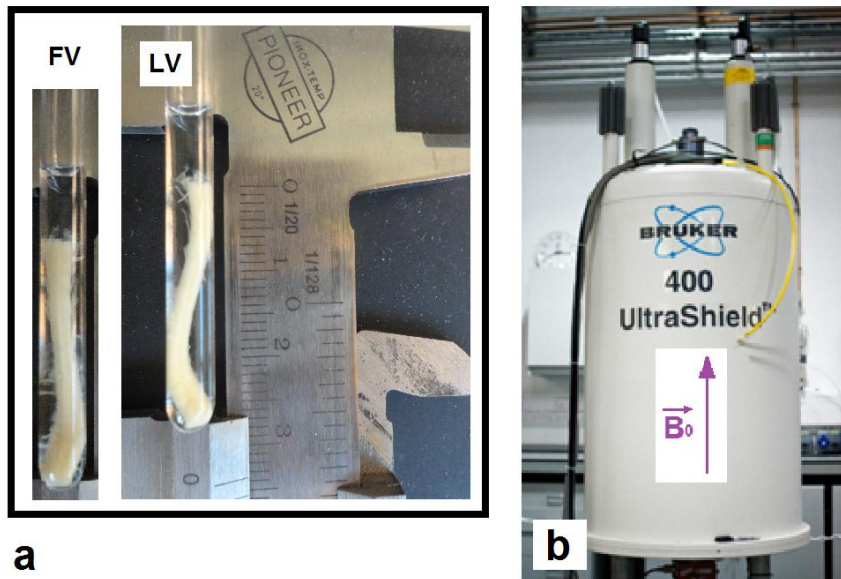


Figure 4.1 – *In vitro* study of mouse spinal cord. a) The fixed mouse spinal cord (MSC) is placed in a capillary filled with post-fixative solution (FV, frontal view; LV, lateral view). The tissue extends for about 2.6 cm in length and has maximum section of 4 mm x 2.5 mm at the level of the cervical and lumbar enlargements. b) The NMR spectrometer used for the acquisition provided a static field intensity of 9.4 T (corresponding to a Larmor frequency of 400 Hz). The orientation of the main static field is indicated.

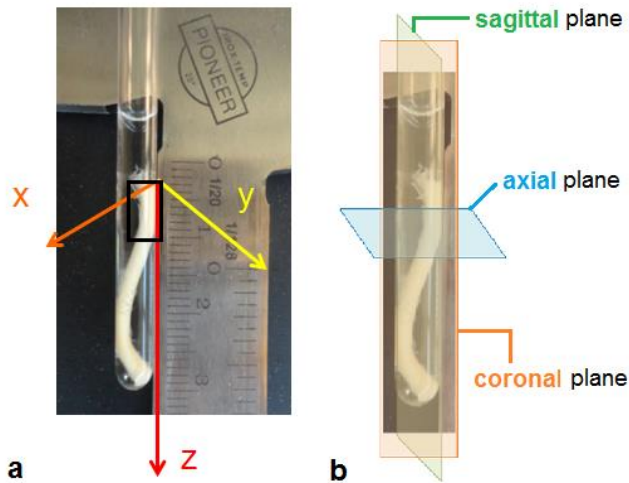


Figure 4.2 – Directions and planes of acquisition. a) The signal was acquired along 3 orthogonal directions, indicated in the figure. The slice package, placed in the cervical section, is highlighted in black. b) The 3D acquisition was repeated in order to acquire axial, coronal and sagittal slices.

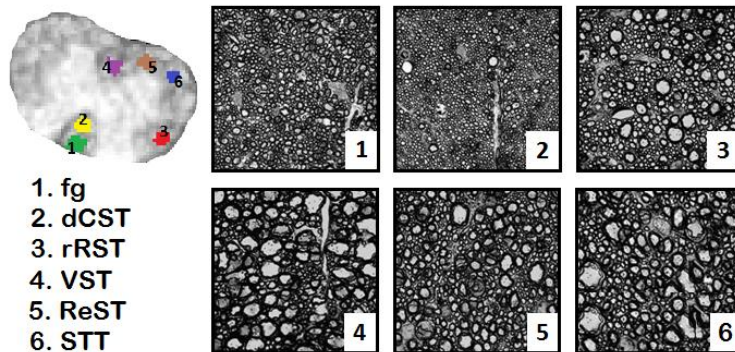


Figure 4.3 – Optical microscopy of various white matter spinal cord tracts from the C6/C7 section. Reproduced from Ong et al.'s paper [73]. Each image has a pixel resolution of $0.1 \times 0.1 \mu\text{m}$. The dorsal tracts are the funiculus gracilis, fg (1) and the dorsal Cortico-Spinal Tract, dCST (2); the lateral tract considered is the right Rubro-Spinal Tract, rRST (3); the ventral tracts are the Vestibulo-Spinal Tract, VST (4), the Reticulo-Spinal Tract, ReST (5), and the Spino-Thalamic Tract, STT (6). The regions of interest (ROIs) are superimposed on a My map on the left.

Average regional white matter tract histologic characteristic			
	dCST	FG	RST
Axon diameter	0.81±0.06	0.99±0.06	1.16±0.04
Axon diameter SD	0.31±0.08	0.47±0.06	0.71±0.10
Myelin fraction	0.45±0.07	0.47±0.05	0.43±0.04
Axon count	1670±267	1101±146	791±122
	ReST	STT	VST
Axon diameter	1.36±0.09	1.44±0.11	1.82±0.26
Axon diameter SD	0.89±0.10	0.98±0.18	1.40±0.13
Myelin fraction	0.41±0.04	0.42±0.08	0.41±0.06
Axon count	574±79	436±68	289±78

Figure 4.4 – Table of characteristics of the considered spinal cord tracts. These features were extrapolated by means of segmentation of optical images, and then mean values and SD were computed. Axon diameter and axon diameter SD are expressed in μm . From the axon count, considering the width of original microscopy images, the axon density was derived (as number of axons/ mm^2). Data reproduced from Ong et al.'s paper [73].

4.3 Results

The DWIs shown in **Figure 4.5** show an inversion of contrast between WM and GM (lighter in the b_0 image) with increasing diffusion gradient strength, g (thus with increasing b -value). The fluid surrounding the spinal cord, which exhibits free-diffusion, is attenuated to background intensity at the highest b -value. The SNR decreased in parallel to b -value increment, and it was higher for the central slices in the slice package, because of the lack of border effects. The SNR in the b_0 image varied between a minimum of 27 to a maximum of 32, depending on the slice, and the SNR for the highest b -value ($b=4000 \text{ s/mm}^2$) was 4 for the z -direction, 13 for the x -direction, 14 for the y -direction of acquisition. The SNR was however higher for every g than the lowest acceptable value according to Jones et al. [77].

The behavior of DW signal vs q -value expressed in m^{-1} is depicted in **Figure 4.6** for a selected voxel in a central slice, and it is distinct for WM and GM. The DW-signal, normalized to the b_0 -image, was fit to the theoretical model expressed in (4.1), and provided a value of the γ -exponent for each direction. Parametric maps of the three γ -exponent are depicted in **Figure 4.7** for a central axial slice.

A complete set of parametric maps of $M\gamma$ and $A\gamma$ for axial, coronal and sagittal slices of the cervical section of the spinal cord is shown in **Figures 4.8-4.9**. The AD-metrics provides a new contrast, highlighting the interfaces between tissues, as can be seen considering the external lamina of the spinal cord and the separation between WM and GM. For the same reason, a spinal root is easily detectable. The comparison between AD-metrics, DTI-metrics and $T2^*$ is provided in **Figure 4.10**. While in MD and FA maps the WM and GM appear homogeneous, in $M\gamma$ and $A\gamma$ maps the WM shows a variegated grainy texture. Notice that $T2^*$ is particularly sensitive to magnetic impurities, such as air bubbles.

The plots of AD-metrics as a function of $R2^*$ are shown in **Figure 4.11** for axial and sagittal slices, considering different tissues. Negative linear trends were found between $M\gamma$ and $R2^*$ in coronal slices, though they were not significant. Conversely, significant strong linear correlations were found between $M\gamma$ and $R2^*$ in axial slices ($r=-0.97$, $P<0.01$) and in sagittal slices ($r=-0.95$, $P=0.01$). Moreover, $\gamma_{//}$ showed a strong negative correlation with $R2^*$ in axial slices ($r=-0.99$, $P=0.001$), whereas $A\gamma$ was positively correlated with $R2^*$ ($r=0.97$, $P<0.01$). No significant correlations were found neither for the γ_{\perp} nor for DTI-metrics.

Considering the morphology of WM tracts, both DTI-metrics and $R2^*$ seemed to be uncorrelated with the histological features considered, whereas among the AD-metrics γ_{\perp} and $A\gamma$ showed significant correlations with all the features. In particular, γ_{\perp} and $A\gamma$ decrease in parallel to axon diameters increase (γ_{\perp} : $r=-0.85$, $P<0.05$; $A\gamma$: $r=-0.94$; $P<0.05$) and axon diameter SD increase (γ_{\perp} : $r=-0.86$, $P<0.05$; $A\gamma$: $r=-0.94$; $P=0.005$), and increase proportionally to axon density (γ_{\perp} : $r=0.95$, $P<0.005$; $A\gamma$: $r=0.85$; $P<0.05$) and to the myelin fraction (γ_{\perp} : $r=0.90$, $P<0.05$; $A\gamma$: $r=0.88$; $P<0.05$), as shown in **Figures 4.12-4.13**.

Concerning the ANOVA tests, AD-metrics revealed to discriminate better than DTI-metrics and $T2^*$ in some regions, for example $\gamma_{//}$ and γ_{\perp} can discriminate ReST from STT (respectively, with $P<0.005$, $P<0.05$), whereas $T2^*$ and $R2^*$ cannot; AD-metrics (except for $M\gamma$) can discriminate dCST from VST ($\gamma_{//}$: $P<0.001$; γ_{\perp} : $P<0.05$; $A\gamma$: $P<0.0001$), instead $T2^*$ cannot. Finally, DTI-metrics was able to discriminate between RST and dCST better than AD-metrics and $R2^*$ ($D_{//}$: $P<0.0001$; MD: $P<0.05$). The other comparisons were not significant.

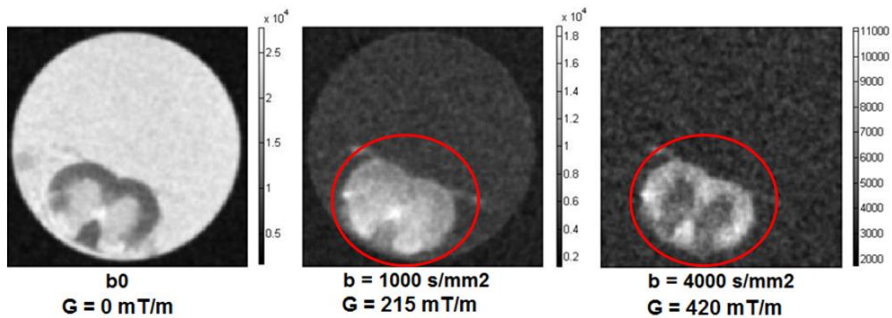


Figure 4.5 – Diffusion weighted images of an axial slice. The maps show the same slice of the spinal cord inside the capillary, with the dorsal part next to the capillary wall, acquired at increasing gradient strengths. The image on the left is acquired with an effective b -value of 154 s/mm^2 , because of the imaging gradients. The central canal containing CSF has an intensity comparable with the fluid surrounding the cord; the gray matter is slightly darker; the white matter is the most external tissue, and the darkest among the three. The intensity is indicated by the colorbar and expressed in arbitrary units.

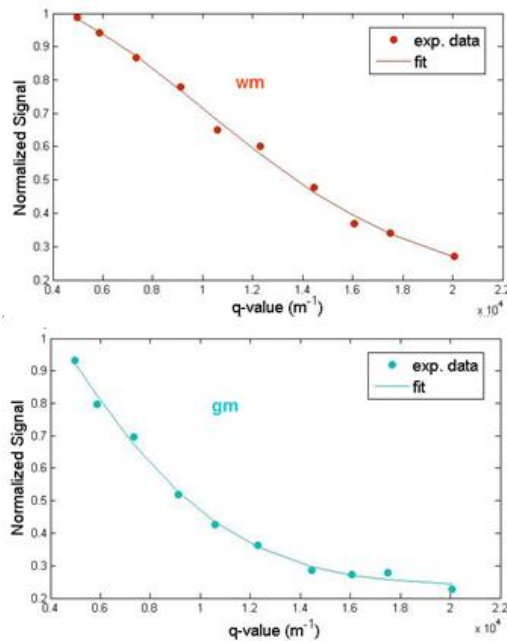


Figure 4.6 – Plot of the normalized DW-signal vs q -value for a selected voxel. The signal of DWIs was normalized with respect to the signal of the b_0 -image, for a selected voxel in white matter and gray matter of the same axial slice. The q -value is proportional to the diffusion gradient strength, and expressed in m^{-1} . Experimental values are indicated by dots, the theoretical fit by the continuous curve. Notice the different behavior of signal depending on the tissue chosen.

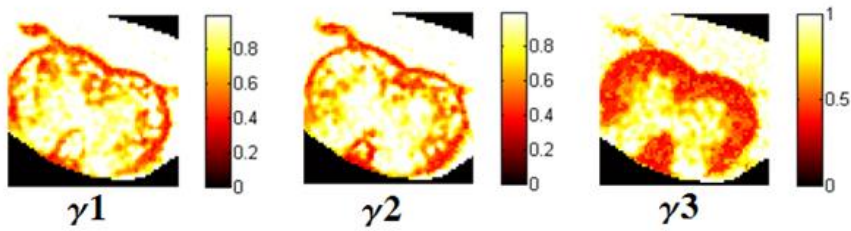


Figure 4.7 – Parametric maps of AD γ exponent. The γ stretched exponent extracted along 3 orthogonal directions is shown for an axial slice. From left to right, γ is acquired along x, y, and z direction, and ranges from 0 to 1 (the intensity scale is indicated by the colorbar).

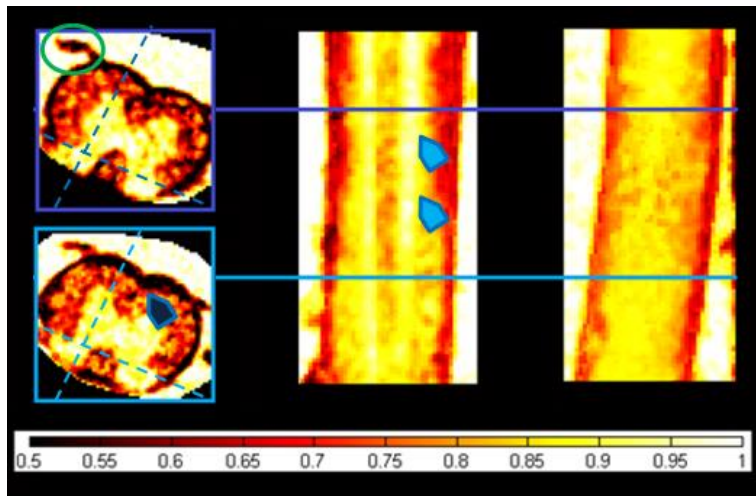


Figure 4.8 – Mean- γ ($M\gamma$) parametric maps of axial, coronal and sagittal slices. A complete set of axial, coronal and sagittal slices of the cervical section of the spinal cord is shown. Horizontal lines indicate the localization of the considered axial slices along the length of the spinal cord. Dashed lines indicate the corresponding coronal and sagittal cut in the axial slices. The contrast provided by γ highlights all the interfaces, especially the external lamina and the separation between gray and white matter (as indicated by the pointers). A spinal root is also clearly visible (green circle).

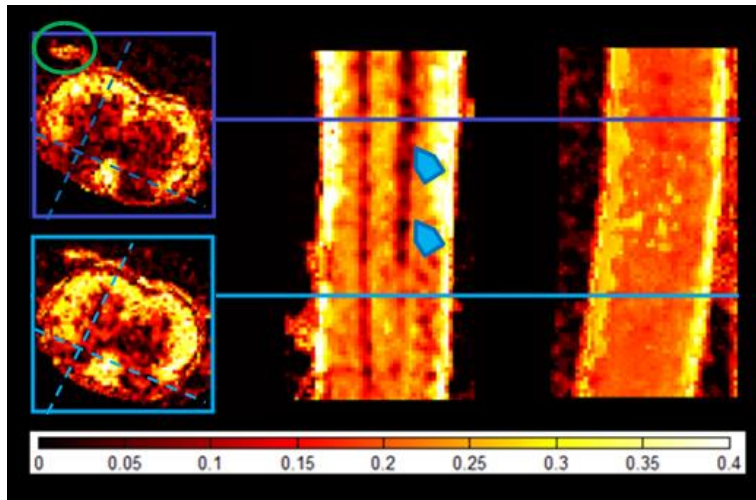


Figure 4.9 – γ -Anisotropy (A_γ) parametric maps of axial, coronal and sagittal slices. The contrast between white and gray matter is inverted with respect to M_γ . See caption of Fig.4.8 for further details.

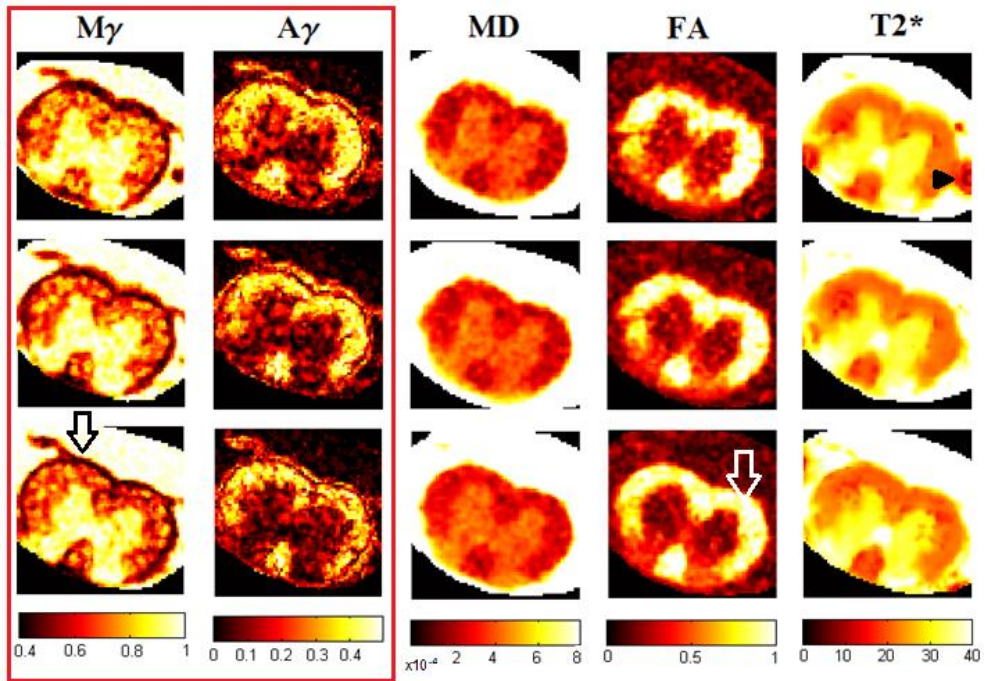


Figure 4.10 – Parametric maps of 3 successive axial slices. From left to right, AD-metrics, DTI-metrics and T2* parametric maps of axial slices are shown. The comparison between the new derived parameters and MD and FA reveals the potentiality of γ contrast: the spinal roots are clearly visible, as well as the lamina detaching the cord from the surrounding PBS solution (black arrow); the white matter appears grainy compared to the homogeneous pattern of FA map (white arrow). Notice that T2* is particularly sensitive to magnetic impurities, such as the presence of air bubbles (black arrowhead).

Pseudo super-diffusion of water in mouse spinal cord: in vitro study

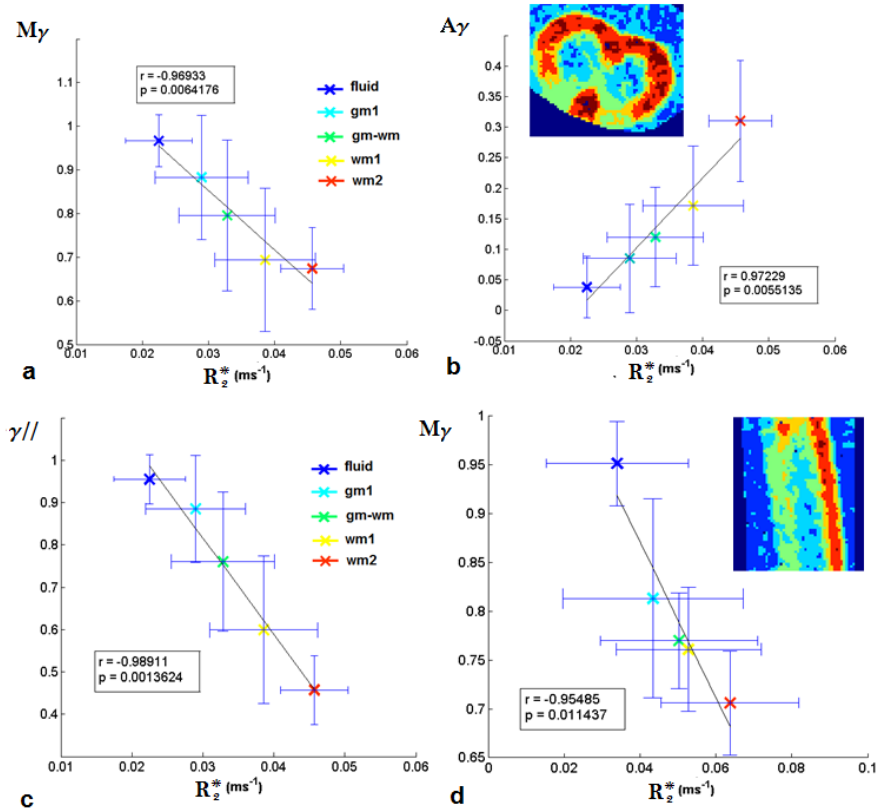


Figure 4.11 – Plots of AD-metrics as a function of R_2^* . AD-metrics (M_y , A_y and longitudinal or $\gamma//$) plotted as a function of R_2^* in axial slices (a-c) and in sagittal slices (d). The tissue was divided in different regions by applying thresholds on MD map. The distinct regions are listed in the legend and comprise: the medium surrounding the spinal cord (fluid), two ROIs in the white matter (wm1, wm2), one in the gray matter (gm1), and one at the interface (gm-wm). The Pearson's correlation coefficient is indicated in the box, together with the level of significance, p . The black line represents the linear fit.

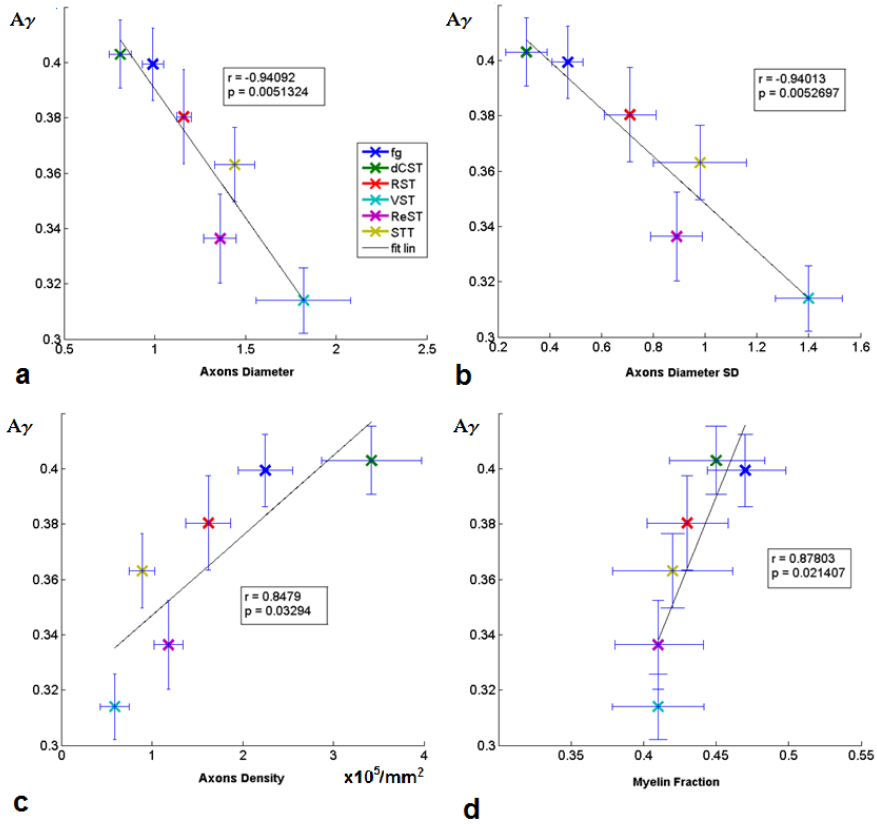


Figure 4.12 – γ -anisotropy (A_γ) vs histological characteristics of spinal cord tracts. The ROIs are listed in the legend. A_γ showed significant strong correlations with all the considered features: axons diameter (a), axons diameter SD (b), axons density (c) and myelin fraction (d). Axons diameter and their SD are measured in μm (not indicated in the figure). The vertical errorbars are standard error of the means (SEM). The Pearson's correlation coefficient is indicated in the box, together with the level of significance, p . The black line represents the linear fit.

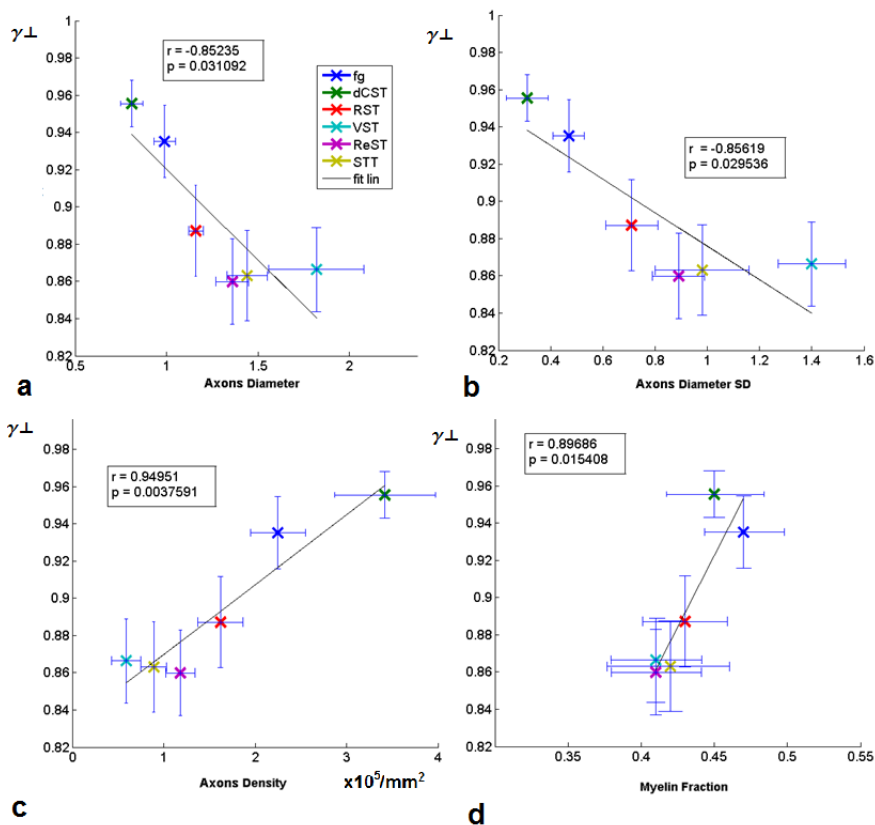


Figure 4.13 Radial- γ (γ_{\perp}) vs histological characteristics of spinal cord tracts. The ROIs are listed in the legend. γ_{\perp} showed significant strong correlations with all the considered features: axons diameter (a), axons diameter SD (b), axons density (c) and myelin fraction (d). Axons diameter and their SD are measured in μm (not indicated in the figure). The vertical errorbars are standard error of the means (SEM). The Pearson's correlation coefficient is indicated in the box, together with the level of significance, p . The black line represents the linear fit.

4.4 Discussion

The SNR for the highest b-value ($b=4000 \text{ s/mm}^2$) was 4 for the z-direction, 13 for the x-direction, 14 for the y-direction of acquisition. This suggests that the DW signal is more attenuated in the z-direction, that is along the main

orientation of axonal fibers, meaning that in this direction the diffusion is facilitated compared to the orthogonal plane.

The parametric maps reported in **Figures 4.8-4.9** and in **Figure 4.10** show that AD γ -exponent provides a new contrast, highlighting the interfaces between tissues, such as the external lamina of the spinal cord and the separation between WM and GM, as previously seen in inert phantoms and cerebral tissue at 9.4 T and in human brain at 3.0 T [20, 22, 26].

Significant strong linear correlations were found between AD-metrics and $R2^*$ in axial slices and sagittal slices (**Figure 4.11**), whereas no correlations were found for DTI-metrics. As explained in Chavhan et al., [72], the rate of relaxation is constituted by two terms, one influenced by spin-spin interactions, and the other proportional to external and internal magnetic field distortions. The internal field distortions are generated by local magnetic susceptibility differences, $\Delta\chi$. In WM these $\Delta\chi$ exist between water and tissue, and are typically in the order of 0.001-0.01 ppm. During its translational motion water experiences these inhomogeneities, mainly due to the presence of internodal myelin, astrocytes, glial cells. For example, as shown in Yablonskiy et al., the alternating proteo-lipid-protein in the presence of a static magnetic field determines susceptibility differences at the surface of myelin [40]. As suggested by Palombo et al. and by Capuani et al., the effect of $\Delta\chi$ impart an additional phase shift to the diffusing spins, resulting in a *pseudo*-superdiffusion process [20, 26]. The correlations between AD-metrics and $R2^*$ obtained in MSC suggests that γ is sensitive to $\Delta\chi$ in the order of 0.001-0.01 ppm, with the maximum effect on the axial- γ , probably because water from either inter-axonal space or intra-axonal space, diffusing in the preferential orientation parallel to the fibers, encounters several $\Delta\chi$ due to the presence of microglia (**Figure 4.14**).

Among the AD-metrics γ_{\perp} and A_{γ} showed significant correlations with all the histological features considered (**Figures 4.12-4.13**), whereas neither DTI-metrics nor $R2^*$ seemed to be correlated with the morphology. In particular, the radial diffusivity did not show significant correlations with axon diameters, as found by Schwartz et al. [74]. WM in the spinal cord is organized in bundles of fibers which have peculiar axonal size, axonal density and myelin fraction. In particular, γ_{\perp} and A_{γ} were inversely related to axon diameters (confirming results from Palombo et al. in polystyrene microbeads suspensions [26]), and proportional to axonal density in WM tracts. This is probably connected to the

second factor affecting γ -contrast, the multi-compartmentalization. The possible implications of these results could be in the investigation of alterations of WM structure, for example in demyelinating diseases such as Multiple Sclerosis (MS). This pathology occurs principally in the WM of the central nervous system. The changes in WM structure are believed to be the result of either damage and removal of highly aligned cellular structures or replacement of axonal fibers with amorphous cells, and are correlated with the clinical outcome of the patient. In general, MS patients present an increased amount of radial water diffusion and a decreased anisotropy of diffusion direction in the region of the lesions, in the surrounding of the lesion tissue, and in the remote normal appearing WM [9]. Together with myelin disruption, axonal injuries and axonal loss affecting long tracts (such as the CST) relate closely to functional disability. In MS axonal loss is widespread in both brain and spinal cord, and its extent is tract specific and size selective [78], meaning that the smallest fibers are first dismantled. According to the results obtained, an MS patient would present an alteration in the AD-metrics compatible with a decreased radial- γ , and a decreased γ -anisotropy in the region of the lesions. In fact, we know that myelin is attacked and thus myelin fraction is reduced, but the size and morphology of the surroundings (glial cells, astrocytes) also changes, determining further differences in magnetic susceptibility.

Finally, considering the results of ANOVA test, AD-metrics revealed to discriminate better than DTI-metrics and T2* ReST from STT and dCST from VST whereas did not differentiate dCST from RST, on the contrary of DTI-metrics. The discrimination of dCST from VST may be justified by the size of the compartments: in fact, dCST is characterized by small and densely packed axons, whereas VST present larger and more dispersed axons. It is difficult to find a justification to the lack of significance for the other comparisons, but considering that γ is influenced also by local $\Delta\chi$ there could be an interplay of these two effects limiting the discriminative power on the basis of intensity value averaged over a macroscopic voxel.

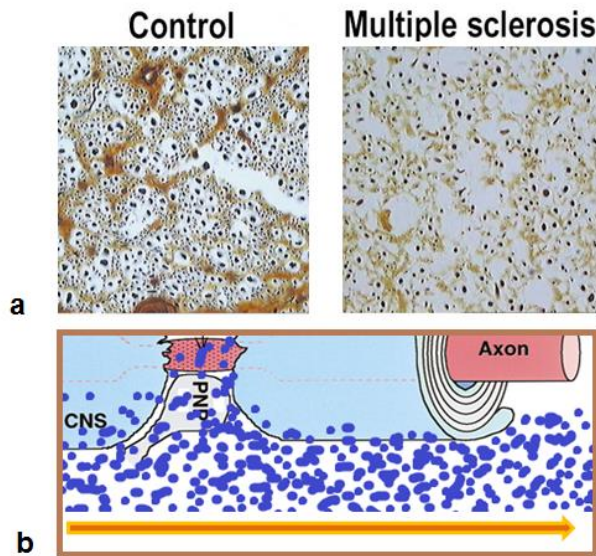


Figure 4.14 – Myelin in the central nervous system. a) Palmgren-stained transverse section of corticospinal tract axons in the spinal cord in a control case and in a case of multiple sclerosis. There is a selective reduction in the density of small fibers compared with large fibers, which are relatively preserved (reproduced from De Luca et al.'s paper [14]). b) Sketch representing the heterogeneity of the environment experienced by water in central nervous system (CNS): a myelinated axon is depicted, with a perinodal process. The preferential direction is indicated by the arrow (edited from Salzer et al.'s paper [79]).

4.5 Conclusions

In this work I used AD γ -imaging technique to investigate cervical sections of a fixed mouse spinal cord. In order to highlight the new additional information provided by AD approach I compared AD images with results obtained by using conventional DTI and relaxometry, and I investigated the relation between AD-metrics and the rate of relaxation $R2^*$, which is known to be influenced by magnetic susceptibility. Finally, I compared AD-metrics with histological characteristics of the considered white matter tracts.

The results of this investigation confirm previous results obtained performing

AD γ -imaging in phantoms, in excised human tissue and in human brain, concerning the contrast provided by pseudo-superdiffusion. In fact, parametric maps of γ seem to highlight the interfaces between compartments with distinct magnetic properties, and the significant correlation found between γ and local magnetic inhomogeneity in inert phantoms was here replicated, through the strong correlation between γ and $R2^*$.

Moreover, differently from previous works, the peculiar anisotropic structure of spinal cord investigated at high magnetic field (9.4 T) highlights new features of pseudo-superdiffusion analysis. Specifically, AD γ -imaging is potential able to detect microstructural information of white matter tracts in spinal cord more specific and complementary to those provided by DTI, and may be useful to monitor micrometric changes occurring in un-healthy neural tissue.

Chapter 5 *Pseudo* super-diffusion of water in healthy human brain: *in vivo* study

This Chapter describes how to perform AD γ -imaging in *in vivo* experiments on human brain, characterized by a complex geometry. Some details on specific data-processing accounting for diffusion-related image artifacts are provided. The γ -tensor is extracted and its scalar invariants are derived. The relation between *pseudo* super-diffusion of water and magnetic susceptibility differences between regions with myelinated axons variously oriented in space, and between regions with distinct iron content is here investigated. Finally the implications of these results in the field of MRI-diagnostics are discussed [41, 80].

5.1 Rationale

5.1.1 Anatomy of the human brain

In the previous Chapter we introduced the spinal cord, one of the two main constituents of the CNS. Here a brief description of human brain anatomy is provided. For more details we address the reader to the book by Saladin [81].

The brain is protected by three layers of tissue called meninges (dura mater, arachnoid, pia mater), and located inside the skull. It is composed of three main structures:

- the cerebrum, the largest part of the brain, is composed of right and left hemispheres. It performs higher functions like interpreting touch, vision and

hearing, as well as speech, reasoning, emotions, learning, and fine control of movement;

- the cerebellum, located under the cerebrum, plays an important role in the coordination of muscle movements, and the maintenance of posture and balance;

- the brainstem includes the midbrain, pons, and medulla, and acts as a relay center connecting the cerebrum and cerebellum to the spinal cord. It performs many automatic functions such as breathing, heart rate, body temperature, wake and sleep cycles, digestion, sneezing, coughing, vomiting, and swallowing.

Considering a sagittal plane the cerebrum can be divided in two parts, the right and left hemispheres, joined by a bundle of fibers called the *corpus callosum* that delivers messages from one side to the other.

The cerebral hemispheres have distinct fissures, which divide the brain into lobes. Each hemisphere has 4 lobes: frontal, temporal, parietal, and occipital. Each lobe may be divided, once again, into areas that serve very specific functions. It's important to understand that each lobe of the brain does not function alone. There are very complex relationships between the lobes of the brain and between the right and left hemispheres.

Messages within the brain are carried along pathways. Messages can travel from one gyrus to another, from one lobe to another, from one side of the brain to the other, and to structures found deep in the brain, which are included in the GM.

The surface of the cerebrum has a folded appearance called the cortex. The cortex contains about 70% of the 100 billion nerve cells. Their bodies make up the gray matter (GM). Beneath the cortex are long connecting fibers between neurons, called axons, which make up the white matter (WM). Other than WM and GM the brain has hollow fluid-filled cavities called ventricles. Inside the ventricles the cerebrospinal fluid (CSF) is poured by a ribbon-like structure called the choroid plexus. The CSF flows within and around the brain and spinal cord to help cushion it from injury. This circulating fluid is constantly being absorbed and replenished.

5.1.1.1 White Matter (WM) fibers

The WM fibers of the cerebrum can be grouped in 3 main categories [82]: commissural fibers, association fibers, and projection fibers. The corpus callosum is a commissural fiber, comprised of three regions with characteristic axon diameter distributions and axonal density [83]: the genu (gcc), the body (bcc) and the splenium (scc), going from the frontal lobe to the occipital lobe. An example of association fibers is provided by the sagittal stratum (ss), a sheet-like sagittal structure formed by the merging of fibers from the longitudinal fasciculus and reticulo-lenticular part of the internal capsule. Among the projection fibers we list here: the corona radiata, divided into anterior (acr), superior (scr) and posterior (pcr) regions; the posterior thalamic radiations (ptr) (thalamo-cortical and cortico-thalamic fibers); the anterior (alic) and posterior (plic) limb of the internal capsule, formed essentially by the anterior and superior thalamic radiations; the cerebral peduncle (cp) where long corticofugal pathways are concentrated, including the corticospinal, corticopontine, and corticobulbar tracts.

5.1.1.2 Subcortical Gray Matter (GM)

Here we mention some of the most important structures belonging to the subcortical GM [81]. The thalamus (thal) serves as a relay station for almost all information that comes and goes to the cortex, and plays a role in pain sensation, attention, alertness and memory. The limbic system, the center of emotions, learning, and memory, comprising the cingulate gyri, hypothalamus, amygdala and hippocampus. In particular, the hippocampus (hipp) plays an important role in the formation of memory and spatial orientation. The basal ganglia, including the caudate nucleus, putamen and globus pallidus, work with the cerebellum to coordinate fine motions, such as fingertip movements. In particular, the caudate nucleus (caud) forwards to pallidus the inputs coming from the cerebral cortex and from the limbic system; the globus pallidus (or pallidum, pall) delivers messages to thal and controls the posture and the manual dexterity; the putamen (put) regulates the movement and the motor learning.

5.1.2 Magnetic susceptibility differences in the brain and their evaluation

The magnetic susceptibility χ_m quantifies the degree of attraction/repulsion experienced by a material when it is inserted in a magnetic field, and it corresponds to the ratio between the magnetization (M) and the magnetic field itself. The volumetric magnetic susceptibility is thus dimensionless, and considering the substances treated here (nervous tissues) is in the order of 10^{-6} , and hence expressed conveniently in ppm. Considering that we used MRI, it is important to stress that the magnetization M depends on the orientation of the sample with respect to the static field, and may emerge in other directions. Generally in the field of MRI instead of a single value of χ_m , a tensor of rank 2 is considered, $\overrightarrow{\chi_m}$, where the ij-component is given by $\chi_{ij} = \frac{M_i}{B_j}$, representing the magnetization arising in i-direction, because of the magnetic field acting in the j-direction. According to the tendency that non-ferromagnetic materials show in attracting or repelling the magnetic field, the materials are divided into diamagnetic and paramagnetic, as seen in Par. 1.1.2. The diamagnetic materials have $\chi_m < 0$ (such as the water molecule, with $\chi_{H_2O} \cong -9.05 \text{ ppm}$) will be repelled by the magnetic field, whereas the paramagnetic materials with $\chi_m > 0$ (such as aluminum, with $\chi_{Al} \cong 22 \text{ ppm}$) will be attracted.

In general, microstructural tissue compartments have unique magnetic susceptibilities (henceforth indicated simply by χ) driven by their chemical compositions and molecular arrangements. In the presence of \mathbf{B}_0 , differences in magnetic susceptibility between adjacent compartments generate different amount of magnetization due to the relation: $M = \chi B_0$. As a consequence local magnetic inhomogeneity generated by $\Delta\chi B_0$ are found at the interface between different tissues. χ inhomogeneity determines field shifts, or distortions (ΔB_0), which cause frequency shifts in the Larmor frequency ($\Delta f = \Delta\omega/2\pi$).

In the brain tissue χ inhomogeneity arises from differences in non-heme iron²⁰ content and iron-storage proteins and from various degrees of myelin density and orientation. The contrast within distinct GM regions is motivated mainly by intrinsic differences in unbound iron concentrations ([Fe]). The subcortical GM presents intrinsically higher [Fe] compared to the cortical GM. Furthermore,

²⁰ With the attribute non-heme we refer to free dispersed iron, that is iron not bound to transport or storage proteins.

iron accumulates preferentially in some subcortical GM structures, such as the thalamus, substantia nigra, the basal ganglia and the hippocampus. It is important to underline that the contrast between WM and GM is not originated by significant differences in [Fe]: in fact, both the concentration of non-heme and heme iron (especially bound to ferritin) are comparable in WM and cortical GM. Furthermore, the contrast persists even after iron extraction, as shown by some studies on mouse brains [84]. The main source of contrast in WM lies in the presence of myelin fibers. In fact, the contrast between WM and GM is considerably reduced in case of demyelination. The χ inhomogeneity in WM is detectable at a microscopic [40] and macroscopic level, considering respectively the alternation of proteo-lipid-protein layers in the myelin sheath and the presence of elongated compartments. In fact, the frequency shift measured through a GRE sequence depends on the orientation angle of the myelinated fiber with respect to the magnetic field, according to the relation [39]:

$$\frac{\Delta f}{f_0} = \frac{4}{3}\pi\chi_{iso} + 2\pi\chi_L \sin^2 \Phi \quad (5.1)$$

where χ_{iso} is a contribution to tissue magnetic susceptibility from isotropically distributed components of cellular structures (free floating organelles, proteins, and lipids), χ_L is a contribution to tissue magnetic susceptibility from longitudinally arranged components (neurofilaments and myelin sheath) and Φ is the angle between direction of the external magnetic field B_0 and orientation of neuronal fibers.

The quantification of magnetic susceptibility differences ($\Delta\chi$) due to various orientations in white matter is an issue well addressed by a technique called Susceptibility Tensor Imaging (STI) that quantifies the amount of magnetic susceptibility anisotropy, due to the micro-architecture and chemical arrangement of the neural tissue being probed [85, 86]. However, in order to compute the susceptibility tensor it is necessary to acquire the signal along at least six different orientations of the sample with respect to the static magnetic field B_0 [86]. This represents an intrinsic limitation of STI imaging, since the sample rotation is hardly practicable in the case of clinical applications in humans.

The assessment of magnetic susceptibility inhomogeneity due to iron in the human brain is of paramount importance in the field of MRI diagnostics. Iron (as well as other redox metals, see [37]) plays a key role in the maintenance of

brain homeostasis. On the other hand, an inappropriate amount or availability of iron causes the onset of toxic reactions that produces free radicals. Indeed, an abnormal amount of iron and iron-storage proteins was found in Parkinson's disease [17], Alzheimer's disease [37], Multiple Sclerosis [87, 88], and other disabling disorders as migraine and chronic daily headache [89]. The evaluation of iron content *in vivo* is currently performed through the use of Quantitative Susceptibility Mapping methods (QSM) [90], for which a strong correlation between chemically determined iron concentration and bulk magnetic susceptibility was shown in deep gray matter structures. On the other hand, this technique is not as much accurate in the white matter, where the contribution from diamagnetic myelinated fibers causes misinterpretation of data [91]. Furthermore, there are some critical points in the use of QSM. QSM provides susceptibility maps from the background corrected phase images, using complex algorithms that present intrinsic problems (see Discussion for further details).

Motivated by previous results obtained *in vitro*, I investigated here the dependence of the AD- γ parameter quantifying *pseudo*-superdiffusion of water, on local $\Delta\chi$ driven by magnetic field inhomogeneity in human brains.

5.2 Materials and Methods

5.2.1 Data acquisition

Eight healthy volunteers (4 men, 4 women; mean age +/- standard deviation [SD] = 25 +/- 1 years) participated in this study²¹, after providing informed written consent, according to the national laws and to the local ethics committee guidelines. None of the subjects had a history of stroke or head injury, nor of any other neurological or psychiatric disease. The volunteers underwent MRI examination using a 3.0 T Siemens Magnetom Allegra (Siemens Medical Solutions, Erlangen, Germany), with a circularly polarized transmit-receive coil. The maximum gradient strength was 40 mT/m with a maximum slew rate of 400 T/m/s. The same MRI protocol was applied to all the subjects,

²¹ The study was approved by the Scientific Ethics Committee of Santa Lucia Foundation (Rome, Italy).

including T_2^* -weighted images (T_2^* WIs), and Diffusion Tensor Imaging (DTI) scanning. Particular care was taken to center the subject in the head coil and to restrain the subject's movements with cushions and adhesive medical tape.

T_2^* WIs were acquired using an Echo Planar Imaging sequence (EPI) with TR=5000 ms, flip-angle=90°, 4 different TEs=(10, 20, 35, 55)ms, matrix size=128x128, number of axial slices=32; slice thickness=3 mm, in-plane resolution=1.8x1.8mm²; Diffusion-Weighted Double Spin-Echo-Echo Planar Imaging (DW DSE-EPI) was acquired with TR/TE=6400ms/107ms; $\Delta/\delta=72\text{ms}/35\text{ms}$, and with the same geometry of T_2^* WIs. DW-Images (DWIs) were collected by using Diffusion-sensitizing gradients along 20 non-collinear directions sampled on a half sphere (see **Figure 5.1**) at 14 different b-values (100, 200, 300, 400, 500, 700, 800, 1000, 1500, 2000, 2500, 3000, 4000, 5000) s/mm² plus the b=0 (b₀) image with no diffusion weighting. The b-values were changed by varying the diffusion gradient strength and keeping Δ and δ constant. The number of sample averages (NSA) was 2 for each b-value, and the total acquisition time for the DW DSE-EPI protocol (applied without the use of parallel imaging) was approximately 52 minutes. An anterior-posterior phase encoding direction was used for all the scans. The axial slice package was positioned parallel to the anterior-posterior commissure axis and perpendicular to the mid-sagittal plane.

5.2.2 Data analysis

The pipeline of data acquisition, pre-processing and analysis is provided in **Figure 5.2**. The pre-processing of data was performed with the use of FMRIB Software Library, v5.0 (FSL, [75]). The T_2^* WIs were realigned to the image acquired with TE=10ms, in order to correct for head movements, via a 6 degrees of freedom (DOF) transformation, using the FSL linear image registration tool (FLIRT) [92]. The T_2^* WI acquired with TE=10ms was then registered to the b₀-image, via a 12 DOF affine transformation with Normalized-Correlation cost function and tri-linear interpolation. Finally, the combination of the two transformation matrices was applied to all T_2^* WIs. The DWIs were realigned with respect to the b₀ and corrected for subjects' movements and eddy-current induced distortions adopting the b₀-image as a reference image.

5.2.2.1 Correction of eddy current induced distortions

While the eddy current correction is not necessary for in vitro experiments, because the inductive losses due to eddy currents are negligible for small samples, for large samples as the human head it is a mandatory step. In fact in this case the losses due to eddy currents dominate the resistance R of the coils that causes thermal noise [46], and much more noise is provoked by the induced distortions. The eddy currents are generated by the interference with conductive materials or most of all owing to the rapid switching of intense diffusion gradients. These electric induced currents possess an inductance, thus generate magnetic field that distort the main magnetic field and the diffusion gradients. The distortions effect is more evident with the use of strong diffusion gradients (or high b -values). Consequently, the DWIs appear distorted, with image scaling artifacts (such as compression), from gradients in phase-encode direction, global position shifts (from shifts in the B_0 field), or shearing artifacts (from induced gradients in the frequency-encoding direction).

The correction for eddy current distortions is a delicate passage in the analysis of DW-data. In previous works concerning the use of AD- γ imaging in the human brain, De Santis et al. and Palombo et al. [22, 29] addressed to this issue by using in FSL the function *eddy_correct*. The algorithm underneath this function allows to correct for eddy currents but in a generic way, since it is automated and does not consider neither the used b -values nor the chosen set of gradient directions.

Here I implemented this step of data analysis by using the *EDDY* tool, that, according to recent results, has shown better performances compared to the FSL's earlier *eddy_correct* function [93]. *EDDY* tool requires in input the set of gradient directions, the b -values and some acquisition parameters that take into account the acquisition direction and verse (A/P or P/A, R/L or L/R, S/I or I/S), the used TE, the EPI factor, the number of slices and the diffusion gradient duration. The procedure is a bit time-consuming with respect to *eddy_correct*, but it is an acceptable cost to pay in the pre-processing step, since it reduces significantly image artifacts even at the highest b -value used. A better correction would be obtained by performing the preliminary step of TOPUP, which starting from two b_0 -images acquired in opposite directions is able to reconstruct the map of magnetic field inhomogeneity (for example due to the presence of strong magnetic susceptibility differences at the interface between water and air in the frontal sinus). Owing to the lack of these acquisitions I

skipped this preliminary step, obtaining however a sensible reduction of eddy current distortions.

5.2.2.2 Extraction of parametric maps

The DTI maps were extracted using all the DWIs acquired up to $b=1500 \text{ s/mm}^2$ with DTIFIT tool, which returns the maps of eigenvalues ($\lambda_1, \lambda_2, \lambda_3$, with $\lambda_1 > \lambda_2 > \lambda_3$), eigenvectors ($\mathbf{v}_1, \mathbf{v}_2, \mathbf{v}_3$), Mean Diffusivity (MD) and Fractional Anisotropy (FA). The axial ($D_{//}$) and radial (D_{\perp}), diffusivities were computed as follows: $D_{//} = \lambda_1$, $D_{\perp} = (\lambda_2 + \lambda_3)/2$. The T2*WIs and the DWIs were filtered using pixel-wise adaptive Wiener filtering (window size of 2x2 pixels) in MATLAB R2012b (MATLAB Release 2012b, The MathWorks, Inc., Natick, Massachusetts, United States). Custom-made MATLAB scripts were employed to extract R_2^* from the set of T2*WIs with a linear least-square fitting, and to extract the γ -exponents ($\gamma_1, \gamma_2, \gamma_3$, with $\gamma_1 > \gamma_2 > \gamma_3$) projected along the three axes of DTI-reference frame (DTI-rf) [22] from the set of DWIs acquired up to $b=5000 \text{ s/mm}^2$, using trust-region-reflective least square algorithm for minimization with a non-linear fitting procedure and parallel computing [94]. The theoretical model used is an extension of the procedure adopted for the MSC experiment. Differently from the in vitro investigation, where the estimation of an apparent γ along 3 orthogonal directions was acceptable considering the simple geometry and the cylindrical symmetry, in the case of human brain we need to estimate a whole tensor. I adopted here the same approximation used in De Santis et al. [22], that consists in considering the scalar products between the DTI eigenvectors and the gradient vectors. This procedure is equivalent to project the $\vec{\gamma}$ components in the DTI-reference frame. The theoretical model used in the fitting procedure is the following:

$$\frac{S(b)_i}{S_0} = A \exp \left[-D_{gen_1} (b(\mathbf{v}_1 \cdot \mathbf{g}_i))^{\gamma_1} - D_{gen_2} (b(\mathbf{v}_2 \cdot \mathbf{g}_i))^{\gamma_2} - D_{gen_3} (b(\mathbf{v}_3 \cdot \mathbf{g}_i))^{\gamma_3} \right] + c \quad (5.2)$$

for the normalized DW signal acquired along the i-direction, as a function of b-values. The AD occurring in the i-direction is considered as the linear combination of the AD occurring along 3 orthogonal directions, representing the main AD axes. Correspondingly 3 values of γ and the generalized diffusion constant Dgen are obtained as outputs on a voxel by voxel basis. The c constant

takes into account the noise floor, thus the fact that for infinite b-values the signal attenuates to a non zero value.

The choice of projecting the stretched γ -exponents along the axes of DTI-rf is based on the assumption that, to a first approximation, the AD and Gaussian diffusion share the same rotationally invariant reference frame [22]. From a computational point of view, this assumption corresponds to inserting the computed diffusion eigenvectors as fixed inputs within the theoretical expression used to fit the experimental DW-data. The algorithm used in the fitting procedure requires an initialization of the parameters to be estimated. In order to test for the stability of the fit, we performed the fit by initializing the γ -exponents to 1.0, and to 0.75. The differences found in the estimated γ -exponents were in the order of 10^{-4} , thus we proved that the fit was quite stable. Therefore, we initialized the stretched exponents to 1.0, since this is the value corresponding to Gaussian diffusion, and we expected to compute slightly inferior values in the analyzed tissue [20]. Once estimated the projected γ -exponents, the following AD-parameters were computed: mean- γ ($M\gamma = \frac{\gamma_1 + \gamma_2 + \gamma_3}{3}$), axial- γ ($\gamma_{//} = \gamma_1$), radial- γ ($\gamma_{\perp} = \frac{\gamma_2 + \gamma_3}{2}$), γ -anisotropy ($A\gamma = \sqrt{\frac{3[(\gamma_1 - M\gamma)^2 + (\gamma_2 - M\gamma)^2 + (\gamma_3 - M\gamma)^2]}{2(\gamma_1^2 + \gamma_2^2 + \gamma_3^2)}}$), where $\gamma_{//}$ represented the projection of the anomalous exponent in the direction described by the first eigenvector \mathbf{v}_1 of the Gaussian diffusion tensor, whereas γ_{\perp} was derived by an average of the other two orthogonal projections. Parametric maps of each subject were produced for DTI-metrics, AD-metrics and R_2^* .

5.2.2.3 Signal to Noise Ratio and its effect on AD- γ estimation

Low Signal to Noise Ratio (SNR) of DWIs acquired at higher b-values is an obvious drawback for AD techniques. In fact, the higher the b-value, the higher the signal attenuation and the stronger the effect of eddy current distortions, that could be not accounted for completely with the application of EDDY tool without TOPUP. SNR of each DW image acquired at a certain b-value was assessed and the consequences of a low SNR on the gamma parameter estimation were investigated in two distinct ways.

In order to estimate the SNR of DWIs, the method recently proposed by Descoteaux and Jones was used [77, 95]. The signal was estimated in the

splenium of the corpus callosum, and the background noise was estimated considering an area placed outside the brain, then the SNR was computed taking the ratio between the mean of the signal and the SD of the noise. SNR was evaluated for each b-value and diffusion gradient direction. The splenium of the corpus callosum was chosen because of its stressed directionality, which is left-right oriented with respect to the laboratory frame. Since we expect the most attenuated DW signal along the direction of the facilitated diffusion, that is along the main axonal direction, the SNR in the left-right (x) direction represents a good indication of the quality of the DW-data [77, 95]. The SNR of the splenium of the corpus callosum could be considered as representative for the SNR in WM. An area placed in the right thalamus, was considered to estimate the SNR in the GM, operating similarly.

The effect of DWIs SNR on AD γ estimation was investigated extrapolating a relation between γ and the SNR of the b0-image on the basis of the study by Jones and Basser [96]. Approximating the theoretical model proposed in (5.1) to the expression $S(b) = S_0 e^{-b^\gamma D(b)}$ the following expression is derived:

$$b_{max}^\gamma = \frac{\ln\left(\frac{\sqrt{2}}{\sqrt{\pi}} SNR_0\right)}{D(b)_{max}} \quad (5.3)$$

Where SNR_0 is the signal to noise ratio of b0 image and $D(b)_{max}$ is the maximum reliable value of the generalized effective diffusion constant D_{eff} obtainable by using b_{max} . The γ values extracted from the splenium of the corpus callosum and the thalamus and the experimental SNR_0 obtained from DW images were used to calculate all the $D(b)_{max}$ associated to each b-value. Then by inverting relation (5.3) theoretical γ -values were obtained, for a given simulated SNR_0 , and compared with the experimental values.

Moreover, the effect of DWIs SNR on AD γ estimation was investigated by adding Rician²² Noise to the DWIs. The simulated Rician Noise was added to the DWIs with the use of MATLAB, then the script for γ extraction was run using the altered DWIs that were Gaussian filtered, as explained before. The procedure was repeated for increasing values of s, or the scale parameter, indicating increasing width of Rician distribution or, in other terms, exasperating noise. The behavior of SNR and Contrast to Noise Ratio (CNR) vs s

²² In probability theory, the Rice distribution, or Rician distribution is the probability distribution of the magnitude of a circular bivariate normal random variable with potentially non-zero mean.

was also examined considering two WM ROIs, one with orthogonal fibers one with parallel fibers with respect to \mathbf{B}_0 .

Finally, since AD- γ imaging technique requires the use of wide range of b-values, which are known to be affected by low SNR, with the aim to investigate the commitment between the choice of b-values and the contrast of γ -maps M_γ in of different brain regions was evaluated considering different b-values ranges, spanning from 0-400 s/mm², (i.e. b=0, 100, 200, 300, 400 s/mm²), to 0-5000 s/mm² (i.e. b=0, 100, 200, 300, 400, 500, 700, 800, 1000, 1500, 2000, 2500, 3000, 4000, 5000 s/mm²). Specifically, the number of data points considered in the fit procedure, corresponding to the acquired DWIs volumes, varies as follows: 5 for the range 0-400 s/mm²; 8 for the range 0-800 s/mm²; 9 for the range 0-1000 s/mm²; 10 for the range 0-1500 s/mm²; 11 for the range 0-2000 s/mm²; 12 for the range 0-2500 s/mm²; 13 for the range 0-3000 s/mm²; 14 for the range 0-4000 s/mm²; 15 for the range 0-5000 s/mm².

5.2.2.4 Automated selection of WM and GM regions and fibers orientation estimation

In **Figure 5.3** the selected Regions of Interest (ROIs) in GM and WM are shown for a representative axial, coronal and sagittal slice. The ROIs were extracted for each slice using a hybrid approach: standard WM and GM atlases were projected onto the subjects' individual space, and the resulting masks of ROIs were eventually eroded to avoid partial volume effects. The FA individual maps were normalized to the FMRIB58_FA standard space template, using a full-affine transformation. The calculated transformation matrix was subsequently inverted in order to map the ICBM DTI-81 Atlas [82] into native space of individual subjects, as described in Cherubini et al. [97]. Similarly, the Harvard-Oxford subcortical Atlas [98] was normalized to MD maps with a 12 DOF affine transformation, returning personalized GM atlases.

Finally, the ROIs selection was automatically performed by a customized MATLAB script: the cerebral-spinal fluid (CSF) and the ventricles were excluded by masking the R_2^* maps, zeroing all the pixels with R_2^* lower than 8 s⁻¹ and higher than 80 s⁻¹; the resulting mask was combined with a mask obtained by the intersection of two thresholds: $FA \geq 0.6$ and $v_1 \geq 0.8$, in order to select coherent WM fibers and avoiding partial volume effects at the contours of the WM-ROIs. The approximation of considering parallel axons in

each fiber bundle, neglecting the orientation dispersion, was reasonable considering the threshold applied to both FA and v_1 , which allowed to select coherent fibers bundles.

If we consider a reference frame where the main direction of axonal fiber determines the x-direction, we might expect that the v_1 , representing the direction of preferential motion, adheres with the axon orientation. Sometimes this is not verified, because of the unavoidable tilting of the axonal frame with respect to \mathbf{B}_0 . Thus a threshold of $v_1 \geq 0.8$ would be so high that only few voxels of WM ROIs would be considered. For this reason the v_1 threshold was corrected for the orientation Φ of WM fibers with respect to the \mathbf{B}_0 field.

The orientation angle Φ was estimated in a voxel considering the components

of \mathbf{v}_1 as follows: $\Phi^* = \tan^{-1}\left(\frac{V_{1z}}{\sqrt{V_{1x}^2 + V_{1y}^2}}\right)$, and then computing $\Phi = \frac{\pi}{2} - \Phi^*$.

The effect of the employed v_1 threshold on the correlation between AD-metrics and R_2^* in the WM was investigated and proved that, within certain limits, provided that the number of under-threshold voxels is sufficient, the significance of the linear correlation is barely affected (see Discussion for further details). Finally, ROIs masks were eroded by 2 pixels to avoid partial volume effects or contamination from adjacent structures.

Among the selected GM ROIs I focused on the main components of the basal ganglia (putamen, *put*; globus pallidus, or pallidum, *pall*; caudate nucleus, *caud*), and the hippocampus (*hipp*), located in the medial temporal lobe, because of their high iron content with respect to the surrounding tissue [99].

Among the selected WM ROIs I considered bundles of fibers parallel and orthogonal to \mathbf{B}_0 . The WM tracts perpendicular to \mathbf{B}_0 included (**Figure 5.3**) commissural fibers such as the genu, body and splenium of the corpus callosum (*gcc*, *bcc*, *scc*, respectively), oriented in the left-right direction, association fibers such as the sagittal stratum (*ss*) and the posterior thalamic radiations (*ptr*), and projection fibers such as the cerebral peduncle (*cp*), the anterior corona radiata (*acr*), oriented in anterior-posterior direction; the WM tracts parallel to \mathbf{B}_0 included the posterior limb of the internal capsule (*plic*), oriented in superior-inferior direction.

5.2.2.5 Iron content and magnetic susceptibility of selected ROIs

In order to test the reliability of the acquired R_2^* , the correlation between R_2^* and iron content was tested in GM ROIs. Non-heme iron concentrations ($[Fe]$) of the basal ganglia (*caud*, *put*, *pall*) and thalamus (*thal*) were taken from the pivotal study by Hallgren and Sourander [99].

Magnetic susceptibility values of distinct WM and GM ROIs were taken from the work of W. Li et al. [100], for WM ROIs of *gcc*, *scc*, *ss* and GM ROIs of *caud*, *put*, *pall*. In the cited work QSM is performed at 3.0 T, in a cohort of healthy volunteers. Here the magnetic susceptibility χ -values are referred to the χ of CSF. Therefore they are negative for diamagnetic WM ROIs and positive for the paramagnetic GM ROIs.

5.3 Statistical analysis

DTI-metrics, AD-metrics and R_2^* were evaluated in each selected ROI, averaging over the pool of voxels, and computing the relative SD. Then mean values +/- SEM (standard error of the mean) were estimated; the presence of significant differences among means was investigated by using the Analysis of Variance (ANOVA), verifying the homogeneity of variances with a Levene's test. Bonferroni's correction was applied in the case of homogeneous variances, while Games-Howell correction was used in the case of non-homogeneous variances [101]. The correlation between diffusion metrics and χ -metrics and between diffusion metrics and R_2^* was assessed by means of Pearson's correlation test. P-values < 0.05 were considered statistically significant.

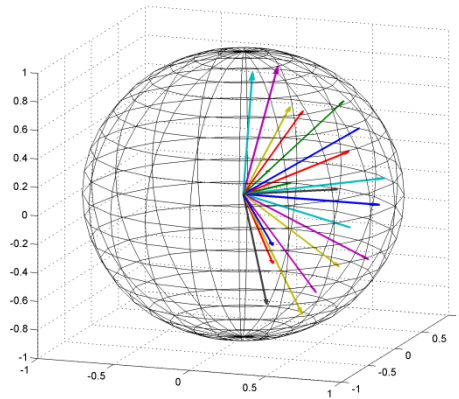


Figure 5.1 – Gradient vectors scheme. 3D representation of the orientations of diffusion sensitizing gradients. The set of gradient directions is spread homogeneously over a hemisphere. The 3D plot was realized with MATLAB R2012b.

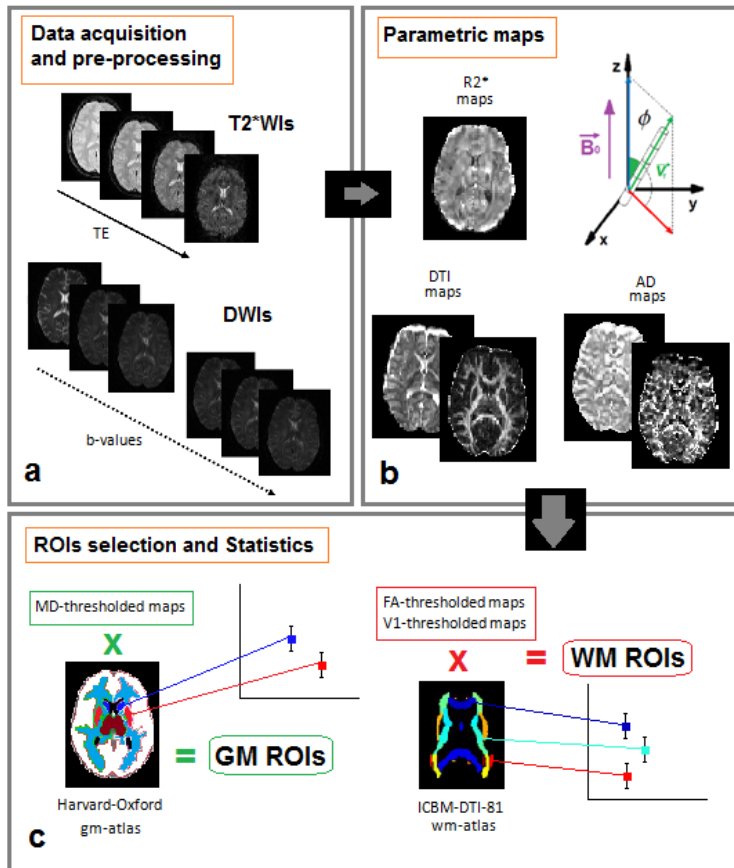


Figure 5.2 – Flow-chart illustrating the methods. a) Realignment of T2*WIs and DWIs, eddy current correction, coregistration of T2*WIs to b_0 and the extraction of Diffusion Tensor Imaging (DTI)-maps were performed with FSL (v5.0). b) The orientation of WM fibers Φ with respect to the magnetic field was estimated using trigonometric relations. R2*-maps and AD-maps were computed with MATLAB scripts (MATLAB R2012b), using non-linear least-square algorithms. AD-metrics (mean- γ , $M\gamma$, axial- γ , $\gamma//$, radial- γ , γ_{\perp} , γ -anisotropy, $A\gamma$) were computed with formulas analogous to DTI-metrics (MD=Mean Diffusivity, FA=Fractional Anisotropy). c) A composition of thresholds on MD, FA and V1 maps and the use of standard atlases was adopted for WM and GM ROIs selection.

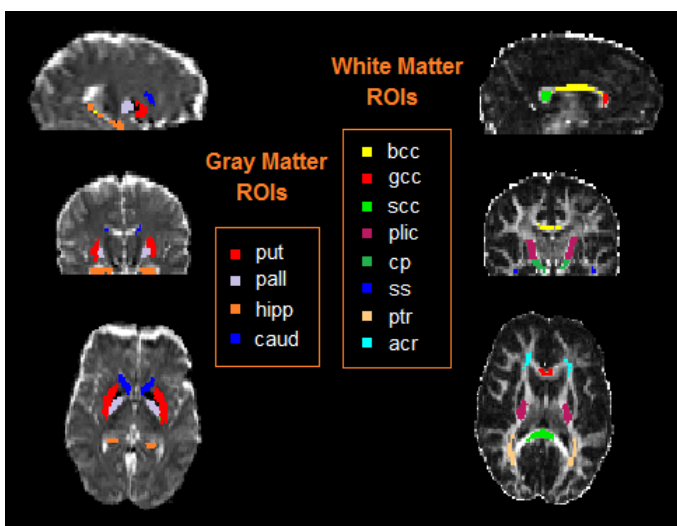


Figure 5.3 - Gray Matter (GM) and White Matter (WM) selected ROIs. a) Superimposition of GM ROIs selected from the Harvard-Oxford sub-cortical atlas adapted to the subject's reference space over the respective MD map and of WM ROIs selected from the ICBM-DTI-81 atlas adapted to the individual subject's reference space over the respective FA map. A representative subject in the cohort was chosen for the sake of clarity (put=putamen; pall=pallidum; hipp=hippocampus; caud=caudate nuclei; bcc=body of the corpus callosum; gcc=genu of the corpus callosum; scc=splenium of the corpus callosum; plic=posterior limb of the internal capsule; cp=cerebral peduncle; ss=sagittal stratum; ptr=posterior thalamic radiations; acr=anterior corona radiata).

5.4 Results

5.4.1 Signal to Noise Ratio and its effect on AD γ estimation

The SNR of DWIs computed in the splenium and in the thalamus for each b-value and direction of acquisition is shown in **Figure 5.4**. The highest SNR is obtained in the b0-image. The SNR in the splenium of the corpus callosum was approximately 32 in the b0-image, 18 in b=1000 s/mm², and 5 in b=5000 s/mm² images, considering an average value over all 20 gradient directions. The lowest SNR in each b-value is obtained in correspondence of the left-right or x-direction for the splenium (**Figure 5.4b**). In fact the splenium is left-right oriented, and in the x-direction the diffusion is more facilitated and consequently, the signal is more attenuated. Specifically, in the x-direction at

$b=1500$ s/mm² SNR was 6.5, while in the x-direction at $b=5000$ s/mm² it was 3.2. When considering the GM tissue, the SNR of a ROI placed in the right thalamus in the b_0 -image was approximately 44. It was approximately 15 in $b=1000$ s/mm², and 4.5 in $b=5000$ s/mm² images, considering an average value over the 20 gradient directions.

In **Figure 5.5**, γ -values from the splenium of the corpus callosum and the thalamus of a single subject are displayed as a function of the simulated SNR₀ of b_0 images used to extract γ . The plot shows that γ decreases proportionally with the SNR₀. Moreover, it displays that experimental γ values extracted (indicated by the arrows) are underestimated compared to the γ values derived using an ideal SNR₀=100. The decrease of γ value becomes particularly critical for SNR₀<20. For SNR₀>20 γ is underestimated compared to the estimation obtained with the ideal SNR₀=100. However, the difference between experimental γ values and those derived using SNR₀=100 is around 2%.

The effect of artificial addition of Rician noise to the DWIs is shown in **Figure 5.6**. The two extreme cases are here reported: $s=0$ corresponds to the set of rawdata, with the intrinsic original noise; $s=50$ corresponds to the worst-case scenario, where even at $b=200$ s/mm² the DWI is really noisy. The comparison between the original DWI at $b=200$ s/mm² and that one at $b=5000$ s/mm² evidences an inversion of contrast between WM and GM. The effect of Rician noise addition over SNR and the CNR between two WM ROIs is shown in **Figure 5.7**. The scale parameters (s) of considered Rician PDFs are: $s=0,10,15,30,50$. In a first trial the same analysis was performed for values of $s=0,2,4,6,8$, but negligibly effects were reported for SNR, as well as for CNR. The values of $M\gamma$ evaluated in the two considered WM ROIs (*acr*, anterior corona radiata and *plic*, posterior limbs of internal capsule) do not vary remarkably within a wide range of s ($0 < s < 15$), but for extreme simulated noise levels ($s=50$) they are altered of more than 10%.

In **Figure 5.8** $M\gamma$ values evaluated in the CSF, WM and GM of a cohort subject as a function of the b -value ranges are displayed. $M\gamma$ values obtained by using b -value ranges from 0-400 to 0-1500 s/mm² are not reliable values because, as it has long been recognized [61, 62], a significant deviation of the experimental data from the mono exponential decay is observed beyond $b=1500$ s/mm². On the other hand, the graph shows that the inclusion of b values higher than 2000 s/mm² improves the γ parameter contrast. In particular, at b -value ranges around 0-4000 s/mm² the maximum difference between CSF, GM and two different WM regions (characterized by fibers mainly oriented perpendicular and parallel to B_0 direction) can be obtained.

Pseudo super-diffusion of water in healthy human brain: in vivo study

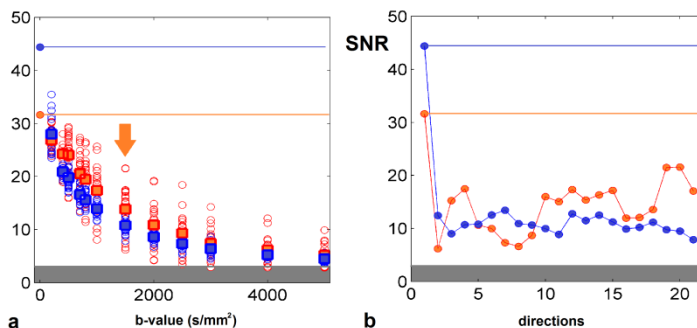


Figure 5.4 – Signal to Noise Ratio (SNR) of DWIs as a function of b-value and diffusion gradient direction. a) The SNR of a ROI in the splenium (red circles), and SNR of a ROI in the thalamus (blue circles), are plotted against the b-value (only some of the b-values are specified in the x-axis). The values of SNR corresponding to different gradient directions at the same b-value are plotted in a unique column, with the relative mean value indicated (solid squares for the splenium, solid circles for the thalamus). The SNR of the b0-image is indicated by the horizontal lines. The values of SNR for b-value $b=1500$ s/mm² are indicated by the arrow, and are plotted in more details on the right. b) The SNR of DWIs at $b=1500$ s/mm² varies depending on the diffusion gradient direction. The grey area in the plots indicates the inferior limit allowed for the reliability of DW data (SNR=3), according to Jones et al. [96]. Data are referred to a representative subject.

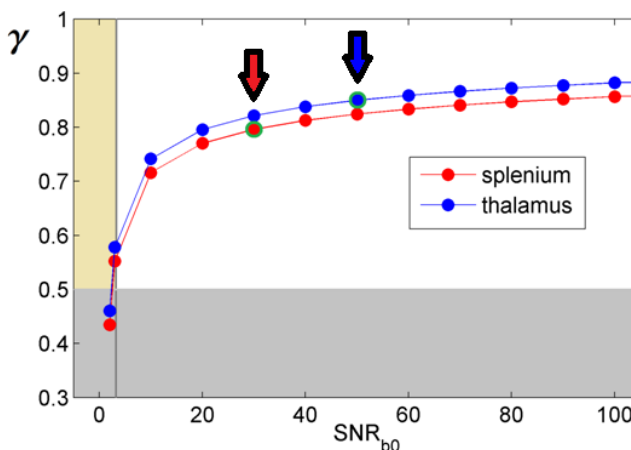


Figure 5.5 - Mean values of γ plotted against the simulated SNR of b0 image, for a ROI placed in the splenium and in the thalamus. The plot shows a decrease of γ value proportional to SNR_{b0}. The experimental γ values are indicated by a red arrow for the splenium, and by a blue arrow for the thalamus and corresponds respectively to SNR_{b0}=29 and SNR_{b0}=49. Data are referred to a representative subject. The vertical gray rectangle excludes the values of SNR<3, and the horizontal gray rectangle denotes the unacceptable γ values, because lower than 0.5.

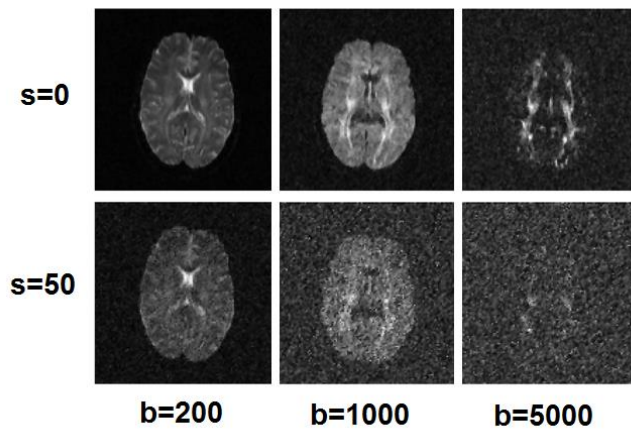


Figure 5.6 – *Effect of Rician Noise over DWIs appearance. Comparison between the original DWIs dataset, without any addition of Rician Noise (upper row, $s=0$), and a set of DWIs with the addition of simulated Rician Noise, in the worst-case scenario (lower row, $s=50$), for increasing b -values, measured in s/mm^2 . Data are referred to the same axial slice of a representative subject.*

Pseudo super-diffusion of water in healthy human brain: in vivo study

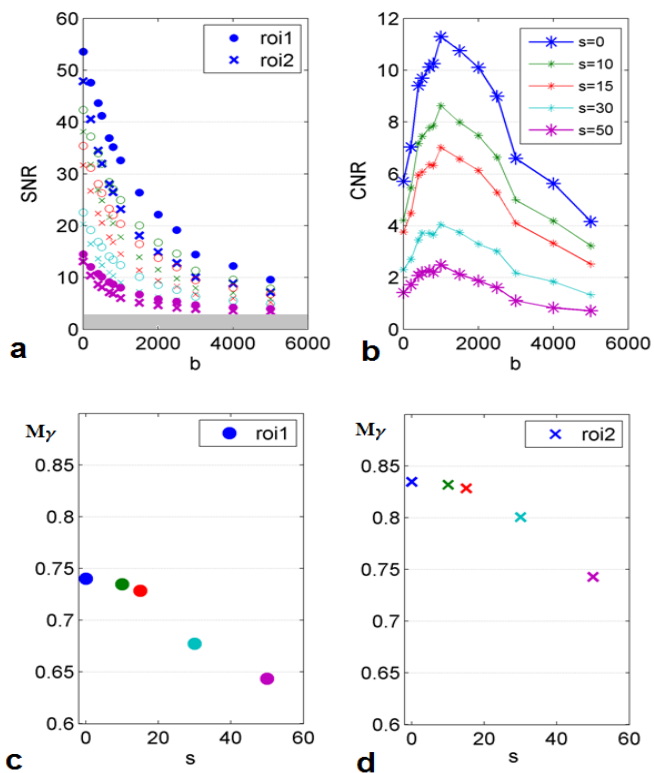


Figure 5.7 – Effect of Rician Noise over signal, contrast and M_y estimation. a,b) Signal to Noise Ratio (SNR) and Contrast to Noise Ratio (CNR) of two WM ROIs (roi1=acr, roi2=plic), plotted against the b -value, for increasing values of Rician noise s , listed in the legend. The raw DWIs (without any Rician Noise addition) correspond to blue markers and lines. The DWIs with the highest noise (with a Rician distribution with $s=50$ correspond to purple markers and lines. c,d) M_y evaluated in the two considered WM ROIs.

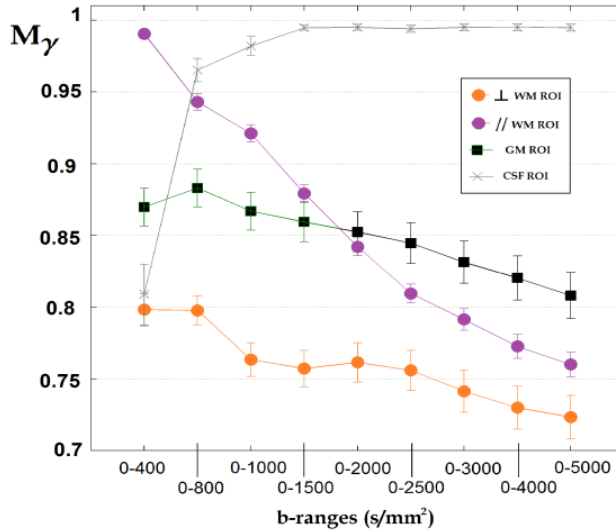


Figure 5.8 - Estimated M_γ values as a function of the b -values range. M_γ values with the relative standard deviations were estimated from DWIs, by considering different b -values ranges (reported in the x -axis) in WM ROIs with fibers parallel and orthogonal to the static magnetic field B_0 , in a GM ROI, and in a ROI placed in the CSF.

5.4.2 Anomalous diffusion in WM vs free diffusion in CSF

Using least squares minimization algorithms, the script extracting AD- γ with the relation expressed in (5.2) performs a curve fitting of the normalized signal vs b -value for each diffusion gradient direction. The use of a selected sensitizing gradient tunes the sensitivity of the diffusion investigation towards water diffusion along the specified direction. **Figure 5.9** shows an anisotropic behavior of the DW signal decay in 3 orthogonal directions, depending on the cerebral tissue considered. The diffusion is isotropic in the CSF, where the signal decay is mono-exponential. Deviations from this behavior are found in the other two tissues, with a slight anisotropy in the thalamus and a remarkably anisotropy in the splenium. In particular, in the splenium the L/R direction corresponds to the direction in which the diffusion is facilitated, because it is oriented as WM fibers in corpus callosum. The other two directions show a signal compatible with restricted diffusion. Here the anisotropy considered is

that one of the signal decay, but it is a different concept compared to ‘fractional anisotropy’ derived in the DTI.

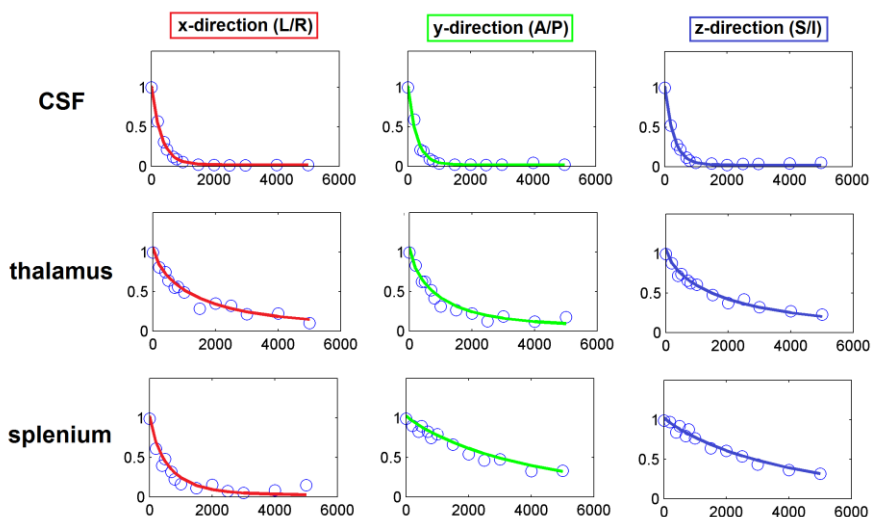


Figure 5.9 – Anisotropic behavior of the DW signal vs b -value. DW signal acquired along 3 orthogonal directions and normalized to the signal of the b_0 -image is plotted against b -value (measured in s/mm^2) for a voxel placed in three different cerebral tissues (CSF, thalamus representative of GM, splenium representative of WM, from top to bottom).

5.4.3 R_2^* reflects magnetic inhomogeneity in WM and GM ROIs

The average orientation that an axon bundle forms with the B_0 is provided by $\Phi = 90^\circ - \Phi^*$, where Φ^* is obtained using the components of the main diffusion eigenvector \mathbf{v}_1 (Figure 5.10a). By looking at the maps of FA and of fibers angles Φ , shown in Figure 5.10b, we may notice that ROIs with fibers differently oriented with respect to B_0 show a similar contrast in FA maps, but a different contrast in the orientation Φ -map. The orientation is reference-frame independent, being derived using the diffusion eigenvector. In Figure 5.10c the value of R_2^* in selected WM ROIs is plotted vs Φ (i.e., the average orientation of WM fibers in a certain ROI). The plot shows that ROIs with a

prevalence of \mathbf{B}_0 -parallel fibers (indicated with blue dots) are characterized by lower R_2^* values compared to those with a prevalence of \mathbf{B}_0 -orthogonal fibers (indicated with red dots). The box in the plot shows that there is a significant, albeit moderate, linear correlation between R_2^* and Φ . Furthermore, a sine function fits well with R_2^* values vs Φ data (green curve).

The behavior of R_2^* vs iron content is shown in **Figure 5.10d**. A strong linear correlation ($r=-0.950$) between R_2^* and $[\text{Fe}]$ was found in GM ROIs. We considered only *thal*, *caud*, *put* and *pall* brain regions because of the lack of information about iron content extracted with uniform experimental methods in other sub-cortical GM ROIs.

These results suggest that R_2^* obtained is affected by the orientation of myelinated fibers, and depends on the iron content in GM, and justify the study of AD- γ dependence on $\Delta\chi$ through its dependence on R_2^* .

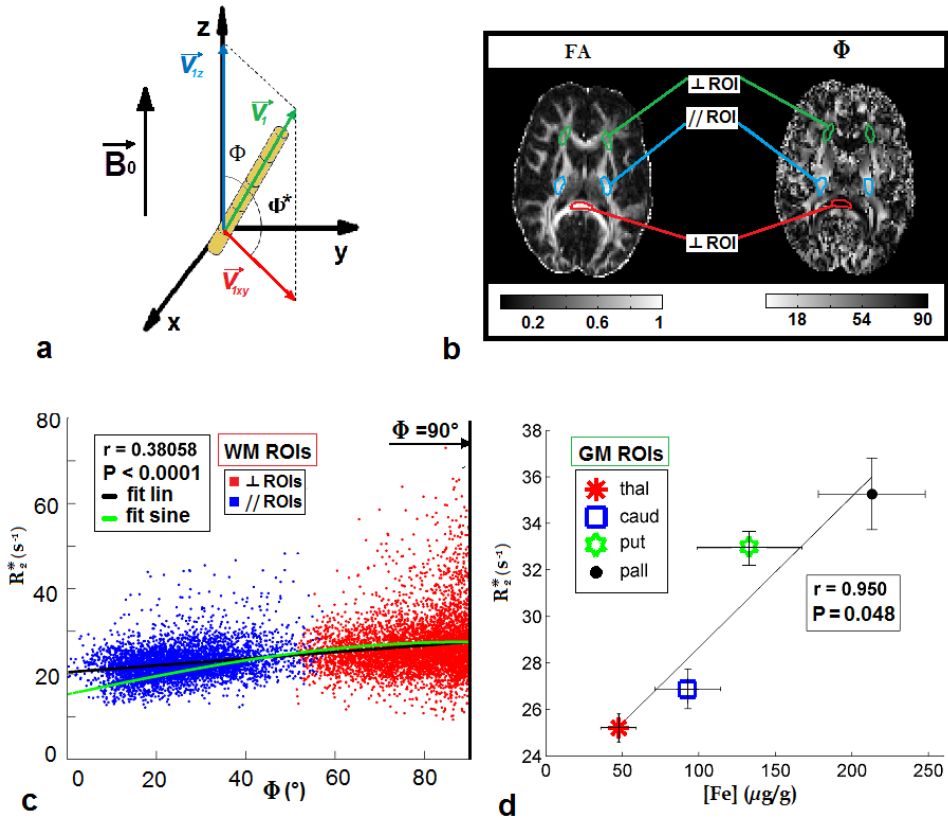


Figure 5.10 – R_2^* dependence on magnetic inhomogeneity in WM and GM. *a)* Sketch indicating the main orientation of a WM tract. V_1 is the main diffusion eigenvector. Here a single myelinated axon, represented by a succession of cylinders (internodal myelin), is depicted. The angle that the axon forms with the direction of the static magnetic field B_0 is provided by $\Phi=90^\circ-\Phi^*$. *b)* FA map and the map of average Φ for a subject in the cohort. ROIs with a orthogonal fibers are colored in green (acr) and red (scc); ROIs with parallel fibers are colored in light blue (plic). *c)* R_2^* of WM ROIs with parallel fibers (blue dots) and orthogonal fibers (red dots), plotted against their orientation. The data are linearly fitted (black line), and fitted with a sine function (green curve). *d)* R_2^* of thalamus (thal), caudate nuclei (caud), putamen (put) and globus pallidus (pall), estimated from the parametric R_2^* maps and plotted vs non-heme iron contents taken from literature [99]. Pearson's correlation coefficient r is reported in the box, together with the level of significance, P .

5.4.4 AD-metrics provide a peculiar contrast compared to DTI-metrics

The parametric maps of MD, FA, axial-D, radial-D (measured in mm^2/s) constituting the DTI-metrics, the maps of $M\gamma$, $A\gamma$, axial- γ and radial- γ , (dimensionless) constituting the AD-metrics, and the maps of R_2^* are provided in **Figure 5.11** for a representative subject. In **Figure 5.12**, $M\gamma$ and MD maps of the same subject are illustrated to show the different image contrast provided by AD and DTI-metrics. $M\gamma$ provides a novel contrast compared to MD map, and in particular it highlights the interfaces between compartments with different magnetic susceptibility, for example in (1) the interface between the splenium and the CSF is enhanced (in the CSF $\gamma = 1$); the borders of thalamus are more evident in $M\gamma$ map compared to MD map (2), because of the high magnetic susceptibility inhomogeneity caused by its high iron content; the area surrounding the ventricles is more heterogeneous compared to MD map (3). These results underline the central role of the local $\Delta\chi$ in providing γ contrast.

The ANOVA test revealed the presence of significant differences among parameters computed in different areas of brain parenchyma. Statistical analysis showed that the variation of the same parameter within the same anatomical fiber bundle or a sub-cortical area across individuals was remarkably limited. In regard to GM ROIs, *caud* was well discriminated from *put* by $M\gamma$ ($P < 0.005$), γ_{\perp} ($P = 0.001$) and $A\gamma$ ($P = 0.001$), R_2^* ($P = 0.001$), D_{\perp} ($P < 0.05$) and FA ($P < 0.0001$), and from *pall* by all the AD-metrics with $P < 0.0001$ (for $A\gamma$ $P < 0.05$), by R_2^* ($P = 0.005$), $D_{//}$ ($P < 0.005$) and FA ($P < 0.0001$). On the other hand, MD, $D_{//}$ and D_{\perp} could discriminate *put* from *pall* with a high level of significance ($P < 0.0001$), whereas AD-metrics did not distinguish between them. $\gamma_{//}$ was the only parameter able to discriminate between *caud* and *hipp* ($P = 0.002$). Finally, $A\gamma$ discriminated between *put* and *hipp* ($P = 0.001$) and between *pall* and *hipp* ($P < 0.05$), while FA differentiated all these structures ($P < 0.0001$). Regarding WM ROIs ANOVA test showed that R_2^* was able to discriminate significantly only between *gcc* and *ss* ($P < 0.05$), *pllc* and *acr* ($P < 0.05$), or *pllc* and *ss* ($P < 0.01$). Regarding the DTI-metrics, FA was the parameter with the highest number of significant comparisons, except for *gcc-bcc*, *gcc-scc* ($P > 0.05$). None of the DTI-metrics discriminated neither *gcc* from *bcc*, nor *gcc* from *scc*, which were instead discriminated by $A\gamma$ with $P < 0.0001$. $M\gamma$, γ_{\perp} and $A\gamma$ were the only diffusion derived parameters able to distinguish *pllc* from *gcc* (respectively, with $P < 0.05$, $P = 0.01$, $P < 0.0001$). On the other hand,

AD-metrics did not discriminate between *bcc* and *scc* (except for $A\gamma$, with $P<0.026$), while the DTI-metrics did (MD and D_{\perp} with $P<0.0001$, FA with $P=0.001$, $D_{//}$ with $P<0.05$).

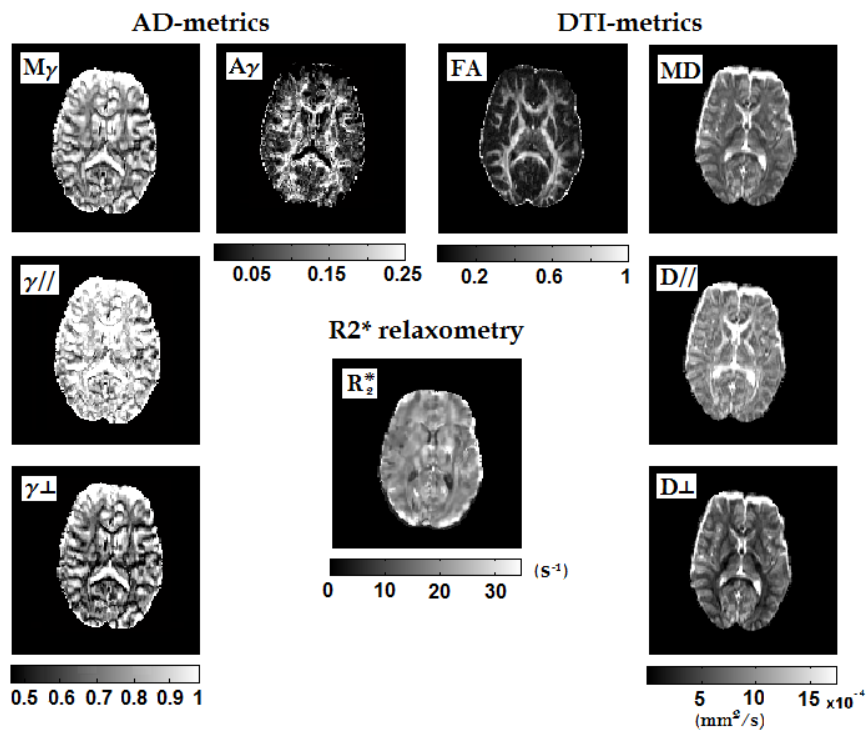


Figure 5.11 – AD-metrics, DTI-metrics and R_2^* parametric maps in the subject's native space, for the same axial slice (obtained from a single subject). The maps in the left show the AD-derived parameters: mean- γ ($M\gamma$), axial- γ ($\gamma_{//}$), radial- γ (γ_{\perp}), γ -anisotropy ($A\gamma$); the maps on the right show the DTI-derived parameters: mean-diffusivity (MD), axial and radial diffusivity ($D_{//}$ and D_{\perp}), and fractional anisotropy (FA). The rate of relaxation (R_2^*) is illustrated in the middle. The color-bar is reported next to each map with distinct contrast.

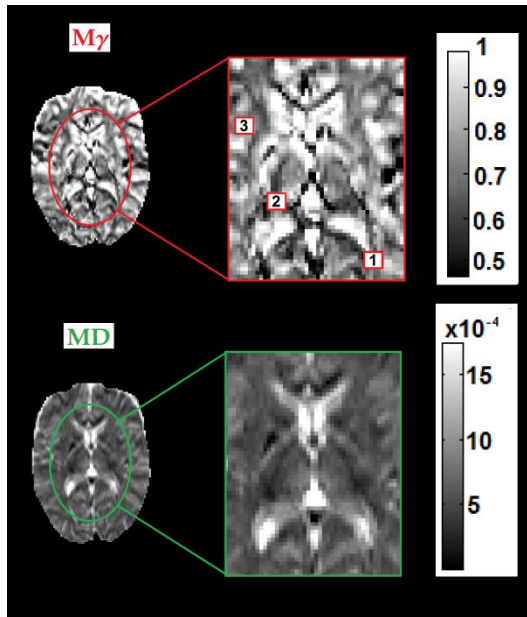


Figure 5.12 - Mean- γ ($M\gamma$) and Mean Diffusivity (MD) parametric maps for a randomly chosen subject in the cohort, and magnification of the area containing the thalamus, the splenium of corpus callosum, and the ventricles. Several anatomical details are listed: (1) interface between the splenium and the CSF; (2) borders of the thalamus; (3) the surrounding of the ventricles.

5.4.5 AD-metrics correlates with R_2^* in WM and GM ROIs

In **Figure 5.13** linear correlation plots between AD-metrics and R_2^* are shown, for WM ROIs and GM ROIs. The error bars indicate inter-subjects SD; only plots with a positive Pearson's correlation test are shown ($P < 0.05$). A strong negative correlation was found between $M\gamma$, $\gamma_{//}$ and R_2^* , (respectively, $r = -0.786$, $P = 0.022$; $r = -0.822$, $P = 0.012$). On the other hand, γ_{\perp} showed a moderate negative trend with R_2^* ($r = -0.666$, $P = 0.071$, not shown in the figure), and no correlation was found between $A\gamma$ and R_2^* . In GM ROIs a strong negative correlation was found between $M\gamma$ and R_2^* ($r = -0.997$, $P = 0.003$), γ_{\perp} and R_2^* ($r = -0.989$, $P = 0.011$), while $\gamma_{//}$ exhibited a negative linear trend with R_2^* , and $A\gamma$ a positive one, not shown in the figure because they were both not significant. In WM ROIs no significant correlations were found between any of the DTI parameters and R_2^* . In **Table 1** the mean values \pm SEM of AD and R_2^* metrics measured in the selected ROIs shown in **Figure 5.3** are listed. $M\gamma$, $\gamma_{//}$, γ_{\perp} and

$A\gamma$ in WM and GM are significantly different ($P < 0.0001$), with $M\gamma$ lower in the WM compared to the GM ($M\gamma_{WM} = 0.761 \pm 0.052$, $M\gamma_{GM} = 0.851 \pm 0.036$), according to previous studies [19, 27, 28]. Similar results were obtained for the axial-exponent, ($\gamma_{//WM} = 0.891 \pm 0.050$, $\gamma_{//GM} = 0.909 \pm 0.027$) and for the radial-exponent ($\gamma_{\perp WM} = 0.693 \pm 0.060$, $\gamma_{\perp GM} = 0.822 \pm 0.043$). In contrast, $A\gamma$ was higher in the WM compared to GM ($A\gamma_{WM} = 0.183 \pm 0.041$, $A\gamma_{GM} = 0.077 \pm 0.023$). Finally, $R_2^*_{WM} = (26.02 \pm 3.88) \text{ s}^{-1}$ and $R_2^*_{GM} = (30.97 \pm 4.55) \text{ s}^{-1}$. $R_2^*_{WM}$ is in good agreement with previous studies performed at $B_0 = 3.0 \text{ T}$ in a cohort of subjects with ages around 25 years [102, 103].

5.4.6 Relation between AD-metrics and magnetic susceptibility

The behavior of AD-metrics as a function of magnetic susceptibility in a subset of ROIs is reported in **Figure 5.14**. The vertical error bars represent the computed SEM for the measured parameters, and the horizontal error bars represent the SD on χ -values taken from literature [100]. The behavior of the investigated parameters vs χ was characterized by an opposite trend for WM compared to GM ROIs. As a consequence, the data points belonging to the two groups of ROIs were fitted separately. The lack of significance in the Pearson's correlation tests may be motivated by the limited size of the sample (3 ROIs per group, thus 3 mean values per group). In WM ROIs, $M\gamma$, $\gamma_{//}$ and γ_{\perp} increase in parallel to χ increase. Conversely, in GM ROIs they decrease when χ increases, with the highest value of r for $\gamma_{//}$ in both cases ($r = 0.957$ and $r = -0.985$, respectively).

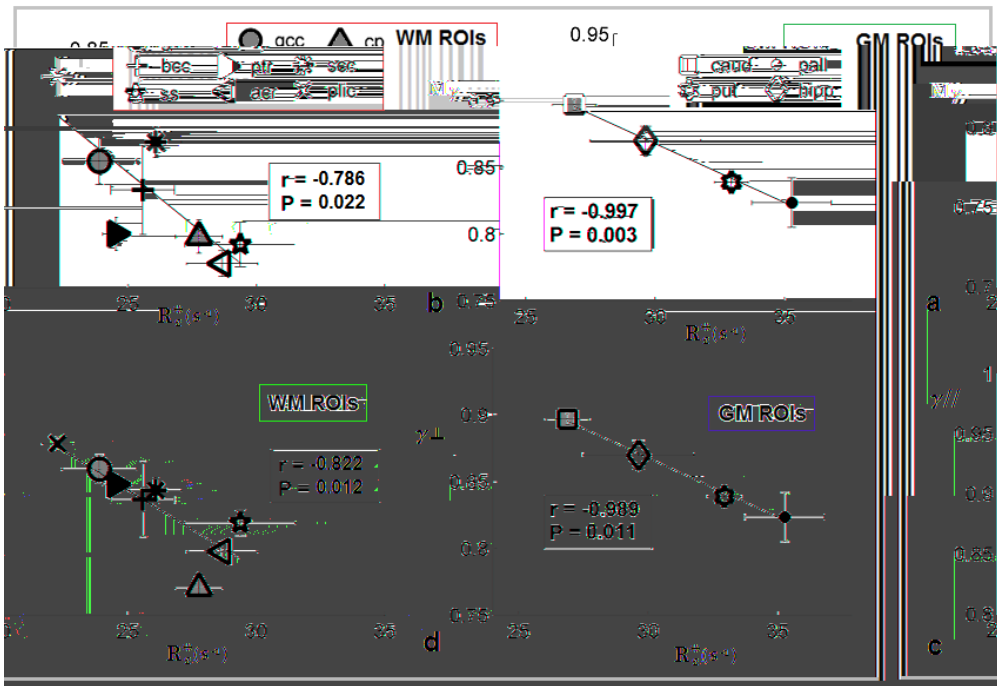


Figure 5.13 - AD-metrics plotted vs $R2^*$. Mean values of mean- γ ($M\gamma$), axial- γ ($\gamma_{//}$) in WM-ROIs (a,c) and of $M\gamma$ and radial- γ (γ_{\perp}), as a function of $R2^*$ in GM-ROIs (b,d). Error bars indicate inter-subjects SD; the linear fit, Pearson's correlation coefficient and the significance level are indicated (gcc=genu of corpus callosum, cc; bcc=body of cc; scc=splenium of cc; plic=posterior limb of internal capsule; cp=cerebral peduncle; ptr=posterior thalamic radiations; acr=anterior corona radiata; ss=sagittal stratum; caud=caudate; put=putamen; pall=pallidum; hipp=hippocampus).

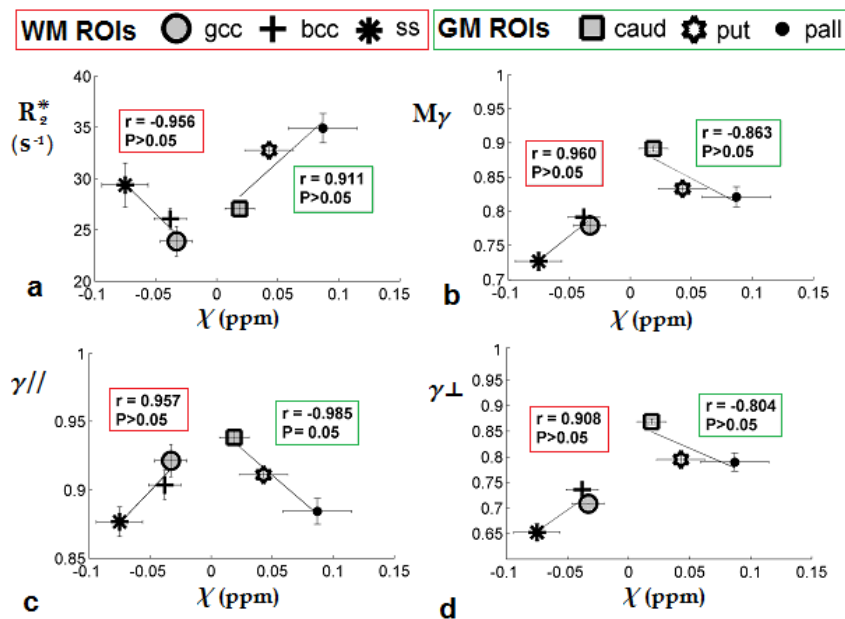


Figure 5.14 - R_2^* and AD-derived parameters plotted against χ in WM and GM ROIs. Susceptibility values are taken from W.Li et al., 2011 [100], and are referred to those in the CSF. The vertical error bars represent the computed SEM for the measured parameters, and the horizontal error bars represent the SD on χ -values taken from the literature. The trends are indicated by linear fits, that are treated separately for WM and GM ROIs. Pearson's correlation coefficients, r , are reported in the boxes, together with the level of significance, P (red boxes for WM ROIs, green boxes for GM ROIs). For the list of ROIs acronyms see Table 1.

Table 1 - AD-metrics and R_2^* mean values obtained in selected ROIs^a

WM ^b ROIs	M γ		$\gamma_{//}$		γ^{\perp}		A γ		$R_2^*(s^{-1})$	
	Mean	SEM	Mean	SEM	Mean	SEM	Mean	SEM	Mean	SEM
<i>gcc</i>	0.780	0.015	0.921	0.012	0.709	0.017	0.224	0.009	23.89	1.44
<i>bcc</i>	0.761	0.028	0.896	0.031	0.694	0.027	0.180	0.011	25.58	1.24
<i>scc</i>	0.792	0.010	0.904	0.011	0.735	0.010	0.158	0.007	26.08	1.01
<i>plic</i>	0.833	0.012	0.943	0.006	0.778	0.016	0.151	0.009	22.25	0.60
<i>cp</i>	0.732	0.011	0.823	0.007	0.687	0.014	0.129	0.009	27.76	0.92
<i>ptr</i>	0.734	0.010	0.909	0.008	0.646	0.013	0.230	0.011	24.54	0.51
<i>acr</i>	0.715	0.008	0.853	0.008	0.646	0.009	0.189	0.006	28.67	1.38
<i>ss</i>	0.727	0.014	0.877	0.011	0.652	0.017	0.202	0.012	29.37	2.16
GM^c ROIs	Mean	SEM	Mean	SEM	Mean	SEM	Mean	SEM	Mean	SEM
<i>caud</i>	0.892	0.004	0.938	0.005	0.869	0.005	0.061	0.005	27.07	0.78
<i>put</i>	0.833	0.007	0.911	0.004	0.795	0.009	0.098	0.005	32.78	0.59
<i>pall</i>	0.821	0.015	0.884	0.009	0.790	0.018	0.090	0.008	34.92	1.43
<i>hipp</i>	0.856	0.010	0.902	0.008	0.833	0.011	0.061	0.004	29.10	2.01

^aThe error on the estimation of each parameter was taken as the standard error of the mean (SEM). M γ , $\gamma_{//}$, γ^{\perp} , A γ are dimensionless quantities.

^bgcc=genu of corpus callosum; bcc=body of corpus callosum; scc=splenium of corpus callosum; plic=posterior limb of internal capsule; cp=cerebral peduncle; ptr=posterior thalamic radiations; acr=anterior corona radiata; ss=sagittal stratum;

^ccaud=caudate nuclei; put=putamen; pall=pallidum; hipp=hippocampus.

5.5 Discussion

5.5.1 Overview of experimental methods and reliability of DWIs

Motivated by previous results obtained in vitro on inert samples, excised human tissues [20, 26] and fixed mouse spinal cord [42] the aim of this work was to investigate if the AD γ -imaging in the human brain imaged at 3.0 T

depends on the χ anisotropy distribution in addition to the multi-compartmentalization of water.

Since the critical point in AD- γ imaging is the fact that the DW signal is acquired up to high b-values ($b_{\max}=5000$ s/mm² in this experiment), it is fundamental to estimate the SNR in order to establish the reliability of DWIs data.

In **Figure 5.4** the SNR of the splenium of the corpus callosum and the thalamus from a single subject is plotted against the b-value. In all experiments, the SNR was higher than 3, which is the lowest acceptable value for considering DW data reliable [77]. Moreover, the plot in **Figure 5.5** shows that experimental γ values extracted are slightly underestimated compared to the γ values derived using an ideal SNR₀=100. In fact the difference between experimental γ values and those derived using SNR₀=100 is around 2%. The addition of artificial Rician noise to the DWIs didn't affect neither SNR nor CNR for $s < 8$, and the value of $M\gamma$ did not vary remarkably within a wide range of s ($0 < s < 15$). Instead, SNR and CNR were considerably reduced as well as $M\gamma$ (reduction of more than 10%) for $s=50$. However, such a noise is pretty unlikely from an experimental point of view (it was the worst-case scenario). The graph in **Figure 5.8** shows that the inclusion of b values higher than 2000 s/mm² improves the γ parameter contrast. In particular at b-value ranges around 0-4000 s/mm² the maximum difference between CSF, GM and two different WM regions (characterized by fibers differently oriented) can be obtained.

5.5.2 R₂* reflects magnetic susceptibility inhomogeneity in WM and GM ROIs

As a preliminary study, the dependence of R₂* on χ variations at 3.0 T in was investigated in the cohort of healthy subjects (**Figure 5.10**). As illustrated in Chavhan et al., [72], transverse relaxation in GRE sequences is a combination of intrinsic T₂ relaxation and relaxation caused by magnetic field inhomogeneities. Considering the rate of relaxation, this means: $R_2^* = 1/T_2^* = 1/T_2 + \gamma\Delta B_0$, where γ is the gyromagnetic ratio. This turns out into $R_2^* = R_2 + R_2'$. In order to validate our method, we considered the two main aspects that influence R₂' through the occurrence of local B₀ inhomogeneity, hence both the orientation of myelinated axons in WM and the amount of iron content in subcortical GM

structures. Rudko et al. [104], suggested that R_2^* depends on tissue orientation in WM and cortical GM, performing GRE at 18 different sampling angles on fixed rat brains at 9.4 T. In their work, these authors showed that R_2^* had a sinusoidal dependence on the orientation of the tissue in WM, whereas no orientation dependence is present in the basal ganglia, where R_2^* is influenced by iron concentration only.

On a first approximation, a significant linear correlation between R_2^* and Φ was found ($r=0.381$, $P<0.0001$). Moreover, this seems to replicate previous findings by Rudko et al. [104]. Indeed the sine function fitted well to data (green curve in **Figure 5.10**). However, owing to the lower intensity of H_0 (which in our case was 3.0 T), the effect of local ΔB_0 on R_2' , and thus on R_2^* , is less evident compared to that observed by Rudko et al.

The relation between iron content and R_2^* in human brain is supported by a conspicuous amount of works [91, 105-107]. According to literature, we found a strong linear correlation ($r=-0.950$, $P=0.05$) between R_2^* and iron content [Fe] values taken from literature (**Figure 5.10d**).

These results suggest that the measured R_2^* reflects $\Delta\chi$ inhomogeneity due to the orientation dispersion in WM, and $\Delta\chi$ inhomogeneity in the deep GM nuclei due to differences in iron content.

5.5.3 AD-metrics relation with χ and R_2^*

After studying the link between R_2^* and $\Delta\chi$ in brain, the relation between AD-metrics and R_2^* was examined and that one between AD-metrics and χ in WM and GM.

Considering χ as taken from literature, we found the peculiar behavior of R_2^* vs χ (**Figure 5.14**). The dependence of AD-metrics on χ in both WM and GM ROIs (shown in **Figure 5.14**) is consistent with the results presented in **Figure 5.13**, in which the significant linear correlations between AD-derived parameters and R_2^* are shown. Conversely, we did not find significant correlations between any of the DTI-metrics with R_2^* , in agreement with Nair et al. [108]. In Nair et al.'s work DW-data of shiverer and wild type mice are compared. It is shown that DTI-metrics are only feebly affected by $\Delta\chi$ variation at 9.4 T. We infer that at lower H_0 strengths the effect of χ on DTI-derived parameters is neglected.

In particular, AD-metrics showed a strong negative correlation with R_2^* in both WM and GM (**Figure 5.13**). These results suggest that the AD-metrics are sensitive to R_2^* inhomogeneity due to $\Delta\chi$ in human WM and GM, originating respectively by differences in myelin density/orientation and $\Delta\chi$ at the interfaces between myelin and the neighboring cells, and by local differences in iron content.

With respect to the factors contributing to R_2^* in GM, the $\Delta\chi$ causing R_2' variations have a dominant role compared to R_2 effect due to microstructure. The similar trend of AD-metrics vs R_2^* and AD-metrics vs χ in GM is thus reasonable, considering that both R_2^* and χ are related to iron content in deep GM nuclei. In fact, experimental evidence indicates that there is a high linear correlation between R_2^* and the non-heme iron concentration, especially in sub-cortical GM [105-107].

Differently from GM ROIs, $M\gamma$, $\gamma//$ and $\gamma\perp$ vs χ showed increasing trends in WM (**Figure 5.14**), although the correlation was not significant or marginally significant due to the small amount of points (*gcc*, *scc*, *ss*). Moreover, $M\gamma$ and $\gamma//$ vs R_2^* showed significant strong negative correlations (see **Figure 5.13**). These results may be interpreted considering the origin of magnetic susceptibility inhomogeneity in WM.

5.5.4 Magnetic susceptibility inhomogeneity in WM

In WM there is an interplay between two factors contributing to R_2^* : 1) R_2' variations along myelinated fibers are caused by $\Delta\chi$ at microscopic and macroscopic scale due to different WM orientations with respect to \mathbf{B}_0 and to the modulated shape of axonal fibers [109-111]; 2) R_2 variations in WM are mainly due the differentiated microstructure, thus the distribution of axonal diameters, myelin fraction, and axonal density.

$\Delta\chi$ anisotropy at the microscopic scale originates from the radial arrangement of oriented lipo-protein chains constituting the multi-layers of the myelin sheaths [39, 40, 85]. By considering a χ anisotropy of the membrane lipids from isolated human lipo-proteins of about -0.223 ppm [112] and a lipid volume fraction in WM of about 16% [85], $\Delta\chi$ is in the order of 0.018 ppm [38]. In fact not only the lipid density, but also the way lipids are spatially organized with

respect to \mathbf{B}_0 are important factors contributing to the $\Delta\chi$ anisotropy in WM (**Figure 5.15**).

The $\Delta\chi$ anisotropy at a macroscopic scale arises from the presence of elongated compartments, provided with the myelin sheath and containing cytoplasm, and exhibits a sine-squared orientational dependence $\sim \sin^2\Phi$ with Φ the angle of the axon with respect to \mathbf{B}_0 [113].

By looking at the values listed in Table 1, we notice that M_γ , $\gamma_{//}$ and γ_\perp are higher in WM fiber bundles oriented parallel to \mathbf{B}_0 (for example *pllc*), compared to the ones oriented orthogonally to \mathbf{B}_0 (for example *gcc*, *scc*). Conversely R_2^* is lower in *pllc* compared to other ROIs, confirming previous results [104, 114-116] and according to the orientational dependence of χ found by Duyn et al. [113].

5.5.5 Discrimination of WM and GM ROIs

Considering WM ROIs, DTI-metrics discriminated with higher level of significance between ROIs with fiber bundles similarly oriented with respect to \mathbf{B}_0 , whereas AD-metrics were more effective in discriminating between ROIs with \mathbf{B}_0 -parallel fibers from ROIs with \mathbf{B}_0 -orthogonal fibers (for example *pllc* from *gcc*, *acr*, *ptr*, *ss*). This is most likely due to the orientational dependence of χ , which is reflected by the AD- γ exponent, as shown in these results. Focusing on a bundle of myelinated fibers homogeneously oriented with respect to \mathbf{B}_0 , such as the corpus callosum, DTI-metrics were able to discriminate between the body and the splenium of the corpus callosum. Conversely, AD-metrics were unable to discriminate between them, with the exception of A_γ .

This outcome could be a replication of AD *in vitro* studies performed on phantoms with known $\Delta\chi$ and simplified microstructural heterogeneity [20, 25, 26], which proved that the AD γ -exponent is influenced by both the $\Delta\chi$ inhomogeneity and the multi-compartmentalization of the environment explored by diffusing water molecules. In the corpus callosum the competition between the two effects (diffusion multi-compartmentalization and $\Delta\chi$) upon which the γ AD-contrast is based may smooth the local differences of γ -exponent between regions. In fact, from a microstructural point of view, the corpus callosum is characterized by a uniform and dense distribution of axon diameters in the genu and splenium, presenting instead a wider distribution of

axon diameters, with a lower density, in the body [83]. Hence the AD-exponent should reflect the differential diffusion compartmentalization explored by water. On the other hand, myelinated fibers in the corpus callosum maintain the same orientation with respect to \mathbf{B}_0 , which turns out in the uniformity of $\Delta\chi$ due to the lack of orientation dispersion. Moreover, about the strength of G_{int} originating from $\Delta\chi$ between axons and closest tissues, it depends not only on the magnitude and direction of \mathbf{B}_0 , but also on the reciprocal relationship between the diffusion length of water molecules (l_d), and their dephasing length (l^*) [117, 118].

The investigation of AD and DTI-metrics behavior in the corpus callosum compared to other WM regions constituted by fibers oriented perpendicularly to corpus callosum, provides further indication about the simultaneous dependence of AD-contrast on both multi-compartmentalization and $\Delta\chi$ effects in tissue.

Similarly to what found in the WM, the results of multiple comparisons between GM regions may be justified considering the concomitant effect of $\Delta\chi$ and microstructure on AD-metrics. As a general comment, we may notice that those GM ROIs which were well discriminated by AD-metrics (i.e., as *caud* from *put* and *caud* from *pall*) were also well discriminated by R_2^* , most likely owing to the predominance of $\Delta\chi$ effect compared to the multi-compartmentalization effect. For what concerns the discrimination between *put* and *pall*, instead, DTI-metrics were more effective, and this is in agreement with recent results showing an increased value of FA in the globus pallidus, compared to that observed in the putamen, caudate nucleus and thalamus [119].

5.5.6 Is AD-imaging appealing in the field of neurology?

The assessment of magnetic susceptibility inhomogeneity in the human brain is of paramount importance in the field of MRI diagnostics. Indeed, on the basis of recent results, the link between an abnormal iron deposition in brain gray matter and the onset and development of several neurodegenerative diseases is generally recognized by the scientific community. Iron (as well as other redox metals, see [37]) plays a key role in the maintenance of brain homeostasis. On the other hand, an inappropriate amount or availability of iron causes the onset of toxic reactions that produces free radicals. An explanatory description of the

chain reaction that produces oxidative stress (see **Figure 5.16**) in nervous cells is provided in [17]. As a matter of fact, an abnormal amount of iron and iron-storage proteins was found in Parkinson's disease [17], Alzheimer's disease [37], Multiple Sclerosis [87, 88], and other disabling disorders as migraine and chronic daily headache [89]. The evaluation of iron content in vivo is currently performed through the use of Quantitative Susceptibility Mapping methods (QSM) [90], for which a strong correlation between chemically determined iron concentration and bulk magnetic susceptibility was shown in deep gray matter structures [91]. On the other hand, this technique is not as much accurate in the white matter, where the contribution from diamagnetic myelinated fibers causes misinterpretation of data [91]. Furthermore, there are some critical points in the use of QSM.

QSM provides susceptibility maps from the background corrected phase images, using complex algorithms such as HEIDI (Homogeneity Enabled Incremental Dipole Inversion), based on the division of the Fourier space into three sub-domains, solving the inverse field-to-source problem from gradient echo (GRE) phase to susceptibility. The Fourier transform of susceptibility ($\chi(k)$), with k the k -space vector, cannot be determined in regions near the conical surfaces defined by $k^2 - 3k_z^2 = 0$. A threshold method may approximate $\chi(k)$ values at the conical surfaces [120] but originates residual artifacts and noise amplifications, especially at high field. Another method is to increase the number of sampling orientations, by rotating the object in the scanner in at least three directions [86], prolonging the scan time and make it hardly feasible for routine in vivo studies.

In summary, even if the spatial resolution achievable is good ($0.5 \times 0.5 \times 2 \text{ mm}^3$) with the use of fast imaging sequences [121], the main difficulties are: the need to use sophisticated and time consuming algorithms to ensure a good quality and accuracy of QSM images; the lack of a uniform reconstruction method to solve the inverse field-to-source problem; the presence of non-local phase effects, because the bulk susceptibility, depending on the geometry and orientation of the object, causes a phase information that could be spatially distant from the source of susceptibility changes; the dependence of the noise from the chosen algorithm [121]. Last but not the least, veins present a magnetic susceptibility of 0.45 ppm, that is higher compared to the χ of deep gray matter structures [121]. This causes further streaking artifacts, and may cover the information related to the regions of interest in the assessment of iron deposition. Conversely, the AD-MRI benefits from the susceptibility

induced contrast, as we suggest in our paper, and can be tuned to avoid the contribute of strong paramagnetic vessels. In fact, AD-MRI is based on water diffusion, and it involves the use of a range of b -values starting from 100 s/mm^2 to 5000 s/mm^2 , considering thus slower and faster dynamics. The contribution of vessels may be suppressed by considering b -values higher than about 200 s/mm^2 [122], which allows to eliminate the perfusion contribution of blood flowing in the vessels, affecting negligibly the estimation of AD- γ parameter. In conclusion, AD-MRI could be an alternative or complementary technique for the assessment of the bulk susceptibility inhomogeneity in *in vivo* studies on human brain.

5.5.7 Critical points, limitations and improvements

The set of diffusion sensitizing vectors used was sampled on a half sphere (**Figure 5.1**). An improvement in the acquisition will be simply obtained with the extension to the whole sphere, without duplicating the acquisition time. In fact, sampling on the whole sphere does not imply twice as many directions. From a diffusion perspective, sampling along v and $-v$ is exactly equivalent, thus the two schemes sample the diffusion evenly and equally well (and with the same total acquisition time). The advantage, besides, pertains to the optimization in the correction of eddy current distortions: a set of diffusion gradients spread on the whole sphere facilitates correcting for eddy currents [57, 123]. Furthermore, the whole-sphere scheme can be easily derived from the half-sphere scheme, replacing half the vectors by their negations.

A critical point of the data analysis is the use of thresholds to select only coherent WM fiber bundles. The conjecture here is that the choice of the threshold might bias the relation between AD-metrics and R_2^* . In order to quantify this possible bias, FA and v_1 thresholds were varied and the Pearson's correlation test between AD-metrics and R_2^* was repeated (**Figure 5.17**). The thresholds used are indicated in the plots by the red circles. The highest significance, indicated by arrows in the plots, is obtained applying very high thresholds (FA>0.7, v_1 >0.87), but already for v_1 >0.85 the number of voxels is considerably reduced, in a way that significantly affects the statistics.

A factor that potentially may have mitigated the dependence of the AD-metrics on $\Delta\chi$ is the fact that, according with De Santis et al. [22] the DTI reference frame approximation was used to extract M_γ , A_γ , $\gamma_{//}$ and γ_\perp , meaning that a coincidence between the DTI and AD reference frame was implied. In the present study, the projection of γ parameters along the DTI eigenvectors could hide part of the dependence of γ -imaging contrast on $\Delta\chi$. Therefore, it would be interesting to repeat this analysis by evaluating the AD-metrics in the reference frame of anomalous diffusion [21]. From a computational point of view this translates into the increasing of variables from 7 to 16, in order to estimate the $\vec{\gamma}$ -eigenvectors. The number of unknowns is still acceptable in a set-up with 15 b-values and 20 directions of acquisition.

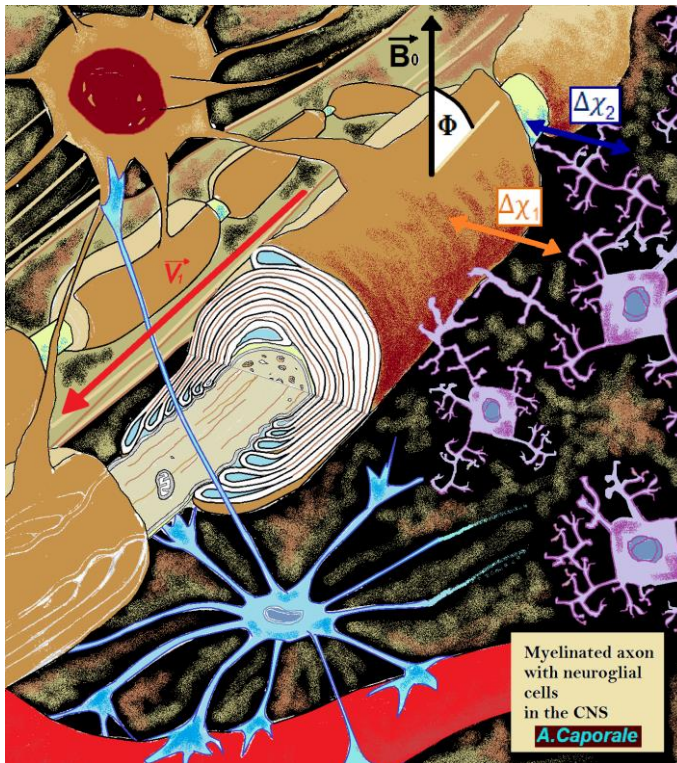


Figure 5.15 - Susceptibility anisotropy in WM with respect to the static magnetic field. The diagram shows the composite environment experienced by a diffusing water molecule in WM. The direction of the facilitated diffusivity of extracellular water is indicated by the main diffusion eigenvector, V_1 (red arrow). At the top left an oligodendrocyte myelinating a couple of axons through its processes is depicted. The cutaway view of the myelinated axon in the middle of the image illustrates the myelin sheath surrounding the axon, and forming cytoplasmic wedges at the proximity of the node of Ranvier (a few myelin layers have been depicted for the sake of clarity). An astrocyte, illustrated at the bottom in light blue, branches towards the oligodendrocyte, the axon and a capillary. Microglial cells colored in light purple are linked to the internodal myelin. The $\Delta\chi$ varies along the axonal direction, depending on the myelin sheath and its surroundings: $\Delta\chi_1$ arises at the interface between the internodal myelin and the extracellular water, or eventually, the microglia (highlighted by the orange double arrow); $\Delta\chi_2$ arises at the interface between the axonal membrane at the node of Ranvier and the interstitial water or glial cells (highlighted by the blue double arrow). From a macroscopic point of view, $\Delta\chi$ anisotropy is generated by the orientation of myelinated fibers with respect to the static magnetic field B_0 , indicated by Φ in the sketch. The drawing, realized by hand and with the help of Paint, is not in scale.

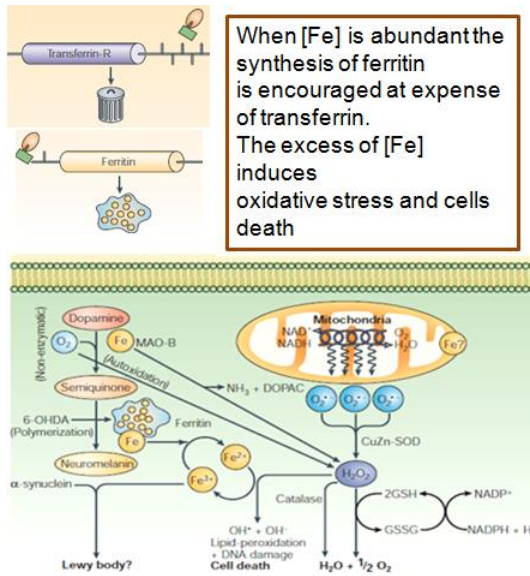


Figure 5.16 – Pictorial view of the oxidative stress hypothesis proposed by Zecca et al. [17], explaining the role of free iron and iron bounded to transport and storage proteins. Image reproduced and edited from the same paper.

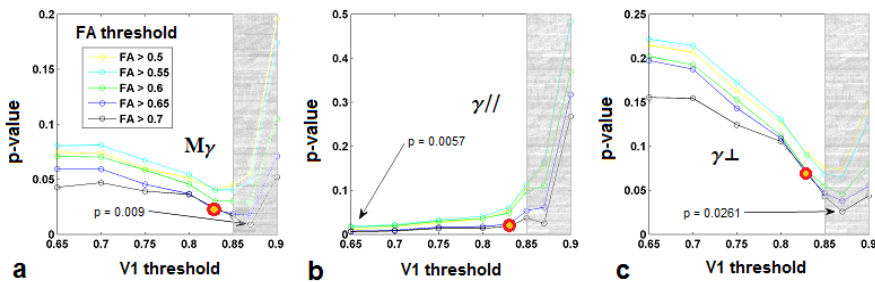


Figure 5.17 – Analysis of the effect of FA and V1-thresholds on the significance of correlations between AD-metrics and R_2^* . Significance of Pearson's correlation test between Mean- γ (My) (a), axial- γ ($\gamma//$) (b), radial- γ ($\gamma\perp$) (c) and R_2^* is plotted vs v_1 thresholds, reported on the x-axis, for different FA thresholds, listed in the legend. The P-values corresponding to the thresholds used for data analysis are indicated by the red circles in the plots. The minimum P-value is indicated by the arrow. The number of voxels is considerably reduced for v_1 thresholds higher than 0.85, represented by the gray region.

5.6 Conclusions

In this work, the dependence of the AD γ -imaging on magnetic susceptibility differences $\Delta\chi$ in the brain, due to myelin orientation with respect to \mathbf{B}_0 in the WM, and iron content in the GM was investigated. DW data by changing diffusion gradient strengths at a constant value of gradient duration Δ were acquired in a cohort of 25-years healthy subjects at 3.0 T. In this way the specific AD contrast of the derived γ -maps quantified the intravoxel diffusion heterogeneity in space, the so called *pseudo*-superdiffusion. The parameter γ was obtained essentially through a fit of a stretched exponential function to DW data, with the DTI-reference frame approximation.

At the state of the art in literature there is no specific study investigating the correlation between AD-metrics and the well known and established R_2^* parameter in vivo, and none of the papers concerning the applications of AD in in vivo studies provided information on the implications of SNR and b-value range selection in the estimation of γ and the related contrast.

The results obtained suggest that AD-metrics may reflect the inhomogeneity coming from $\Delta\chi$ among various tissues and compartments, and thus it might be useful as an indirect measure of myelin integrity and iron content.

There is an evident interplay between two factors affecting AD γ -contrast: on one hand the multi-compartmentalization (thus the different lengths by which water diffuse into heterogeneous media and complex systems such as the brain tissue), on the other hand the susceptibility differences between different compartments. This last feature of γ parameters is exclusively due to the fact that we quantify γ by using MRI techniques.

As the internal gradients generated by the difference of susceptibility increase with the increasing intensity of the magnetic field, this effect would be more remarkable at higher magnetic fields (7.0 T and higher).

A second conclusion of this work is related to its potential impact in non Gaussian diffusion applications at high magnetic fields. The employment of high-field MRI (7.0 T) scanners for human brain investigation is becoming more and more popular. Depending on $\Delta\chi$ driven magnetic field inhomogeneity, the new contrast provided by the AD- γ imaging could open new perspectives in all MRI fields in which it is important to detect local $\Delta\chi$ changes, such as superparamagnetic contrast molecular imaging, functional imaging (Balla, Sanchez-Panchuelo et al. 2014), and neuroimaging aimed at monitoring both

microstructural changes and alterations due to iron [124] or other
iron/paramagnetic impurities accumulation.

Conclusions

The objectives of this research activity were the evaluation of γ stretched exponent in biological tissues, the investigation of the contrast provided, and the clarification of the potential of AD- γ imaging in detecting microstructure characteristics of the tissues probed. A collateral but necessary goal to achieve was the implementation of the technique that allows to reconstruct 3D parametric maps of γ and related scalar invariants.

The investigation regarded the application of AD- γ imaging in *in vitro* and *in vivo* experiments. The *in vitro* study was planned to gain the required knowledge about the effective applicability of the technique, and to prepare the ground for the investigation of the two factors determining the peculiar contrast provided. For the *in vitro* study a fixed mouse spinal cord was sampled at high magnetic field (9.4 T). This choice was motivated by two reasons: the simple geometry of the spinal cord, with its cylindrical symmetry and a preferential longitudinal orientation of myelinated axons allowed to quantifying γ exponent related to *pseudo*-superdiffusion along 3 orthogonal directions; the use of high field was convenient for the enhancement of local internal gradients driven by magnetic susceptibility differences which are known to affect the γ -contrast.

Once tested *in vitro*, the AD- γ imaging was then applied to healthy human brains at magnetic field compatible with clinical studies (3.0 T). The *in vivo* application required additional knowledge and experimental trials to account for noise and distortions induced by the use of non-standard diffusion gradients (concerning intensity and their profile), and a particular pre-processing. Furthermore, the complex geometry of the brain, with the presence of bundles of myelinated fibers variously oriented with respect to the magnetic field required the estimation of a full γ -tensor. This tensor was derived in the reference frame extracted with conventional diffusion techniques (specifically DTI), and implementing a stretched fitting procedure with the use of sophisticated least-squared algorithm, yet with an acceptable computational cost.

The hypothesis of coincidence between the DTI-reference frame and the AD-reference frame is a first order approximation, that could present an intrinsic

limitation of this technique. However, it is in principle possible to estimate the γ -tensor in the specific reference frame of superdiffusion, with the introduction of more unknowns in the fitting procedure. This requires further investigation in the stability of the fitting procedure with respect to an increased number of variables.

Another major critical aspect is the need to maximize the signal without prolonging the acquisition time in *in vivo* studies. The total acquisition time strongly depends on the performances of the spectrometer used for the investigation, other than on the selected acquisition parameters. In particular, in this work the acquisitions were performed on a Siemens Allegra scanner at 3.0 T. This device is not equipped with modern features that allow a parallelization of imaging. With this implementation, the acquisition time would be reduced considerably (by setting a particular modality called SENSE to double the value used for this acquisition, the time required would be reduced of 50%). The advantage of acquiring in parallel modality is to halve the acquisition time, allowing to increase the number of same acquisitions, raising thus the signal to noise ratio of diffusion weighted images.

The results of the *in vitro* study on fixed mouse spinal cord confirm previous results concerning the contrast provided by pseudo-superdiffusion. In fact, parametric maps of γ showed to be able to highlight the interfaces between compartments with distinct magnetic properties, and the significant correlation found between γ and local magnetic inhomogeneity emerged here in the strong correlation between γ and $R2^*$. Moreover, I found that AD γ -imaging is potential able to detect microstructural information of white matter tracts in spinal cord more specific and complementary to those provided by DTI, through the correlation of AD-metrics with histological features of the investigated tracts, such as the axon diameter distribution and axonal density. These microstructural features are of paramount importance in the early diagnosis of several neurodegenerative diseases, such as Multiple Sclerosis, where the demyelination is tract specific and size selective, and occurs first in the smallest fibers.

In the *in vivo* study the dependence of the AD γ -imaging on magnetic susceptibility differences $\Delta\chi$ in the brain, due to myelin orientation with respect to \mathbf{B}_0 in the WM and iron content in the GM, was investigated in a cohort of 25-years healthy subjects at 3.0 T. I found that AD-metrics, differently from DTI-metrics, is significantly related to $R2^*$, and this suggests that AD-metrics may reflect the inhomogeneity coming from $\Delta\chi$ among various tissues

and compartments, and thus it might be useful as an indirect measure of myelin integrity and iron content. As the internal gradients generated by the difference of susceptibility increase with the increasing intensity of the magnetic field, this effect would be more remarkable at higher magnetic fields (7.0 T and higher). Recently the employment of high-field MRI (7.0 T) scanners for human brain investigation has spread. The new contrast provided by the AD- γ imaging, depending on $\Delta\chi$ driven magnetic field inhomogeneity, could open new perspectives in all MRI fields aimed at the detection of local $\Delta\chi$ changes, such as superparamagnetic contrast molecular imaging, functional imaging and neuroimaging aimed at monitoring both microstructural changes and alterations due to iron or iron deposition.

The correlation between AD-metrics and histological features of micro-compartments found in mouse spinal cord is of paramount importance in the early diagnosis of several neurodegenerative diseases, such as Multiple Sclerosis, where the demyelination is tract specific and size selective. The correlation between AD-metrics and magnetic inhomogeneity found in both mouse spinal cord and in human brain coming from $\Delta\chi$ among various tissues and compartments, might be useful as an indirect measure of myelin integrity and iron content. On the other hand, DTI-metrics didn't reflect magnetic susceptibility inhomogeneity neither in the *ex vivo* investigation, nor in the *in vivo* experiment. This lack of significant correlations between the conventional DTI-metrics with $\Delta\chi$ indicates that the techniques based on Anomalous Diffusion allow a more sensitive and specific investigation of tissue properties.

In conclusion, the two factors affecting the γ contrast, hence multi-compartmentalization and magnetic susceptibility inhomogeneity bestow the investigation of tissue microstructure through diffusion with an exquisite sensitivity and specificity. The outcomes of this research activity are promising concerning the perspective of adoption of AD- γ imaging as a novel diagnostic tool for *in vivo* assessment of myelin integrity and abnormal iron deposition in sub-cortical brain structures.

References

1. Bassler, P.J. and D.K. Jones, *Diffusion-tensor MRI: theory, experimental design and data analysis—a technical review*. NMR in Biomedicine, 2002. **15**(7-8): p. 456-467.
2. Jones, D.K., *Studying connections in the living human brain with diffusion MRI*. cortex, 2008. **44**(8): p. 936-952.
3. Le Bihan, D., et al., *Diffusion tensor imaging: concepts and applications*. Journal of magnetic resonance imaging, 2001. **13**(4): p. 534-546.
4. Sundgren, P., et al., *Diffusion tensor imaging of the brain: review of clinical applications*. Neuroradiology, 2004. **46**(5): p. 339-350.
5. Callaghan, P.T., *Translational dynamics and magnetic resonance: principles of pulsed gradient spin echo NMR*. 2011: Oxford University Press.
6. Salat, D., et al., *Age-related alterations in white matter microstructure measured by diffusion tensor imaging*. Neurobiology of aging, 2005. **26**(8): p. 1215-1227.
7. Song, S.-K., et al., *Dysmyelination revealed through MRI as increased radial (but unchanged axial) diffusion of water*. Neuroimage, 2002. **17**(3): p. 1429-1436.
8. Beaulieu, C., *The basis of anisotropic water diffusion in the nervous system—a technical review*. NMR in Biomedicine, 2002. **15**(7-8): p. 435-455.
9. Filippi, M., et al., *Diffusion tensor magnetic resonance imaging in multiple sclerosis*. Neurology, 2001. **56**(3): p. 304-311.
10. Lebel, C., et al., *Microstructural maturation of the human brain from childhood to adulthood*. Neuroimage, 2008. **40**(3): p. 1044-1055.
11. Caporale A, D.T.M., Nezzo M, Miano R, Mauriello A, Bove P, Manenti G, Capuani S *Differential diagnostic power of DTI parameters as a function of b-values to detect micro-structural changes due to prostate cancer*. 2017: Academic Radiology.
12. Nezzo, M., et al., *Mean diffusivity discriminates between prostate cancer with grade group 1&2 and grade groups equal to or greater than 3*. European Journal of Radiology, 2016. **85**(10): p. 1794-1801.
13. Moseley, M., et al., *Early detection of regional cerebral ischemia in cats: comparison of diffusion-and T2-weighted MRI and spectroscopy*. Magnetic resonance in medicine, 1990. **14**(2): p. 330-346.
14. DeLuca, G., G. Ebers, and M. Esiri, *Axonal loss in multiple sclerosis: a pathological survey of the corticospinal and sensory tracts*. Brain, 2004. **127**(5): p. 1009-1018.
15. Padhani, A.R., et al., *Diffusion-weighted magnetic resonance imaging as a cancer biomarker: consensus and recommendations*. Neoplasia, 2009. **11**(2): p. 102-125.

16. Barkhof, F., et al., *Comparison of MRI criteria at first presentation to predict conversion to clinically definite multiple sclerosis*. Brain, 1997. **120**(11): p. 2059-2069.
17. Zecca, L., et al., *Iron, brain ageing and neurodegenerative disorders*. Nature Reviews Neuroscience, 2004. **5**(11): p. 863-873. doi:10.1038/nrn1537.
18. De Santis, S., et al., *Why diffusion tensor MRI does well only some of the time: variance and covariance of white matter tissue microstructure attributes in the living human brain*. Neuroimage, 2014. **89**: p. 35-44.
19. Zhou, X.J., et al., *Studies of anomalous diffusion in the human brain using fractional order calculus*. Magnetic resonance in medicine, 2010. **63**(3): p. 562-569. doi:10.1002/mrm.22285.
20. Capuani, S., et al., *Spatio-temporal anomalous diffusion imaging: results in controlled phantoms and in excised human meningiomas*. Magnetic resonance imaging, 2013. **31**(3): p. 359-365. doi:10.1016/j.mri.2012.08.012.
21. Cavalieri, M., et al., *New insights into γ -stretched exponential Anomalous-Diffusion imaging experiments* Proceedings of the 21th scientific meeting, International Society for Magnetic Resonance in medicine. , 2013.
22. De Santis, S., et al., *Anisotropic anomalous diffusion assessed in the human brain by scalar invariant indices*. Magnetic resonance in medicine, 2011. **65**(4): p. 1043-1052. doi:10.1002/mrm.22689.
23. De Santis, S.a.C., S. . *Non-gaussian diffusion mr maps of human brain*. . in *International Society for Magnetic Resonance in Medicine, 17th Scientific Meeting*. 2009. Honolulu.
24. Ingo, C., et al., *On random walks and entropy in diffusion-weighted magnetic resonance imaging studies of neural tissue*. Magnetic resonance in medicine, 2014. **71**(2): p. 617-627. doi:10.1002/mrm.24706.
25. Palombo, M., et al., *Spatio-temporal anomalous diffusion in heterogeneous media by nuclear magnetic resonance*. The Journal of chemical physics, 2011. **135**(3): p. 034504. doi:10.1063/1.3610367.
26. Palombo, M., et al., *The γ parameter of the stretched-exponential model is influenced by internal gradients: validation in phantoms*. Journal of Magnetic Resonance, 2012. **216**: p. 28-36. doi:10.1016/j.jmr.2011.12.023.
27. GadElkarim, J.J., et al., *Fractional order generalization of anomalous diffusion as a multidimensional extension of the transmission line equation*. IEEE Journal on Emerging and Selected Topics in Circuits and Systems, 2013. **3**(3): p. 432-441. doi:10.1109/JETCAS.2013.2265795.
28. Magin, R.L., et al., *Anomalous diffusion expressed through fractional order differential operators in the Bloch–Torrey equation*. Journal of Magnetic Resonance, 2008. **190**(2): p. 255-270. doi:10.1016/j.jmr.2007.11.007.
29. Palombo, M., et al., *New insight into the contrast in diffusional kurtosis images: Does it depend on magnetic susceptibility?* Magnetic resonance in medicine, 2015. **73**(5).

30. Özarlan, E., et al., *Observation of anomalous diffusion in excised tissue by characterizing the diffusion-time dependence of the MR signal*. Journal of Magnetic Resonance, 2006. **183**(2): p. 315-323.
31. Metzler, R. and J. Klafter, *The random walk's guide to anomalous diffusion: a fractional dynamics approach*. Physics reports, 2000. **339**(1): p. 1-77.
32. Metzler, R. and J. Klafter, *The restaurant at the end of the random walk: recent developments in the description of anomalous transport by fractional dynamics*. Journal of Physics A: Mathematical and General, 2004. **37**(31): p. R161.
33. Caporale A, D.T.M., Nezzo M, Miano R, Mauriello A, Bove P, Capuani S, Manenti G. , *Pros and cons in the use of anomalous diffusion tensor imaging of the prostate at 3.0T*, in *ECR, Abstract Submission*. 2017: Vienna.
34. Guerreri M, C.A., Palombo M, De Berardinis I, Macaluso E, Bozzali M, Capuani S. *Anomalous diffusion parameters are sensible to microstructural variations in brain due to aging*. in *25th ISMRM meeting*. 2016.
35. Haacke, E.M., et al., *Correlation of putative iron content as represented by changes in R2* and phase with age in deep gray matter of healthy adults*. Journal of Magnetic Resonance Imaging, 2010. **32**(3): p. 561-576. doi:10.1002/jmri.22293.
36. Li, W., et al., *Association between increased magnetic susceptibility of deep gray matter nuclei and decreased motor function in healthy adults*. NeuroImage, 2015. **105**: p. 45-52. doi:10.1016/j.neuroimage.2014.10.009.
37. TODORICH, B.M. and J.R. CONNOR, *Redox metals in Alzheimer's disease*. Annals of the New York Academy of Sciences, 2004. **1012**(1): p. 171-178. doi:10.1196/annals.1306.014.
38. Li, W., et al., *Magnetic susceptibility anisotropy of human brain in vivo and its molecular underpinnings*. Neuroimage, 2012. **59**(3): p. 2088-2097. doi:10.1016/j.neuroimage.2011.10.038.
39. Sukstanskii, A.L. and D.A. Yablonskiy, *On the role of neuronal magnetic susceptibility and structure symmetry on gradient echo MR signal formation*. Magnetic resonance in medicine, 2014. **71**(1): p. 345-353. doi:10.1002/mrm.24629.
40. Yablonskiy, D.A. and A.L. Sukstanskii, *Biophysical mechanisms of myelin-induced water frequency shifts*. Magn Reson Med, 2014. **71**(6): p. 1956-1958. doi:10.1002/mrm.25214.
41. Caporale, A., et al., *The γ -parameter of Anomalous Diffusion quantified in human brain by MRI depends on local magnetic susceptibility differences*. NeuroImage, 2016.
42. Caporale A, P.M., Capuani S. *Anomalous diffusion stretched exponential gamma-imaging model provides new information on spinal cord microstructure*. in *23th ISMRM meeting Proceedings*. 2014. Toronto.

43. Caporale A, P.M., Wehrli F, Tata AM, Capuani S, *Anomalous diffusion stretched exponential gamma-imaging model provides new information on spinal cord microstructure*. 2017 - in preparation.
44. Caporale A, N.M., Di Trani MG, Miano R, Mauriello A, Bove P, Manenti G, Capuani S. , *Differential diagnostic power of DTI parameters as a function of b-values to detect micro-structural changes due to prostate cancer*, in *Magnetic Resonance Imaging*.
45. Levitt, M.H., *Spin dynamics: basics of NMR*. John Wiley&Sons, Chichester, 2001.
46. Callaghan, P.T., *Principles of nuclear magnetic resonance microscopy*. 1993: Oxford University Press on Demand.
47. Lauterbur, P.C., *Image formation by induced local interactions: examples employing nuclear magnetic resonance*. *Nature*, 1973. **242**: p. 190-191.
48. Mansfield, P., *Imaging by nuclear magnetic resonance*. *Journal of Physics E: Scientific Instruments*, 1988. **21**(1): p. 18.
49. Nishimura, D.G., *Principles of magnetic resonance imaging*. 1996: Stanford University.
50. Koay, C.G., Ozarslan, E, *Conceptual Foundations of Diffusion in Magnetic Resonance*. *Concepts in Magnetic Resonance Part A*, 2013. **42A** (4): p. 116–129.
51. Basser, P.J., J. Mattiello, and D. LeBihan, *MR diffusion tensor spectroscopy and imaging*. *Biophysical journal*, 1994. **66**(1): p. 259.
52. Kingsley, P.B., *Introduction to diffusion tensor imaging mathematics: Part I. Tensors, rotations, and eigenvectors*. *Concepts in Magnetic Resonance Part A*, 2006. **28**(2): p. 101-122.
53. Einstein, A., *Über die von der molekularkinetischen Theorie der Wärme geforderte Bewegung von in ruhenden Flüssigkeiten suspendierten Teilchen*. *Annalen der physik*, 1905. **322**(8): p. 549-560.
54. Stejskal, E.O. and J.E. Tanner, *Spin diffusion measurements: spin echoes in the presence of a time-dependent field gradient*. *The journal of chemical physics*, 1965. **42**(1): p. 288-292.
55. Tanner, J.E., *Use of the stimulated echo in NMR diffusion studies*. *The Journal of Chemical Physics*, 1970. **52**(5): p. 2523-2526.
56. Basser, P.J., J. Mattiello, and D. LeBihan, *Estimation of the effective self-diffusion tensor from the NMR spin echo*. *Journal of Magnetic Resonance, Series B*, 1994. **103**(3): p. 247-254.
57. Jones, D., M. Horsfield, and A. Simmons, *Optimal strategies for measuring diffusion in anisotropic systems by magnetic resonance imaging*. *Magn. Reson. Med.*, 1999. **42**.
58. Lee, S.H., *Temperature dependence on structure and self-diffusion of water: A molecular dynamics simulation study using SPC/E model*. *Bull. Korean Chem. Soc*, 2013. **34**(12): p. 3801.

59. Reischauer, C., et al., *High-resolution diffusion tensor imaging of prostate cancer using a reduced FOV technique*. European journal of radiology, 2011. **80**(2): p. e34-e41.
60. Bennett, K.M., et al., *Characterization of continuously distributed cortical water diffusion rates with a stretched-exponential model*. Magnetic resonance in medicine, 2003. **50**(4): p. 727-734.
61. Alexander, D.C., Barker, G. J. , and Arridge, S. R, *Detection and modeling of non-gaussian apparent diffusion coefficient profiles in human brain data*. Magn Reson Med, 2002. **48**(2): p. 331–340.
62. Mulkern, R.V., et al., *Multi-component apparent diffusion coefficients in human brain²*. NMR Biomed, 1999. **12**: p. 51-62.
63. Kim, J.H., et al., *Detecting axon damage in spinal cord from a mouse model of multiple sclerosis*. Neurobiology of disease, 2006. **21**(3): p. 626-632.
64. Watson, C., *The mouse nervous system*. 2012: Academic Press.
65. Cohen, Y., D. Anaby, and D. Morozov, *Diffusion MRI of the spinal cord: from structural studies to pathology*. NMR in Biomedicine, 2016.
66. Kim, T., et al., *Diffusion Tensor Imaging of Ex Vivo Cervical Spinal Cord Specimens: The Immediate and Long-Term Effects of Fixation on Diffusivity*. The Anatomical Record, 2009. **292**(2): p. 234-241.
67. Chin, C.L., et al., *Assessment of axonal fiber tract architecture in excised rat spinal cord by localized NMR q-space imaging: Simulations and experimental studies*. Magnetic resonance in medicine, 2004. **52**(4): p. 733-740.
68. Dula, A.N., et al., *Multiexponential T₂, magnetization transfer, and quantitative histology in white matter tracts of rat spinal cord*. Magnetic resonance in medicine, 2010. **63**(4): p. 902-909.
69. Peled, S., et al., *Water diffusion, T₂, and compartmentation in frog sciatic nerve*. Magnetic resonance in medicine: official journal of the Society of Magnetic Resonance in Medicine/Society of Magnetic Resonance in Medicine, 1999. **42**(5): p. 911.
70. Assaf, Y., et al., *New modeling and experimental framework to characterize hindered and restricted water diffusion in brain white matter*. Magnetic Resonance in Medicine, 2004. **52**(5): p. 965-978.
71. Sehy, J.V., J.J. Ackerman, and J.J. Neil, *Evidence that both fast and slow water ADC components arise from intracellular space*. Magnetic resonance in medicine, 2002. **48**(5): p. 765-770.
72. Chavhan, G.B., et al., *Principles, techniques, and applications of T₂*-based MR imaging and its special applications 1*. Radiographics, 2009. **29**(5): p. 1433-1449. doi:10.1148/rg.295095034.
73. Ong, H.H., et al., *Indirect measurement of regional axon diameter in excised mouse spinal cord with q-space imaging: simulation and experimental studies*. Neuroimage, 2008. **40**(4): p. 1619-1632.

74. Schwartz, E.D., et al., *Ex vivo evaluation of ADC values within spinal cord white matter tracts*. American journal of neuroradiology, 2005. **26**(2): p. 390-397.
75. Jenkinson, M., et al., *Fsl*. Neuroimage, 2012. **62**(2): p. 782-790. doi:10.1016/j.neuroimage.2011.09.015.
76. Ong, H.H. and F.W. Wehrli, *Quantifying axon diameter and intra-cellular volume fraction in excised mouse spinal cord with q-space imaging*. Neuroimage, 2010. **51**(4): p. 1360-1366.
77. Jones, D.K., T.R. Knösche, and R. Turner, *White matter integrity, fiber count, and other fallacies: the do's and don'ts of diffusion MRI*. Neuroimage, 2013. **73**: p. 239-254. doi:10.1016/j.neuroimage.2012.06.081.
78. Bergers, E., et al., *Axonal damage in the spinal cord of MS patients occurs largely independent of T2 MRI lesions*. Neurology, 2002. **59**(11): p. 1766-1771.
79. Salzer, J.L., *Clustering sodium channels at the node of Ranvier: close encounters of the axon–glia kind*. Neuron, 1997. **18**(6): p. 843-846.
80. Caporale, A., Palombo, M., Macaluso E., Guerreri M., Bozzali M., Capuani S, *The γ -parameter of Anomalous Diffusion quantified in human brain by MRI depends on local magnetic susceptibility differences*. 2016: NeuroImage.
81. Saladin, K.S., *Anatomy & physiology*. 1998: WCB/McGraw-Hill.
82. Mori, S., et al., *Stereotaxic white matter atlas based on diffusion tensor imaging in an ICBM template*. Neuroimage, 2008. **40**(2): p. 570-582. doi:10.1016/j.neuroimage.2007.12.035.
83. Aboitiz, F., et al., *Individual differences in brain asymmetries and fiber composition in the human corpus callosum*. Brain research, 1992. **598**(1-2): p. 154-161. doi:10.1016/0006-8993(92)90179-D.
84. Lodygensky, G.A., et al., *In vivo assessment of myelination by phase imaging at high magnetic field*. Neuroimage, 2012. **59**(3): p. 1979-1987.
85. Lee, J., et al., *Sensitivity of MRI resonance frequency to the orientation of brain tissue microstructure*. Proceedings of the National Academy of Sciences, 2010. **107**(11): p. 5130-5135. doi:10.1073/pnas.0910222107.
86. Liu, C., *Susceptibility tensor imaging*. Magnetic resonance in medicine, 2010. **63**(6): p. 1471-1477. doi:10.1002/mrm.22482.
87. Blazejewska, A.I., et al., *Increase in the iron content of the substantia nigra and red nucleus in multiple sclerosis and clinically isolated syndrome: A 7 Tesla MRI study*. Journal of Magnetic Resonance Imaging, 2015. **41**(4): p. 1065-1070.
88. Schmierer, K., et al., *High field (9.4 Tesla) magnetic resonance imaging of cortical grey matter lesions in multiple sclerosis*. Brain, 2010. **133**(3): p. 858-867. doi:10.1093/brain/awp335.
89. Tepper, S.J., et al., *Iron Deposition in Pain-Regulatory Nuclei in Episodic Migraine and Chronic Daily Headache by MRI*. Headache: The Journal of

- Head and Face Pain, 2012. **52**(2): p. 236-243. doi:10.1111/j.1526-4610.2011.02056.x.
90. Duyn, J.H., et al., *High-field MRI of brain cortical substructure based on signal phase*. Proceedings of the National Academy of Sciences, 2007. **104**(28): p. 11796-11801. doi:10.1073/pnas.0610821104.
 91. Langkammer, C., et al., *Susceptibility induced gray–white matter MRI contrast in the human brain*. Neuroimage, 2012. **59**(2): p. 1413-1419. doi:10.1016/j.neuroimage.2011.08.045.
 92. Jenkinson, M., et al., *Improved optimization for the robust and accurate linear registration and motion correction of brain images*. Neuroimage, 2002. **17**(2): p. 825-841. doi:10.1006/nimg.2002.1132.
 93. Graham, M.S., I. Drobnyak, and H. Zhang, *Realistic simulation of artefacts in diffusion MRI for validating post-processing correction techniques*. Neuroimage, 2016. **125**: p. 1079-1094. doi:10.1016/j.neuroimage.2015.11.006.
 94. Luszczek, P., *Parallel programming in MATLAB*. International Journal of High Performance Computing Applications, 2009. **23**(3): p. 277-283. doi:10.1177/1094342009106194.
 95. Descoteaux, M., et al., *Multiple q-shell diffusion propagator imaging*. Medical image analysis, 2011. **15**(4): p. 603-621. doi:10.1016/j.media.2010.07.001.
 96. Jones, D.K. and P.J. Basser, *“Squashing peanuts and smashing pumpkins”: How noise distorts diffusion-weighted MR data*. Magnetic Resonance in Medicine, 2004. **52**(5): p. 979-993.
 97. Cherubini, A., et al., *Characterization of white matter fiber bundles with T₂* relaxometry and diffusion tensor imaging*. Magnetic resonance in medicine, 2009. **61**(5): p. 1066-1072. doi:10.1002/mrm.21978.
 98. Desikan, R.S., et al., *An automated labeling system for subdividing the human cerebral cortex on MRI scans into gyral based regions of interest*. Neuroimage, 2006. **31**(3): p. 968-980. doi:10.1016/j.neuroimage.2006.01.021.
 99. Hallgren, B. and P. Sourander, *The effect of age on the non-haemin iron in the human brain*. Journal of neurochemistry, 1958. **3**(1): p. 41-51. doi:10.1111/j.1471-4159.1958.tb12607.x.
 100. Li, W., B. Wu, and C. Liu, *Quantitative susceptibility mapping of human brain reflects spatial variation in tissue composition*. Neuroimage, 2011. **55**(4): p. 1645-1656. doi:10.1016/j.neuroimage.2010.11.088.
 101. Field, A., *Discovering statistics using IBM SPSS statistics*. 2013: Sage.
 102. Li, T.Q., et al., *Characterization of T₂* heterogeneity in human brain white matter*. Magnetic resonance in medicine, 2009. **62**(6): p. 1652-1657. doi:10.1002/mrm.22156.

103. Nam, Y., D. Han, and D.-H. Kim, *Single-scan R² measurement with macroscopic field inhomogeneity correction*. Neuroimage, 2012. **63**(4): p. 1790-1799. doi:10.1016/j.neuroimage.2012.08.062.
104. Rudko, D.A., et al., *Origins of R²* orientation dependence in gray and white matter*. Proceedings of the National Academy of Sciences, 2014. **111**(1): p. E159-E167. doi:10.1073/pnas.1306516111.
105. Gelman, N., et al., *MR imaging of human brain at 3.0 T: preliminary report on transverse relaxation rates and relation to estimated iron content*. Radiology, 1999. **210**(3): p. 759-767. doi:10.1148/radiology.210.3.r99fe41759.
106. Mitsumori, F., et al., *Toward understanding transverse relaxation in human brain through its field dependence*. Magnetic resonance in medicine, 2012. **68**(3): p. 947-953. doi:10.1002/mrm.23301.
107. Yao, B., et al., *Susceptibility contrast in high field MRI of human brain as a function of tissue iron content*. Neuroimage, 2009. **44**(4): p. 1259-1266. doi:10.1016/j.neuroimage.2008.10.029.
108. Nair, G., et al., *Myelination and long diffusion times alter diffusion-tensor-imaging contrast in myelin-deficient shiverer mice*. Neuroimage, 2005. **28**(1): p. 165-174. doi:10.1016/j.neuroimage.2005.05.049.
109. Budde, M.D. and J.A. Frank, *Neurite beading is sufficient to decrease the apparent diffusion coefficient after ischemic stroke*. Proceedings of the National Academy of Sciences, 2010. **107**(32): p. 14472-14477. doi: 10.1073/pnas.1004841107.
110. Jensen, J.H., et al., *Diffusional kurtosis imaging: The quantification of non-gaussian water diffusion by means of magnetic resonance imaging*. Magnetic Resonance in Medicine, 2005. **53**(6): p. 1432-1440.
111. Ronen, I., et al., *Microstructural organization of axons in the human corpus callosum quantified by diffusion-weighted magnetic resonance spectroscopy of N-acetylaspartate and post-mortem histology*. Brain Structure and Function, 2014. **219**(5): p. 1773-1785. doi:10.1007/s00429-013-0600-0.
112. Lounila, J., et al., *Effects of orientational order and particle size on the NMR line positions of lipoproteins*. Physical review letters, 1994. **72**(25): p. 4049. doi:10.1103/PhysRevLett.72.4049.
113. Duyn, J., *MR susceptibility imaging*. Journal of magnetic resonance, 2013. **229**: p. 198-207. doi:10.1016/j.jmr.2012.11.013.
114. Chen, W.C., S. Foxley, and K.L. Miller, *Detecting microstructural properties of white matter based on compartmentalization of magnetic susceptibility*. Neuroimage, 2013. **70**: p. 1-9. doi:10.1016/j.neuroimage.2012.12.032.
115. Denk, C., et al., *The influence of white matter fibre orientation on MR signal phase and decay*. NMR in Biomedicine, 2011. **24**(3): p. 246-252. doi:10.1002/nbm.1581.

116. Sati, P., et al., *In vivo quantification of T_2 anisotropy in white matter fibers in marmoset monkeys*. *Neuroimage*, 2012. **59**(2): p. 979-985. doi:10.1016/j.neuroimage.2011.08.064.
117. Di Pietro, G., M. Palombo, and S. Capuani, *Internal magnetic field gradients in heterogeneous porous systems: comparison between Spin-Echo and Diffusion Decay Internal Field (DDIF) method*. *Applied Magnetic Resonance*, 2014. **45**(8): p. 771-784. doi:10.1007/s00723-014-0556-0.
118. Mitchell, J., et al., *Nuclear magnetic resonance relaxation and diffusion in the presence of internal gradients: the effect of magnetic field strength*. *Physical Review E*, 2010. **81**(2): p. 026101. doi:10.1103/PhysRevE.81.026101.
119. Gong, N.-J., et al., *Aging in deep gray matter and white matter revealed by diffusional kurtosis imaging*. *Neurobiology of aging*, 2014. **35**(10): p. 2203-2216. doi:10.1016/j.neurobiolaging.2014.03.011.
120. Shmueli, K., et al., *Magnetic susceptibility mapping of brain tissue in vivo using MRI phase data*. *Magnetic resonance in medicine*, 2009. **62**(6): p. 1510-1522.
121. Haacke, E.M., et al., *Quantitative susceptibility mapping: current status and future directions*. *Magnetic resonance imaging*, 2015. **33**(1): p. 1-25.
122. Le Bihan, D., et al., *Separation of diffusion and perfusion in intravoxel incoherent motion MR imaging*. *Radiology*, 1988. **168**(2): p. 497-505.
123. Kingsley, P.B., *Introduction to diffusion tensor imaging mathematics: Part III. Tensor calculation, noise, simulations, and optimization*. *Concepts in magnetic resonance part A*, 2006. **28**(2): p. 155-179.
124. Fujiwara, S., et al., *Quantification of iron in the non-human primate brain with diffusion-weighted magnetic resonance imaging*. *Neuroimage*, 2014. **102**: p. 789-797.
125. Fitzpatrick, R., *Oscillations and waves: An introduction*. 2013: CRC Press.

Appendix A – Basics and collateral knowledge

A1. The Polarization of Electromagnetic Waves

The electric component of an electromagnetic plane wave can oscillate in any direction normal to the direction of wave propagation (which is parallel to the so called \mathbf{k} -vector). Suppose that the wave is propagating in the z-direction. It follows that the electric field can oscillate in any direction that lies in the x-y plane. The actual direction of oscillation determines the *polarization* of the wave. For instance, a vacuum electromagnetic wave of angular frequency ω that is polarized in the x-direction has the associated electric field:

$$\mathbf{E} = E_0 \cos(\omega t - kz)\mathbf{e}_x \quad (\text{A.1})$$

where $\omega = k \cdot c$. Likewise, a wave polarized in the y-direction has the electric field:

$$\mathbf{E} = E_0 \cos(\omega t - kz)\mathbf{e}_y \quad (\text{A.2})$$

These two waves are termed *linearly polarized*, since the electric field vector oscillates in a straight-line. However, other types of polarization are possible. For instance, if we combine two linearly polarized waves of equal amplitude, one polarized in the x-direction, and one in the y-direction, that oscillate $\pi/2$ radians out of phase, then we obtain a *circularly polarized* wave:

$$\mathbf{E} = E_0 \cos(\omega t - kz)\mathbf{e}_x + E_0 \sin(\omega t - kz)\mathbf{e}_y \quad (\text{A.3})$$

This nomenclature arises from the fact that the tip of the electric field vector traces out a circle in the plane normal to the direction of wave propagation. To be more exact, the previous wave is a *right-hand* circularly polarized wave, since if the thumb of the right-hand points in the direction of wave propagation then the electric field vector rotates in the same sense as the fingers of this hand. Conversely, a left-hand circularly polarized wave takes the form:

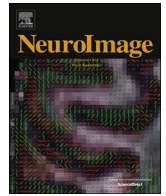
$$\mathbf{E} = E_0 \cos(\omega t - kz)\mathbf{e}_x - E_0 \sin(\omega t - kz)\mathbf{e}_y \quad (\text{A.4})$$

Finally, if the x- and y-components of the electric field in the previous two expressions have different (non-zero) amplitudes then we obtain right-hand and left-hand *elliptically polarized* waves, respectively. This nomenclature

arises from the fact that the tip of the electric field vector traces out an ellipse in the plane normal to the direction of wave propagation [125].

Appendix B – Scientific dissemination

B1 - The γ -parameter of Anomalous Diffusion quantified in human brain by MRI depends on local magnetic susceptibility differences



The γ -parameter of anomalous diffusion quantified in human brain by MRI depends on local magnetic susceptibility differences

A. Caporale^{a,b,*}, M. Palombo^{b,c}, E. Macaluso^d, M. Guerreri^{b,e}, M. Bozzali^f, S. Capuani^b

^a Morpho-functional Sciences, Department of Anatomical, Histological, Forensic and of the Locomotor System Science, Sapienza University of Rome, Italy

^b CNR ISC UOS Roma Sapienza, Physics Department Sapienza University of Rome, Rome, Italy

^c MIRcen, CEA/DSV/I²BM, Fontenay-aux-Roses, France

^d ImpAct Team, Lyon Neuroscience Research Center, Lyon, France

^e Morphogenesis & Tissue Engineering, Department of Anatomical, Histological, Forensic and of the Locomotor System Science, Sapienza University of Rome, Italy

^f Neuroimaging Laboratory Santa Lucia Foundation, Rome, Italy

ARTICLE INFO

Keywords:

Anomalous diffusion imaging
 R_2^*
 Magnetic susceptibility difference
 DTI
 Iron

ABSTRACT

Motivated by previous results obtained in vitro, we investigated the dependence of the anomalous diffusion (AD) MRI technique on local magnetic susceptibility differences ($\Delta\chi$) driven by magnetic field inhomogeneity in human brains. The AD-imaging contrast investigated here is quantified by the stretched-exponential parameter γ , extracted from diffusion weighted (DW) data collected by varying diffusion gradient strengths. We performed T_2^* and DW experiments in eight healthy subjects at 3.0 T. T_2^* -weighted images at different TEs=(10,20,35,55) ms and DW-EPI images with fourteen b-values from 0 to 5000 s/mm² were acquired. AD-metrics and Diffusion Tensor Imaging (DTI) parameters were compared and correlated to R_2^* and to $\Delta\chi$ values taken from literature for the gray (GM) and the white (WM) matter. Pearson's correlation test and Analysis of Variance with Bonferroni post-hoc test were used. Significant strong linear correlations were found between AD γ -metrics and R_2^* in both GM and WM of the human brain, but not between DTI-metrics and R_2^* . Depending on $\Delta\chi$ driven magnetic field inhomogeneity, the new contrast provided by AD- γ imaging reflects $\Delta\chi$ due to differences in myelin orientation and iron content within selected regions in the WM and GM, respectively. This feature of the AD- γ imaging due to the fact that γ is quantified by using MRI, may be an alternative strategy to investigate, at high magnetic fields, microstructural changes in myelin, and alterations due to iron accumulation. Possible clinical applications might be in the field of neurodegenerative diseases.

1. Introduction

Within the past few years there has been much effort to improve Magnetic Resonance imaging (MRI) techniques to provide susceptibility maps, such as gradient echo (GRE) phase imaging (Rauscher et al., 2005), Susceptibility Weighted-Imaging (SWI) (Haacke et al., 2004), Quantitative Susceptibility Mapping (QSM) (Duyn et al., 2007) and Susceptibility Tensor Imaging (STI) (Liu, 2010). Indeed, quantifying susceptibility is profitable because its variations are related to abnormally increased iron concentrations that characterize some neurological diseases such as Parkinson's disease (Zecca et al., 2004), Alzheimer's disease (Todorich and Connor, 2004), Multiple Sclerosis (Schmierer et al., 2010), and other disabling disorders such as migraine and chronic daily headache (Tepper et al., 2012). On the other hand,

the evaluation of iron content in vivo is a practical problem that has not a reliable and sensitive method to be solved, despite the efforts done so far (Bartzokis et al., 1997, 2007; Pfefferbaum et al., 2010). Moreover, the quantification of magnetic susceptibility differences ($\Delta\chi$) at the interface between neighbouring tissues could be of great help for highlighting tissues oriented along different directions compared to the main magnetic field (Chen et al., 2013). In this regard, STI quantifies the amount of magnetic susceptibility anisotropy, which is due to the micro-architecture and chemical arrangement of the neural tissue being probed (Lee et al., 2010; Liu, 2010). However, in order to compute the susceptibility tensor it is necessary to acquire the signal along at least six different orientations of the sample with respect to the static magnetic field \mathbf{B}_0 (Liu, 2010). This represents an intrinsic limitation of STI imaging, since the sample rotation is hardly practic-

Abbreviations: AD, Anomalous Diffusion; DW, Diffusion Weighted; GM, Gray Matter; ROI, Region Of Interest; SD, Standard Deviation; SEM, Standard Error of the Mean; T_2^* WIs, T_2^* Weighted Images; VOI, Volume Of Interest; WM, White Matter

* Corresponding author at: CNR ISC UOS Roma Sapienza, Physics Department, Sapienza University of Rome, Piazzale Aldo Moro, 5, 00185, Rome, Italy.

E-mail address: alessandra.stella.caporale@gmail.com (A. Caporale).

<http://dx.doi.org/10.1016/j.neuroimage.2016.12.051>

Received 11 July 2016; Accepted 19 December 2016

Available online 21 December 2016

1053-8119/© 2016 Elsevier Inc. All rights reserved.

able in the case of clinical applications in humans.

In anomalous diffusion (AD) models, γ -maps representative of the stretching parameter γ derived from fitting a stretched function $S(b) = S(0)\exp(-(\delta D)^\gamma)$ to diffusion weighted (DW) data, provide an interesting and novel source of contrast in MRI (Magin et al., 2008; De Santis et al., 2011; Hall and Barrick, 2012; Ingo et al., 2014). By using a tensor representation of AD, scalar invariant indices such as the mean γ (M_γ) and the γ anisotropy (A_γ) can be quantified in cerebral tissues (De Santis et al., 2011). In particular, the AD contrast obtained by using DW data acquired as a function of b-values and collected by changing diffusion gradient (g_{diff}) strength at a constant value of Δ is due to intravoxel diffusion heterogeneity in space. Specifically, water molecules diffuse with considerably different free lengths, and this mechanism is quantified by the stretched exponential parameter γ . Some authors indicate this peculiar AD mechanism as 'water jumping', formally derived in the space fractional derivatives approach (Magin et al., 2008; Ingo et al., 2014); other authors refer to this mechanism with the expression 'pseudo-superdiffusion' processes (Palombo et al., 2011, 2012; Capuani et al., 2013) due to both water multi-compartmentalization and $\Delta\chi$ at the interface between different compartments (Palombo et al., 2012). In vitro studies performed by Capuani et al. on phantoms with capillaries filled with polystyrene micro-beads dispersed in water (Palombo et al., 2011, 2012; Capuani et al., 2013) showed a strong inverse correlation between measured internal gradients (G_{int}) generated by $\Delta\chi$ and the γ parameter. This strong correlation can be explained considering the coupling between diffusion gradients (g_{diff}) and G_{int} which causes an irreversible DW signal loss that can be modeled as a pseudo-superdiffusion process. Specifically, local gradients induce a phase shift to the spins within a space region strictly close to the interfaces, which adds up to the phase shift given by the g_{diff} pulse, namely originating an effective gradient $G_{eff} = G_{int} + g_{diff}$. When G_{int} and g_{diff} are in the same order of magnitude, some spins contribute to increase the DW signal attenuation; other spins (that can be located far from the first ones) acquire a phase that will help to increase the signal. Due to indistinguishable spins associated with water molecules, this scenario mimics a superdiffusion regime. The water signal disappears in one spot and appears in another one, thus simulating long jumps of water molecules.

In γ -MRI the water diffusion is analyzed by means of the AD-model, and this contrast mechanism seems to increase the sensitivity of the technique to tissue interfaces. This suggests a dependence of the signal of diffusing spins on local magnetic inhomogeneities (Palombo et al., 2012; Capuani et al., 2013). Magnetic inhomogeneities can be quantified by G_{int} (De Santis et al., 2010) or by the transverse relaxation rate ($R_2^* = 1/T_2^*$). An alternative approach to take into account field inhomogeneity is modeling the T2 decay as fractional order (Reiter et al., 2016).

The $\Delta\chi$ inhomogeneity in the brain parenchyma mainly arises from the presence of diamagnetic myelin sheaths and paramagnetic iron-laden cells, and determines local magnetic field distortions, which affect both the magnitude and phase of the MR signal (Yablonskiy and Haacke, 1994). In the white matter (WM) the iron content does not vary substantially across fiber bundles (Li et al., 2009), nor does myelin density, despite the presence of magnitude and frequency differences in GRE signal observed among myelinated fibers. It is rather the orientation of myelinated fiber bundles with respect to \mathbf{B}_0 that affects both phase and amplitude of the GRE signal decay (Yablonskiy and Haacke, 1994; Chen et al., 2013; Rudko et al., 2014). Indeed, recent studies showed that R_2^* in WM tracts perpendicular to \mathbf{B}_0 is double than that of in parallel fibers (Sati et al., 2012).

In this work, we aim at highlighting, for the first time in brain tissue, that AD γ -metrics, which are known to depend on water multi-compartmentalization, also depend on magnetic susceptibility, when quantified by DW-MRI. The working hypothesis of the γ -imaging method is that γ -contrast embodies information deriving from both $\Delta\chi$ -maps and DW-maps. Therefore, with the goal of investigating the

potential ability of γ MRI technique in reflecting the $\Delta\chi$ anisotropy distribution in human brains, we planned to obtain AD (M_γ , A_γ , axial- γ and radial- γ) and R_2^* parametric maps of the human brain in 8 healthy subjects, and test the correlation between the AD-derived parameters and R_2^* . Mean values of AD-metrics in WM regions including fibers with different orientations with respect to \mathbf{B}_0 and in GM regions characterized by different iron contents will be investigated, and compared with values of $\Delta\chi$ taken from literature, and with measured R_2^* .

2. Materials and methods

2.1. Data acquisition

This study was approved by the Scientific Ethics Committee of Santa Lucia Foundation (Rome, Italy). Eight healthy volunteers (4 men, 4 women; mean age \pm standard deviation [SD] = 25 ± 1 years) participated in this study, after providing informed written consent, according to the national laws and to the local ethics committee guidelines. None of the subjects had a history of stroke or head injury, nor of any other neurological or psychiatric disease. The volunteers underwent MRI examination using a 3.0 T Siemens Magnetom Allegra (Siemens Medical Solutions, Erlangen, Germany), with a circularly polarized transmit-receive coil. The maximum gradient strength was 40 mT/m with a maximum slew rate of 400 T/m/s. The same MRI protocol was applied to all the subjects, including T_2^* -weighted images (T_2^* WIs), and Diffusion Tensor Imaging (DTI) scanning. Particular care was taken to center the subject in the head coil and to restrain the subject's movements with cushions and adhesive medical tape.

T_2^* WIs were acquired using an Echo Planar Imaging sequence (EPI) with TR=5000 ms, flip-angle=90°, 4 different TEs=(10, 20, 35, 55) ms, matrix size=128×128, number of axial slices=32; slice thickness=3 mm, in-plane resolution=1.8×1.8 mm²; Diffusion-Weighted Double Spin-Echo-Echo Planar Imaging (DW DSE-EPI) was acquired with TR/TE=6400 ms/107 ms; Δ/δ =72 ms/35 ms, and with the same geometry of T_2^* WIs. DW-Images (DWIs) were collected by using Diffusion-sensitizing gradients along 20 non-collinear directions at 14 different b-values (100, 200, 300, 400, 500, 700, 800, 1000, 1500, 2000, 2500, 3000, 4000, 5000) s/mm² plus the b=0 (b0) image with no diffusion weighting. The b-values were changed by varying the diffusion gradient strength and keeping Δ and δ constant. The number of sample averages (NSA) was 2 for each b-value, and the total acquisition time for the DW DSE-EPI protocol (applied without the use of parallel imaging) was approximately 52 min. An anterior-posterior phase encoding direction was used for all the scans. The axial slice package was positioned parallel to the anterior-posterior commissure axis and perpendicular to the mid-sagittal plane.

2.2. Data analysis

All the schematic steps describing the image processing are illustrated in Fig. 1.

The pre-processing of data was performed with the use of FMRIB Software Library, v5.0 (FSL, (Jenkinson et al., 2012)). The T_2^* WIs were realigned to the image acquired with TE=10 ms, in order to correct for head movements, via a 6 degrees of freedom (DOF) transformation, using the FSL linear image registration tool (FLIRT) (Jenkinson et al., 2002). The T_2^* WI acquired with TE=10ms was then registered to the b0-image, via a 12 DOF affine transformation with Normalized-Correlation cost function and tri-linear interpolation. Finally, the combination of the two transformation matrices was applied to all T_2^* WIs. The DWIs were realigned with respect to the b0 and corrected for eddy-current induced distortions and subjects' movements, adopting the b0-image as a reference image, with the use of EDDY tool, which had shown better performances compared to the FSL's earlier *eddy_correct* function (Graham et al., 2016). The DTI

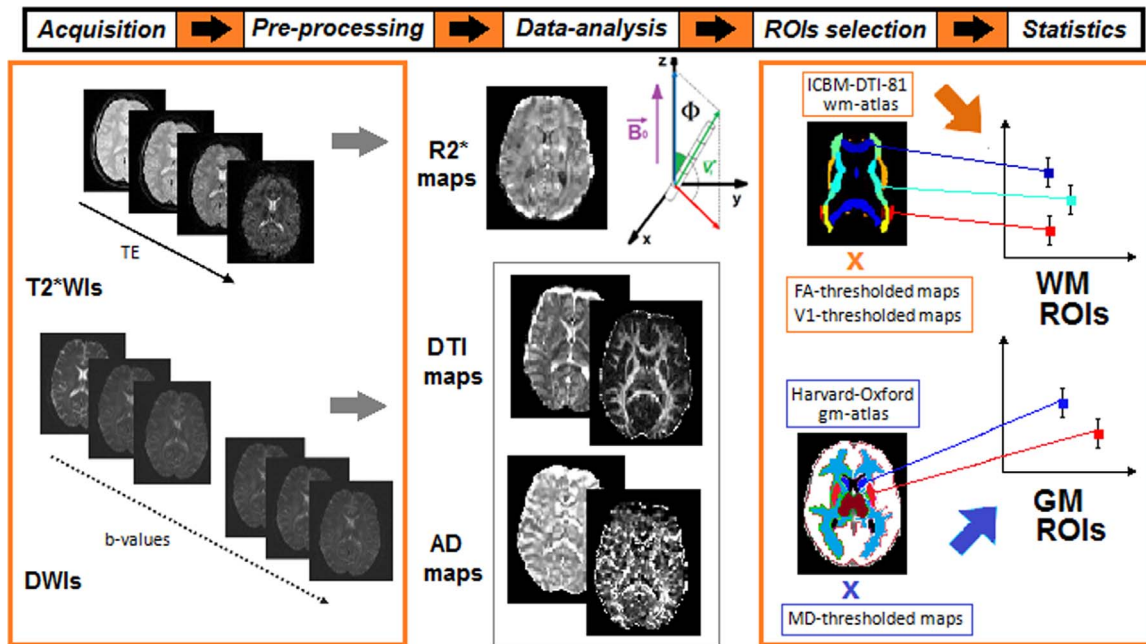


Fig. 1. Data analysis flow-chart. Schematic representation of data acquisition, pre-processing and post-processing, with the indication of the criteria followed for the selection of the regions of interest (ROIs). More details are reported in Section 2.2.

maps were extracted using all the DWIs acquired up to $b=1500$ s/mm² with DTIFIT tool, which returns the maps of eigenvalues ($\lambda_1, \lambda_2, \lambda_3$, with $\lambda_1 > \lambda_2 > \lambda_3$), eigenvectors ($\mathbf{v}_1, \mathbf{v}_2, \mathbf{v}_3$), Mean Diffusivity (MD) and Fractional Anisotropy (FA). The axial ($D_{//}$) and radial (D_{\perp}), diffusivities were computed as follows: $D_{//} = \lambda_1$, $D_{\perp} = (\lambda_2 + \lambda_3)/2$. The T2*WIs and the DWIs were filtered using pixel-wise adaptive Wiener filtering (window size of 2x2 pixels) in MATLAB R2012b (MATLAB Release 2012b, The MathWorks, Inc., Natick, Massachusetts, United States). Custom-made MATLAB scripts were employed to extract R_2^* from the set of T2*WIs with a linear least-square fitting, and to extract the γ -exponents ($\gamma_1, \gamma_2, \gamma_3$, with $\gamma_1 > \gamma_2 > \gamma_3$) projected along the three axes of DTI-reference frame (DTI-rf) (De Santis et al., 2011) from the set of DWIs acquired up to $b=5000$ s/mm², using trust-region-reflective least square algorithm for minimization with a non-linear fitting procedure and parallel computing (Luszczek, 2009; Sharma and Martin, 2009). The choice of projecting the stretched γ -exponents along the axes of DTI-rf is based on the assumption that, to a first approximation, the AD and Gaussian diffusion share the same rotationally invariant reference frame (De Santis et al., 2011). From a computational point of view, this assumption corresponds to inserting the computed diffusion eigenvectors as fixed inputs within the theoretical expression used to fit the experimental DW-data. The algorithm used in the fitting procedure requires an initialization of the parameters to be estimated. In order to test for the stability of the fit, we performed the fit by initializing the γ -exponents to 1.0, and to 0.75. The differences found in the estimated γ -exponents were in the order of 10^{-4} , thus we proved that the fit was quite stable. Therefore, we initialized the stretched exponents to 1.0, since this is the value corresponding to Gaussian diffusion, and we expected to compute slightly inferior values in the analyzed tissue (De Santis et al., 2011). Once estimated the projected γ -exponents, the following AD-parameters were computed: mean- γ ($M\gamma = \frac{\gamma_1 + \gamma_2 + \gamma_3}{3}$), axial- γ ($\gamma_{//} = \gamma_1$), radial- γ ($\gamma_{\perp} = \frac{\gamma_2 + \gamma_3}{2}$), γ -anisotropy ($A\gamma = \sqrt{\frac{3[(\gamma_1 - M\gamma)^2 + (\gamma_2 - M\gamma)^2 + (\gamma_3 - M\gamma)^2]}{2(\gamma_1^2 + \gamma_2^2 + \gamma_3^2)}}$), where $\gamma_{//}$ represented the projection of the anomalous exponent in the direction described by the first eigenvector \mathbf{v}_1 of the Gaussian diffusion tensor, whereas γ_{\perp} was derived by an average of the other two orthogonal projections. Parametric maps of each subject were produced for DTI-metrics, AD-metrics and R_2^* .

2.2.1. Signal to Noise Ratio, and γ dependence on SNR

Since low Signal to Noise Ratio (SNR) of DWIs acquired at higher b-values is an obvious drawback for non Gaussian diffusion techniques, we assessed both the SNR of each DW image acquired at a certain b-value and the consequences of a low SNR on the gamma parameter estimation.

In order to estimate the SNR of DWIs we followed the strategy adopted in several recent papers (Descoteaux et al., 2011; Jones et al., 2013). Considering axial slices, we selected an area in the splenium of the corpus callosum to compute the signal, and an area placed outside the brain to compute the background noise, and took the ratio between the mean of the signal and the SD of the noise, as a function of the b-value and of the diffusion gradient direction. The average value of SNR over the cohort of subjects was then computed. We chose the splenium of the corpus callosum because of its stressed directionality, which is left-right oriented with respect to the laboratory frame. Since we expect the most attenuated DW signal along the direction of the facilitated diffusion, that is along the main axonal direction, the SNR in the left-right (x) direction represents a good indication of the quality of the DW-data (Descoteaux et al., 2011; Jones et al., 2013). We considered the SNR of the splenium of the corpus callosum as representative for the SNR in WM. We also considered an area placed in the right thalamus, to estimate the SNR in the GM, operating as described.

In order to estimate how SNR of DWIs affects γ values, we considered the study by Jones and Basser (2004). On the basis of that work, the γ computation along each single direction derived from $S(b) = S_0 e^{-b^{\gamma} D(b)}$, instead of the $S(b)$ mono-exponential decay, was considered and the following relation was obtained:

$$b_{max}^{\gamma} = \frac{\ln\left(\sqrt{\frac{2}{\pi}} SNR_0\right)}{D(b)_{max}} \quad (1)$$

where, SNR_0 is the signal to noise ratio of $b=0$ image and $D(b)_{max}$ is the maximum reliable value of the generalized effective diffusion constant D_{eff} obtainable by using b_{max} .

Two brain regions from a subject representative of our cohort were selected, one in the splenium of the corpus callosum (WM tissue) and one in the thalamus (a structure containing GM nuclei). We measured γ values by considering all the b-values in the range 0–5000 s/mm²

($b=100, 200, 300, 400, 500, 700, 800, 1000, 1500, 2000, 2500, 3000, 4000, 5000$ s/mm²). Then we used the γ values extracted from the splenium of the corpus callosum and the thalamus and the experimental SNR₀ obtained from DW images, to calculate all the D(b)max values associated to each b value. Once we obtained all values of D(b)max we used the relationship (1) to derive the γ values as a function of SNR₀, by varying SNR₀ from 1 to 100.

With the aim to justify the choice of b -values carried out to obtain the AD γ maps analyzed in this paper, and its commitment with the contrast of γ -maps, we measured My in different brain regions as a function of several b -values ranges, spanning from 0 to 400 s/mm², (i.e. $b=0, 100, 200, 300, 400$ s/mm²), to 0–5000 s/mm² (i.e. $b=0, 100, 200, 300, 400, 500, 700, 800, 1000, 1500, 2000, 2500, 3000, 4000, 5000$ s/mm²).

2.2.2. ROIs/VOIs selection

The Regions of Interest (ROIs) were extracted for each slice using a hybrid approach: standard WM and GM atlases were projected onto the subjects' individual space, and the resulting masks of ROIs were eventually eroded to avoid partial volume effects. Finally, the ROIs were composed in Volumes of Interest (VOIs) by adding all adjacent slices. Although we extracted values of R_2^* , AD and DTI metrics from VOIs, for consistency with previous literature, we will keep defining them as ROIs throughout the manuscript. The FA individual maps were normalized to the FMRIB58_FA standard space template, using a full-affine transformation. The calculated transformation matrix was subsequently inverted in order to map the ICBM DTI-81 Atlas (Mori et al., 2008) into native space of individual subjects, as described in Cherubini et al. (Cherubini et al., 2009). Similarly, the Harvard-Oxford subcortical Atlas (Desikan et al., 2006) was normalized to MD maps with a 12 DOF affine transformation, returning personalized GM atlases. An example of atlases adapted to the subject's space and superimposed over FA and MD maps is provided in Fig. 2a.

Finally, the ROIs selection was automatically performed by a customized MATLAB script: the cerebral-spinal fluid (CSF) and the ventricles were excluded by masking the R_2^* maps, zeroing all the pixels with R_2^* lower than 8 s⁻¹ and higher than 80 s⁻¹; the resulting mask was combined with a mask obtained by the intersection of two thresholds: $FA \geq 0.65$ and $v_1 \geq 0.83$, in order to select coherent WM fibers and avoiding partial volume effects at the contours of the WM-ROIs. We made an approximation when considering parallel axons in

each fiber bundle, neglecting the orientation dispersion. This approximation was reasonable considering the threshold applied to both FA and v_1 , which allowed us to select coherent fibers bundles. If we consider a reference frame where the main direction of axonal fiber determines the x -direction, we expect that the v_1 , representing the direction of preferential motion, adheres with the axon orientation. Sometimes this is not verified, because of the unavoidable tilting of the axonal frame with respect to \mathbf{B}_0 . Thus a threshold of $v_1 \geq 0.83$ would be so high that only few voxels of WM ROIs would be considered. For this reason we corrected the v_1 threshold for the orientation Φ of WM fibers (Fig. 2b), which was estimated in a voxel considering the components of \mathbf{v}_1 as follows: $\Phi^* = \tan^{-1}\left(\frac{V_{1z}}{\sqrt{V_{1x}^2 + V_{1y}^2}}\right)$, and then computing $\Phi = \frac{\pi}{2} - \Phi^*$. We investigated the effect of the employed v_1 threshold on the correlation between AD-metrics and R_2^* in the WM, proving that, within certain limits, provided that the number of under-threshold voxels is sufficient, the significance of the linear correlation is barely affected (see Section 4.4 for further details). Finally, ROIs masks were eroded by 2 pixels to avoid partial volume effects or contamination from adjacent structures.

Among the selected WM ROIs we considered bundles of fibers parallel and orthogonal to \mathbf{B}_0 . The WM tracts perpendicular to \mathbf{B}_0 included (Fig. 2a) commissural fibers such as the genu, body and splenium of the corpus callosum (*gcc*, *bcc*, *scc*, respectively), oriented in the left-right direction, association fibers such as the sagittal stratum (*ss*) and the posterior thalamic radiations (*ptr*), and projection fibers such as the cerebral peduncle (*cp*), the anterior corona radiata (*acr*), oriented in anterior-posterior direction; the WM tracts parallel to \mathbf{B}_0 included the posterior limb of the internal capsule (*plc*), oriented in superior-inferior direction. Among the GM ROIs (Fig. 2a) we focused on the main components of the basal ganglia (putamen, *put*; globus pallidus, or pallidum, *pall*; caudate nucleus, *caud*), and the hippocampus (*hipp*), located in the medial temporal lobe, because of their high iron content with respect to the surrounding tissue (Hallgren and Sourander, 1958).

2.2.3. Magnetic susceptibility and iron content of selected ROIs

Magnetic susceptibility values of distinct WM and GM ROIs were taken from the work of Li et al. (2011), for WM ROIs of *gcc*, *scc*, *ss* and GM ROIs of *caud*, *put*, *pall*. In the work of Li et al. (2011) QSM is performed at 3.0 T, the same magnetic field strength of our experiment,

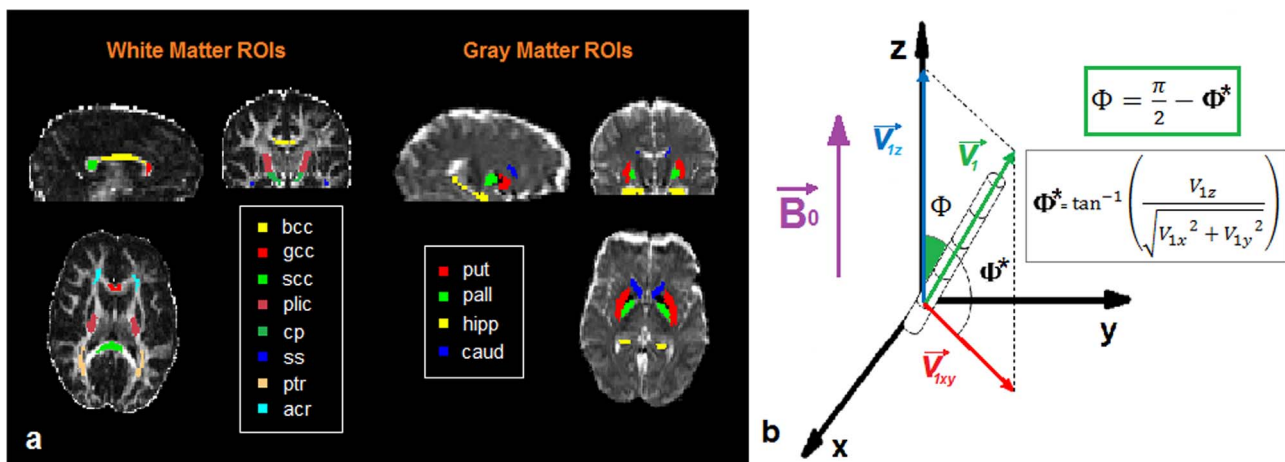


Fig. 2. White (WM) and Gray Matter (GM) selected ROIs and WM tracts orientation. a. Superimposition of WM ROIs selected from the ICBM-DTI-81 atlas adapted to the individual subject's reference space over the respective FA map, and of GM ROIs selected from the Harvard-Oxford sub-cortical atlas adapted to the subject's reference space over the respective MD map. A representative subject was chosen for the sake of clarity. *bcc*=body of the corpus callosum; *gcc*=genu of the corpus callosum; *scc*=splenium of the corpus callosum; *plc*=posterior limb of the internal capsule; *cp*=cerebral peduncle; *ss*=sagittal stratum; *ptr*=posterior thalamic radiations; *acr*=anterior corona radiata; *put*=putamen; *pall*=pallidum; *hipp*=hippocampus; *caud*=caudate nuclei. b. Schematic representation of the criteria used to estimate the main orientation of a WM tract. The main diffusion eigenvector \mathbf{v}_1 provides the orientation of the fibers bundle, that is reference frame-independent. Here a single myelinated axon, sketched as a succession of cylinders representing the internodal myelin, is depicted for the sake of clarity. The angle that the axon forms with the direction of the static magnetic field \mathbf{B}_0 is provided by $90^\circ - \Phi^*$, where Φ^* is computed using the transverse and longitudinal components of \mathbf{v}_1 . (For a better interpretation of this figure legend, the reader is referred to the web version of this article.)

in a cohort of healthy volunteers. Here the magnetic susceptibility (χ)-values are referred to the χ of CSF. Therefore they are negative for diamagnetic WM ROIs and positive for the paramagnetic GM ROIs. In order to test the reliability of the acquired R_2^* , we considered non-heme iron concentrations ([Fe]) of the basal ganglia (*caud*, *put*, *pall*) and thalamus (*thal*) taken from the pivotal study by Hallgren and Sourander (1958).

2.3. Statistical analysis

DTI-metrics, AD-metrics and R_2^* were evaluated in each selected ROI, averaging over the pool of voxels, and computing the relative SD. Then mean values \pm SEM (standard error of the mean) were estimated; the presence of significant differences among means was investigated by using the Analysis of Variance (ANOVA) test, verifying the homogeneity of variances with a Levene's test. Bonferroni's correction was applied in the case of homogeneous variances, while Games-Howell correction was used in the case of non-homogeneous variances. The correlation between diffusion metrics and χ -metrics and between diffusion metrics and R_2^* was assessed by means of Pearson's correlation test. P-values < 0.05 were considered statistically significant.

3. Results

3.1. SNR of DWIs and γ dependence on SNR

The reliability of γ -maps depends on the SNR of DWIs at each b-value. We found that the SNR in the splenium of the corpus callosum was approximately 32 in the b0-image, 18 in $b=1000$ s/mm², and 5 in $b=5000$ s/mm², images, considering an average value over all 20 gradient directions. Moreover, in the x-direction at $b=1500$ s/mm² SNR was 6.5, while in the x-direction at $b=5000$ s/mm² it was 3.2 (see Fig. 3b).

When considering the GM tissue, the SNR of a ROI placed in the right thalamus in the b0-image was approximately 44. It was approximately 15 in $b=1000$ s/mm², and 4.5 in $b=5000$ s/mm² images, considering an average value over the 20 gradient directions. In

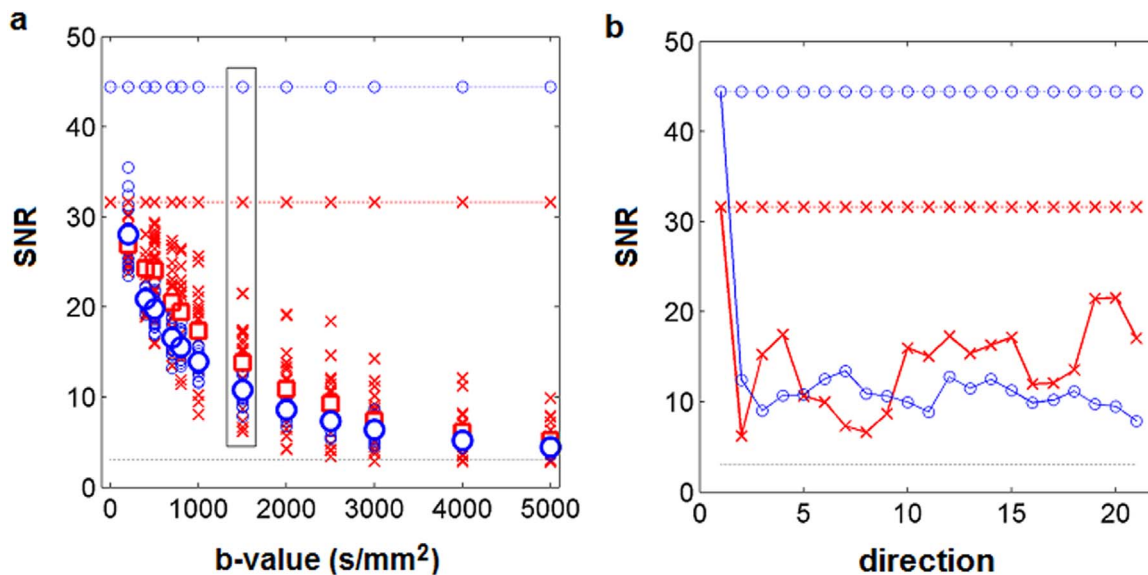


Fig. 3. SNR of DWIs as a function of b-value and diffusion gradient direction. a. The SNR of a ROI in the splenium (crosses), and SNR of a ROI in the thalamus (circles), are plotted against the b-value (only some of the b-values are specified in the axis), for a representative subject in the cohort. The values of SNR corresponding to different gradient directions at the same b-value are plotted in a unique column, with the relative mean value indicated (thick-solid squares for the splenium, thick-solid circles for the thalamus). The highest SNR represents the value computed in the b0-image, and is indicated by the straight dashed line with the superimposition of crosses for the splenium, and circles for the thalamus. The rectangle represents the values of SNR for b-value $b=1500$ s/mm² plotted with major details in the figure on the right. b. The SNR of DWIs at $b=1500$ s/mm², varying depending on the diffusion gradient direction. The lowest value of SNR corresponds to the left-right or x-direction. The horizontal black line in the plots indicates the inferior limit allowed for the reliability of DW data (SNR=3), according to Jones et al. (2013).

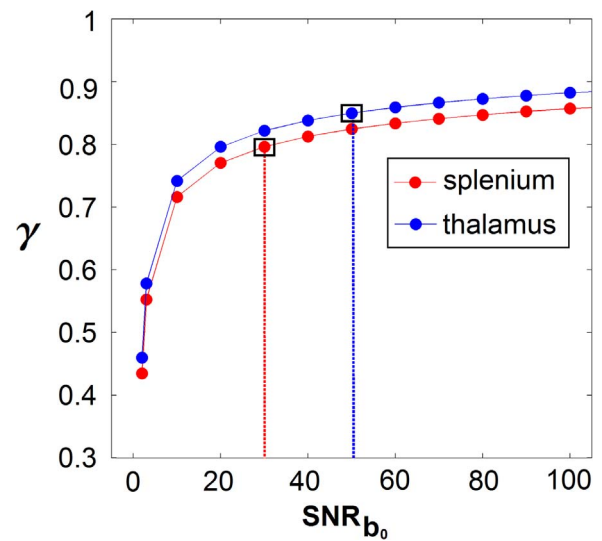


Fig. 4. Mean values of γ as a function of the SNR of b=0 image. Mean values of γ as a function of the SNR of b=0 image (SNR_{b_0}) were obtained in the splenium of the corpus callosum and in the thalamus from a studied subject. The graph indicates a decrease of γ value which is proportional to SNR_{b_0} decrease. This reduction becomes particularly critical for SNR_{b_0} values less than 20. On the other hand, for SNR_{b_0} higher than 20, γ values are underestimated compared to those derived using an ideal $SNR_{b_0}=100$ but with a maximum variation of 2%. Please note that the experimental γ values (marked with a black square) were extracted by using a $SNR_{b_0}=29$ and 49 for the splenium of the corpus callosum and the thalamus, respectively.

Fig. 3a the SNR of the splenium of the corpus callosum and the thalamus from a single subject is plotted against the b-value. In all experiments, the SNR was higher than 3, which is the lowest acceptable value for considering DW data reliable (Jones et al., 2013).

In Fig. 4, γ values from the splenium of the corpus callosum and the thalamus of a single subject are displayed as a function of the SNR_{b_0} of b=0 images (SNR_{b_0}) used to extract γ . The graph in Fig. 4 shows that γ value decreases proportionally with the SNR_{b_0} . Moreover, it displays that experimental γ values we extracted (marked with a black square)

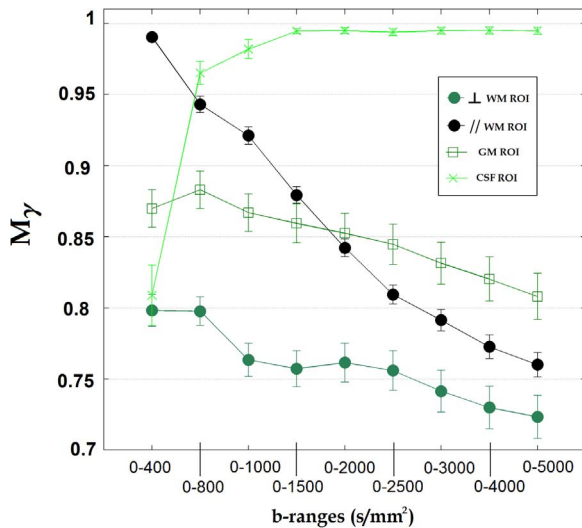


Fig. 5. My values with the relative SD as a function of the b-values ranges. My values were estimated from ROIs listed in the insert, where \perp WM is a region characterized by fibers mainly directed perpendicularly the B_0 direction and \parallel WM is a region characterized by fibers mainly directed along the B_0 . Please note that b-values higher than 2000 s/mm^2 improve the γ parameter contrast. In particular at b-value ranges around $0\text{--}4000 \text{ s/mm}^2$ the maximum difference between CSF, GM and two different WM regions (characterized by fibers mainly oriented perpendicular and parallel to B_0 direction) is obtained. Conversely, γ values obtained by using b-values ranging till only 1500 s/mm^2 are not reliable because data until $b=1500 \text{ s/mm}^2$ are better fitted to a mono-exponential decay function.

are underestimated when compared to the γ values derived using an ideal $\text{SNR}_{b_0}=100$. However, the difference between experimental γ values and those derived using $\text{SNR}_{b_0}=100$ is around 2%.

3.2. Image contrast in γ maps

In Fig. 5, My values evaluated in the CSF, WM and GM of a cohort subject as a function of the b-value ranges are displayed. My values obtained by using b-value ranges from $0\text{--}400$ to $0\text{--}1500 \text{ s/mm}^2$ are not reliable values because, as it has long been recognized (Mulkern et al., 1999; Alexander et al., 2002) a significant deviation of the experimental data from the mono-exponential decay is observed after $b=1500 \text{ s/mm}^2$. On the other hand, the graph in Fig. 5 shows that the inclusion of b values higher than 2000 s/mm^2 improves the γ parameter contrast. In particular at b-value ranges around $0\text{--}4000 \text{ s/mm}^2$ the maximum difference between CSF, GM and two different WM regions (characterized by fibers mainly oriented perpendicular and parallel to B_0 direction) can be obtained. In Fig. 6, My and MD maps of the same subject used for Fig. 5 are illustrated to show the different image contrast provided by AD and DTI metrics. Please note that the γ -map strongly suggests the use of AD γ contrast to highlight boundaries and barriers between tissues with different magnetic susceptibilities. Moreover the results reported here, highlight the central role of the local $\Delta\chi$ in providing γ contrast.

3.3. R_2^* depends on fibers orientation and iron content

In Fig. 7b the value of R_2^* in selected WM ROIs is plotted vs Φ (i.e., the average orientation of WM fibers in a certain ROI).

Fig. 7 shows that ROIs with a prevalence of B_0 -parallel fibers (indicated with blue dots) are characterized by lower R_2^* values compared to those with a prevalence of B_0 -orthogonal fibers (indicated with red dots). The box in the plot shows that there is a significant, albeit moderate, linear correlation between R_2^* and Φ . Furthermore, a sine function fits well with R_2^* values vs Φ data (green curve in Fig. 7b). By looking at the Fig. 7a, we may notice that ROIs with fibers differently oriented with respect to B_0 show a similar contrast in FA maps, but a

different contrast in orientation Φ -map. Fig. 8 shows the behavior of R_2^* computed in the basal ganglia and the thalamus vs iron content.

A strong linear correlation ($r=-0.950$) between R_2^* and $[\text{Fe}]$ was found. We considered only *thal*, *caud*, *put* and *pall* brain regions because of the lack of information about iron content extracted with uniform experimental methods in other sub-cortical GM ROIs. These results suggest that R_2^* obtained in a cohort of 8 healthy subjects at 3.0 T is affected by the orientation of myelinated fibers, and depends on the iron content in GM. This feature of R_2^* justifies the procedure chosen to show that the γ AD metrics depends on the local magnetic susceptibility differences in brain, when γ is quantified by MRI.

3.4. AD-metrics relation with magnetic inhomogeneity

Fig. 9 shows the DTI, AD and R_2^* maps from a single subject, while in Table 1 the mean values \pm SEM of AD and R_2^* metrics measured in the selected ROIs shown in Fig. 2a are summarized.

As a first step of analysis the diffusion-derived parameters were correlated to values of χ found in literature. In Fig. 10 the graphs of R_2^* and AD-metrics vs χ are displayed.

The vertical error bars represent the computed SEM for the measured parameters, and the horizontal error bars represent the SD on χ -values taken from literature (Li et al., 2011). The behavior of the investigated parameters vs χ was characterized by an opposite trend for WM compared to GM ROIs. As a consequence, the data points belonging to the two groups of ROIs were fitted separately. The lack of significance in the Pearson's correlation tests may be motivated by the limited size of the sample (3 ROIs per group, thus 3 mean values per group). In WM ROIs, M_γ , γ_{\parallel} and γ_{\perp} (Fig. 10b–d) increase in parallel to χ increase. Conversely, in GM ROIs they decrease when χ increases, with the highest value of r for γ_{\parallel} in both cases ($r=0.957$ and $r=-0.985$, respectively).

3.5. AD-metrics are significantly correlated to R_2^*

In Fig. 11 linear correlation plots between AD-metrics and R_2^* are shown, for WM ROIs (Fig. 11a, b) and GM ROIs (Fig. 11c, d).

The error bars indicate inter-subjects SD; only plots with a positive Pearson's correlation test are shown ($P < 0.05$). A strong negative correlation was found between M_γ , γ_{\parallel} and R_2^* , (respectively, $r=-0.786$, $P=0.022$; $r=-0.822$, $P=0.012$). On the other hand, γ_{\perp} showed a moderate negative trend with R_2^* ($r=-0.666$, $P=0.071$, not shown in the figure), and no correlation was found between A_γ and R_2^* . In GM ROIs a strong negative correlation was found between M_γ and R_2^* ($r=-0.997$, $P=0.003$), γ_{\perp} and R_2^* ($r=-0.989$, $P=0.011$), while γ_{\parallel} exhibited a negative linear trend with R_2^* , and A_γ a positive one, not shown in the figure because they were both not significant. In WM ROIs no significant correlations were found between any of the DTI parameters and R_2^* .

3.6. DTI-metrics, AD-metrics and R_2^* potential in discriminate WM and GM ROIs

The ANOVA test revealed the presence of significant differences among parameters computed in different areas of brain parenchyma. M_γ , γ_{\parallel} , γ_{\perp} and A_γ in WM and GM are significantly different ($P < 0.0001$), with M_γ lower in the WM compared to the GM ($M_{\gamma\text{WM}}=0.761 \pm 0.052$, $M_{\gamma\text{GM}}=0.851 \pm 0.036$), according to previous studies (Magin et al., 2008; Zhou et al., 2010; GadElkarim et al., 2013). Similar results were obtained for the axial-exponent, ($\gamma_{\parallel\text{WM}}=0.891 \pm 0.050$, $\gamma_{\parallel\text{GM}}=0.909 \pm 0.027$) and for the radial-exponent ($\gamma_{\perp\text{WM}}=0.693 \pm 0.060$, $\gamma_{\perp\text{GM}}=0.822 \pm 0.043$). In contrast, A_γ was higher in the WM compared to GM ($A_{\gamma\text{WM}}=0.183 \pm 0.041$, $A_{\gamma\text{GM}}=0.077 \pm 0.023$). Finally, $R_2^*_{\text{WM}}=(26.02 \pm 3.88) \text{ s}^{-1}$ and $R_2^*_{\text{GM}}=(30.97 \pm 4.55) \text{ s}^{-1}$. $R_2^*_{\text{WM}}$ is in good agreement with previous studies performed at $B_0=3.0 \text{ T}$ in a cohort of subjects with ages around 25 years (Li et al., 2009; Nam et al.,

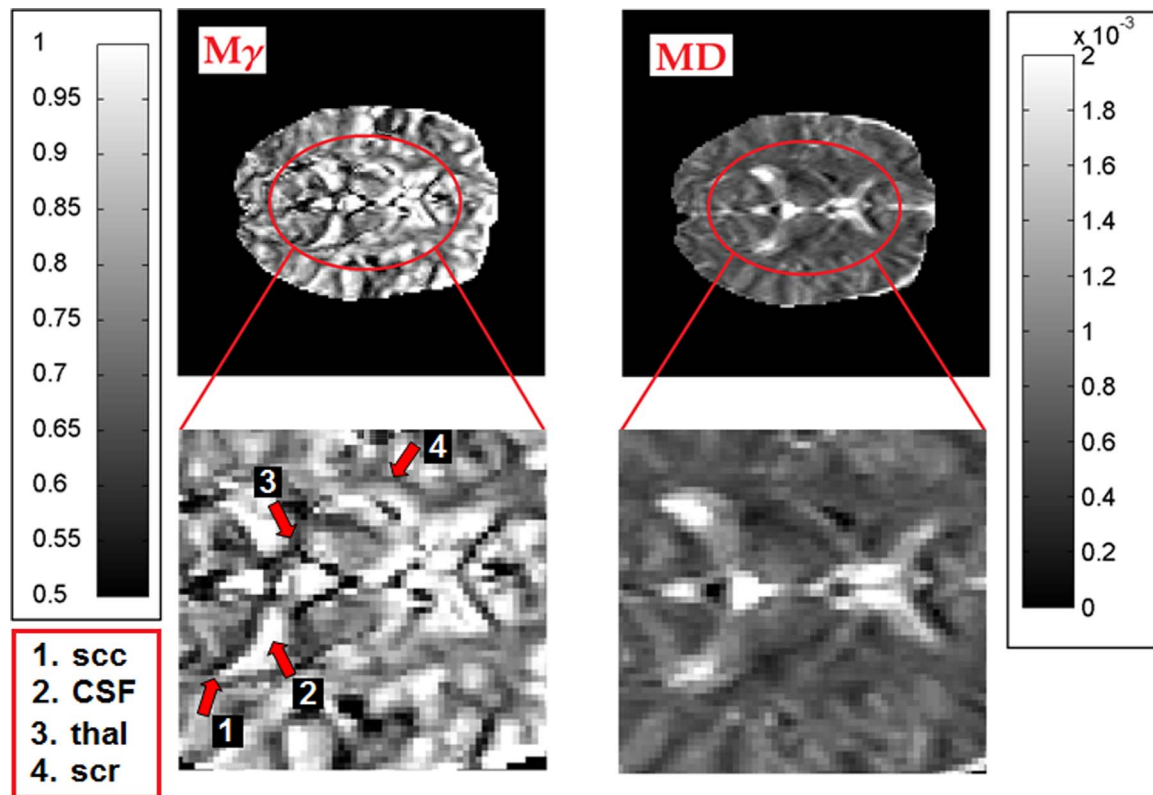


Fig. 6. Mean γ (My) and Mean Diffusivity (MD) parametric maps. My and MD maps of the subject whose data were used in Fig. 5 and magnification of the area containing the regions of interest listed in the legend (*scc*=splenium of corpus callosum; *CSF*=cerebrospinal fluid; *thal*=thalamus; *scr*=superior corona radiate). My provides a different contrast compared to MD map. Specifically it highlights the interfaces between tissues with different magnetic susceptibility. For example in (1) the interface between white matter fibers and the CSF is enhanced; in the CSF $\gamma=1$ (2); the boundaries of thalamus are more highlighted in My map compared to MD map (3); WM fibers with different orientations with respect to \mathbf{B}_0 , i.e. *scc* and *scr*, show different contrast (4). As a general comment, the zoomed brain area is more heterogeneous and detailed in My compared to MD map.

2012). Statistical analysis showed that the variation of the same parameter within the same anatomical fiber bundle or a sub-cortical area across individuals was remarkably limited. ANOVA test showed that R_2^* was able to discriminate significantly only between *gcc* and *ss* ($P < 0.05$), *plc* and *acr* ($P < 0.05$), or *plc* and *ss* ($P < 0.01$). Regarding

the DTI-metrics, FA was the parameter with the highest number of significant comparisons, except for *gcc-bcc*, *gcc-scc* ($P > 0.05$). None of the DTI-metrics discriminated neither *gcc* from *bcc*, nor *gcc* from *scc*, which were instead discriminated by $\Delta\gamma$ with $P < 0.0001$. My, γ_{\perp} and $\Delta\gamma$ were the only diffusion derived parameters able to distinguish *plc* from

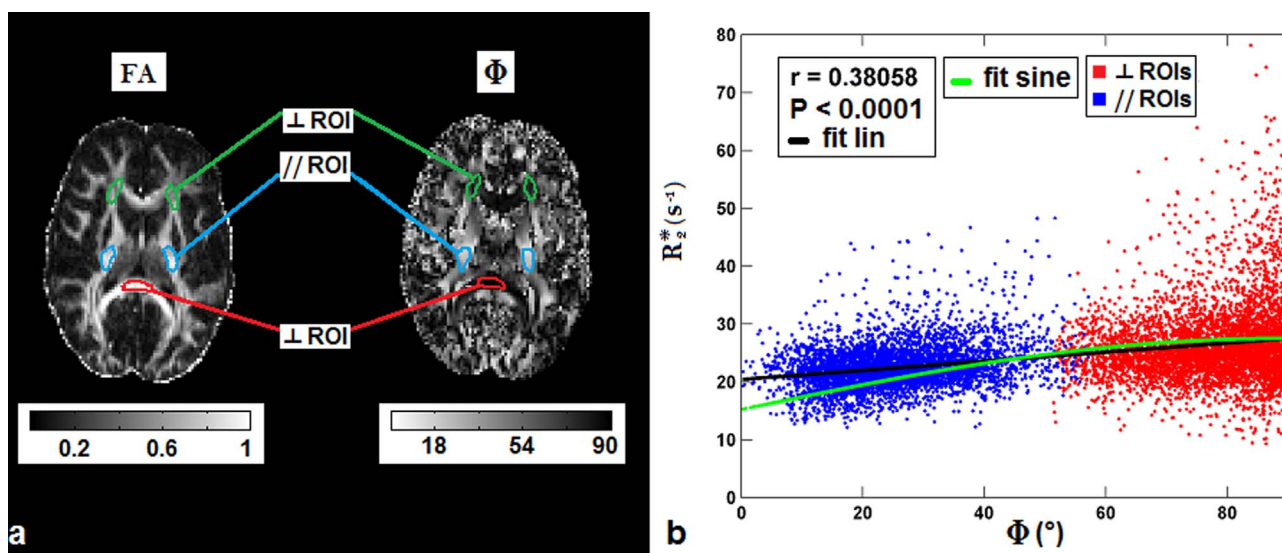


Fig. 7. FA and fiber orientation Φ -maps, and R_2^* vs Φ in WM and GM ROIs. a. FA map and the map of average Φ , the orientation of WM fiber bundles with respect to \mathbf{B}_0 , computed using the spatial components of \mathbf{v}_1 diffusion eigenvector, for a subject in the cohort. ROIs with a prevalence of orthogonal fibers are drawn in green (anterior corona radiata) and red (splenium); ROIs with a prevalence of parallel fibers are drawn in light blue (posterior limb of internal capsule). The two types of ROIs presents a similar contrast in FA map, and a different contrast in Φ -map. b. R_2^* of ROIs with parallel fibers (blue dots) and orthogonal fibers (red dots), plotted against their orientation. The data are linearly fitted (black line), and fitted with a sine function (green curve). The Pearson's correlation coefficient r is indicated in the box, together with the level of significance, P . (For interpretation of the references to color in this figure legend, the reader is referred to the web version of this article.)

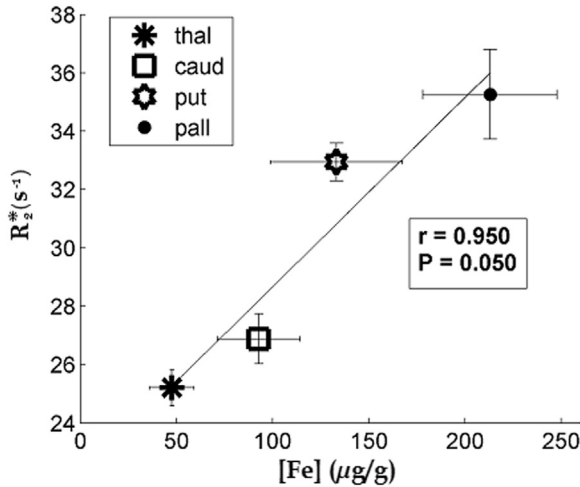


Fig. 8. R_2^* plotted vs iron content in sub-cortical GM ROIs. R_2^* of thalamus (*thal*), caudate nuclei (*caud*), putamen (*put*) and globus pallidus (*pall*), estimated from the parametric R_2^* maps and plotted vs non-heme iron concentration taken from literature (Hallgren and Sourander, 1958). Pearson's correlation coefficient is reported in the box, together with the level of significance, P .

gcc (respectively, with $P < 0.05$, $P = 0.01$, $P < 0.0001$). On the other hand, AD-metrics did not discriminate between *bcc* and *scc* (except for A_γ , with $P < 0.026$), while the DTI-metrics did (MD and D_\perp with $P < 0.0001$, FA with $P = 0.001$, $D_{//}$ with $P < 0.05$). In regard to GM ROIs, *caud* was well discriminated from *put* by M_γ ($P < 0.005$), γ_\perp ($P = 0.001$) and A_γ ($P = 0.001$), R_2^* ($P = 0.001$), D_\perp ($P < 0.05$) and FA ($P < 0.0001$), and from *pall* by all the AD-metrics with $P < 0.0001$ (for A_γ $P < 0.05$), by R_2^* ($P = 0.005$), $D_{//}$ ($P < 0.005$) and FA ($P < 0.0001$). On the other hand, MD, $D_{//}$ and D_\perp could discriminate *put* from *pall* with a high level of significance ($P < 0.0001$), whereas AD-metrics did not distinguish between them. $\gamma_{//}$ was the only parameter able to discriminate between *caud* and *hipp* ($P = 0.002$). Finally, A_γ discriminated between *put* and *hipp* ($P = 0.001$) and between *pall* and *hipp* ($P < 0.05$), while FA differentiated all these structures ($P < 0.0001$).

4. Discussion

In general, microstructural tissue compartments have unique magnetic susceptibilities χ driven by their chemical compositions and

molecular arrangements. In the presence of B_0 , differences in magnetic susceptibility between adjacent compartments generate different amount of magnetization due to the relation: $M = \chi B_0$. As a consequence local magnetic inhomogeneity generated by $\Delta\chi B_0$ are found at the interface between different tissues. In the brain tissue these $\Delta\chi$ arise from differences in non-heme iron content and iron-storage proteins and from various degrees of myelin density and orientation. Several authors have stressed the importance of $\Delta\chi$ assessment and quantification in the brain (Todorich and Connor, 2004; Youdim et al., 2004; Haacke et al., 2010; Schmierer et al., 2010; Tepper et al., 2012; Li et al., 2014, 2015).

Here we investigated the dependence of AD γ -metrics on brain compartments $\Delta\chi$, and tested the potential of AD γ imaging to discriminate between cerebral tissues on the basis of their $\Delta\chi$.

In Fig. 12, the principal actors investigated in this work are shown. $\Delta\chi$ anisotropy at the microscopic scale originates from the radial arrangement of oriented lipo-protein chains constituting the multi-layers of the myelin sheaths (Lee et al., 2010; Sukstanskii and Yablonskiy, 2014; Yablonskiy and Sukstanskii, 2014). By considering χ anisotropy in the membrane lipids from isolated human lipo-proteins of about -0.223 ppm (Lounila et al., 1994), and a lipid volume fraction in WM of about 16% (Lee et al., 2010), $\Delta\chi$ is in the order of 0.018 ppm (Li et al., 2012). In fact not only the lipid density, but also the way lipids are spatially organized with respect to B_0 are important factors contributing to the $\Delta\chi$ anisotropy in the WM. The $\Delta\chi$ anisotropy at a macroscopic scale arises from the presence of elongated compartments, provided with the myelin sheath and containing cytoplasm, and exhibits a sine-squared orientational dependence $\sim \sin^2\Phi$ with Φ the angle of the axon with respect to B_0 (Duyn, 2013).

In our previous results obtained in vitro (Palombo et al., 2012; Capuani et al., 2013) we highlighted that the γ parameter depended on $\Delta\chi$ in addition to the multi-compartmentalization of water.

This work was specifically dedicated to the investigation of the correlation between AD γ -metrics and $\Delta\chi$ in human brains at 3.0 T.

For this purpose, to validate our investigative method, we first confirmed that our measured R_2^* depends on fibers orientation in the WM and iron content in the GM, and is correlated to magnetic susceptibility values taken from the literature (Li et al., 2011). Then we studied the linear correlation between AD γ metrics and R_2^* to highlight the relationship between AD γ metrics and $\Delta\chi$.

4.1. R_2^* depends on fibers orientation and iron content

Transverse relaxation in GRE sequences is a combination of

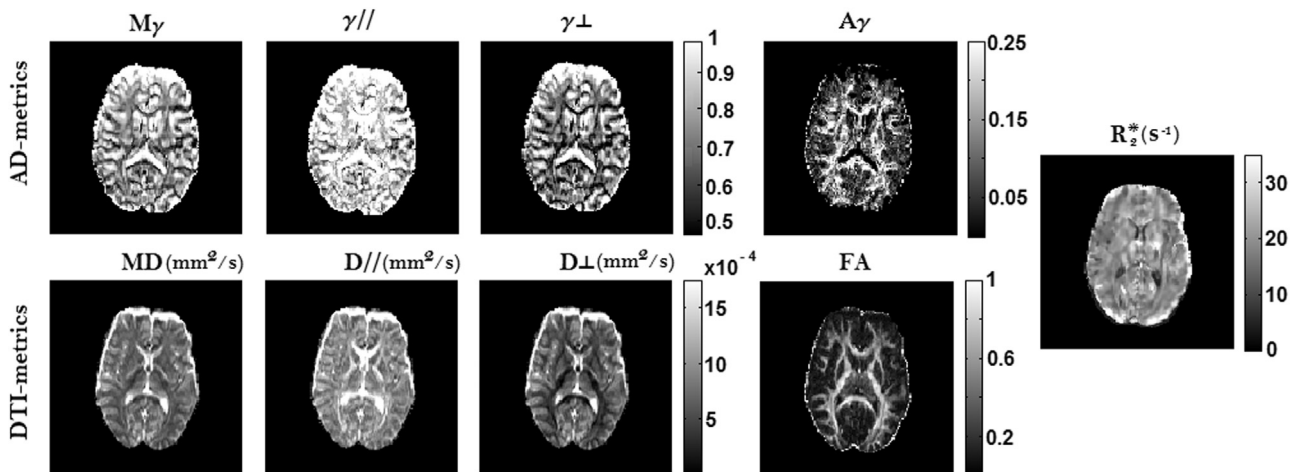


Fig. 9. AD, DTI and R_2^* parametric maps in the subject's native space. Different parametric maps for the same axial slice obtained from a single subject. The images in the upper row show the AD-derived parameters: mean- γ (M_γ), axial- γ ($\gamma_{//}$), radial- γ (γ_\perp), γ -anisotropy (A_γ); the images in the lower row show the DTI-derived parameters: mean-diffusivity (MD), axial and radial diffusivity ($D_{//}$ and D_\perp), and fractional anisotropy (FA). The rate of relaxation (R_2^*) is illustrated on the right. The color-bar is reported next to each map with distinct contrast.

Table 1
AD-metrics and R_2^* mean values obtained in selected ROIs.^a

WM ^b ROIs	My		$\gamma//$		$\gamma\perp$		Ay		$R_2^*(s^{-1})$	
	Mean	SEM	Mean	SEM	Mean	SEM	Mean	SEM	Mean	SEM
gcc	0.780	0.015	0.921	0.012	0.709	0.017	0.224	0.009	23.89	1.44
bcc	0.761	0.028	0.896	0.031	0.694	0.027	0.180	0.011	25.58	1.24
scc	0.792	0.010	0.904	0.011	0.735	0.010	0.158	0.007	26.08	1.01
plic	0.833	0.012	0.943	0.006	0.778	0.016	0.151	0.009	22.25	0.60
cp	0.732	0.011	0.823	0.007	0.687	0.014	0.129	0.009	27.76	0.92
ptr	0.734	0.010	0.909	0.008	0.646	0.013	0.230	0.011	24.54	0.51
acr	0.715	0.008	0.853	0.008	0.646	0.009	0.189	0.006	28.67	1.38
ss	0.727	0.014	0.877	0.011	0.652	0.017	0.202	0.012	29.37	2.16
GM^cROIs	Mean	SEM	Mean	SEM	Mean	SEM	Mean	SEM	Mean	SEM
caud	0.892	0.004	0.938	0.005	0.869	0.005	0.061	0.005	27.07	0.78
put	0.833	0.007	0.911	0.004	0.795	0.009	0.098	0.005	32.78	0.59
pall	0.821	0.015	0.884	0.009	0.790	0.018	0.090	0.008	34.92	1.43
hipp	0.856	0.010	0.902	0.008	0.833	0.011	0.061	0.004	29.10	2.01

^a The error on the estimation of each parameter was taken as the standard error of the mean (SEM). My, $\gamma//$, $\gamma\perp$, Ay are dimensionless quantities.
^b gcc=genus of corpus callosum; bcc=body of corpus callosum; scc=splenium of corpus callosum; plic=posterior limb of internal capsule; cp=cerebral peduncle; ptr=posterior thalamic radiations; acr=anterior corona radiata; ss=sagittal stratum;
^c caud=caudate nuclei; put=putamen; pall=pallidum; hipp=hippocampus.

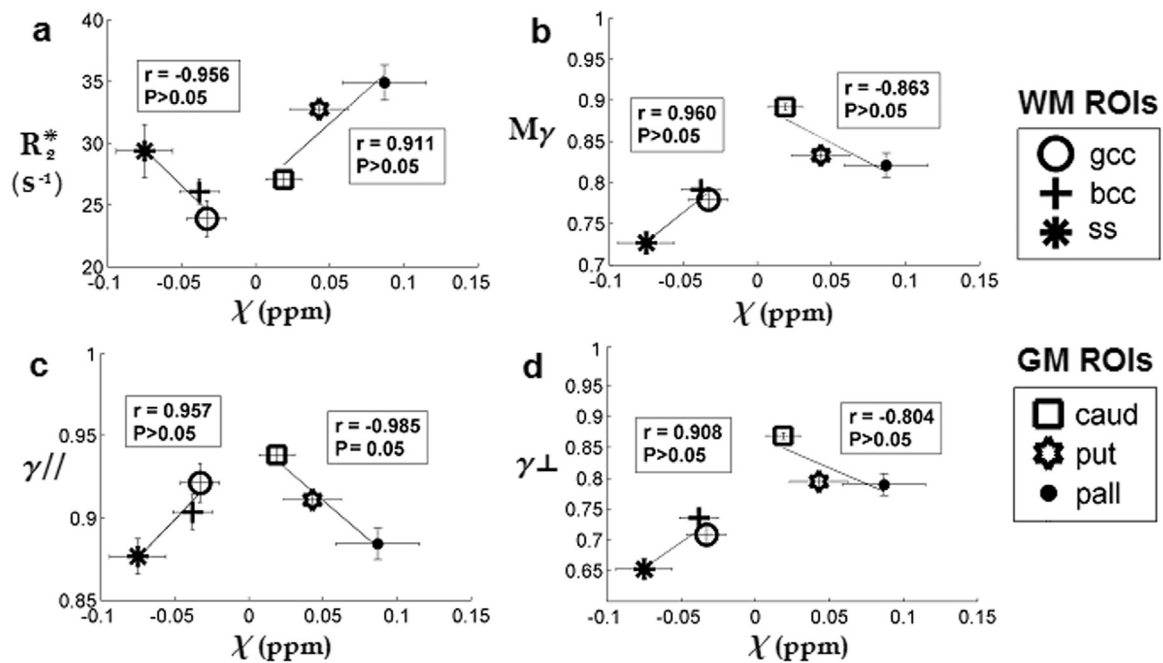


Fig. 10. R_2^* and Anomalous Diffusion-derived parameters vs χ in WM and GM ROIs. R_2^* (a), and mean- γ (My), axial- γ ($\gamma//$), radial- γ ($\gamma\perp$), respectively depicted in (b–d), are plotted vs χ . Susceptibility values are taken from Li et al. (2011), and are referred to those in the CSF. The vertical error bars represent the computed SEM for the measured parameters, and the horizontal error bars represent the SD on χ -values taken from the literature. The trends are indicated by linear fits, that are treated separately for WM and GM ROIs. Pearson's correlation coefficients, r, are reported in the boxes, together with the level of significance, P. For the list of ROIs acronyms see Table 1.

intrinsic T_2 relaxation and relaxation caused by magnetic field inhomogeneities (Chavhan et al., 2009). Considering the rate of relaxation, this means: $R_2^* = 1/T_2^* = 1/T_2 + \gamma\Delta B_0$, where γ is the gyromagnetic ratio and $\gamma\Delta B_0$ the magnetic field inhomogeneity. This turns into $R_2^* = R_2 + R_2'$. In order to validate our investigative method, we considered the two main aspects that influence R_2^* : the orientation of myelinated axons in WM and the amount of iron content in subcortical GM structures. Rudko et al. (2014) suggested that R_2^* depends on tissue orientation in WM and cortical GM, performing GRE at 18 different sampling angles on fixed rat brains at 9.4 T. In their work, these authors showed that R_2^* had a sinusoidal dependence on the orientation of the tissue in WM, whereas no orientation dependence is present in the basal ganglia, where R_2^* is influenced by iron concentration only.

On a first approximation, in our study we found a significant linear

correlation between R_2^* and Φ ($r = 0.381$, $P < 0.0001$). Our result seems to replicate previous findings by Rudko et al. (2014). Indeed the sine function fitted well to our data (green curve in Fig. 7b). However, owing to the lower strength of B_0 (which in our case was 3.0 T), the effect of local ΔB_0 on R_2' , and thus on R_2^* , is less evident compared to that observed by Rudko et al.

According to literature (Gelman et al., 1999; Yao et al., 2009; Langkammer et al., 2012; Mitsumori et al., 2012), we found a strong linear correlation ($r = -0.950$, $P = 0.05$) between R_2^* in GM and iron content [Fe] values taken from literature (Fig. 8).

These results suggest that the measured R_2^* reflects $\Delta\chi$ inhomogeneity due to the orientation dispersion in WM, and $\Delta\chi$ inhomogeneity in the deep GM nuclei due to differences in iron content. We believe that this evidence justifies the study of the dependence of AD-metrics on $\Delta\chi$ through the investigation of its dependence on R_2^* .

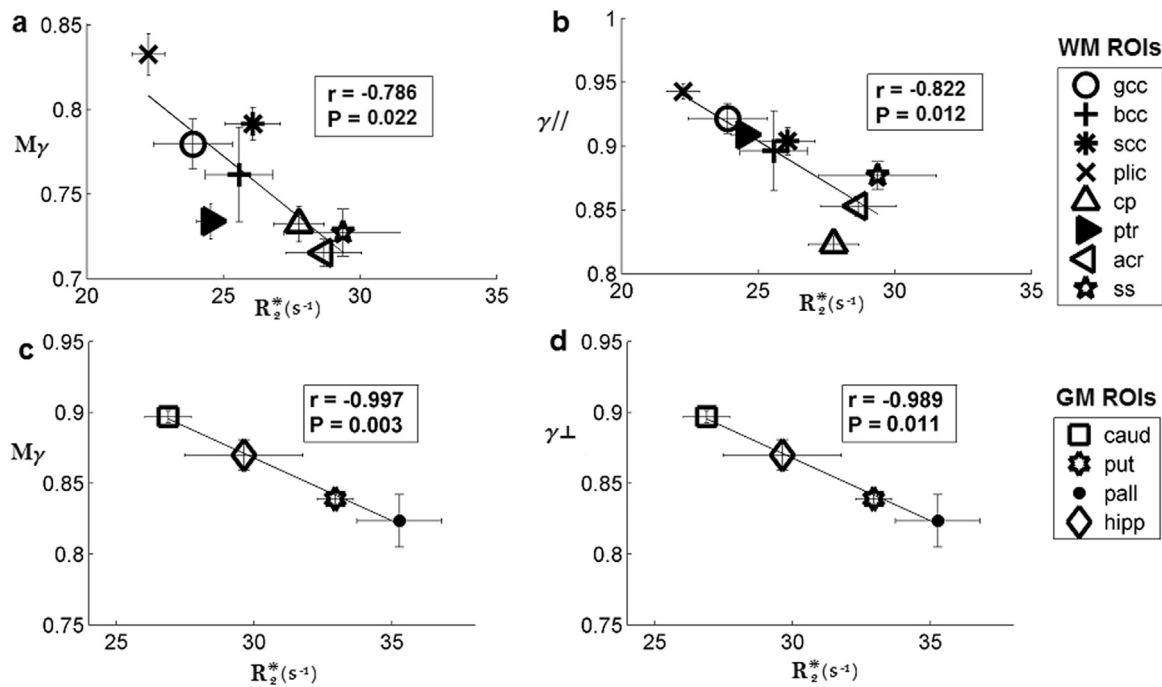


Fig. 11. AD-derived parameters as a function of R_2^* . Mean values of mean- γ (M_γ) and axial- γ ($\gamma_{//}$) as a function of R_2^* in the corresponding WM ROI (a, b) and of mean- γ (M_γ) and radial- γ (γ_{\perp}), as a function of R_2^* in the corresponding GM ROI (c, d). Error bars indicate inter-subjects SD; the linear fit is reported, together with the Pearson's correlation coefficient (r) and the significance level (P). For the list of ROIs acronyms see Table 1.

4.2. The reliability of AD γ values and the peculiar γ -MRI contrast

AD and DTI maps displayed in Figs. 6 and 9 show the different image contrast provided by AD when compared to DTI metrics. In particular, according to previous in vitro results (Palombo and Gabrielli, 2012), (Capuani and Palombo, 2013) γ contrast highlights interfaces between microstructural compartments characterized by different magnetic susceptibility (Fig. 6). Results displayed in Figs. 3–5, ensure that the values of γ parameters we estimated are not affected by low SNR and therefore M_γ , $\gamma_{//}$ and γ_{\perp} maps and measurement (Table 1) can be considered reliable. We have also shown (Fig. 5) that, exploiting all the potential of γ -MRI contrast in discriminating between brain tissues, DW acquisitions should be collected in the b-values range of 0–4000 s/mm². Moreover, to take into account multi-diffusion compartments, at least 10 b-values (some high, some low) should be considered. By using the abovementioned protocol with DW data collected by changing g_{diff} strength at a constant Δ , the obtained γ maps highlight boundaries and barriers among different brain tissues.

4.3. γ AD-metrics significantly correlate with R_2^*

The dependence of AD-metrics on $\Delta\chi$ taken from literature in both WM and GM ROIs (Fig. 10) is consistent with the results presented in Fig. 11, in which the significant linear correlations between AD γ -derived parameters and R_2^* are shown. Conversely, we did not find significant correlations between any of the DTI-metrics with R_2^* , in agreement with Nair et al. (2005) work performed on mouse brain. It is shown that DTI-metrics are only weakly affected by $\Delta\chi$ variation at 9.4 T. We infer that at lower B_0 strengths the effect of χ on DTI-derived parameters is negligible.

In particular, AD-metrics showed a strong negative correlation with R_2^* in both WM and GM (Fig. 11). These results suggest that the AD-metrics are sensitive to R_2^* inhomogeneity due to $\Delta\chi$ in human WM and GM, originating by differences in myelin density/orientation and $\Delta\chi$ at the interfaces between myelin -neighboring cells, and by local differences in iron content.

In particular, the similar trend of AD-metrics vs R_2^* and AD-metrics vs χ in GM, suggests that the $\Delta\chi$ causing R_2^* variations in GM have a dominant role compared to R_2 effect due to microstructure. Considering that both R_2^* and χ are related to iron content in deep GM nuclei (Gelman et al., 1999; Yao et al., 2009; Mitsumori et al., 2012), our results indicate that there is a correlation between γ AD parameters and the non-heme iron concentration, especially in sub-cortical GM.

In this perspective our study suggests that γ metrics could be a new method to map iron deposits in GM. Our results suggest that γ contrast embodying information deriving from both $\Delta\chi$ and DW maps is more sensitive compared to conventional diffusion methods. The usual approaches to visualize iron deposition are often prone to confounding artifacts (as an example R_2^* images) or difficult to apply in clinical investigation (as an example STI). The γ imaging seems to overcome these limits, resulting more sensitive to iron deposition than DW investigation. In this regard a recent work of Fujiwara et al. (2014) performed on non-human primate brain, underlined that diffusion coefficient D was not correlated to iron concentration in GM at 3.0 T.

Differently from GM ROIs, M_γ , $\gamma_{//}$ and γ_{\perp} vs χ showed increasing trends in WM (Fig. 10b–d), although the correlation was not significant or marginally significant due to the small number of points (*gcc*, *scc*, *ss*). Moreover M_γ and $\gamma_{//}$ vs R_2^* showed significant strong negative correlations (see Fig. 11a, b). These results may be interpreted considering that in WM there is an interplay between two factors contributing to R_2^* : 1) R_2^* variations along myelinated fibers are caused by $\Delta\chi$ at microscopic and macroscopic scale (Fig. 12) due to different WM orientations with respect to \mathbf{B}_0 , and to the modulated shape of axonal fibers (Budde and Frank, 2010; Novikov et al., 2014; Ronen et al., 2014); 2) R_2 variations in WM are mainly due to the differentiated microstructure, thus the distribution of axonal diameters, myelin fraction, and axonal density. By looking at the values listed in Table 1, we notice that M_γ , $\gamma_{//}$ and γ_{\perp} are higher in WM fiber bundles oriented parallel to \mathbf{B}_0 (for example *pllc*), compared to the ones oriented orthogonally to \mathbf{B}_0 (for example *gcc*, *scc*). Conversely R_2^* is lower in *pllc* compared to other ROIs, confirming previous results (Denk et al., 2011; Sati et al., 2012; Chen et al., 2013; Rudko et al., 2014) and according to the orientational dependence of χ found

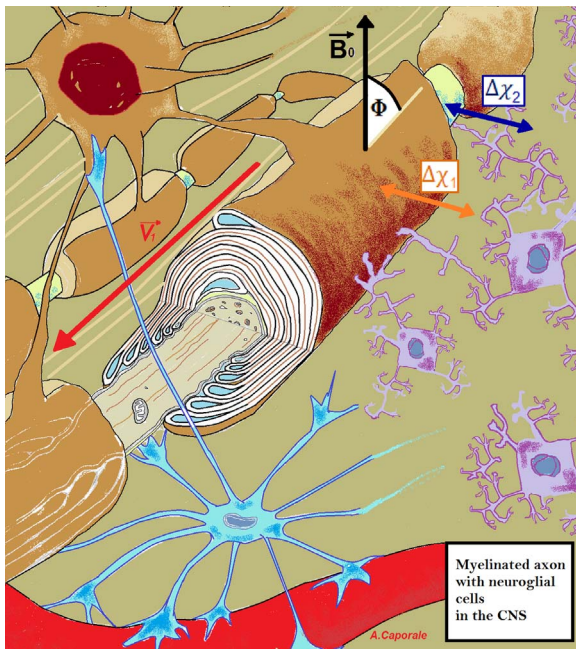


Fig. 12. Susceptibility anisotropy in WM with respect to the static magnetic field. The diagram shows the composite environment experienced by a diffusing water molecule in WM. The direction of the facilitated diffusivity of extracellular water is indicated by the red arrow, that is the main diffusion eigenvector, \mathbf{v}_1 . An oligodendrocyte, depicted at the top left, is myelinating a couple of axons through its processes. The cutaway view of the myelinated axon in the middle of the image illustrates the myelin sheath surrounding the axon, and forming cytoplasmic wedges at the proximity of the node of Ranvier (a few myelin layers have been depicted for the sake of clarity). An astrocyte, illustrated at the bottom in light blue, branches towards the oligodendrocyte, the axon and a capillary. Microglial cells colored in light purple are linked to the internodal myelin. The $\Delta\chi$ varies along the axonal direction, depending on the myelin sheath and its surroundings: $\Delta\chi_1$ arises at the interface between the internodal myelin and the extracellular water, or eventually, the microglia (highlighted by the orange double arrow); $\Delta\chi_2$ arises at the interface between the axonal membrane at the node of Ranvier and the interstitial water or glial cells (highlighted by the blue double arrow). From a macroscopic point of view, $\Delta\chi$ anisotropy is generated by the orientation of myelinated fibers with respect to the static magnetic field \mathbf{B}_0 , indicated by Φ in the sketch. The diagram is out of scale. (For interpretation of the references to color in this figure legend, the reader is referred to the web version of this article.)

by Duyn (2013).

4.4. γ -AD discrimination between brain regions

AD in vitro studies performed on phantoms with known $\Delta\chi$ and simplified microstructural heterogeneity (Palombo et al., 2011, 2012; Capuani et al., 2013) proved that the AD γ -exponent is influenced by both the $\Delta\chi$ inhomogeneity and the multi-compartmentalization of the environment explored by diffusing water molecules. The interplay between these two effects is a matter of fact in complex tissues such as the human brain, and this may shed some light on the results of multiple comparisons tests about the ability of AD-metrics and DTI-metrics in discriminating among brain regions. Considering WM ROIs, for example, DTI-metrics discriminated with higher level of significance between ROIs with fiber bundles similarly oriented with respect to \mathbf{B}_0 , whereas AD-metrics were more effective in discriminating between ROIs with \mathbf{B}_0 -parallel fibers from ROIs with \mathbf{B}_0 -orthogonal fibers (for example *pllc* from *gcc*, *acr*, *ptr*, *ss*) (see Figs. 5 and 6). This is most likely due to the orientational dependence of χ , which is reflected by the AD- γ exponent, as shown in our results. Focusing on a bundle of myelinated fibers homogeneously oriented with respect to \mathbf{B}_0 , such as the corpus callosum, DTI-metrics were able to discriminate between the body and the splenium of the corpus callosum. Conversely, AD-metrics were unable to discriminate between them, with the exception of A_γ . We hypothesize that in the corpus callosum the competition

between the two effects (diffusion multi-compartmentalization and $\Delta\chi$) upon which the γ AD-contrast is based may smooth the local differences of γ -exponent between regions. In fact, from a microstructural point of view, the corpus callosum is characterized by a uniform and dense distribution of axon diameters in the genu and splenium, presenting instead a wider distribution of axon diameters, with a lower density, in the body (Aboitiz et al., 1992). Hence the AD-exponent, should reflect the differential diffusion compartmentalization explored by water. On the other hand, myelinated fibers in the corpus callosum maintain the same orientation with respect to \mathbf{B}_0 , which turns out in the uniformity of $\Delta\chi$ due to the lack of orientation dispersion. Moreover, about the strength of G_{int} originating from $\Delta\chi$ between axons and closest tissues, it depends not only on the magnitude and direction of \mathbf{B}_0 , but also on the reciprocal relationship between the diffusion length of water molecules (l_d), and their dephasing length (l^*) (Mitchell et al., 2010; Di Pietro et al., 2014).

We believe that the investigation of AD and DTI-metrics behavior in the corpus callosum compared to other WM regions constituted by fibers oriented perpendicularly to corpus callosum, provides further indication about the simultaneous dependence of AD-contrast on both multi-compartmentalization and $\Delta\chi$ effects in tissue.

Similarly to what we found in the WM, the results of multiple comparisons between GM regions may be justified considering the concomitant effect of $\Delta\chi$ and microstructure on AD-metrics. As a general comment, we notice that those GM ROIs which were well discriminated by AD-metrics (i.e., as *caud* from *put* and *caud* from *pal*) were also well discriminated by R_2^* , most likely owing to the predominance of $\Delta\chi$ effect compared to the multi-compartmentalization effect. For what concerns the discrimination between *put* and *pal*, instead, DTI-metrics were more effective, and this is in agreement with recent results showing an increased value of FA in the globus pallidus, compared to that observed in the putamen, caudate nucleus and thalamus (Gong et al., 2014).

4.5. Factors and limits to take into account

A critical point of the data analysis is the use of thresholds to select only coherent WM fiber bundles. The conjecture here is that the choice of the threshold might bias the relation between AD-metrics and R_2^* . In order to quantify this possible bias, we varied FA and v_1 thresholds and repeated Pearson's correlation test, the significance of which is displayed in Fig. 13.

The thresholds used in our data analysis are indicated in the plots by the red dot. The highest significance, indicated by arrows in the plots, is obtained applying very high thresholds (FA > 0.7, v_1 > 0.87), but already for v_1 > 0.85 the number of voxels is considerably reduced, in a way that significantly affects the statistics.

A factor that potentially may have mitigated the dependence of the AD-metrics on $\Delta\chi$ is the fact that, according with De Santis et al. (2011) we used DTI reference frame to extract M_γ , A_γ , $\gamma_{//}$ and γ_{\perp} . In the present study, the projection of γ parameters along the DTI eigenvectors could hide part of the dependence of γ -imaging contrast on $\Delta\chi$. Therefore, we planned to repeat this analysis by evaluating the AD-metrics in the reference frame of anomalous diffusion (Cavaliere et al., 2013).

The results discussed in this paper indicate that the γ parameter of AD depends on both diffusion multi-compartmentalization (as already shown in previous works) and $\Delta\chi$ (as we show here) when MRI is used. After establishing the existence of this dual dependence of the γ parameter we can study how to separate the two dependencies. This is possible by using efficient bipolar diffusion gradients to acquire DW data. Indeed, as shown in Palombo et al. (2012) by using a pulse field gradient sequence with bipolar diffusion gradients, the dependence of γ on $\Delta\chi$ is strongly reduced. In our opinion this may be true also in the case of in vivo experiments. As a consequence, γ parameters quantified by bipolar diffusion gradients should be dependent on the water multi-compartmentalization.

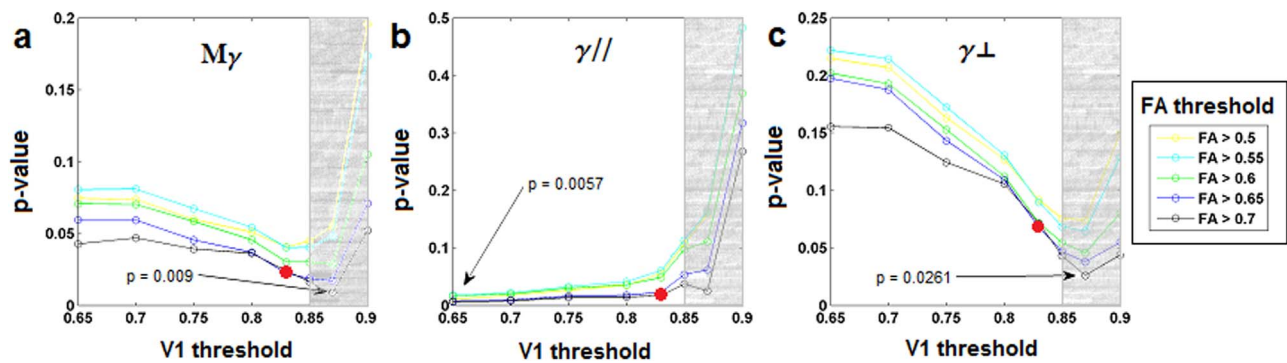


Fig. 13. Behavior of p-value of AD-metrics and R_2^* Pearson's correlation test vs FA and v_1 thresholds. Significance of Pearson's correlation test between Mean- γ (My) (a), axial- γ ($\gamma_{//}$) (b), radial- γ (γ_{\perp}) (c) and R_2^* , plotted vs v_1 thresholds, reported on the x-axis, for different FA thresholds, listed in the legend. The P-values corresponding to the thresholds used for data analysis are indicated by the red dot in the plots. The minimum P-value is indicated by the arrow. The number of voxels is considerably reduced for v_1 thresholds higher than 0.85, represented by the gray region in the plots. (For interpretation of the references to color in this figure legend, the reader is referred to the web version of this article.)

5. Conclusions

In this work, motivated by previous results obtained in vitro, we investigated the dependence of the AD-imaging on magnetic susceptibility differences $\Delta\chi$ in the brain, due to myelin orientation with respect to \mathbf{B}_0 in the WM, and iron content in the GM. We acquired DW data by changing diffusion gradient strengths at a constant value of Δ in a cohort of 25-years healthy subjects at 3.0 T. By using the modality for which data acquisition is obtained by changing g_{diff} strength at a constant value of Δ , the specific AD contrast that we quantified was the intravoxel diffusion heterogeneity in space, the so called pseudo-superdiffusion, which is described by a superdiffusion motion propagator. Water molecules diffuse with considerably different lengths, and this mechanism is quantified by the stretching parameter γ , obtained through a fit of a stretched exponential function to DW data.

To our knowledge, this is the first study that investigated the correlation between AD-metrics and the well known and established R_2^* parameter in vivo. Our results suggest that AD-metrics may reflect the inhomogeneity coming from $\Delta\chi$ among various tissues and compartments, and thus it might be useful as an indirect measure of myelin integrity and iron content.

In our opinion, the results reported and discussed in this manuscript suggest two important conclusions. First, the different lengths by which water diffuse into heterogeneous media and complex systems (such as the brain tissue) are due not only to water multi-compartmentalization, as already underlined by several authors, but also to susceptibility differences between different compartments. This last feature of γ parameters is exclusively due to the fact that we quantify γ by using MRI techniques.

As the internal gradients generated by the difference of susceptibility increase with the increasing intensity of the magnetic field, we expect this effect to be more remarkable at higher magnetic fields (7.0 T and higher). A second conclusion of this work is related to its potential impact in non Gaussian diffusion applications at high magnetic fields. The employment of high-field MRI (7.0 T) scanners for human brain investigation is becoming more and more popular. Depending on $\Delta\chi$ driven magnetic field inhomogeneity, the new contrast provided by the AD- γ imaging could open new perspectives in all MRI fields in which it is important to detect local $\Delta\chi$ changes, such as superparamagnetic contrast molecular imaging, functional imaging (Balla et al., 2014), and neuroimaging aimed at monitoring both microstructural changes and alterations due to iron (Fujiwara et al., 2014) or other iron/paramagnetic impurities accumulation.

References

Abowitz, F., Scheibel, A.B., Fisher, R.S., Zaidel, E., 1992. Individual differences in brain asymmetries and fiber composition in the human corpus callosum. *Brain Res.* 598 (1–2), 154–161. (doi: 110.1016/0006-8993(1992)90179-D).

Alexander, D.C., Barker, G.J., Arridge, S.R., 2002. Detection and modeling of non-

Gaussian apparent diffusion coefficient profiles in human brain data. *Magn. Reson. Med.* 48 (2), 331–340. <http://dx.doi.org/10.1002/mrm.10209>.

Balla, D.Z., Sanchez-Panchuelo, R.M., Wharton, S.J., Hagberg, G.E., Scheffler, K., Francis, S.T., Bowtell, R., 2014. Functional quantitative susceptibility mapping (fQSM). *Neuroimage* 100, 112–124. <http://dx.doi.org/10.1016/j.neuroimage.2014.06.011>.

Bartzokis, G., Beckson, M., Hance, D.B., Marx, P., Foster, J.A., Marder, S.R., 1997. MR evaluation of age-related increase of brain iron in young adult and older normal males. *Magn. Reson. Imaging* 15 (1), 29–35. [http://dx.doi.org/10.1016/S0730-1725X\(1096\)00234-00232](http://dx.doi.org/10.1016/S0730-1725X(1096)00234-00232).

Bartzokis, G., Tishler, T.A., Lu, P.H., Villablanca, P., Altschuler, L.L., Carter, M., Huang, D., Edwards, N., Mintz, J., 2007. Brain ferritin iron may influence age- and gender-related risks of neurodegeneration. *Neurobiol. Aging* 28 (3), 414–423. (doi: 410.1016/j.neurobiolaging.2006.1002.1005).

Budde, M.D., Frank, J.A., 2010. Neurite beading is sufficient to decrease the apparent diffusion coefficient after ischemic stroke. *Proc. Natl. Acad. Sci.* 107 (32), 14472–14477. (doi: 14410.11073/pnas.1004841107).

Capuani, S., Palombo, M., Gabrielli, A., Orlandi, A., Maraviglia, B., Pastore, F.S., 2013. Spatio-temporal anomalous diffusion imaging: results in controlled phantoms and in excised human meningiomas. *Magn. Reson. Imaging* 31 (3), 359–365. (doi: 310.1016/j.mri.2012.1008.1012).

Cavaliere, M., Palombo, M., Alessandro, G., Gabrielli, A., Bifone, A., Capuani, S., 2013. New insights into γ -stretched exponential anomalous-diffusion imaging experiments proceedings of the 21th scientific meeting. *Int. Soc. Magn. Reson. Med.*

Chavhan, G.B., Babyn, P.S., Thomas, B., Shroff, M.M., Haacke, E.M., 2009. Principles, techniques, and applications of T_2^* -based MR imaging and its special applications 1. *Radiographics* 29 (5), 1433–1449. (doi: 1410.1148/rg.295095034).

Chen, W.C., Foxley, S., Miller, K.L., 2013. Detecting microstructural properties of white matter based on compartmentalization of magnetic susceptibility. *Neuroimage* 70, 1–9. <http://dx.doi.org/10.1016/j.neuroimage.2012.1012.1032>.

Cherubini, A., Péran, P., Hagberg, G.E., Varsi, A.E., Luccichenti, G., Caltagirone, C., Sabatini, U., Spalletta, G., 2009. Characterization of white matter fiber bundles with T_2^* relaxometry and diffusion tensor imaging. *Magn. Reson. Med.* 61 (5), 1066–1072. (doi: 1010.1002/mrm.21978).

De Santis, S., Gabrielli, A., Bozzali, M., Maraviglia, B., Macaluso, E., Capuani, S., 2011. Anisotropic anomalous diffusion assessed in the human brain by scalar invariant indices. *Magn. Reson. Med.* 65 (4), 1043–1052. (doi: 1010.1002/mrm.22689).

De Santis, S., Rebuffi, M., Di Pietro, G., Fasano, F., Maraviglia, B., Capuani, S., 2010. In vitro and in vivo MR evaluation of internal gradient to assess trabecular bone density. *Phys. Med. Biol.* 55 (19), 5767. <http://dx.doi.org/10.1088/0031-9155/55/19/010>.

Denk, C., Torres, E.H., MacKay, A., Rauscher, A., 2011. The influence of white matter fibre orientation on MR signal phase and decay. *NMR Biomed.* 24 (3), 246–252. (doi: 210.1002/nbm.1581).

Descoteaux, M., Deriche, R., Le Bihan, D., Mangin, J.-F., Poupon, C., 2011. Multiple q-shell diffusion propagator imaging. *Med. Image Anal.* 15 (4), 603–621. (doi: 610.1016/j.media.2010.1007.1001).

Desikan, R.S., Ségonne, F., Fischl, B., Quinn, B.T., Dickerson, B.C., Blacker, D., Buckner, R.L., Dale, A.M., Maguire, R.P., Hyman, B.T., 2006. An automated labeling system for subdividing the human cerebral cortex on MRI scans into gyral based regions of interest. *Neuroimage* 31 (3), 968–980. (doi: 910.1016/j.neuroimage.2006.1001.1021).

Di Pietro, G., Palombo, M., Capuani, S., 2014. Internal magnetic field gradients in heterogeneous porous systems: comparison between spin-echo and diffusion decay internal field (DDIF) method. *Appl. Magn. Reson.* 45 (8), 771–784. (doi: 710.1007/s00723-00014-00556-00720).

Duyn, J., 2013. MR susceptibility imaging. *J. Magn. Reson.* 229, 198–207. (doi: 110.1016/j.jmr.2012.1011.1013).

Duyn, J.H., van Gelderen, P., Li, T.-Q., de Zwart, J.A., Koretsky, A.P., Fukunaga, M., 2007. High-field MRI of brain cortical substructure based on signal phase. *Proc. Natl. Acad. Sci.* 104 (28), 11796–11801. (doi: 11710.11073/pnas.0610821104).

Fujiwara, S., Uhrig, L., Amadon, A., Jarraya, B., Le Bihan, D., 2014. Quantification of

- iron in the non-human primate brain with diffusion-weighted magnetic resonance imaging. *Neuroimage* 102, 789–797. <http://dx.doi.org/10.1016/j.neuroimage.2014.08.049>.
- GadElkarim, J.J., Magin, R.L., Meerschaert, M.M., Capuani, S., Palombo, M., Kumar, A., Leow, A.D., 2013. Fractional order generalization of anomalous diffusion as a multidimensional extension of the transmission line equation. *IEEE J. Emerg. Sel. Top. Circuits Syst.* 3 (3), 432–441. (doi: 410.1109/JETCAS.2013.2265795).
- Gelman, N., Gorell, J.M., Barker, P.B., Savage, R.M., Spickler, E.M., Windham, J.P., Knight, R.A., 1999. MR imaging of human brain at 3.0 T: preliminary report on transverse relaxation rates and relation to estimated iron content. *Radiology* 210 (3), 759–767. (doi: 710.1148/radiology.1210.1143.r1199fe41759).
- Gong, N.-J., Wong, C.-S., Chan, C.-C., Leung, L.-M., Chu, Y.-C., 2014. Aging in deep gray matter and white matter revealed by diffusional kurtosis imaging. *Neurobiol. Aging* 35 (10), 2203–2216. (doi: 2210.1016/j.neurobiolaging.2014.2203.2011).
- Graham, M.S., Drobnyak, I., Zhang, H., 2016. Realistic simulation of artefacts in diffusion MRI for validating post-processing correction techniques. *NeuroImage* 125, 1079–1094. (doi: 1010.1016/j.neuroimage.2015.1011.1006).
- Haacke, E.M., Miao, Y., Liu, M., Habib, C.A., Katkuri, Y., Liu, T., Yang, Z., Lang, Z., Hu, J., Wu, J., 2010. Correlation of putative iron content as represented by changes in R_2^* and phase with age in deep gray matter of healthy adults. *J. Magn. Reson. Imaging* 25 (2), 286–294. (doi: 510.1002/jmri.22293).
- Haacke, E.M., Xu, Y., Cheng, Y.C.N., Reichenbach, J.R., 2004. Susceptibility weighted imaging (SWI). *Magn. Reson. Med.* 52 (3), 612–618. (doi: 610.1002/mrm.20198).
- Hall, M.G., Barrick, T.R., 2012. Two-step anomalous diffusion tensor imaging. *NMR Biomed.* 25 (2), 286–294. (doi: 210.1002/nbm.1747).
- Hallgren, B., Sourander, P., 1958. The effect of age on the non-heme iron in the human brain. *J. Neurochem.* 3 (1), 41–51. <http://dx.doi.org/10.1111/j.1471-4159.1958.tb12607.x>.
- Ingo, C., Magin, R.L., Colon-Perez, L., Triplett, W., Mareci, T.H., 2014. On random walks and entropy in diffusion-weighted magnetic resonance imaging studies of neural tissue. *Magn. Reson. Med.* 71 (2), 617–627. (doi: 610.1002/mrm.24706).
- Jenkinson, M., Bannister, P., Brady, M., Smith, S., 2002. Improved optimization for the robust and accurate linear registration and motion correction of brain images. *Neuroimage* 17 (2), 825–841. (doi: 810.1006/nimg.2002.1132).
- Jenkinson, M., Beckmann, C.F., Behrens, T.E., Woolrich, M.W., Smith, S.M., 2012. Fsl. *Neuroimage* 62 (2), 782–790. (doi: 710.1016/j.neuroimage.2011.1009.1015).
- Jones, D.K., Basser, P.J., 2004. Squashing peanuts and smashing pumpkins: how noise distorts diffusion-weighted MR data. *Magn. Reson. Med.* 52, 979–993. <http://dx.doi.org/10.1002/mrm.2028>.
- Jones, D.K., Knösche, T.R., Turner, R., 2013. White matter integrity, fiber count, and other fallacies: the do's and don'ts of diffusion MRI. *Neuroimage* 73, 239–254. (doi: 210.1016/j.neuroimage.2012.1006.1081).
- Langkammer, C., Krebs, N., Goessler, W., Scheurer, E., Yen, K., Fazekas, F., Ropele, S., 2012. Susceptibility induced gray–white matter MRI contrast in the human brain. *Neuroimage* 59 (2), 1413–1419. (doi: 1410.1016/j.neuroimage.2011.1408.1045).
- Lee, J., Shmueli, K., Fukunaga, M., van Gelderen, P., Merkle, H., Silva, A.C., Duyn, J.H., 2010. Sensitivity of MRI resonance frequency to the orientation of brain tissue microstructure. *Proc. Natl. Acad. Sci.* 107 (11), 5130–5135. (doi: 5110.1073/pnas.0910221107).
- Li, T.Q., Yao, B., van Gelderen, P., Merkle, H., Dodd, S., Talagala, L., Koretsky, A.P., Duyn, J., 2009. Characterization of T_2^* heterogeneity in human brain white matter. *Magn. Reson. Med.* 62 (6), 1652–1657. (doi: 1610.1002/mrm.22156).
- Li, W., Langkammer, C., Chou, Y.-H., Petrovic, K., Schmidt, R., Song, A.W., Madden, D.J., Ropele, S., Liu, C., 2015. Association between increased magnetic susceptibility of deep gray matter nuclei and decreased motor function in healthy adults. *NeuroImage* 105, 45–52. <http://dx.doi.org/10.1016/j.neuroimage.2014.1010.1009>.
- Li, W., Wu, B., Avram, A.V., Liu, C., 2012. Magnetic susceptibility anisotropy of human brain in vivo and its molecular underpinnings. *Neuroimage* 59 (3), 2088–2097. (doi: 2010.1016/j.neuroimage.2011.2010.2038).
- Li, W., Wu, B., Batrachenko, A., Bancroft-Wu, V., Morey, R.A., Shashi, V., Langkammer, C., Bellis, M.D., Ropele, S., Song, A.W., 2014. Differential developmental trajectories of magnetic susceptibility in human brain gray and white matter over the lifespan. *Human. Brain Mapp.* 35 (6), 2698–2713. (doi: 2610.1002/hbm.22360).
- Li, W., Wu, B., Liu, C., 2011. Quantitative susceptibility mapping of human brain reflects spatial variation in tissue composition. *Neuroimage* 55 (4), 1645–1656. (doi: 1610.1016/j.neuroimage.2010.1611.1088).
- Liu, C., 2010. Susceptibility tensor imaging. *Magn. Reson. Med.* 63 (6), 1471–1477. (doi: 1410.1002/mrm.22482).
- Lounila, J., Ala-Korpela, M., Jokisari, J., Savolainen, M., Kesäniemi, Y., 1994. Effects of orientational order and particle size on the NMR line positions of lipoproteins. *Phys. Rev. Lett.* 72 (25), 4049. (doi: 4010.1103/PhysRevLett.4072.4049).
- Luszczek, P., 2009. Parallel programming in MATLAB. *Int. J. High Perform. Comput. Appl.* 23 (3), 277–283. (doi: 210.1177/1094342009106194).
- Magin, R.L., Abdullah, O., Baleanu, D., Zhou, X.J., 2008. Anomalous diffusion expressed through fractional order differential operators in the Bloch–Torrey equation. *J. Magn. Reson.* 190 (2), 255–270. (doi: 210.1016/j.jmr.2007.1011.1007).
- Mitchell, J., Chandrasekera, T., Johns, M., Gladden, L., Fordham, E., 2010. Nuclear magnetic resonance relaxation and diffusion in the presence of internal gradients: the effect of magnetic field strength. *Phys. Rev. E* 81 (2), 026101. (doi: 026110.021103/PhysRevE.026181.026101).
- Mitsumori, F., Watanabe, H., Takaya, N., Garwood, M., Auerbach, E.J., Michaeli, S., Mangia, S., 2012. Toward understanding transverse relaxation in human brain through its field dependence. *Magn. Reson. Med.* 68 (3), 947–953. (doi: 910.1002/mrm.23301).
- Mori, S., Oishi, K., Jiang, H., Jiang, L., Li, X., Akhter, K., Hua, K., Faria, A.V., Mahmood, A., Woods, R., 2008. Stereotaxic white matter atlas based on diffusion tensor imaging in an ICBM template. *Neuroimage* 40 (2), 570–582. (doi: 510.1016/j.neuroimage.2007.1012.1035).
- Mulkern, R.V., Gudbjartsson, H., Westin, C.F., Zengingonul, H.P., Gartner, W., Guttman, C.R., et al., 1999. Multi-component apparent diffusion coefficients in human brain. *NMR Biomed.* 12 (1), 51–62. [http://dx.doi.org/10.1002/\(sici\)1099-1492\(199902\)12:1](http://dx.doi.org/10.1002/(sici)1099-1492(199902)12:1).
- Nair, G., Tanahashi, Y., Low, H.P., Billings-Gagliardi, S., Schwartz, W.J., Duong, T.Q., 2005. Myelination and long diffusion times alter diffusion-tensor-imaging contrast in myelin-deficient shiverer mice. *Neuroimage* 28 (1), 165–174. (doi: 110.1016/j.neuroimage.2005.1005.1049).
- Nam, Y., Han, D., Kim, D.-H., 2012. Single-scan R_2^* measurement with macroscopic field inhomogeneity correction. *Neuroimage* 63 (4), 1790–1799. (doi: 1710.1016/j.neuroimage.2012.1708.1062).
- Novikov, D.S., Jensen, J.H., Helpert, J.A., Fieremans, E., 2014. Revealing mesoscopic structural universality with diffusion. *Proc. Natl. Acad. Sci.* 111 (14), 5088–5093. (doi: 5010.1073/pnas.1316944111).
- Palombo, M., Gabrielli, A., De Santis, S., Cametti, C., Ruocco, G., Capuani, S., 2011. Spatio-temporal anomalous diffusion in heterogeneous media by nuclear magnetic resonance. *J. Chem. Phys.* 135 (3), 034504. (doi: 034510.031063/034501.3610367).
- Palombo, M., Gabrielli, A., De Santis, S., Capuani, S., 2012. The γ parameter of the stretched-exponential model is influenced by internal gradients: validation in phantoms. *J. Magn. Reson.* 216, 28–36. <http://dx.doi.org/10.1016/j.jmr.2011.1012.1023>.
- Pfefferbaum, A., Adalsteinsson, E., Rohlfing, T., Sullivan, E.V., 2010. Diffusion tensor imaging of deep gray matter brain structures: effects of age and iron concentration. *Neurobiol. Aging* 31 (3), 482–493. (doi: 410.1016/j.neurobiolaging.2008.1004.1013).
- Rauscher, A., Sedlacik, J., Barth, M., Mentzel, H.-J., Reichenbach, J.R., 2005. Magnetic susceptibility-weighted MR phase imaging of the human brain. *Am. J. Neuroradiol.* 26 (4), 736–742.
- Reiter, D.A., Magin, R.L., Li, W., Trujillo, J.J., Velasco, M.P., Spencer, R.G., 2016. *Magn. Reson. Med.* 76 (3), 953–962. <http://dx.doi.org/10.1002/mrm.25913>.
- Ronen, I., Budde, M., Ercan, E., Anness, J., Techawiboonwong, A., Webb, A., 2014. Microstructural organization of axons in the human corpus callosum quantified by diffusion-weighted magnetic resonance spectroscopy of N-acetylaspartate and post-mortem histology. *Brain Struct. Funct.* 219 (5), 1773–1785. (doi: 1710.1007/s00429-00013-00600-00420).
- Rudko, D.A., Klassen, L.M., de Chikera, S.N., Gati, J.S., Dekaban, G.A., Menon, R.S., 2014. Origins of R_2^* orientation dependence in gray and white matter. *Proc. Natl. Acad. Sci.* 111 (1), E159–E167. (doi: 110.1073/pnas.1306516111).
- Sati, P., Silva, A.C., van Gelderen, P., Gaitan, M.I., Wohler, J.E., Jacobson, S., Duyn, J.H., Reich, D.S., 2012. In vivo quantification of T_2^* anisotropy in white matter fibers in marmoset monkeys. *Neuroimage* 59 (2), 979–985. (doi: 910.1016/j.neuroimage.2011.1008.1064).
- Schmierer, K., Parkes, H.G., So, P.-W., An, S.F., Brandner, S., Ordidge, R.J., Yousry, T.A., Miller, D.H., 2010. High field (9.4 T) magnetic resonance imaging of cortical grey matter lesions in multiple sclerosis. *Brain* 133 (3), 858–867. (doi: 810.1093/brain/awp1335).
- Sharma, G., Martin, J., 2009. MATLAB®: a language for parallel computing. *Int. J. Parallel Program.* 37 (1), 3–36. <http://dx.doi.org/10.1007/s10766-10008-10082-10765>.
- Sukstanskii, A.L., Yablonskiy, D.A., 2014. On the role of neuronal magnetic susceptibility and structure symmetry on gradient echo MR signal formation. *Magn. Reson. Med.* 71 (1), 345–353. (doi: 310.1002/mrm.24629).
- Tepper, S.J., Lowe, M.J., Beall, E., Phillips, M.D., Liu, K., Stillman, M.J., Horvat, M., Jones, S.E., 2012. Iron deposition in pain-regulatory nuclei in episodic migraine and chronic daily headache by MRI. *Headache: J. Head Face Pain* 52 (2), 236–243. (doi: 210.1111/j.1526-4610.2011.02056.x).
- Todorich, B.M., Connor, J.R., 2004. Redox metals in Alzheimer's disease. *Ann. N.Y. Acad. Sci.* 1012 (1), 171–178. (doi: 110.1196/annals.1306.1014).
- Yablonskiy, D.A., Haacke, E.M., 1994. Theory of NMR signal behavior in magnetically inhomogeneous tissues: the static dephasing regime. *Magn. Reson. Med.* 32 (6), 749–763. (doi: 710.1002/mrm.1910320610).
- Yablonskiy, D.A., Sukstanskii, A.L., 2014. Biophysical mechanisms of myelin-induced water frequency shifts. *Magn. Reson. Med.* 71 (6), 1956–1958. (doi: 1910.1002/mrm.25214).
- Yao, B., Li, T.-Q., van Gelderen, P., Shmueli, K., de Zwart, J.A., Duyn, J.H., 2009. Susceptibility contrast in high field MRI of human brain as a function of tissue iron content. *Neuroimage* 44 (4), 1259–1266. (doi: 1210.1016/j.neuroimage.2008.1210.1029).
- Zecca, L., Youdim, M.B., Riederer, P., Connor, J.R., Crichton, R.R., 2004. Iron, brain ageing and neurodegenerative disorders. *Nat. Rev. Neurosci.* 5 (11), 863–873. (doi: 810.1038/nrn1537).
- Zhou, X.J., Gao, Q., Abdullah, O., Magin, R.L., 2010. Studies of anomalous diffusion in the human brain using fractional order calculus. *Magn. Reson. Med.* 63 (3), 562–569. (doi: 510.1002/mrm.22285).